Likelihood-based Optimization in Strong-motion Seismology

Sebastian von Specht

Likelihood-based Optimization in Strong-motion Seismology

Cumulative dissertation
for the degree of
doctor rerum naturalium
(Dr. rer. nat.)
in Seismology

submitted to the Faculty of Science
at the University of Potsdam

by

Sebastian von Specht

Supervisors:
Prof. Dr. Fabrice Cotton
Prof. Dr. Frank Scherbaum

submitted on 22nd of May 2019
defended on 25th of October 2019

Declaration of Authorship

I, Sebastian Specht (alias: Sebastian von Specht), hereby declare that, to the best of my knowledge, this work does not bear resemblance to any other work in whole or in part and has been completed by myself. I did not use any other sources and means than specified. Furthermore, this work has not been previously submitted to any university. All sources have been referred to and this work gives adequate credit to others for their work. I, in no way, claim to have created this information myself.

Date Signature

Zusammenfassung

Der Teil der Seismologie, der sich mit starker Bodenbewegung beschäftigt, bezieht sich auf seismische Ereignisse, die allgemein ein Gefahrenpotenzial für die Gesellschaft darstellen. Die Seismologie der starken Bodenbewegung wird von zwei Aspekten angetrieben: An erster Stelle kommt die gesellschaftliche Notwendigkeit, die Erdbebengefährdung zu verstehen und das damit verbundene Risiko zu vermeiden. Während die Gefährdung durch Erdbeben kaum Änderungen in der Geschichte der Menschheit unterlag, so wächst das Risiko andererseits kontinuierlich an. Eine wachsende Bevölkerung, insbesondere in den am stärksten von Erdbeben geprägten Regionen der Welt, und eine mehr und mehr störungsanfällige Infrastruktur, tragen dazu bei, seismische Ereignissen vermehrt ausgesetzt zu sein, bei gleichzeitig höherem Schadenspotenzial. Der zweite Antrieb in der Seismologie wird mit vielen anderen Forschungsfeldern geteilt: der technische Fortschritt. Die verfügbaren Möglichkeiten beim Verarbeiten immer größerer Datenmengen sind beispiellos in der Geschichte und sind bisher noch nicht erschöpft. Beide Triebfedern stellen aber auch neue Herausforderungen dar, inwiefern die Daten zu interpretieren sind und wie man sie nutzbar macht.

Andererseits ist die wissenschaftliche Frage klar: Was können wir aus Bruchprozessen (als Erdbebenursachen), dem Aufbau der Erde (als Medium, durch welches sich die seismischen Wellen ausbreiten), sowie deren Interaktion (inwiefern beeinflusst das Beben das umgebende Gesteinsmedium)? Diese Frage ist breit gestellt und diese Abhandlung kann sich letztlich nur auf einige Punkte beziehen und Antworten dazu liefern. Um Antworten zu finden, habe ich mehrere neue Algorithmen und Modelle entwickelt, die allesamt auf dem Konzept der Likelihood-Funktion beruhen.

Seismizität (sowie auch die Bevölkerung) ist stark an den Rändern der tektonischen Platten konzentriert. An den Plattenrändern treten verschiedene Erdbebentypen mit teils erheblich abweichenden Eigenschaften auf. Daher ist es von Wichtigkeit, Erdbeben nach ihrem Verwerfungstyp zu klassifizieren. Das Ziel von ACE (angular clusterization with expectation-maximization, zu dt. ungefähr Winkelgruppenbestimmung mit Erwartungswertmaximierung) ist genau diese Klassifizierung. Auf geomechanischen Prinzipien basierend, können die Erdbebenklassifizierungen mittels ACE nicht nur auf Themen der Bodenbewegungen angewandt werden, sondern auch zur Untersuchung des Spannungsfeldes der Erde herangezogen werden.

Der Entwicklung von verlässlichen Bodenbewegungsmodellen bedarf es Wellenformdaten hoher Güte. Instrumenten bezogene Fehler können die Qualität beeinträchtigen, jedoch ist eine manuelle Korrektur großer Datenmengen nicht mehr umsetzbar. Um Instrumentenfehler, die sich in Verschiebungen in den Daten zeigen, zu reduzieren, habe ich eine Nulllinienkorrektur entwickelt (ICBM, integrated combined baseline modification, zu dt. integriert kombinierte Nulllinienmodifikation). Dieser Algorithmus wird in der Datenvorbereitung eingesetzt und ist insbesondere dann notwendig, wenn integrierte Größen auf Grundlage von Beschleunigungsdaten bestimmt werden, wie statischer Versatz eines Erdbebens als auch abgestrahlte seismische Energie.

Abgestrahlte seismische Energie spielt eine herausragende Rolle in der Entwicklung einer neuen Art von Bodenbewegungsmodell, welches anstellen von Magnituden stationsabhängige Energieabschätzungen nutzt, um die Erdbebenabstrahlcharakteristik auf tieferen Frequenzen des Erdbebenspektrums zu beschreiben. Diese Art Bodenbewegungsmodell ist besser geeignet, wenn Bodenbewegungen in Bezug zu Hangrutschungen, welche durch Erdbeben verursacht wurden, gesetzt werden. Als Beispiel dienen hier die Hangrutschungen, die 2016 durch das Erdbeben in Zentralkyuschu (Japan) mit einer Momentenmagnitude von 7.1 verursacht wurden. In dieser Fallstudie wird auch aufgezeigt, wie die Bewegungsrichtung der Hangrutschungen zu einem gewissen Grad durch die Ausrichtung des seismischen Wellenfeldes beeinflusst werden.

Das bevorzugte mathematische Modell in der Seismologie zur Beschreibung starker Bodenbewegungen ist das gemischte Modell. Jedoch lässt der weitläufig angewendete Formalismus nur die Einbettung von Gewichten in Form von Messunsicherheiten zu. Gewichte wie sie von ACE erzeugt werden, die in keinem direkten Bezug zur Messgröße stehen, liefern zwangsläufig verzerrte Ergebnisse. Um dieses Problem zu umgehen, habe ich Parameterschätzer auf Basis einer gewichteten Likelihood hergeleitet. Die rigorose Herleitung erlaubt sämtliche Arten des gemischten Modells, wie sie zur Beschreibung von Bodenbewegungen genutzt werde, mit Datengewichtungen zu kombinieren. Dieser Formalismus in Verbindung mit ACE erlaubt die Entwicklung nachvollziehbarer Modelle und vermeidet Entscheidungen auf subjektiver Expertenmeinung.

Abstract

The branch of seismology that deals with strong motion refers to seismic events that are hazardous to society in general. Two aspects drive the development in strong-motion seismology: First comes the societal need to understand the earthquake hazard and to mitigate the associated risk. While the hazard changed little during human history, the risk increases steadily. A growing population—also in the most earthquake-prone regions of the world—and a more and more vulnerable infrastructure contribute to higher exposure to seismic events and higher vulnerability in case an earthquake struck. The second driver in strong-motion seismology is shared with many other fields: the technological advancement. The available options for processing more and more data is unprecedented in human history and are still not exhausted. Both drivers also pose new challenges as in how to interpret and make use of the data.

The scientific question, on the other hand, is clear: What can we learn from the rupture process (the source of earthquakes), Earth's structure (the medium through which seismic wave travels), and their interactions (how does an earthquake affect its surrounding medium)? The question is broad and this thesis can focus only for specific aspects of this question and provide answers for them. To reach the answers, I developed several new algorithms and models, all rooted in the concept of the likelihood function.

Seismicity (and population alike) is concentrated along the tectonic plate boundaries. Different earthquake types occur at these boundaries and their characteristics in terms of ground shaking are considerably different. It is therefore important to classify earthquakes according to their style of faulting. This classification is the objective of ACE (angular clusterization with expectation-maximization). Founded on the geomechanical principles, ACE provides earthquake classifications which can be applied not only for ground-motion related topics but also to study the Earth's stress field.

The development of reliable ground-motion models requires waveform data of high quality. Instrument related errors can compromise the data quality, however, with large archives of waveform data, the correction for spurious s cannot be handled manually anymore. To alleviate the effect of instrument related data shifts, I developed the integrated combined baseline modification (ICBM). This routine is implemented during the data pre-processing and is particularly necessary when determining integrated quantities from acceleration records, such as coseismic displacement and radiated seismic energy.

Radiated seismic energy plays a major role in the development of a new type of ground-motion model that uses the site-dependent energy estimates to model the seismic radiation pattern at lower frequencies of the earthquake amplitude spectrum. This kind of ground-motion model performs better when relating ground motion to earthquake triggered landslides, which is demonstrated with the landslides triggered by the 2016 M_W 7.1 Kumamoto earthquake which struck central Kyushu (Japan). In this case study, it is also shown that the landslide movement direction is to some extent linked to the seismic wave polarization.

The preferred mathematical model in ground-motion model development is the mixed-effect model. However, the most widely used formalism does not allow data weighting beyond directly related measurement errors and weights derived from ACE would inadvertently bias the model. To overcome this problem, I derived the model estimators on the basis of the weighted likelihood. The derivation is exhaustive to allow for any of the currently used model types on the basis of mixed effects to be augmented with data weighting. This formalism in connection with ACE allows for a transparent model development and also avoids model choices on subjective expert judgment.

Contents

List of Figures

List of Tables

O nova picturae miracula, transit ad esse
Quod nihil esse potest! picturaque simia veri,
Arte nova ludens, in res umbracula rerum
Vertit et in verum mendacia singula mutat.

O new miracle of the image. It becomes to be
what cannot be and the image of the truth,
playing in the new art, turns the shadows of things into things,
and transforms the falsehood of the image into truth.

Alain de Lille (Alanus ab Insulis),
c. 1128–1202/03, Anticlaudianus, I, V. 123–125

Chapter 1

Introduction

The study of Earth as a distinct science is young compared to mathematics and the three classical natural sciences of physics, chemistry, and biology. Its young age of some 200 years can be also credited to the necessary advancements in the classical sciences. The real breakthrough of the Earth sciences, however, would not occur until the twentieth century. The 1906 San Francisco earthquake triggered the formation of the Seismological Society of America, the first such society to solely investigate earthquakes. The first seismometer to ever record an earthquake on the other side of the planet was in 1889 (von Rebeur-Paschwitz, 1889) and a few decades on, systematic studies of earthquakes all around the world gave way to the discovery of the inner Earth's structure with its liquid outer core by Lehmann (1936). In the same time theoretical concepts about the origin of continent drift and the distribution of fossil records and geological units led A. Wegener in the 1910s and 1920s (Wegener, 1915, 1924) to develop the idea of plate tectonics which was later confirmed by remnant magnetization in ocean basalts in the middle of the twentieth century, today known as the Vine–Matthews–Morley hypothesis (Vine & Matthews, 1963). Today, plate tectonics and seismology are linked, as plate tectonics is recognized as the primary driver for Earth's seismicity.

Earth sciences have always been linked to other scientific fields and advances therein. In recent decades technological development brought even faster progress and the generally simple and coarse models make way to more differentiated models. Today we know that the Earth's inner core is inhomogenuous and with today's computational power available we can even extract information about the Earth's interior from what still is sometimes called seismic noise (Huang et al., 2015).

The currently growing generation of Earth scientists is working at new frontiers and while mathematics was always part of Earth sciences—with geophysics in particular—new challenges arise in how to interpret the plethora of data. The strategies and skills to solve problems for current students differ drastically from the study times of their predecessors. With the advent of widespread computer usage and the information age, the available options for processing ever increasing amounts of data shifted to such proportions that one easily loses sight of all of them, and is limited in the end by our imagination. Besides the prerequisite knowledge of a programming language (or some other means of data processing), mathematics and statistics became indispensably connected to many Earth science fields as a means to know what to program in the first place.

in this thesis, the focus is on strong-motion seismology , i.e. the part of seismology linked to damaging earthquakes, which is linked to hazard assessment and connects this work also to engineering. Besides strong-motion seismology, other fields of Earth sciences are touched such as geomechanics and geomorphology. For the model development, the mathematical focus is—in most general terms—on the likelihood function. Even if not explicitly stated everywhere because it occurs and is related to expectation-maximization, information entropy, or least squares and its relatives, the likelihood is part throughout the thesis.

1.1 Strong-motion seismology

This section will not cover the entire field of strong-motion seismology, but provide an overview of what will be encountered in the chapters to come. Strong motion refers to ground shaking that is of engineering concern and due to scaling relations of earthquakes relates to earthquakes of $M_W > 4.5$. There is therefore a large focus on the seismically active regions along the tectonic plate boundaries, since these regions are not only prone to earthquakes but also densely populated (Fig. 1.1). Seismicity in these regions occurs at the interface of two plates—usually an oceanic plate is subducted underneath another plate—resulting in the most devastating earthquakes recorded. Nearly all major earthquake with $M_W > 8$ are reverse-faulting interface earthquakes at oceanic-continental collision zones. The second type of earthquakes associated with subduction zones occur in the subducting slab of the oceanic plate underneath another plate. While these typically normal-faulting events are of lower magnitudes than the interface events, they are still considerable. Major strike-slip fault systems are the third major source of earthquakes at plate boundaries. These faults exist along plate boundaries (e.g. the San Andreas fault in California) as well as behind the subduction zones, further to the interior of the continental plates (e.g. the median tectonic line in Japan). Due to their shallow depths and location on land, earthquakes even of lesser magnitudes at these faults are very hazardous, as cities and infrastructure are frequently close to major strike-slip faults (to name a few: the Bay area in California, the Kansai region

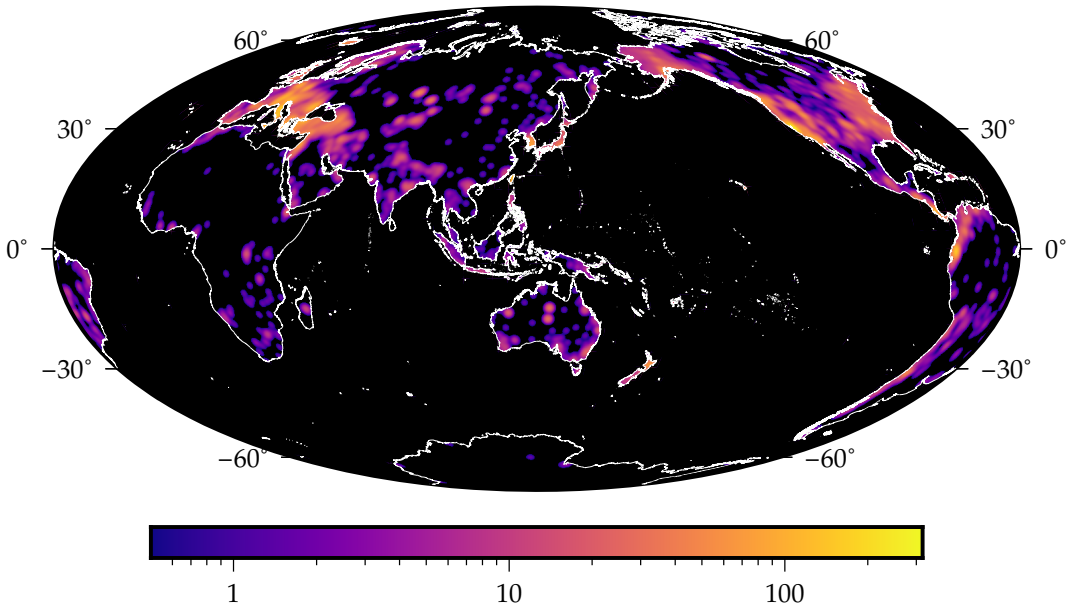

Number of seismic stations per 10^5 km^2

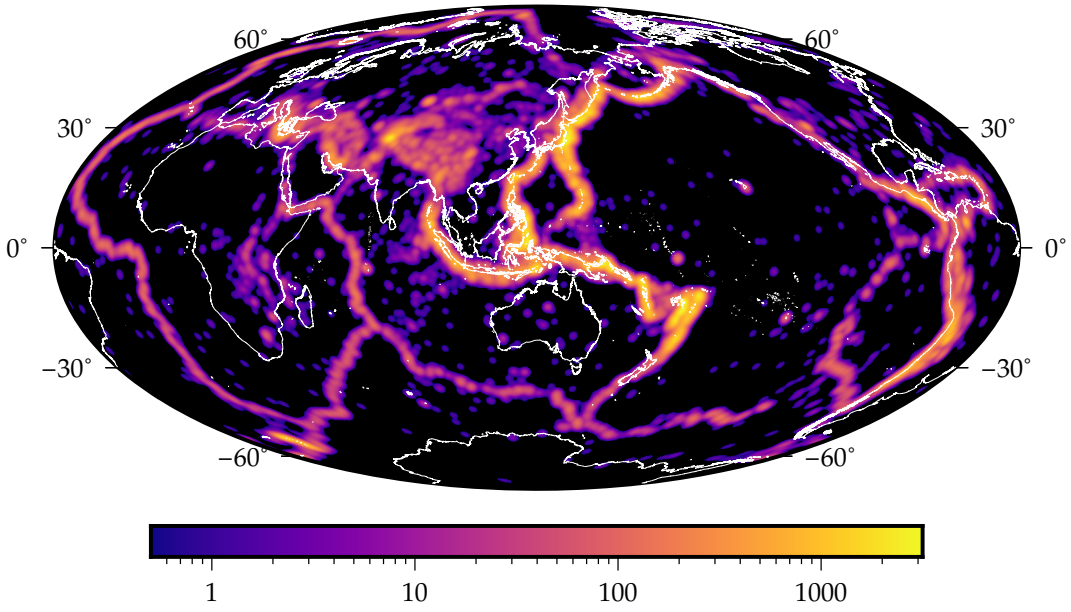

Number of earthquakes per 10^5 km^2

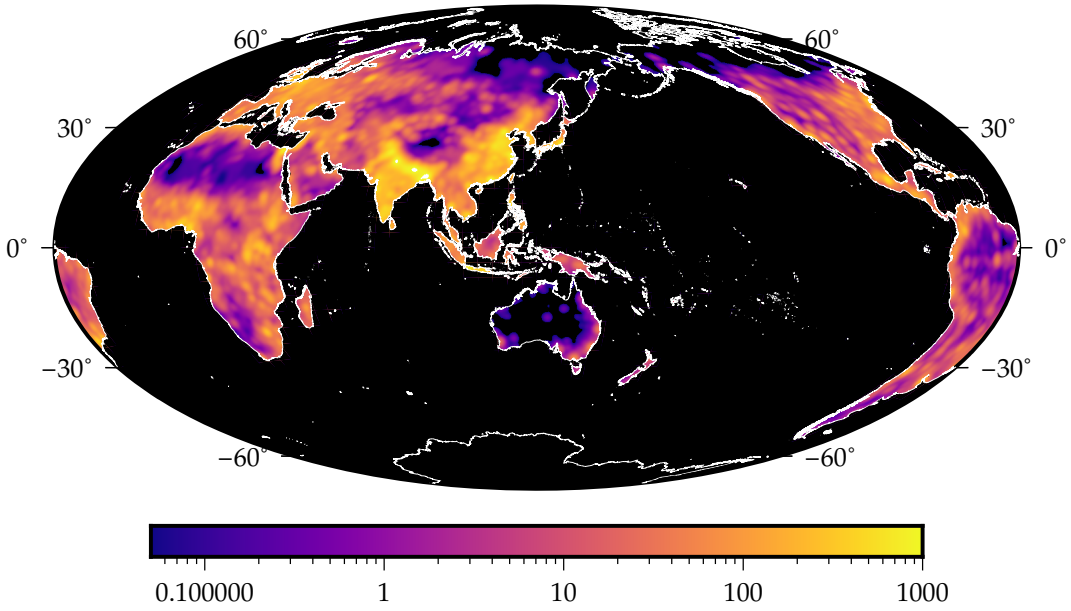

Population density [capita per km^2]

Figure 1.1: top: Global distribution of stations registered with ISC (International Seismological Centre) and operating as of May 2019. Most stations are located in the northern hemisphere with high concentrations in Europe, East Asia and North America.
Middle: Global earthquake distribution of the EHB catalog (1960-2016). The EHB catalog includes only events with high-precision hypocenters, thus the plate boundaries are sharply outlined. The ring of fire—encircling the entire Pacfic Ocean—has highest earthquake rates, affecting all adjacent regions. Nearly all recorded M_W 9.0 earthquakes occurred on the ring of fire (The Sumatra earthquake in 2004 is the only exception)
. Bottom: Global population density projection for 2020. Regions heavily affected by seismicity are also often densely populated, like the Mediterranean region in Europe, East and Southeast Asia, and the most of the west coast of the Americas.

in Japan, the metropolitan area of Istanbul (Turkey)).

The main focus of strong-motion seismology is to understand and model ground shaking in a way that the models can be used in engineering and hazard assessment. Since the development of the first ground motion models in the 1950s, a certain standard of data and model processing developed over the decades (Kramer, 1996). The procedure consists of two steps: (1) Data pre-processing and (2) model development. The processing can be cumbersome and tasks may be conducted on case-by-case basis, e.g. in waveform processing (Boore & Bommer, 2005). Automatization is therefore one reason to handle the ever increasing data amount (Fig. 1.2). With more data, finer details of the processes governing ground shaking can be investigated, relying on more advanced data processing techniques.

The pre-processing of the data consists of a series of steps to prepare the data for the model development(Boore & Bommer, 2005). Here, the data consists of waveforms measured on accelerometers and metadata covering

1. earthquake location (hypocenter or rupture plane),
2. station location and site conditions (e.g. V_{S30}, κ)
3. magnitude (preferably in non saturating magnitude scales like M_W or M_E)
4. event type (interface, intraslab, crustal)

From the metadata, the distances between earthquakes and stations are computed. The three most widely used metrics are the hypocentral distance, the Joyner-Boore distance (shortest distance along the surface between a surface projection of the rupture plane and a station) and the rupture plane distance (shortest distance between the rupture plane and a station). Earthquake classification can be based on hypocenter location with respect to a predefined geometry related to the plate interface, or if moment tensors or focal mechanisms are available, the rake angles or the plunge of the P-axis is used as an indicator.

Since ground-motion models (GMMs) are defined in the response spectral domain—with recent developments in the Fourier spectral domain as well—the pre-processing of the waveforms aims to reduce biases that are inherent in the spectral computations of signals of finite length.

The typical workflow for a single record consists of the following steps:

1. Cut waveform window from continuous data. The data window should contain pre-event waveforms (noise) and the event including the coda.
2. Baseline correction. This step removes the static offset and the linear trend in the data. Otherwise and due to the finite signal length, all spectral estimates would be increased. The baseline correction is also important when spectral properties of the integrated traces are investigated (peak ground velocity, peak ground displacement)
3. Zero-padding and tapering. The extracted data window can be seen as a convolution of an infinite signal with a rectangular (box) function of finite length. The rectangular function has undesirable spectral properties (large sidelobes) which contaminate the signal spectrum. To reduce the distortion, the signal is tapered with a smoothly decaying function (e.g. cosine) on either side and zeros are padded on either side.
4. Computation of spectra. Based on the Fourier transforms of the pre-event (noise) signal and of the event itself a signal-to-noise (S/N) ratio is determined. If the S/N exceeds a threshold (e.g. 3) for given frequencies then the response spectrum at these frequencies is determined.

The response spectrum is the most widely used input for parameter inversion of GMMs with extensive databases published (e.g Ancheta et al., 2013; Bastías & Montalva, 2016; Dawood et al., 2016). It is the maximum absolute value of the spectrum of the convolution between a seismic acceleration signal and a harmonic oscillator with a single degree of freedom for a given oscillator period (Weber, 2002). Informally, it describes the maximum excitation of a single-degree-of-freedom oscillator under acceleration. From its definition it can be seen that the Fourier spectrum and the response spectrum are functions of different quantities (signal frequency vs. oscillator frequency) with same units (Hertz).

In some fields, the spectral computation is replaced by easier derived quantities. The quantities peak ground acceleration (PGA), peak ground velocity (PGV), and peak ground displacement (PGD) are the absolute maxima of the strong motion signals in the respective quantity(Kramer, 1996; Weber, 2002). Based on the integration of the squared strong-motion signal are the Arias intensity (integrated squared acceleration) and IV2 (integrated

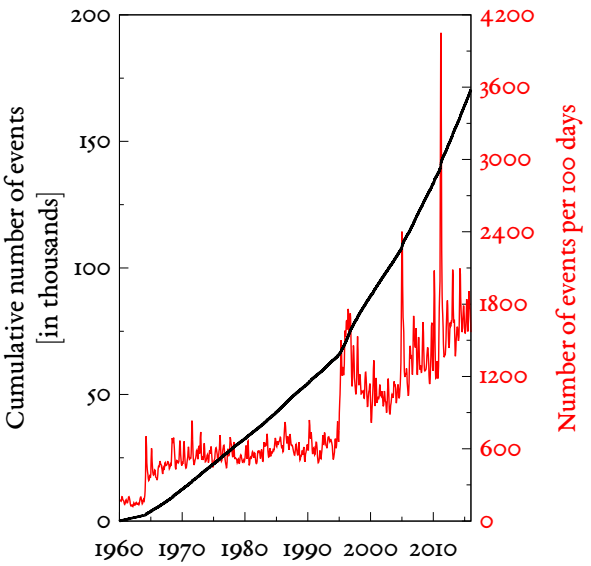

Figure 1.2: Data growth of the EHB catalog (as shown in Fig. 1.1) since 1960 in black with data growth rates in red. The spikes relate to major earthquakes and their aftershocks. Note, how the spikes increase with time, indicating that more stations were available with time progressing. The 2004 Sumatra and 2011 Tohoku earthquakes are the most prominent (both with M_W around 9), while the largest earthquake ever recorded, the 1960 Validivia (Chile) earthquake with M_W 9.5, is just the very first wiggle at the very beginning of the time series.

squared velocity) (Kramer, 1996). The Arias intensity is frequently encountered in landslide related GMMs (Harp & Wilson, 1995; Travasarou et al., 2003; Jibson, 2007, e.g.).

The development of a GMM is more diverse than the pre-processing. This diversity is reflected in the functional forms of the GMMs and in the inversion routines to obtain the parameters of the GMM. Despite the multitude of functional forms, all modern GMMs share a common structure which aims to reflect the mechanics of the ground-motion process (Kramer, 1996). This structure includes—but is not limited to—

1. ground motion is assumed to be log-normally distributed, i.e. the logarithms of ground-motion values are used,
2. a magnitude term,
3. a distance term due to geometrical spreading,
4. a second distance term due to material related wave attenuation,
5. a site condition term (e.g. rock type),
6. and a source term (normal, reverse, strike-slip faulting).

Among the inversion routines, least squares based approaches are by far the most common. Since the 1980s the mixed-effect model has been used in GMM development and is widely used today (Abrahamson & Youngs, 1992; Stafford, 2014). The mixed-effect model is described in full detail in ch. 8.

Of particular interest of the mixed-effect GMMs is the partitioning of the ground motion uncertainties (e.g. Al Atik et al., 2010). Despite more available data and more elaborate functional forms, GMM uncertainties decreased negligibly (Strasser et al., 2009). The reason is the inherent complexity of not only of the seismic processes, but also the media through which the wave travels and the structural variability at the recording site leading to GMMs to take into account these features (e.g Anderson & Brune, 1999; Lin et al., 2011; Dawood & Rodriguez-Marek, 2013). The random effect predictors of the mixed-effect model can be used to identify systematic offsets per earthquake and per station (among other effects not listed here) not covered by the fixed-effect model.

1.2 The likelihood

With this section, I give an overview of the fundamental concept that pertains nearly all model development in this work: the likelihood function.

The likelihood is closely linked to probability functions. A probability function is a function of some (observable) variable(s) with given parameters, while the likelihood is a function of the parameters for given observations. Obviously, this definition does not cover the full concept of neither probability functions nor likelihood functions, but is for the purpose here sufficient.

Let $p(x|\theta)$ be a probability function of variable x with parameter θ, then $\mathcal{L}(\theta|x)$ is the likelihood of parameter θ for x (our observed data)[1]. Like the probability function does the likelihood give a probability and since we have some data and a model we wish to fit to the data, we want to find a parameter, say $\hat{\theta}$, that maximizes the likelihood. This means, we want to determine a parameter that describes most likely the distribution under which our data originated given our model, i.e. we want to maximize our likelihood. The concept of maximum likelihood is widely used in statistics and many concepts and algorithms have been developed since its introduction over 200 years ago by Laplace (1774, translated in Laplace (1986)) and Gauss (1809)[2].

The concept of maximum likelihood is closely linked to least squares introduced by Gauss (1809). The link exists via the normal distribution—also introduced by Gauss—which is described by a two parametric probability function of the form

$$p(x|\mu,\sigma) = \frac{1}{\sqrt{2\pi\sigma^2}} e^{-\frac{(x-\mu)^2}{2\sigma^2}}, \tag{1.1}$$

where μ is the mean, and σ the standard deviation. The functional form of the likelihood for a single observation x is identical to above equation, i.e. $\mathcal{L}(\mu,\sigma|x) =$

[1] There is no fixed notation style for probability and likelihood functions. Some authors prefer the same notation for both. I use $p(\cdot|\cdot)$ and $\mathcal{L}(\cdot|\cdot)$, where the quantities left of the vertical bar are the variables and on the right side are the constants of the functions.

[2] The expression 'likelihood' was introduced by Fisher (1922)

$p(x|\mu,\sigma)$. If we have n independent observations $\mathrm{x} = (x_1, x_2, ..., x_n)$ from the same distribution with μ andσ, than the total likelihood is given by

$$\mathcal{L}(\mu,\sigma|\mathrm{x}) = \prod_{i=1}^{n} p(x_i|\mu,\sigma). \tag{1.2}$$

This product is for two reasons rather unattractive: (1) It is not easy to determine its maximum and (2) it can span enormous number ranges, which can be easily beyond the numerical ranges of most number implementations on computers. Therefore, the likelihood is transformed with the logarithm and it is that function that forms the basis of all maximum likelihood computations. After log-transform the likelihood from Eq. 1.2 becomes

$$\ln \mathcal{L}(\mu,\sigma|\mathrm{x}) = \sum_{i=1}^{n} \ln p(x_i|\mu,\sigma), \tag{1.3}$$

and inserting Eq 1.1:

$$\ln \mathcal{L}(\mu,\sigma|\mathrm{x}) = \sum_{i=1}^{n} -\frac{1}{2}\ln(2\pi) - \ln\sigma - \frac{(x_i-\mu)^2}{2\sigma^2}. \tag{1.4}$$

This equation reveals several interesting aspects. If maximized for either μ or σ, it provides the maximum likelihood estimators $\hat{\mu}$ and $\hat{\sigma}$, which are the sample mean and the sample variance. Furthermore, by neglecting the constant terms and factors, and normalizing σ to one, the log-likelihood in Eq. 1.4 reduces to

$$S = \sum_{i=1}^{n} (x_i - \mu)^2, \tag{1.5}$$

which is the objective function of ordinary linear least squares. By comparison of Eq. 1.4 and 1.5, it is now also obvious that minimizing the sum of squares is equivalent to maximizing the likelihood.

The connection of the likelihood to least squares exists also for other concepts beyond linear least squares, e.g. for nonlinear least squares and generalized least squares. By using other probability functions, the norm of the objective function is changed (least squares is l_2-norm), e.g. by a Laplace distribution in the likelihood corresponds to the least absolute deviation, which is used in robust regression (l_1-norm). Due to the similarity between the normal and Laplace distribution, it is possible to express least absolute deviation in terms of generalized least squares (specifically iteratively reweigted least squares, see ch. 6).

The likelihood is also connected to information theory. There are several related concepts that establish the connection: the two most prominent are the Akaike Information Criterion (AIC, Akaike, 1974) and the Bayesian Information Criterion (BIC, Schwarz, 1978). These information criteria become meaningful when selecting the best-fitting model for given data from a set of models with variable number of parameters. Since an increase of the number of parameters introduces more degrees of freedom, the likelihood will increase as well. This increase in parameters may lead to overfitting the data at some point, which in turn will render the model useless for predictive purpose, as the parameters are only optimized for the observed data. The AIC and BIC safeguard against overfitting by including the number of parameters as well:

$$AIC = 2k - 2\ln\mathcal{L} \tag{1.6}$$

$$BIC = \ln(n)k - 2\ln\mathcal{L}. \tag{1.7}$$

If the number of data is much larger than the number of parameters, then BIC is more suitable for model selection, because BIC penalizes the number of parameters more than AIC.

The idea behind AIC is rooted in information theory as AIC is derived from the Kullback-Leibler divergence (Burnham & Anderson, 2002). Since the true model is unknown, the AIC represents the loss (or gain) of information if one model is chosen over the other. Therefore, the model with minimum AIC is better than all other models for which AIC is known. In consequence, it does not mean that the best model of AIC is a good model; a statement that also holds for the likelihood.

It is the modelers responsibility to define good models, the likelihood tells only which is better.

1.3 Scope of this thesis

At the bottom of every model development is one question: How to abstract the observed nature into a sound model with meaningful parameters? This question has become my primary driver and this PhD thesis is testimony to some of the advancements in modeling at the boundary of Earth sciences and mathematics. The two previous sections provide a basis for the scope of this thesis. Although the primary focus is on data processing in strong-motion seismology, some applications go beyond and touch geomechanics and geomorphology. This interfacing of different fields arises as natural events are interdependent and cannot (and should not!) be treated independently. Furthermore, with the increasing amount of data new possibilities in the processing of strong-motion data and ground-motion model development emerge. I developed new models by using widely used optimization and machine-learning techniques to different stages in ground-motion modeling, and how to integrate these new techniques into existing methodologies.

A critical parameter in the pre-processing in strong-motion seismology is the event type, as outlined in section 1.1. While event classification in some regions of the world is straightforward and can be realized by simple means (South American west coast), other regions like the Mediterranean Sea and its adjacent areas are tectonically very complex as is event classification. Irrespective of the region in the world, there is one common aspect: The data amount increases. While this may pose challenges on the classifications, it also provides new opportunities to learn more what is beyond basic classifications based on ternary plots or rake angles.

Chapter 2 introduces a purely-data driven event classification where the statistical model is rooted in the relations between stress and strain. The algorithm is

dubbed ACE—Angular Classification with Expectation-maximization—and is based on the Expectation-Maximization algorithm by Dempster et al. (1977). ACE identifies clusters of focal mechanisms represented by strike, rake, and dip and assigns probabilities for each event to belong to a cluster. In parallel, based on concepts from information theory, the algorithm optimizes the number of parameters of the mixture model to represent the clusters.

As an event classifier, ACE can be applied in many contexts. ACE based earthquake classifications are used to investigate temporal variations in residuals of GMMs in northern Chile (ch. 3) during the 2014 Iquique earthquake. In conjunction with GPS data, the classified earthquake data is investigated in ch. 4 to identify a preparatory phase before 2014 Iquique earthquake. Since ACE is based on assumptions relating to the stress state in the Earth, ch. 5 deals with ACE based classifications as data weights to reduce uncertainties in stress tensor inversions[3].

During pre-processing, the baseline correction is critical to reduce bias in spectral estimates of the accelerogram. Signals may be contaminated by instrument related discontinuities (jumps) which influence signal quality. The removal of these jumps is complicated, as the number and occurrence times are unknown. However, with increasing amounts of data, such baseline corrections cannot be conducted by hand anymore.

Chapter 6 presents an automated baseline correction routine based on segmented robust linear least squares: ICBM (Integrated Combined Baseline Modification) The algorithm also employs the Bayesian information criterion to optimize the number of jumps. As an example, ICBM is applied to strong-motion data from the 2016 Kumamoto earthquake. A part of the combined seismic network suffers from baseline jumps, which subsequently can strongly affect estimates of static displacement and radiated seismic energy (which is used in ch. 7). With ICBM corrected baseline jumps, the static displacement estimates are en par with InSAR derived displacements.

The 2016 Kumamoto earthquake opened the opportunity to investigate in high detail the impact of a major earthquake rupture, due to the dense Japanese seismic network as well as the location of the earthquake centered in Kyushu (SW Japan). In chapter 7 a ground-motion model is introduced that takes into account the directivity effect of a rupture process. The directivity effect is derived from estimates of radiated seismic energy at the recording sites with the waveforms carefully pre-processed (ch. 6). These energy estimates replace the magnitude commonly encountered in GMMs. Furthermore, the chapter deals with the impact on seismically induced landslides, their location and orientation with respect to the earthquake rupture plane. It is demonstrated that seismically induced landslides are influenced by ground shaking with frequencies below 2 Hz, as is evidenced by the prevalent landslide aspect[4].

In the final chapter 8, the concept of data weighting, e.g. with ACE, is integrated into the development of GMMs. This chapter lays the theoretical foundation for the mixed-effect model—currently the the standard in GMM parameter estimation—with data weighting realized in the weighted likelihood. Parameter estimators for the fixed-effect model and the random-effect variances for any model structure are provided. Another feature in this chapter are analytic representations of the parameter uncertainties of the mixed-effect model. The chapter concludes with the derivation of a GMM with data weights for Chile based on the database of Bastías & Montalva (2016). The model based on ACE weights for earthquakes is compared to the model of Montalva et al. (2017) based on the same data but with expert based event classification.

[3] This is also partially covered in the second half of ch. 2

[4] for the seismologists: aspect is dip azimuth, or strike plus 90°

1.4 Author's publications and contributions

1.4.1 Publications in the frame of the thesis

1. Chapter 2:
   published as: Specht, Sebastian and Heidbach, Oliver and Cotton, Fabrice and Zang, Arno, 2017, Data-driven earthquake focal mechanism cluster analysis, *Scientific Technical Report - GFZ German Research Centre for Geosciences*, 36 pages.
   SvS conceived the study, performed the computations, and performed the graphical design. SvS and OH wrote the manuscript with input from FC and AZ. Theoretical concepts were developed by all authors.

2. Chapter 3:
   published as: Piña-Valdés, Jesús and Socquet, Anne and Cotton, Fabrice and Specht, Sebastian, 2018, Spatiotemporal Variations of Ground Motion in Northern Chile before and after the 2014 Mw 8.1 Iquique Megathrust Event, *Bulletin of the Seismological Society of America*, 108(2), 801–814.
   JPV performed the strong-motion computations, and performed the graphical design and wrote the manuscript. SvS performed the earthquake classification of the catalog, and computed rupture plane distances. AS and FC supervised the study. The manuscript was reviewed by all authors.

3. Chapter 4:
   published as: Socquet, Anne, Piña-Valdés, Jesús, J. Jara, F. Cotton, A. Walpersdorf, N. Cotte, S. Specht, F. Ortega-Culaciati, D. Carrizo, and E. Norabuena (2017), An 8 month slow slip event triggers progressive nucleation of the 2014 Chile megathrust, *Geophysical Research Letters*, 44, 4046–4053.
   AS, JPV, and JJ conceived and wrote the manuscript. SvS performed the earthquake classification of the catalog, and computed rupture plane distances. The manuscript was reviewed by all authors.

4. Chapter 5:
   published as: von Specht, Sebastian, Heidbach, Oliver, Cotton, Fabrice, Zang, Arno, 2018, Uncertainty reduction of stress tensor inversion with data-

driven catalogue selection, *Geophysical Journal International*, 214(3), 2250–2263.
SvS conceived the study, performed the computations, and performed the graphical design. SvS and OH wrote the manuscript with input from FC and AZ. Theoretical concepts were developed by all authors.

5. Chapter 6:
published as: von Specht, Sebastian, 2019, ICBM – Integrated Combined Baseline Modification:
An algorithm for segmented baseline estimation, *Seismological Research Letters*, Early edition, doi: 10.1785/0220190134 .

6. Chapter 7:
published as: von Specht, Sebastian, Öztürk, Uğur, Veh, Georg, Cotton, Fabrice, and Korup, Oliver, 2019, Effects of finite source rupture on landslide triggering: the 2016 M_W 7.1 Kumamoto earthquake, *Solid Earth*, 10, 463–486.
SvS and UO conceived the study and wrote the manuscript. SvS investigated the seismic data and developed most of the code, UO assessed the topographic effects. GV contributed in visualization, and helped in improving the manuscript. FC and OK supervised the study and reviewed the manuscript.

7. Chapter 8:
submitted as: von Specht, S., Cotton, F., Weighted mixed effect regression with data-driven probabilistic earthquake classification, Bulletin of the Seismological Society of America.
SvS and FC conceived the study and wrote the manuscript. SvS developed the theory, conducted the data processing, programming and graphical design.

1.4.2 Publications not associated with the thesis

1. Zang, A., Stephansson, O., Stenberg, L., Plenkers, K., Specht, S., Milkereit, C., Schill, E., Kwiatek, G., Dresen, G., Zimmermann, G., Dahm, T., Weber, M. (2017): Hydraulic fracture monitoring in hard rock at 410 m depth with an advanced fluid-injection protocol and extensive sensor array. - Geophysical Journal International, Vol. 208, No. 2, pp. 790–813.

2. Kwiatek, G., Martínez-Garzón, P., Plenkers, K., Leonhardt, M., Zang, A., von Specht, S., Dresen G., Bohnhoff, M. (2017). Insights Into Complex Subdecimeter Fracturing Processes Occurring During a Water Injection Experiment at Depth in Äspö Hard Rock Laboratory, Sweden. Journal of Geophysical Research: Solid Earth, Vol. 123, No. 8, pp. 6616–6635.

3. Ozturk, U., Marwan, N., von Specht, S., Korup, O., Jensen, J. (2018). A new centennial sealevel record for Antalya, eastern Mediterranean. Journal of Geophysical Research: Oceans, Vol. 123, No. 7, pp. 4503–4517.

4. G. Veh, O. Korup, S. von Specht, S. Roessner, and A. Walz, 2019, Unchanged frequency of moraine-dammed glacial lake outburst floods in the Himalaya, Nature Climate Change, Vol. 9, No. 5, pp. 379–383.

5. Bayona Viveros, J. A., von Specht, S., Strader, A., Hainzl, S., Cotton, F., Schorlemmer, D. (2019). A regionalized seismicity model for subduction zones based on geodetic starin rates, geomechanical parameters and earthquake-catalog data. Bulletin of the Seismological Society of America, Vol. 109, No. 5, pp. 2036–2049.

Chapter 2

Data-driven earthquake focal mechanism cluster analysis

Abstract

Earthquake focal mechanism solutions (FMS) form the basic data input for many applications, e.g. stress tensor inversion or ground-motion prediction equation estimation. In these applications the FMS data is usually binned spatially or in predetermined ranges of rake and dip based on expert elicitation. However, due to the significant increase of FMS data in the past decade an objective data-driven cluster analysis is now possible. Here we present the method ACE (Angular Classification with Expectation-Maximization) that identifies clusters of FMS without a priori information. The identified clusters can be used for the classification of the Style-of-Faulting and as weights for FMS data binning in the aforementioned applications. As an application example we use ACE to identify FMS clusters according to their Style-of-Faulting that are related to certain earthquake types (e.g. subduction interface) in northern Chile, the Nazca Plate and in Kyūshū (Japan). We use the resulting clusters and weights as a priori information for a stress tensor inversion for these regions and show that uncertainties of the stress tensor estimates are reduced significantly[a].

[a] published as: Specht, Sebastian and Heidbach, Oliver and Cotton, Fabrice and Zang, Arno, 2017, Data-driven earthquake focal mechanism cluster analysis, *Scientific Technical Report - GFZ German Research Centre for Geosciences*, 36 pages.

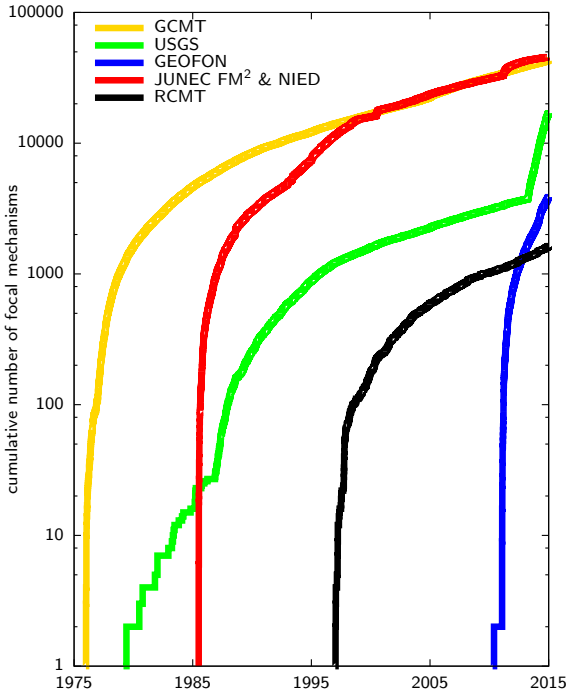

Figure 2.1: Catalog growth over time of GCMT (Global Centroid-Moment-Tensor, Dziewonski et al. (1981); Ekström et al. (2012)), GEOFON (GEOFosrchungsNetz, Hanka & Kind (1994)), USGS (United States Geological Survey), JUNEC FM^2 (Japan University Seismic Network Earthquake Catalog of First-Motion Focal Mechanisms, Ishibe et al. (2014)), NIED (National Research Institue for Earth Science and Disaster Prevention, Japan) and RCMT (European-Mediterranean Regional Centroid Moment Tensor Catalog, Pondrelli et al. (2011)). GCMT, GEOFON and USGS are global catalogs, while the others are regional catalogs: JUNEC FM^2 & NIED and RCMT.

2.1 Introduction

Earthquake focal mechanism solutions (FMS) are of key importance for understanding rupture kinematics and the geometry of faults at depth. They are used e.g. to derive the orientation of maximum horizontal stress and the stress regime for the World Stress Map where they are the key contributor to this global data base (Zoback, 1992; Heidbach et al., 2010). Furthermore, knowledge of the Style-of-Faulting (SoF) and the fault plane orientation are crucial in several fields of seismology, e.g. seismic hazard (GMPE, b-value) and in studying the Earth's stress field and changes within it (Meier et al., 2014). Furthermore, data sets of FMS are used to investigate the seismotectonic setting of sub-regions and to derive the stress tensor orientation and relative magnitudes by means of a formal stress inversion (e.g. Gephart & Forsyth, 1984; Michael, 1984). In these applications the FMS data are usually binned spatially or in predetermined ranges of rake and dip based on expert assessment.

Several methods have been suggested to investigate clusters of FMS and moment tensors (MT), respectively. FMS represent the double couple component of a rupture plane, while moment tensor solutions provide also non-double-couple components. Due to the nodal plane ambiguity of the double couple, cluster analyses so far published are limited to certain aspects of FMS. E.g. Frohlich (1992) reduces the FMS (MT) to the plunge of the vertical components of the PBT axes. By expressing the focal mechanism in terms of their PBT axes, the nodal plane ambiguity is avoided. An advantage of this technique is the way data are presented: The complex geometry of the FMS can be represented in a two-dimensional ternary diagram, where each triangle corner is one end member of the Andersonian Style-of-Faulting (SoF), i.e. normal, reverse and strike-slip faulting. FMS in the center of the plot are classified as "oblique" or "odd". Event clusters are e.g. investigated for their consistency, a metric based on the scalar moment (Frohlich & Apperson, 1992).

Kagan (1991) defines the relative similarity of the FMS (MT) based on the shortest angle to rotate one FMS into another. A major advantage is that results are given in one parameter only, the minimum rotation angle between the FMS (frequently called Kagan angle). The distribution of the rotation angle follows a wrapped Cauchy distribution (Kagan, 1992). Another cluster analysis method is the so-called density-based clustering. It is based on the DBSCAN algorithm of Ester et al. (1996) and assumes that FMS (MT) are distributed with two different "densities" of events (Cesca et al., 2014). This density can be measured in different ways, in case of FMS/MT usually some angular metric, e.g. the above mentioned Kagan angle. Events with high densities (short distance metric values) are joined to one cluster; events with low densities (large distances) are considered to be noise and not included in a cluster. The advantage of this method is that no assumption on the underlying distribution of the data is required. The clusters are defined by two parameters, the minimum number of data per cluster and the threshold of the metric length at which a cluster is identified. Thus, the definition of "high" and "low" densities as well as the minimum size of a cluster are user based.

Another common way of cluster assignment thresholds are based on the expertise and experience of scientists by including additional information such as focal depth and information from structural geology. Though straightforward in its implementation, the final choice of the selected data lacks transparency and does not provide a measure for the quality of the choice. Furthermore, two of the above mentioned techniques are also to some extend subject to expert based judgment. These are the event class boundaries in the ternary plot representation and the two cluster defining parameters of the DBSCAN based method.

In order to avoid the a priori expert assessment of FMS data sets an objective data-driven cluster analysis is needed. This analysis should also deliver weights in terms of the quality of the identified clusters. Given that the amount of FMS data has increased significantly in the past decade (Fig. 2.1), a purely data-driven earthquake focal mechanism cluster analysis is now possible. We develop in this paper the method ACE (Angular Classification with Expectation-Maximization) which identifies clusters of FMS without a priori information. The physical funda-

mentals of our FMS cluster algorithm are based on elasticity theory using the 3D Cauchy stress tensor to formally describe the stress state at a point in a 3D volume. The algorithm is not a stress tensor inversion, but it also differs from the purely descriptive clustering methods presented e.g. in Frohlich & Apperson (1992) or Cesca et al. (2014). ACE follows basic assumptions about the distribution of random stresses (Kagan, 1990). It is a purely data-driven method that investigates the full scope of FMS data by considering both nodal planes and as little assumptions as possible. All parameters controlling the results are estimated in the process, thus mitigating effects from expert based judgment.

The identified clusters can be e.g. used for the classification of the Style-of-Faulting and as weights for FMS data binning in the aforementioned applications. We show how the results of ACE can be used to improve the binning of FMS data for the stress tensor inversions. The improvement is achieved by separating the FMS data into more consistent subpopulations of FMS with weights. The examples from northern Chile (subduction interface), the Nazca Plate and in Kyūshū (Japan) exemplify that the uncertainties of the stress tensor orientation resulting from a formal stress inversion are reduced significantly.

2.2 Cluster analysis of focal mechanisms

2.2.1 Theory

Stress definition

An earthquake can be seen as a sudden deformation process resulting in slip caused by the ambient stress field in the surrounding rock. The 3D stress state is described by a symmetric 3×3 tensor $\boldsymbol{\sigma}$ (Zang & Stephansson, 2010; Jaeger, 1979).

$$\boldsymbol{\sigma} = \begin{pmatrix} \sigma_{11} & \sigma_{12} & \sigma_{13} \\ \sigma_{12} & \sigma_{22} & \sigma_{23} \\ \sigma_{13} & \sigma_{23} & \sigma_{33} \end{pmatrix} \tag{2.1}$$

The stress $\boldsymbol{\sigma}$ can be decomposed into four terms (Kagan, 1990, and ref. therein):

$$\boldsymbol{\sigma} = \boldsymbol{\sigma}_l + \boldsymbol{\sigma}_t + \boldsymbol{\sigma}_f + \boldsymbol{\sigma}_r, \tag{2.2}$$

where $\boldsymbol{\sigma}_l$ is the lithostatic stress, $\boldsymbol{\sigma}_t$ the regional tectonic stress, $\boldsymbol{\sigma}_f$ the stress related to prior earthquakes, and a random stress term $\boldsymbol{\sigma}_r$. The first three terms are assumed to be related to macroscopic phenomena and therefore constant and non-random. The random stress term is due to defects in the rock mass.

Kagan (1990) showed that the orientation of the random stress $\boldsymbol{\sigma}_r$ follows a Cauchy distribution. Based on this assumption, the distribution of the focal mechanism orientations follows a wrapped Cauchy distribution (the concept of wrapped distributions is introduced in the next section) (Kagan, 1990, 1992).

We use the assumption of stress decomposition in Eq. 2.2 to derive a statistical model to describe the distribution of the three FMS angles, namely strike, rake and dip.

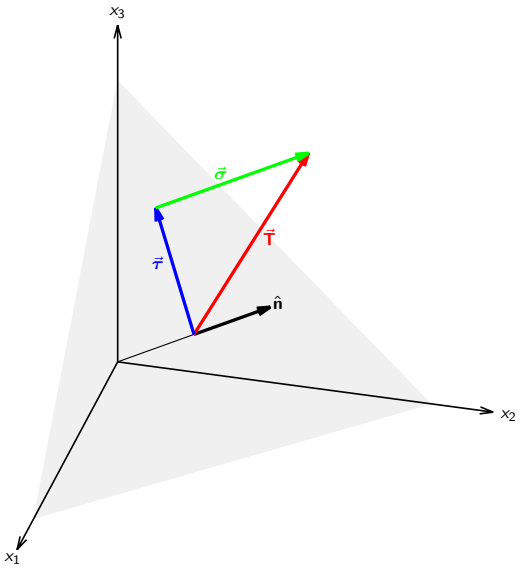

Figure 2.2: Stress vector T (red) acting on a plane (gray area) in 3D space. The stress vector can be decomposed into its normal (green) and shear components (blue). The normal stress component is orthogonal to the plane (parallel to $\hat{\mathrm{n}}$). Its magnitude is given by Eq. 2.4. The shear stress lies in the plane (parallel to it) with orientation given in Eq. 5.16. The eigenvectors of the stress tensor $\boldsymbol{\sigma}$ are orientated parallel to the three axes x_1, x_2, x_3.

In the following we derive the relationship between stress $\boldsymbol{\sigma}$ and the slip and normal vectors of a focal mechanism and their associated angles.

The three eigenvectors of $\boldsymbol{\sigma}$ indicate the principal stress directions and the eigenvalues the principal stress magnitudes. We define the principal stress orientations as $\hat{\mathrm{v}}_1$, $\hat{\mathrm{v}}_2$, $\hat{\mathrm{v}}_3$ with associated stress magnitudes as $S_1 \geq S_2 \geq S_3$ and compressive stress to be positive. The traction T is the force resulting from $\boldsymbol{\sigma}$ acting on a surface with normal n (Fig. 2.2).

$$\mathrm{T} = \boldsymbol{\sigma}\mathrm{n} \tag{2.3}$$

The normal stress σ_n follows from

$$\sigma_n = \mathrm{T} \cdot \mathrm{n} \tag{2.4}$$

and the vector of maximum shear stress s is

$$\mathrm{s} = \mathrm{T} - (\mathrm{T} \cdot \mathrm{n})\mathrm{n} \tag{2.5}$$

The slip $\hat{\mathrm{d}}$ on a fault is oriented in the direction of maximum shear stress (Wallace, 1951). In case of a preexisting fault, Bott (1959) suggested that fracturing occurs in the plane in which the strength was first exceeded and the direction of the initial slip is defined by the direction of the maximum shear stress (Fig. 2.3). Furthermore it is assumed, that fault planes are planar and that stress perturbations and rotations on the fault surfaces are neglected. Under these conditions, it follows, that the slip direction $\hat{\mathrm{d}}$ and the normal vector of the rupture plane $\hat{\mathrm{n}}$ are located in the plane spanned by $\hat{\mathrm{v}}_1$ and $\hat{\mathrm{v}}_3$, or in other words, with

a normal vector parallel to $\hat{v}_2$. This implies that $\hat{v}_2 = \hat{b} = \hat{n} \times \hat{d}$. Lisle (2013) pointed out that directions up to 26° off the maximum shear orientation are at still at 90 % of the shear stress magnitude. Thus, slip and shear stress orientations are not necessarily well aligned. However, the applicability of the Wallace-Bott hypothesis to earthquake rupture processes has been shown by several studies (e.g. Dupin et al., 1993; Pascal, 2002).

Representation of a Focal Mechanism Solution

Expressing a auxiliary/rupture plane of an earthquake with normal vector $\hat{n}$, slip vector $\hat{d}$ and the cross product $\hat{b} = \hat{n} \times \hat{d}$ in terms of the strike (ϕ), rake (λ) and dip (δ) angles (Kanamori & Cipar, 1974):

$$\hat{n} = \begin{pmatrix} -\sin\delta\sin\phi \\ -\sin\delta\cos\phi \\ \cos\delta \end{pmatrix} \tag{2.6}$$

$$\hat{d} = \begin{pmatrix} \sin\lambda\cos\delta\sin\phi + \cos\lambda\cos\phi \\ \sin\lambda\cos\delta\cos\phi - \cos\lambda\sin\phi \\ \sin\lambda\sin\delta \end{pmatrix} \tag{2.7}$$

$$\hat{b} = \begin{pmatrix} \cos\lambda\cos\delta\sin\phi - \sin\lambda\cos\phi \\ \cos\lambda\cos\delta\cos\phi + \sin\lambda\sin\phi \\ \cos\lambda\sin\delta \end{pmatrix} \tag{2.8}$$

The slip vector $\hat{d}$ is in the plane described by the normal vector $\hat{n}$, thus both vectors are orthogonal and their dot product vanishes, i.e. $\hat{n} \cdot \hat{d} = 0$. It follows from the orthogonality of the nodal planes, that the normal vector of one nodal plane is the slip vector of the other and vice versa (e.g. Stein & Wysession, 2003). The two nodal planes of a FMS have subscripts 1 and 2:

$$\hat{n}_1 = \hat{d}_2 \quad \text{and} \quad \hat{d}_1 = \hat{n}_2 \tag{2.9}$$

Due to this symmetry, the nodal planes given by an FMS cannot be separated into rupture and auxiliary planes. And due to the exchangeability of both vectors follows for the null axes:

$$\begin{aligned} \hat{b}_1 &= \hat{n}_1 \times \hat{d}_1 \\ &= \hat{d}_2 \times \hat{n}_2 = -\hat{b}_2 \end{aligned} \tag{2.10}$$

Following the Wallace-Bott hypothesis the shear vector s is in the same direction as the fault slip $\hat{d}$. This relation shows that the slip d can be considered as a function of the stress tensor and the fault surface normal which in turn is a function of strike and dip

$$d(\phi, \delta, \lambda) = d(\phi, \delta, \boldsymbol{\sigma}) = d(n, \boldsymbol{\sigma}) \tag{2.11}$$

The rake λ can be regarded as a function of strike, dip and stress orientations. Consider a given stress tensor where the orientation of an arbitrary intermediate stress $\hat{s}_2 = \hat{b}$ is fixed. Then the following equation can be derived from Eq. 2.8 (see appendix 2.6.1 for derivation):

$$\frac{\partial\lambda(\phi,\delta)}{\partial\phi} = \cos\delta \tag{2.12}$$

$$\frac{\partial\lambda(\phi,\delta)}{\partial\delta} = 0 \tag{2.13}$$

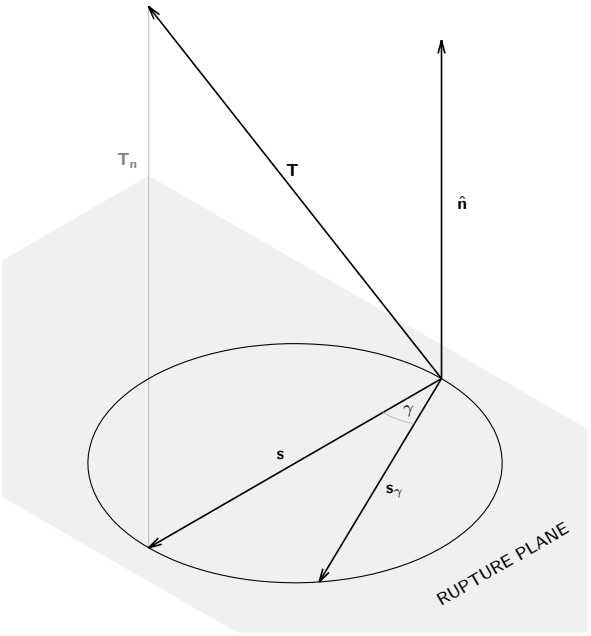

Figure 2.3: Orientation and magnitude of the resultant shear stress / slip on a plane. Maximum shear stress is orientated parallel to stress vector projected onto the rupture plane (Eq. 5.16). According to the Wallace-Bott hypothesis slip is orientated in maximum shear orientation. However, even directions 26° off the maximum shear orientation are still at 90 % of the magnitude of the maximum shear stress.

The same relation holds for a constant slip vector $\hat{d}$ of either nodal plane, then the derivatives in Eq. 2.12 and 2.13 are found by setting the derivative of Eq. 2.7 to zero (see appendix 2.6.1). Figure 2.4 graphically visualizes the derivation of the derivatives. The two derivatives imply that in general on one side no functional relation exists between rake and dip (as is the case for strike and dip). On the other side a relationship exists between strike and rake according to Eq. 2.12. In Figure 2.5 we show FMS nodal plane clusters from synthetic data. Both relations between the angles can also be observed in global data sets, as shown for the entire GCMT catalog in Fig. 2.6.

The implications of the derivatives for the data distribution are taken into consideration for the cluster analysis. The cluster analysis itself is inductive, i.e. nothing is known about the clusters a priori. Any information about the clusters is derived during the run of the analysis. The advantage of not using a priori information comes with its adaptability to the data. Thus additional information, which possibly eludes a deterministic approach for investigating individual events, can be observed. This additional information from the clustering can be used to assign weights to FMS used in other applications, e.g. stress tensor inversion, b-value estimation, regression of ground-motion prediction equations etc.

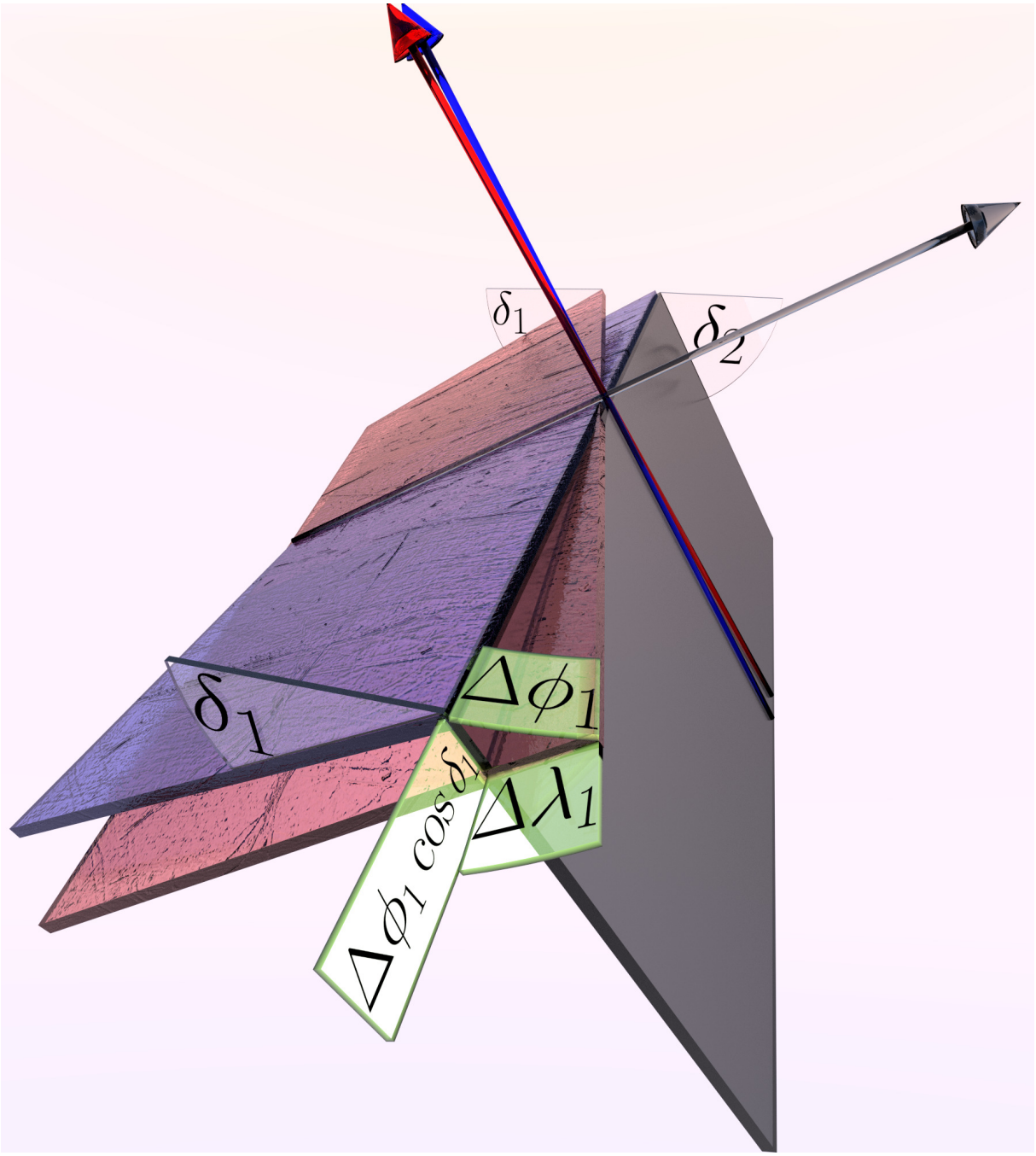

Figure 2.4: Model illustrating the relation between strike and rake of a nodal plane (red & blue rough surfaces, angles with index 1) for a constant slip vector (gray vector, normal of the smooth gray plane, index 2). If a nodal plane's strike ϕ_1 is shifted by an infinitesimal increment $\Delta\phi_1$, then the rake λ_1 is shifted by $\Delta\lambda_1$. The strike is defined on a horizontal plane, while the rake is defined on the nodal plane itself. The distance between the horizontal and the nodal plane shifted by $\Delta\phi_1$ and $\Delta\lambda_1$, respectively, is $\Delta\phi_1 \cos\delta_1$, i.e. $\Delta\lambda_1(\Delta\phi_1)^{-1} = \cos\delta_1$.

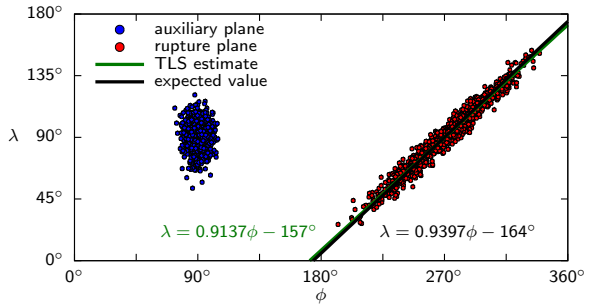

Figure 2.5: Shape dependence of nodal plane clusters. The clusters represent both nodal planes expressed as angles simulated from a near isotropic stress tensor. The variance is caused by adding normally distributed noise to the principal stress axis orientations. The simulated regime is reverse with maximum horizontal (and principal) stress orientation in north-south direction, resulting in an average strike and rake of 90°. The underlying fracture criterion is the Mohr-Coulomb criterion with a friction coefficient of 0.7. The first simulated rupture plane is reactivated in subsequent rupture events, therefore simulating the reactivation of faults. The blue cluster represents here the auxiliary plane and has a mean dip of 70°. Since the dip is close to zero, no relation between strike and rake is observable. The corresponding cluster of the rupture plane is the elongated cluster to the right (red). Due to its shallow mean dip of 20°, a strong relation between strike and rake is apparent. The slope of the cluster in the strike-rake plane, estimated by total least squares (TLS, green line), is close to a slope of $\cos 20° \approx 0.9397$ (black line), which is the expected value of the slope from Eq. 2.12.

2.2.2 Methods

In this section, we introduce the algorithm for identifying clusters of nodal planes from a FMS-catalog: ACE - Angular Classification with Expectation-Maximization. As the acronym implies, the algorithm is based on the expectation-maximization (EM) algorithm (Dempster et al., 1977).

We first introduce the statistical model to describe the data of a nodal plane population (2.2.2). This statistical model is a mixture model of probability distributions - with each component describing one cluster (in the ideal case, otherwise several components describe one cluster). The parameters of the mixture model are determined with the EM-algorithm. Since the cluster population size is unknown, we introduce two additional parameters to control the merging and removal of mixture components at each iteration of the EM-algorithm (section 2.2.2). Based on information theory, we present the optimization of these control parameters to determine the optimal number of components (section 2.2.2). Following in section 2.2.2, we identify subpopulations of nodal plane clusters from the mixture according to their Style-of-Faulting. The cluster subpopulations are the final outcome of ACE and are the basis for subsequent analyses. As an application example we show a weighted stress tensor inversion based on the works of (Michael, 1984; Hardebeck & Michael, 2006). The weights provided by ACE reduce the uncertainties of the inversion. We also investigate the Kagan angle distribution of the cluster subpopulations.

Statistical model of a nodal plane cluster

A focal mechanism is described as a set of three angles $\boldsymbol{\theta} = (\phi, \lambda, \delta)$, consisting of strike ($\phi$), rake ($\lambda$) and dip ($\delta$). Each focal mechanism is fully represented by two angle triples $\boldsymbol{\theta}$, describing the orientation of both nodal planes (i.e. rupture plane and auxiliary plane), respectively.

The last term in Eq. 2.2 is used to describe purely randomly distributed stresses. In order to cover this randomness we use a statistical model to describe the data distribution. The model for one cluster is denoted by the probability density function (PDF) $\mathcal{J}(\boldsymbol{\theta})$. This distribution has limited support in all three dimensions: $\phi \in [0, 360°)$, $\lambda \in [-180°, 180°)$, $\delta \in [0, 90°]$. Additionally, the angles show periodic behavior, which is best illustrated by the mean of the angles $(5°, 355°)$, which is not $180°$ but $0°$. A distribution showing such behavior, i.e. a distribution around a circle (for the 1-dimensional case) is called a wrapped probability distribution (e.g. Mardia & Jupp, 1999).

Any PDF $P(x)$ can be converted to a wrapped PDF $P_w(\omega)$ by wrapping its variable and summing over the period 2π:

$$\omega = x \bmod 2\pi \qquad f_w(\omega) = \sum_{u=-\infty}^{\infty} f(\omega + 2\pi u) \tag{2.14}$$

The distribution of strike, rake and dip is three-dimensional and the model is placed in a model space defined on a 3-dimensional torus (also known as hypertorus; a four-dimensional doughnut, figuratively), which is the product of the three circles each defining the domain of strike, rake, and dip (though the dip spans only a quarter circle by definition). As already shown in the previous section, the rake and the strike of FMS are dependent on each other (Eq. 2.12) if the intermediate stress orientation (cross-product of normal and slip vector) or the slip vector is constant. We refer to a "constant stress orientation" for the first three components of Eq. 2.2 only, the random component is never considered constant, thus the vector orientations themselves are not completely constant.

The distribution of dip and rake of both nodal planes in the complete FMS catalog of the Global Centroid Moment Tensor (GCMT) catalog (Dziewonski et al., 1981; Ekström et al., 2012) from 1976 - 2016 shows, that earthquakes tend to cluster around $\lambda = \{0°, \pm 90°, \pm 180°\}$ (Fig. 2.6a). The distribution shows no correlation between rake and dip for all clusters of the Style-of-Faulting end members as is implied by Eq. 2.13. The independence of the dip from either strike and rake allows to define the distribution as a product:

$$\mathcal{J}(\phi, \lambda, \delta | \mu, \nu, \sigma^2, \tau^2, r, \alpha, \beta, a, b) = \mathcal{N}_w(\phi, \lambda | \mu, \nu, \sigma^2, \tau^2, r) \mathcal{B}(\delta | \alpha, \beta, a, b), \tag{2.15}$$

where $\mathcal{N}_w(\phi, \lambda)$ is the distribution in the strike-rake plane, and $\mathcal{B}(\delta)$ is the distribution of the dip. An advan-

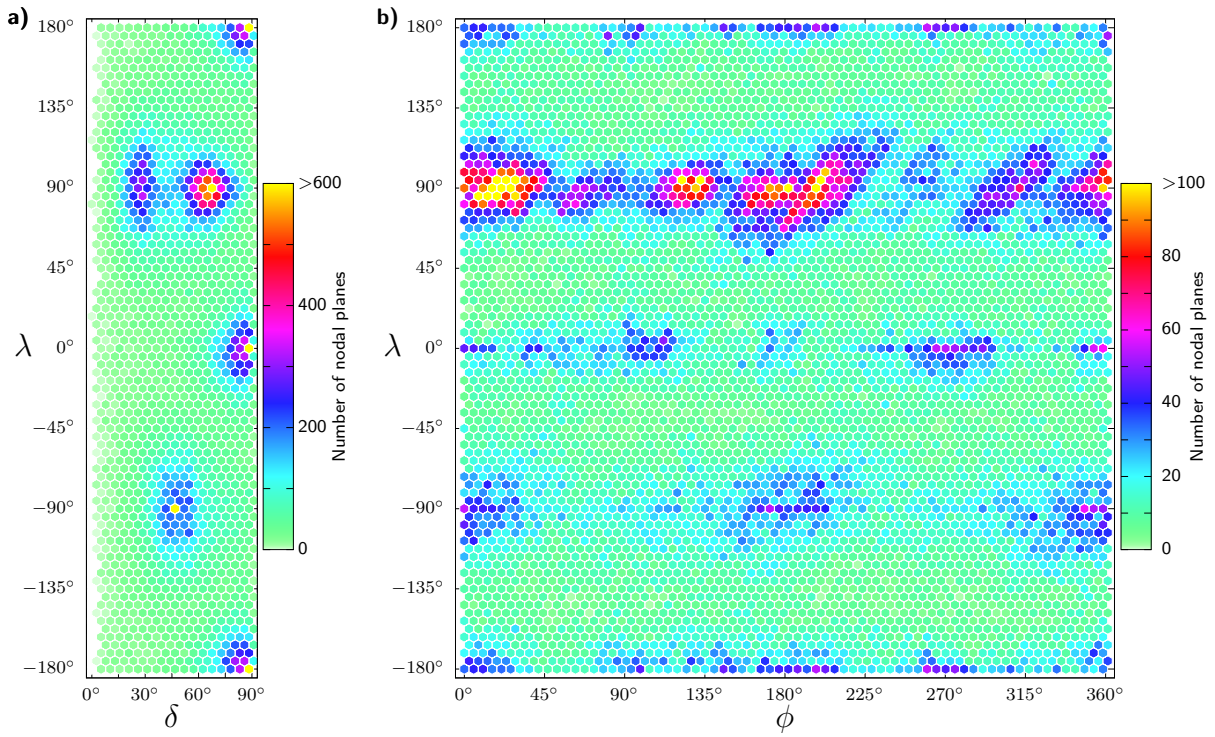

Figure 2.6: a) Distribution of dip (δ) and rake (λ) for the entire GCMT catalog from 1976 to 2016 for both nodal planes ($> 90,000$). Most nodal planes cluster at rakes of $\lambda = \{0°, \pm 90°, \pm 180°\}$, i.e. most events are close to Style-of-Faulting end members of normal, reverse and strike-slip. As indicated by Eq. 2.13 no apparent relation is visible in the distribution. b) Distribution of strike (ϕ) and rake (λ) for the same catalog as in a). Due to the predominant north-south striking of most continental collision zones and mid-ocean ridges, normal and reverse faulting ($\lambda = \pm 90°$) events cluster at strikes of $\phi = 0°$ and $\pm 180°$. Strike-slip events which commonly occur at transform faults perpendicular to the mid-ocean ridges have strikes of $\phi = \{0°, 90°, 180° 270°\}$. Several clusters of reverse faulting events ($\lambda = 90°$) show a linear behavior as indicated by Eq. 2.12 and shown in Fig. 2.5. This linear relationship becomes even more apparent when smaller regions are investigated (Fig. 2.12a, 5.11a, 2.19a).

tage of this model is its separability into a wrapped and an unwrapped distribution. The distribution $\mathcal{N}_w(\phi, \lambda)$ is a bivariate wrapped normal distribution and cannot separated further into two independent distributions due to the dependence introduced by Eq. 2.12, which becomes most apparent for shallow dipping ruptures (e.g. thrust faulting, Fig. 2.6b). However, this distribution covers also those cases where strike and rake are independent from each other, as expected for strike-slip faulting with (nearly) vertically dipping nodal planes.

The dip is defined on the finite interval $[0°, 90°]$, i.e. the dip does not show the same periodicity as both the strike and rake. The distribution of the dip is modeled by a beta distribution $\mathcal{B}(\delta)$. The two distributions and their parameters are described in the following section.

Wrapped normal distribution

The bivariate wrapped normal distribution for the strike ϕ has mean μ and variance σ^2, the distribution for the rake λ has mean ν and variance τ^2 and the bivariate wrapped normal distribution can be written as

$$\mathcal{N}_w(\phi, \lambda | \mu, \nu, \sigma^2, \tau^2, r) = \sum_{u,v \in \mathbb{Z}} \mathcal{N}(\phi + 2\pi u, \lambda + 2\pi v | \mu, \nu, \sigma^2, \tau^2, r) \quad (2.16)$$

where $\mathcal{N}(\cdot)$ is a normal distribution (see Eq. 2.81 in appendix 2.6.2). According to Eq. 2.12, a correlation between ϕ and λ exists, which is expressed by the angular correlation coefficient r (Fisher & Lee, 1983).

The reasons to choose this distribution for describing the strike-rake distribution are the following:

1. All parameters in Eq. 2.16 have analytic representations of their estimators based on maximum likelihood (see appendix 2.6.2 for a more detailed description). This contrasts with the widely used von Mises-Fisher distribution, whose parameters - specifically its concentration and in case of the more general Kent distribution the correlation as well) - can be estimated only iteratively, therefore increasing both inaccuracy and computational time.

2. It is a stable distribution, i.e. a linear combination of independent samples of that distribution results in the same distribution, though with different parameters. This means that e.g. when identifying a cluster with a single distribution even though that cluster originates from two independent (yet similar) distributions, the single distribution is nevertheless a reasonable description of the data. A similar argument for the stable distribution is given by Kagan (1990, 1992) to choose the Cauchy distribution (also a stable

distribution) to describe the FMS rotation distribution.

3. Inherent errors of the FMS data are modeled by the closely related von Mises-Fisher distribution (Silver & Jordan, 1982). Even though we do not include errors of the FMS data directly, we assume that the data distribution is influenced by the von Mises-Fisher distribution.

From the definition of the nodal planes in Eq. 2.6, Eq. 2.7 and Eq. 2.9, it follows that the sign of the rake for both nodal planes of an earthquake is always the same. This constraint also limits the extent of the distribution of nodal planes with a particular Style-of-Faulting along the rake. In conjunction with the relations between strike and rake given in Eq. 2.12, the expected maximum spread of any distribution in Eq. 2.16 along its principal axes in terms of the standard deviation is less then $60°$. Therefore, even the widest spreading cluster to be expected can be sufficiently approximated by a small number of wrappings in Eq. 2.16. It is sufficient to use a wrapping in the range of $\{u, v\} = \{-2, -1, 0, 1, 2\}$.

Beta distribution

The dip is modeled by a generalized beta-distribution with arbitrary interval $[a, b]$ and is given by

$$\mathcal{B}(\delta|\alpha, \beta, a, b) = \frac{(\delta - a)^{\alpha-1}(b - \delta)^{\beta-1}}{(b - a)^{\alpha+\beta-1}B(\alpha, \beta)}, \qquad (2.17)$$

where α and β are the shape parameters, $B(\cdot, \cdot)$ is the beta function and a and b are the interval limits. We follow the definition of Feller (1971) and exclude the limits from the range, i.e. $a < \delta < b$, for numerical stability, as $\mathcal{B} \to \infty$ at the interval limits for $\alpha < 1$ and $\beta < 1$ (See appendix 2.6.3 for a more detailed description of this distribution).

The beta distribution is chosen for the following reasons:

1. like the wrapped normal distribution (Eq. 2.16), the parameters in Eq. 2.17 have analytic representations of their estimators. In this case the estimators are based on the method of moments (see appendix 2.6.3).

2. When $\alpha \approx \beta$ and $\alpha > 2$ the beta distribution is similar to the normal distribution.

3. The distribution has a wide variety of shapes described by two parameters allowing data adaptabilty without resorting to distributions with large number of parameters.

4. Its shape variability allows also for fitting data with skewed distributions, e.g. dips close to 90° in case of strike-slip events.

Style-of-Faulting Index ($SoFI$)

Because of the same sign of the rake λ for both nodal planes for any FMS, the joint distribution $\mathcal{J}$ along the rake is truncated if the cluster consists mostly of either reverse or normal faulting nodal planes[1]. Strike-slip events are an exception, as they cluster around $\lambda = 0°$ or $\lambda = \pm 180°$ and thus contain FMS with rakes of both signs (though both rakes of individual FMS have the same sign). In order to assess the SoF in which $\mathcal{J}$ is located, we introduce the Style-of-Faulting-Index $SoFI$ based on Eq. 2.6, 2.7, 2.8

$$SoFI = \frac{\hat{\mathbf{e}}_3^T \mathrm{A} \hat{\mathbf{e}}_3}{\hat{\mathbf{e}}_3^T \mathrm{C} \hat{\mathbf{e}}_3}, \qquad (2.18)$$

where

$$\mathrm{A} = \hat{\mathbf{n}}\hat{\mathbf{d}}^T + \hat{\mathbf{d}}\hat{\mathbf{n}}^T \qquad (2.19)$$

$$\mathrm{C} = \hat{\mathbf{n}}\hat{\mathbf{n}}^T + \hat{\mathbf{d}}\hat{\mathbf{d}}^T + \hat{\mathbf{b}}\hat{\mathbf{b}}^T \qquad (2.20)$$

$$\hat{\mathbf{e}}_3 = (0, 0, 1)^T, \qquad (2.21)$$

The definition of $SoFI$ is identical for both nodal planes, i.e. $SoFI$ is event based rather than nodal plane based.

Plugging the angle based definitions of the normal and slip vectors from Eq. 2.6 and 2.7 in Eq. 2.18 simplifies to

$$SoFI = \sin\lambda \sin 2\delta \qquad (2.22)$$

According to Eq. 2.22, $SoFI$ is positive in a reverse tectonic regime, negative in a normal tectonic regime and around zero in a strike-slip tectonic regime. The $SoFI$ for the three end members of the tectonic regimes are

$$SoFI = \begin{cases} \frac{\sqrt{3}}{2} & \text{if } \lambda = 90°, \delta = 30° \text{ (reverse)} \\ -\frac{\sqrt{3}}{2} & \text{if } \lambda = -90°, \delta = 60° \text{ (normal)} \\ 0 & \text{if } \lambda = \{0°, \pm 180°\}, \delta = 90° \text{ (strike-slip)} \end{cases} \qquad (2.23)$$

The regime index of distribution $\mathcal{J}$ indicates the predominant regime of that distribution and is calculated as a weighted mean of the individual $SoFI$ of the $2N$ nodal planes (N - number of events) with weights based on $\mathcal{J}$.

$$SoFI = \frac{\sum_{i=1}^{2N} \mathcal{J}_i SoFI_i}{\sum_{i=1}^{2N} \mathcal{J}_i} \qquad (2.24)$$

We use this index as the indicator whether to apply truncation along the rake. The truncation of a distribution is applied, if $|SoFI| > 0.25\sqrt{3}$. The threshold is half the absolute value of $SoFI$ for the end members of reverse or normal faulting. In order to compensate for the truncation of $\mathcal{J}$ and to preserve the second axiom of probability - here specifically in the form of

$$\int \mathcal{J} d\boldsymbol{\theta} = 1 \qquad (2.25)$$

the wrapped normal distribution with truncation along λ

[1] Please see the supplementary regarding $SoFI$.

is

$$\mathcal{N}_{w,T}(\phi,\lambda|\boldsymbol{\theta}_{\mathcal{N}}) = \begin{cases} \frac{1}{F_T}\sum\limits_{u,v\in\mathbb{Z}} \mathcal{N}(\phi+2\pi u,\lambda+2\pi v|\boldsymbol{\theta}_{\mathcal{N}}) & \text{if } |SoFI| > \frac{\sqrt{3}}{4} \\ 0 & \text{if } |SoFI| \leq \frac{\sqrt{3}}{4} \end{cases} \tag{2.26}$$

where $\boldsymbol{\theta}_{\mathcal{N}} = (\mu,\nu,\sigma^2,\tau^2,r)$, and $1/F_T$ is the truncation factor with

$$F_T = \frac{1}{2}\sum_{v\in\mathbb{Z}} \operatorname{erf}\left(\frac{\pi+2v\pi-|\nu|}{\tau\sqrt{2}}\right) - \operatorname{erf}\left(\frac{2v\pi-|\nu|}{\tau\sqrt{2}}\right) \tag{2.27}$$

The $SoFI$ from Eq. 2.22 in Eq. 2.26 for a distribution is estimated by

$$SoFI = \sin\nu \sin\frac{\pi\alpha}{\alpha+\beta}, \tag{2.28}$$

i.e. the means of λ and δ. This definition corresponds to the expression in Eq. 2.24 for the average .

The statistical model in Eq. 2.29 using the truncated wrapped normal distribution in Eq. 2.26 is stated as

$$\mathcal{J}_T(\phi,\lambda,\delta|\mu,\nu,\sigma^2,\tau^2,r,\alpha,\beta,a,b) = \mathcal{N}_{w,T}(\phi,\lambda|\mu,\nu,\sigma^2,\tau^2,r)\mathcal{B}(\delta|\alpha,\beta,a,b), \tag{2.29}$$

or equivalently with $\boldsymbol{\theta}_{\mathcal{N}} = (\mu,\nu,\sigma^2,\tau^2,r)$ and $\boldsymbol{\theta}_{\mathcal{B}} = (\alpha,\beta,a,b)$:

$$\mathcal{J}_T(\phi,\lambda,\delta|\boldsymbol{\theta}) = \mathcal{N}_{w,T}(\phi,\lambda|\boldsymbol{\theta}_{\mathcal{N}})\mathcal{B}(\delta|\boldsymbol{\theta}_{\mathcal{B}}), \tag{2.30}$$

and is the basis for the mixture model and the EM algorithm in the next subsection. For brevity and readability, the subscript T is dropped in the following and the usage of the truncated distribution is implied in all instances.

Identification of nodal plane clusters with the EM algorithm

The EM algorithm iteratively computes the maximum-likelihood estimates in the presence of incomplete data, i.e. some latent variables which are only indirectly detectable in the observations (Dempster et al., 1977). Each iteration of the EM-algorithm consists of two steps: (1) Expectation-step - Estimation of the expected value of the likelihood for the current estimate of the parameters of the statistical model, given the observations. (2) Maximization-step - Calculation of parameters maximizing the likelihood. The iteration process is repeated until the results converge.

The joint distribution $\mathcal{J}$ describes one component of a mixture model, and ideally represents one cluster within the data. Since a population of clusters is present in the data, the parameters of the components that describe the clusters are the latent variables. Using EM, the parameters of the components can be estimated, by simultaneously maximizing their likelihood iteratively.

The kth component in a mixture of K components is described by $\mathcal{J}_k$ which is weighted by w_k. For all K weights holds

$$\sum_{k=1}^{K} w_k = 1, \tag{2.31}$$

and the data are described by the full mixture model

$$M_{\mathcal{J}} = \sum_{k=1}^{K} w_k \mathcal{J}_k. \tag{2.32}$$

Two typical problems of EM are (1) its inability to handle noise, i.e. scattered data not belonging to any cluster, and (2) the number of components must be known a priori.

For our purpose, the noise data problem is solved by designating a PDF specifically for the noise in the data. We assume "noisy data" to have a wrapped uniform distribution, which is a special case of both distributions $\mathcal{N}_w$ ($\sigma,\tau \to \infty$) and $\mathcal{B}$ ($\alpha=\beta=1$) and thus of $\mathcal{J}$ (Eq. 2.33). A wrapped uniform distribution implies that events are caused by random tectonic forces, i.e. not only the random stress term in Eq. 2.2 is variable but the remaining three as well, most notably the tectonic and earthquake related stress terms. Therefore this component of the mixture model contrasts with the data represented by the other components, where the random stress term is the only variable one. We investigate the properties of the identified clusters in terms of the Kagan angle (section 2.3.2 and 2.4).

We handle the second problem of EM, the a priori knowledge of the component number, by running EM with parameters controlling the component number at each iteration. To summarize the purpose of these control parameters:

> Check for overlap between components and merge components, if a threshold is reached ($\to p$).
>
> Check for the size of components and remove those falling below a threshold ($\to q$).

With the control parameters, the extended EM algorithm consists of three steps:

1. The expectation step is performed by calculating Eq. 2.32.
2. The calculated components are checked for their overlap and weight and finally
3. in the maximization step the parameters of the components are updated.

The algorithm is repeated until the model converges or a maximum number of iterations is reached (e.g. 100 is sufficient since in most cases the model converges relatively fast).

At initialization, EM requires parameters set a priori. For N events, there are $2N$ nodal planes and considering a special component for noise, $K = 2N+1$ components in total are initialized, i.e. we assume each nodal plane as a component a priori. It is sufficient to use a representative subset for larger data sets with $> 2,500$ events, as the information gain per event decreases with each additional event in the catalog. The initial values of the kth component $\mathcal{J}_k$ are either based on basic assumptions or are estimated from the underlying data and thus reduce user interference to a minimum.

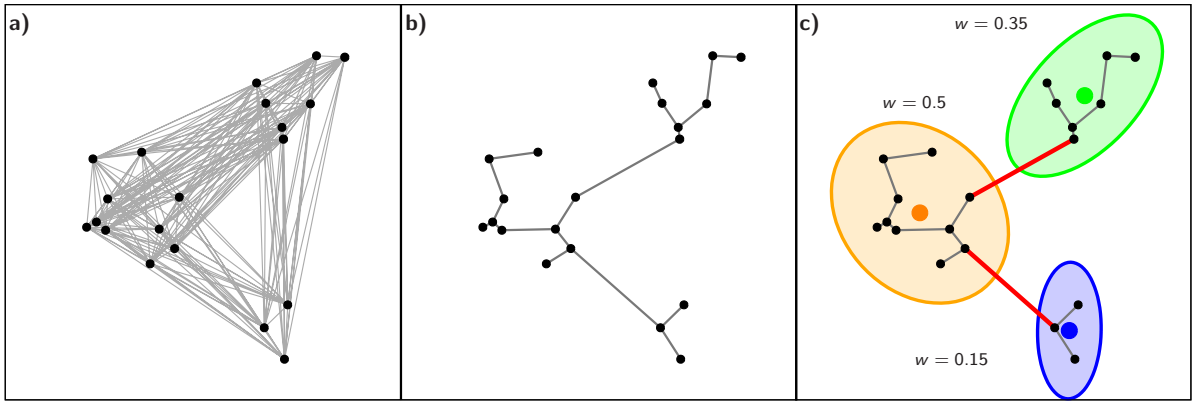

Figure 2.7: Sketch of the application of component merging and removal. a) In the first iteration of EM, all components have identical shape and their centroid is at the nodal plane coordinate (components shown by centroids only). The merging of two components requires a distance metric (gray lines) as criterion, which is the Jensen-Shannon distance. However, in order to merge two components according to control parameter p, not all Jensen-Shannon distances between all pairs are required. It is sufficient to use only a set of those component pairs which connect all component (directly and indirectly). This subset of pairs is found by Kruskal's algorithm (b) and represents those pairs connecting all components with the shortest distance (minimum spanning tree). Next (c), all components with distances below p are merged into one new component (colored ellipses, red lines show distances larger than p). After the component merging, the weights, standing for the size of a component, are checked ($w < qK^{-1}$). The number of merged components here is $K = 3$, and with e.g. $q = 0.5$, the blue component is removed from the mixture (because $0.15 < 0.5/3$). In the subsequent iterations, the step involving Kruskal's algorithm becomes redundant and can be skipped (see text for explanation). This implies for subsequent iterations that only steps shown an (a) and (c) are performed.

1. The strike and rake of the kth nodal plane angle triple are used as the means in the strike-rake plane, $\mu_k = \phi_k$ and $\nu_k = \lambda_k$).
2. Both variances of strike and rake are set to the same value based on a distance estimate from the minimum spanning tree of the data. See section 2.2.2. The variance should sufficiently cover a wider neighborhood around the center of each initial component.
3. No correlation between strike and rake is assumed, $r_k = 0$.
4. The initial component along the dip is modeled using a beta distribution kernel after Chen (1999). The mean of the kernel is δ_k. The variance (or bandwidth in terms of (Chen, 1999)), as for the strike and rake, is based on the distance estimate of the minimum spanning tree. See section 2.2.2
5. The SoF index is based on the rake and dip, $SoFI_k = \sin\lambda_k \sin 2\delta_k$
6. The weight is the mean weight, $w_k = K^{-1}$.

The cluster designated for the noise (with index $k = K$) is initialized as a uniform distribution.

$$\begin{aligned}\mathcal{J}_K &= \mathcal{N}_w(\phi, \lambda|0, 0, \infty, \infty, 0)\mathcal{B}(\delta|1, 1, -1, 91) \\ &= \frac{1}{4\pi^2}\frac{23\pi}{45}\end{aligned} \tag{2.33}$$

Like the other distributions, the weight is at initiation the average weight $w_K = K^{-1}$.

Due to the large number of components at initialization ($K = 2N + 1$), it is very likely that neighboring components have a large overlap. The overlap - or similarity - of two components, represented by their PDF A and B with weights w_A and w_B, respectively, is measured by the Jensen-Shannon distance (Österreicher & Vajda, 2003)

$$\begin{aligned}d_{JS} = &\\ &\left[-\frac{1}{w_A + w_B}\int w_A A \log_2 A + w_B B \log_2 B d\boldsymbol{\theta}\right. \\ &\left. -\int \left(\frac{w_A A + w_B B}{w_A + w_B}\right)\log_2\left(\frac{w_A A + w_B B}{w_A + w_B}\right) d\boldsymbol{\theta}\right]^{\frac{1}{2}}.\end{aligned} \tag{2.34}$$

The Jensen-Shannon distance is in the range between zero (identity of components) and one (completely dissimilar).

When two or more components have an overlap larger then a given threshold, they are merged into one component. The threshold of the Jensen-Shannon distance at which two components are merged is set by the control parameter p. Since p is not known, EM is performed for a set of thresholds p within range $0 < p < 1$.

Some components show little overlap with other components, but contain few events or only one. These remote minor components are undesired as they keep the total number of identified clusters high while containing little information. Therefore, components with weights below qK_i^{-1} are removed from the mixture. The value K_i^{-1} is the average component weight in the ith iteration. The weights are determined after components have been merged (Fig. 2.7c) in each iteration. The control parameter q is in the range $0 \leq q \leq 1$. With $q = 0$, no constraint is applied on the weights and with $q = 1$ total weight uniformity is implied. As with p, q is not known a priori and

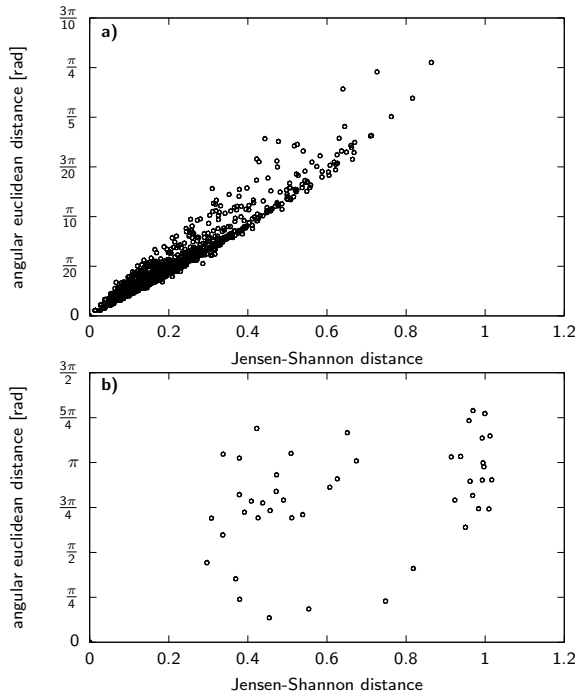

Figure 2.8: Jensen-Shannon distance (Eq. 2.34) versus angular euclidean distance (Eq. 2.36). The Jensen-Shannon distance is based on the pairs of the component probability densities, while the angular euclidean distance is based on the separation means of those components. a) Due to the uniform bandwidth (variance) and weights resulting in similarly shaped components during the first iteration the Jensen-Shannon distance correlates highly with the angular euclidean distance. This fact can be used to use the computationally much simpler angular euclidean distance and apply it with Kruskal's algorithm to significantly reduce the final number of Jensen-Shannon distances during the first iteration. In subsequent iterations (b, second iteration) the correlation between the two metrics disappears due to the adaption of the components to the data resulting in heterogeneously shaped components.

EM is run for a set of different values.

The overlap check and the weight check are at no instance applied to the designated noise component. It can thus be neither removed from the mixture model nor merged into another component. Consequently, no component can be merged into the noise component. If this special component is removed, another component (or several) following the model in Eq. 2.29 will cover the noisy data, which may in turn lead to overfitting. The only parameter controlling the noise component is its weight, which is updated together with the weights of the other components at each iteration.

Application of the minimum spanning tree

The number of distances calculated in the first iteration is $N(2N-1)$. Because the Jensen-Shannon distance has no analytic expression, Eq. 2.34 is evaluated numerically. However, during the first iteration most distances are not required to merge components (Fig. 2.7a). Since all components share the same variances and weights during the first iteration, the Jensen-Shannon distance correlates with the angular euclidean distance between the means of the components (Fig. 2.8). The computationally much simpler euclidean distance is then used in Kruskal's algorithm (Kruskal, 1956) to identify those $2N-1$ component pairs for which the Jensen-Shannon distances are then calculated (Fig. 2.7b).

This reduction of calculations of the Jensen-Shannon distance is based on the triangle inequality:

$$d_{JS}(A,C) \leq d_{JS}(A,B) + d_{JS}(B,C). \tag{2.35}$$

If components A and C are not directly connected, then they are connected via component B (or for the general case, any number of components). Kruskal's algorithm ensures that all components are connected by the minimum sum of all distances, where for each component pair only one distance is given.

The (squared) angular Euclidean distance between two nodal planes is given by

$$\begin{aligned} d_{k,l}^2 = \quad & \left(e^{i\phi_k} - e^{i\phi_l}\right)^2 \\ & + \left(e^{i\lambda_k} - e^{i\lambda_l}\right)^2 \\ & + \left(e^{i\delta_k} - e^{i\delta_l}\right)^2 \end{aligned} \tag{2.36}$$

Given the extension of the nodal plane space, it holds

$$0 \leq d_{k,l} \leq \frac{3}{2}\pi \tag{2.37}$$

In subsequent iterations it is not possible to reduce the number calculations of the Jensen-Shannon distance, because both weights and variances vary and the correlation between the Jensen-Shannon and euclidean distance is not guaranteed anymore. Therefore the minimum spanning tree cannot be based on the Euclidean distance and must be based on the Jensen-Shannon distance, making the minimum spanning tree redundant because no computational advantage is achieved and all possible Jensen-Shannon distances are required due to the uniqueness of all components after the first iteration.

As stated in the list of initial condition, the distances given by minimum spanning tree provide an estimate of the initial variance for both the wrapped normal distribution and the beta distribution. The initial value is derived from the 95 % quantile of the empirical cumulative distribution function of the distances given by the minimum spanning tree.

Optimal parameters for controlling distribution merging and removal

Once the mixture models for different p and q have been calculated, an analysis based on information theory (Shannon, 1948) is applied to select the mixture model that describes the clusters of nodal planes. In the previous section we introduced the Jensen-Shannon distance, which is the square root of the Jensen-Shannon divergence for two distributions. The general form of the Jensen-Shannon di-

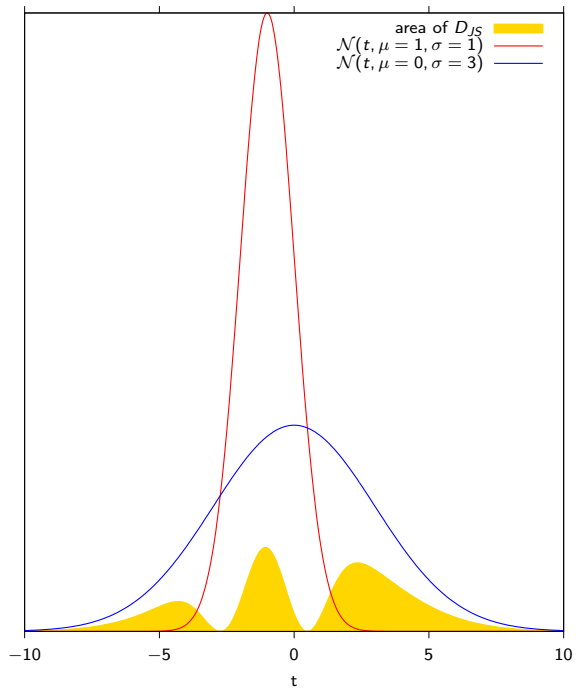

Figure 2.9: The Jensen-Shannon divergence measures the similarity between two distributions. The figure shows two normal distributions (blue, green). The Jensen-Shannon divergence corresponds to the yellow area. Note, how the yellow graph reaches zero where the two distributions intersect, while it increases where the two distributions differ more. It reaches its maximum where the two distributions are most different.

vergence is (Lin, 1991)

$$D_{JS} = H\left(\sum_k w_k P_k\right) - \sum_k w_k H(P_k), \qquad (2.38)$$

where w_k are weights with $\sum_k w_k = 1$. The probability distribution P_k has information entropy $H(P_k)$ (where H is the greek capital letter "eta"), which in case of a continuous distribution P is defined as (Shannon, 1948)

$$H(P) = -\int P(x) \log_b P(x) dx \qquad (2.39)$$

specifically for the distributions of FMS angles (Eq. 2.29)

$$H(\mathcal{J}) = -\int \mathcal{J}(\boldsymbol{\theta}) \log_b \mathcal{J}(\boldsymbol{\theta}) d\boldsymbol{\theta}, \qquad (2.40)$$

where the base b of the logarithm determines the range of the Jensen-Shannon divergence. An illustrating example for the Jensen-Shannon divergence is shown in Fig. 2.9.

If the number of distributions in Eq. 2.38 is equal to base b of the entropy, then the range of the Jensen-Shannon divergence is between 0 and 1. As for the Jensen-Shannon distance in Eq. 2.34, if $D_{JS} = 0$, then all distributions are identical, and if $D_{JS} = 1$ all distributions are fully dissimilar.

The Jensen-Shannon divergence is used to rank the mixture models according to the following criteria:

1. Orthogonality: If the slip vector of one nodal plane is the normal vector of the other plane (and vice versa), then the components representing these planes should behave in the same way (i.e. consistency with Eq. 2.9).

2. Goodness of fit: The mixture model should fit the observed data well.

3. Distinctiveness: Within a mixture model, the individual distributions should be as distinct as possible from each other. In other words, the components should be well separated, show little overlap, and easily distinguishable.

The basis for the first criterion is a change of variable. Here, the variables of a component of mixture model $M_{\mathcal{J}}$ are substituted by the variables of the other nodal plane. The mixture model with substituted variables is labeled $M^S_{\mathcal{J}}$. The change of variables for a probability density function is

$$P(\phi_2, \lambda_2, \delta_2) = P(\phi_1, \lambda_1, \delta_1) |\det \mathrm{J}| \qquad (2.41)$$

Assuming that the variables are changed from one nodal plane representation to the other nodal plane representation, the following relation holds (see appendix 2.6.4 for derivation):

$$\mathcal{J}^S(\phi_2, \lambda_2, \delta_2) = \mathcal{J}(\phi_1, \lambda_1, \delta_1) \frac{\sin \delta_2}{\sin \delta_1} \qquad (2.42)$$

The definition can also be expressed the other way around by exchanging the subscripts.

For the second criterion, it is necessary to represent the data in terms of probabilities of a non-parametric distribution. We use a kernel density estimator (KDE) (Rosenblatt, 1956; Parzen, 1962) similar to the distribution $\mathcal{J}$, with a kernel based on a wrapped bivariate normal distribution and a kernel for the beta distribution (Chen, 1999)with a bandwidth based on a constant variance for strike and rake, and a beta distribution specific bandwidth for the dip (see appendix 2.6.5). The wrapping range is limited to $\{-1, 0, 1\}$ due to the selected small variance σ^2_{KDE} with respect to the whole data range. The choice of the bandwidth is a common problem encountered with kernel density estimates (e.g. Park & Marron, 1990). If a constant variance is used in all entropy estimates, the KDE entropies will correlate with the variance, thus keeping the entropies proportional to each other for different variances.

We compare the mixture model with changed variables to the KDE as well, i.e. joining the first and second criterion. This additional constraint allows for the calculation of the divergence in one step. From Eq. 2.38, the divergence of the mixture model $M_{\mathcal{J}}$, the mixture model with changed variables $M^S_{\mathcal{J}}$, and the KDE h is measured by

$$D^M_{JS} = H\left(\frac{1}{3}\left(M_{\mathcal{J}} + M^S_{\mathcal{J}} + h\right)\right) - \frac{1}{3}\left[H(M_{\mathcal{J}}) + H(M^S_{\mathcal{J}}) + H(h)\right], \qquad (2.43)$$

with

$$M_{\mathcal{J}} = \sum_{k=1}^{K} w_k \mathcal{N}_w(\phi_1, \lambda_1 | \mu_k, \nu_k, \sigma_k^2, \tau_k^2, r_k) \mathcal{B}(\delta_1 | \alpha_k, \beta_k) \tag{2.44}$$

$$M_{\mathcal{J}}^S = \sum_{k=1}^{K} w_k \mathcal{N}_w(\phi_2, \lambda_2 | \mu_k, \nu_k, \sigma_k^2, \tau_k^2, r_k) \mathcal{B}(\delta_2 | \alpha_k, \beta_k) \times \frac{\sin \delta_2}{\sin \delta_1} \tag{2.45}$$

$$h = \frac{1}{2N} \sum_{i=1}^{2N} N_w(\phi_1, \lambda_1 | \phi_i, \lambda_i, \sigma_{KDE}^2) \mathcal{B}(\delta_1 | \alpha_i, \beta_i) \tag{2.46}$$

where the logarithms of the entropies $H(\cdot)$ have base $b = 3$, and the divergence is in the range $[0, 1]$. According to the first two criteria, maximum similarity between the two mixture models and the KDE is desired, i.e. D_{JS}^M needs to be minimized.

For the third criterion, we compute the Jensen-Shannon divergence of all components of mixture model $M_{\mathcal{J}}$, D_{JS}^C. If all components are independent from each other, the Jensen-Shannon divergence reaches its maximum. Since the component describing the noise always overlaps with any other component, it would reduce D_{JS}^C and subsequently its resolving power. Therefore, the noise component (with index $k = K$) is excluded from the calculation of the divergence,

$$D_{JS}^C = H\left(\sum_{k=1}^{K-1} \frac{w_k}{1 - w_K} \mathcal{J}_k\right) - \sum_{k=1}^{K-1} \frac{w_k}{1 - w_K} H(\mathcal{J}_k), \tag{2.47}$$

where the logarithm of the entropies has base $b = K - 1$, and the divergence is in the range $[0, 1]$.

The mixture models associated with two divergences are ranked for all p and q by the following expression:

$$Q_{JS}(p, q) = D_{JS}^M(p, q)^{D_{JS}^C(p,q)} \tag{2.48}$$

The minimum rank jointly minimizes D_{JS}^M and maximizes D_{JS}^C, therefore the mixture model with smallest Q_{JS} best fulfills the three criteria outlined above simultaneously.

Subpopulations of nodal plane clusters with identical SoF

With the best mixture model $M_{\mathcal{J}}^{opt}$, we identify cluster subpopulations that form pairs of nodal planes according to Eq. 2.9. The subpopulations are identified by comparing each component to the component with changed variables (Eq. 2.42), as introduced in the previous section. The probabilities of clusters representing a nodal plane pair are very likely to correlate, while all other combinations are expected to be uncorrelated. The correlation between the probabilities of two distributions $\mathcal{J}_A(\boldsymbol{\theta})$ and $\mathcal{J}_B(\boldsymbol{\theta})$ is measured by the congruence coefficient (Tucker, 1951)

$$r_c = \frac{\sum_{i}^{2N} \mathcal{J}_A(\boldsymbol{\theta}_i) \mathcal{J}_B(\boldsymbol{\theta}_i)}{\sqrt{\sum_{i}^{2N} \mathcal{J}_A(\boldsymbol{\theta}_i)^2 \sum_{i}^{2N} \mathcal{J}_B(\boldsymbol{\theta}_i)^2}} \tag{2.49}$$

Since the probabilities are non-negative, the range of r_c is between zero and one.

The threshold for the congruence coefficients at which two clusters form a nodal plane pair is determined by a change point analysis. We apply a change point analysis similar to the autoregressive likelihood estimation for automated phase picking (Pisarenko et al., 1987; Kushnir et al., 1990). While the phase picking routine is based on a mixture of normal distributions, the distribution of the congruence coefficients is assumed to have arisen under a mixture of two beta distributions, with one distribution for uncorrelated and correlated congruence coefficients, respectively.

The expected number of components of the mixture model $M_{\mathcal{J}}^{opt}$ is low, and may be insufficient for a change point analysis to provide reliable results. Thus, we determine the congruence coefficients by bootstrapping (Efron, 1979) the component probabilities to obtain a sufficiently large sample of congruence coefficients. Bootstrapping not only increases the sample size for the change point analysis, but also includes the uncertainties of the congruence coefficients.

The change point analysis is based on Akaike's information criterion (AIC) (Akaike, 1974)

$$\mathrm{AIC} = 2k - 2 \ln \mathcal{L} \tag{2.50}$$

where k is the number of free parameters and $\mathcal{L}$ is the likelihood of the statistical model, i.e. the mixture of beta distributions. The AIC is used to identify the best mixture of beta distributions. This is identical to identifying the preferred threshold, because the beta distributions are separated at that threshold and otherwise independent from each other. The log-likelihood in Eq. 2.50 for a mixture of two beta distributions (Eq. 2.17) is

$$\ln \mathcal{L} = \sum_{i=1}^{T} \ln \mathcal{B}(r_{ci} | \alpha_l, \beta_l, 0, 1) + \sum_{i=T+1}^{N_r} \ln \mathcal{B}(r_{ci} | \alpha_u, \beta_u, 0, 1) \tag{2.51}$$

where N_r is the total number of congruence coefficients, T is the number of coefficients less than or equal the threshold, and α_l, β_l and α_u, β_u are the four shape parameters (therefore $k = 4$) estimated from the congruence coefficients below (first sum, subscripts with l) and above (second sum, subscripts with u) the threshold congruence coefficient, respectively. The AIC is determined for each congruence coefficient set as the threshold and the preferred threshold is identified where the AIC reaches a minimum.

All cluster combinations with congruence coefficients larger than the threshold are considered to form nodal

plane pairs. Some clusters can be connected to more than one cluster, particularly in the case of strike-slip events, where one cluster will be generally connected to two others. This behavior for strike-slip events is caused by the additional strike ambiguity of subvertically dipping events. Up to four strike-slip clusters can form a subpopulation, while for reverse and normal faulting the size of the subpopulation is two.

2.3 ACE & Stress

2.3.1 Application of ACE to stress mechanics

In the following section we show how to incorporate the results of ACE into applications. As examples, we provide the Kagan angle distribution and stress tensor inversion.

The normalized weight for the ith nodal plane angle triple of a subpopulation with L components from a mixture model with in total K components is given by

$$v_i = \frac{\sum_{l=1}^{L} w_l \mathcal{J}_l(\phi_i, \lambda_i, \delta_i)}{\sum_{k=1}^{K} w_k \mathcal{J}_k(\phi_i, \lambda_i, \delta_i)} \tag{2.52}$$

This normalized weight is the basis any further application.

2.3.2 Kagan angle distribution

Since ACE uses FMS, the final mixture model can be directly used to apply weights to the so-called Kagan angle. The Kagan angle is the smallest angle to rotate one FMS into another. It is determined by finding the rotation quaternion between two FMS that results in the smallest angle (Kagan, 2007). The distribution of this angle follows a rotational Cauchy distribution under the assumption of purely randomly distributed distortions (i.e. faults) in a constant stress field with random variations (Eq. 2.2).

In section 2.2.2, we introduced the definitions of the components of the mixture model. While we assume the joint probability distribution in Eq. 2.29 for all components, we use the special case of a uniform distribution of the angles to represent the FMS noise (i.e. those events not forming clusters) at all instances. In terms of the Kagan angle Φ, a uniform distribution of the angle triple (ϕ, λ, δ) implies a pure random distribution of double couple sources Kagan (1992). The equation of the rotational distribution for randomly distributed double couple orientations is given in Kagan (1992, Eq. (6) therein).

The rotational distributions have no general analytic representation, except for purely randomly distributed FMS (Kagan, 1992, 2007). To generate other rotational distributions we follow the procedure outlined by Kagan (1992). We focus here on the comparison between the rotations of the FMS data and some rotational distributions. Following Kagan (1992, 2013), we consider pure random DC (double couple) rotation distribution, the rotational Cauchy distribution and the rotational Fisher-Bingham distribution for comparison. The Fisher-Bingham distribution (Kent, 1982) is a generalization of the von Mises-Fisher distribution used in Kagan (1992, 2007) and is not limited to an isotropic distribution of normal/slip vectors, i.e. same variances for strike and dip. Kent (1982) defines the Fisher-Bingham distribution as

$$\mathcal{FB}(\mathrm{x}|\kappa, \beta, \mathbf{\Gamma}) \propto e^{\kappa \boldsymbol{\gamma}_1^T \cdot \mathrm{x} + \beta\left[(\boldsymbol{\gamma}_2^T \cdot \mathrm{x})^2 - (\boldsymbol{\gamma}_3^T \cdot \mathrm{x})^2\right]} \quad \text{with } 0 \leq \beta < \frac{\kappa}{2} \text{ and } \mathbf{\Gamma} = (\boldsymbol{\gamma}_1, \boldsymbol{\gamma}_2, \boldsymbol{\gamma}_3) \tag{2.53}$$

with x being the $\hat{\mathrm{n}}$, $\hat{\mathrm{d}}$, or $\hat{\mathrm{b}}$ axes; concentration parameter κ (analogue to an inverse variance), shape factor β and the orthogonal matrix $\mathbf{\Gamma}$ with vectors $\hat{\boldsymbol{\gamma}}_1$ (mean axis), $\hat{\boldsymbol{\gamma}}_2$ (major axis of shape ellipse) and $\hat{\boldsymbol{\gamma}}_3$ (minor axis of shape ellipse). For brevity we left the normalization constant of the distribution out, see Kent (1982) for a detailed description. For $\beta = 0$ the Fisher-Bingham distribution becomes the von Mises-Fisher distribution. Its rotational counterpart is denoted by $\mathcal{FB}_r(\Phi|\kappa, \beta)$ and for $\kappa = \beta = 0$ it becomes the random DC distribution.

To obtain samples for $\mathcal{FB}(\mathrm{x}|\kappa, \beta, \mathbf{\Gamma})$ we use acceptance-rejection sampling (von Neumann, 1951) by accepting a sample of the Fisher-Bingham distribution for the slip, normal and null vectors (Eq. 2.53) if all three are accepted simultaneously. The matrices $\mathbf{\Gamma}$ for each of the three vectors are defined such to represent the orthogonality of the three vectors.

The rotational distributions for the different FMS subpopulations are estimated by taking the probabilities of the mixture model for each angle triple in a subpopulation as weights. We denote the rotational angle between the FMS given by ith and jth angle triple as φ_{ij}. The weight for the rotation angle φ_{ij} is the product of the ith and jth weight from Eq. 2.52. With N angle triples and neglecting rotations between same angle triples, a total of $N(N-1)$ rotations exist. The empirical weighted cumulative distribution function in terms of the rotational angle Φ is

$$F(\Phi) = \frac{\sum_{i,j=1}^{N} v_i v_j \mathrm{I}(\varphi_{ij} \leq \Phi)}{\sum_{i,j=1}^{N} v_i v_j} \text{ with } i \neq j, \tag{2.54}$$

where $\mathrm{I}(x)$ is an indicator function that is one if condition x is true and zero otherwise. The range of the rotation angle is $0° \leq \Phi \leq 120°$ (Kagan, 1992).

2.3.3 Stress Tensor Inversion

Since ACE's theoretical basis is related to stress tensor inversion, the cluster results can be used as a priori information for a stress tensor inversion. The a priori information comes as a definition for FMS subpopulations. Within each subpopulation, e.g. for thrust faulting at a continental plate interface, the stress state can be assumed to be more consistent than for the overall data set. ACE's subpopulations can be seen as a way to treat a FMS catalog not as uniform data set for stress inversion, but as a polyphase data set (Célérier et al., 2012, sec. 7.4 and references therein), i.e. a data set divided into consistent subsets, and stress is

inverted from each subset to arrive at a more substantial picture of the stress state.

We use the least squares (LSQ) approach introduced by Michael (1984), nonetheless ACE's a priori information can be implemented in any other stress inversion technique. Micheal's method is defined by the following relation:

$$\mathrm{s} = \mathrm{A}\mathrm{t} \tag{2.55}$$

s is a vector containing N unit slip vectors and matrix A is based on N normal vectors and t is the reduced stress tensor in vector notation. Two fundamental assumptions are present in Eq. 5.15: The Wallace-Bott hypothesis holds and the slip magnitude is uniform in all directions and unknown (implied by using the unit slip vectors). The difference of the reduced (or deviatoric) stress tensor to the stress tensor in Eq. 2.1 is the absence of an isotropic stress component (pressure p). The deviatoric stress tensor $\boldsymbol{\sigma}^{dev}$ is defined by

$$\boldsymbol{\sigma}^{dev} = \boldsymbol{\sigma} - p\mathrm{I} \tag{2.56}$$

where I is the identity matrix and pressure p is

$$p = \frac{\mathrm{tr}(\boldsymbol{\sigma})}{3} = \frac{\sigma_{11} + \sigma_{22} + \sigma_{33}}{3}, \tag{2.57}$$

thus follows $\boldsymbol{\sigma}^{dev}_{33} = \boldsymbol{\sigma}^{dev}_{11} + \boldsymbol{\sigma}^{dev}_{22}$, i.e. the deviatoric stress tensor has five independent components only. For convenience the stress tensor is expressed in Voigt notation

$$\mathrm{t} = \begin{pmatrix} t_1 \\ t_2 \\ t_3 \\ t_4 \\ t_5 \end{pmatrix} = \begin{pmatrix} \sigma^{dev}_{11} \\ \sigma^{dev}_{22} \\ \sigma^{dev}_{12} \\ \sigma^{dev}_{13} \\ \sigma^{dev}_{23} \end{pmatrix} = \begin{pmatrix} \sigma_{11} - p \\ \sigma_{22} - p \\ \sigma_{12} \\ \sigma_{13} \\ \sigma_{23} \end{pmatrix} \tag{2.58}$$

The matrix A_i is based on the normal vector n_i (subscript i dropped in the following equation) and follows from Eq. 5.16

$$\mathrm{A} = \begin{pmatrix} n_1 - n_1^3 + n_1 n_3^2 & -n_2 n_1^2 + n_2 n_3^2 & -n_3 n_1^2 - n_3 + n_3^3 \\ n_2 - 2 n_2 n_1^2 & n_1 - 2 n_1 n_2^2 & -2 n_1 n_2 n_3 \\ n_3 - 2 n_3 n_1^2 & -2 n_1 n_2 n_3 & n_1 - 2 n_1 n_3^2 \\ -n_1 n_2^2 + n_1 n_3^2 & n_2 - n_2^3 + n_2 n_3^2 & -n_2^2 n_3 - n_3 + n_3^3 \\ -2 n_1 n_2 n_3 & n_3 - 2 n_3 n_2^2 & n_2 - 2 n_2 n_3^3 \end{pmatrix}^T \tag{2.59}$$

Inverting for t results in

$$\mathrm{t} = (\mathrm{A}^T\mathrm{A})^{-1}\mathrm{A}^T\mathrm{s} \tag{2.60}$$

This is the general solution of the over-determined LSQ problem. Weighted LSQ introduces the weight matrix W

$$\mathrm{t} = (\mathrm{A}^T\mathrm{W}\mathrm{A})^{-1}\mathrm{A}^T\mathrm{W}\mathrm{s} \tag{2.61}$$

with weights based on Eq. 2.52

$$\mathrm{W} = \begin{pmatrix} v_1 & 0 & \cdots & 0 \\ 0 & v_2 & \cdots & 0 \\ \vdots & \vdots & \ddots & \vdots \\ 0 & 0 & \cdots & v_N \end{pmatrix} \tag{2.62}$$

If clusters are determined for larger regions it is reasonable to invert for a set of tensors that are linearly dependent in space (Hardebeck & Michael, 2006, modified from Eq. 14)

$$\mathrm{t}_a = (\mathrm{A}^T\mathrm{W}\mathrm{A} + \epsilon^2\mathrm{D}^T\mathrm{D})^{-1}\mathrm{A}^T\mathrm{W}\mathrm{s} \tag{2.63}$$

where D expresses the linear dependency of the neighboring tensors and ϵ is the dependency strength and t_a is the vector of all stress tensors.

$$\mathrm{t}_a = \begin{pmatrix} \mathrm{t}_1 \\ \mathrm{t}_2 \\ \vdots \\ \mathrm{t}_n \end{pmatrix} \tag{2.64}$$

Calculation of the stress tensors according to Eq. 2.61 and 5.23 are performed with the armadillo library for C++ (Sanderson & Curtin, 2016).

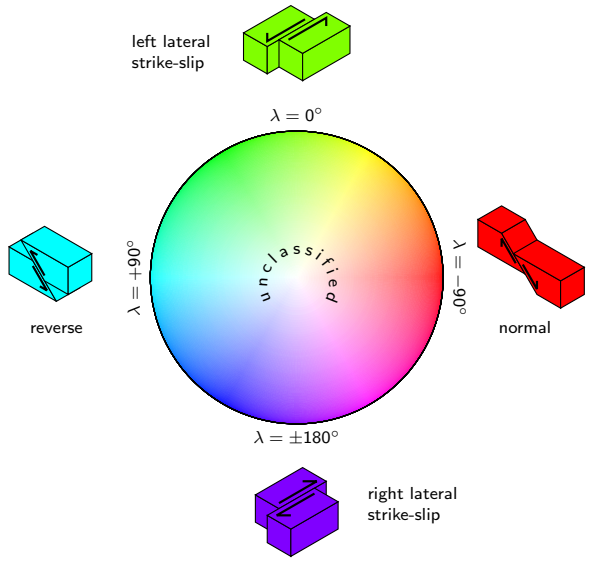

Figure 2.10: Color palette based on the rake to indicate the Style-of-Faulting of nodal plane clusters. The three SoF end members are also shown (for strike-slip both left- and right-lateral are shown). The rake hue corresponds to the hue of the HSL colorspace, with the end members assigned the colors chartreuse (left-lateral strike-slip), cyan (reverse), violet (right-lateral strike-slip) and red (normal). The color brightness corresponds to the probability of a nodal plane/event belonging to a certain cluster. The noise cluster has full brightness (i.e. white) and data in that range are unclassified. These color definitions are used in the subsequent figures.

2.4 Examples

We present three examples of ACE for Northern Chile, the Nazca plate and Kyūshū (Japan). The examples show the best mixture models from ACE for the regions. A comparison of STI with and without ACE based weights are shown as well as the distribution of Kagan angles.

All results of ACE we present here are given as probabilities as defined in Eq. 2.52. In the figures showing the probabilities of the Style-of-Faulting, we use a color

code similar to the World Stress Map, based on the HSV (hue, saturation, [brightness] value) color space. The hue represents the SoF, and brightness represents the probability of the given SoF (Fig. 2.10). While only one color hue is assigned for all events in a component, the brightness shows the probability of each nodal plane to be in that particular component. If several subpopulations of a similar (or even identical) SoF are present, colors are separated by saturation, i.e. one subpopulation appears generally lighter/darker than the other. When the hypocenter associated with a FMS is plotted, the color hue, saturation and lightness value are based on the average of both nodal planes. In case we cannot clearly differentiate between left- and right-lateral strike-slip, green is used.

2.4.1 Northern Chile

We apply ACE to focal mechanism data from the GCMT catalog (Dziewonski et al., 1981; Ekström et al., 2012) from 1976 - 2016 for northern Chile. This catalog contains 848 events, resulting in 1696 nodal planes. For northern Chile five clusters in three subpopulations have been identified, two clusters for normal and reverse faulting, respectively, and one cluster for unclassified SoF (Fig. 2.12a).

The reverse faulting clusters are associated with the plate interface of the colliding South American and Nazca plates, while the normal faulting clusters relate to deeper events in the downgoing slab (Fig. 2.12b,d). The unclassified events are mostly near the surface and are associated with thrusting in the Andes.

Several major events occurred in the region and their corresponding focal mechanisms (Fig. 2.12c) are in the centers of each identified cluster, respectively.

The distributions of the Kagan angle Φ for the Chilean FMS are shown in Fig. 2.11. The empirical cumulative probability distributions (ECDF) are calculated by Eq. 2.54 for each subpopulation in Fig. 2.12. Reverse faulting FMS (cyan curve) show high similarity between themselves as appr. 80 % of the FMS differ by a rotational angle of less than 30°. The normal faulting FMS (red curve) are more diverse and show larger rotational angles (nearly twice as much as for interface FMS), indicating a more complex stress field for these events which are also at larger depths compared to the reverse events. The remaining unclassified events (gray curve) are nearly completely randomly distributed, as their rotational distribution is similar to a purely random distribution of FMS (black curve). The three empirical distributions are fitted to rotational Fisher-Bingham distributions ($\mathcal{FB}_r$, dashed curves), parameters are given in Fig. 2.11. All empirical distributions are well described by the rotational Fisher-Bingham distribution.

Fig. 2.11 shows also the rotation angle distribution for unweighted data (light gray line). The empirical distribution is derived similarly to Kagan (1992). We consider all events in the region with a focal depth shallower than 100 km. Only rotations of FMS with a hypocentral distance of less than 50 km are taken into account. The resulting distribution indicates similarity for most shallow events in Northern Chile. This coincides with the empirical distribution of the interface subpopulation which is mostly at shallow depths (Fig. 2.12d). In agreement with Kagan (1992); Kagan & Jackson (2015) the unweighted distribution is well described a rotational Cauchy distribution (Fig. 2.11, dotted line).

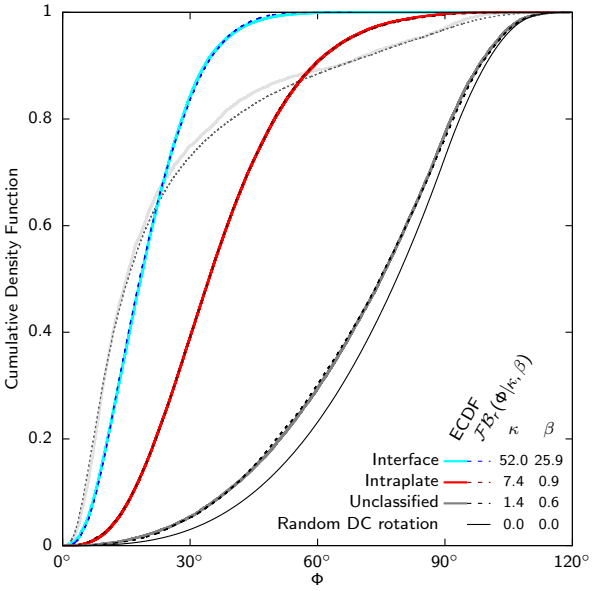

Figure 2.11: Cumulative distribution functions of the rotation angle between pairs of FMS from northern Chile. The colored solid curves are estimated from the FMS data by using the subpopulation probabilities as weights. The empirical distributions are well described by rotational Fisher-Bingham distributions ($\mathcal{FB}_r$, dashed lines, parameters are in table). The angle distribution for unclassified FMS is nearly random since it is close to the pure random DC distribution (thin black line). The solid light gray line shows the rotation angle distribution for pairs of FMS shallower than 100 km and with a hypocenters separated by less than 50 km. This unweighted distribution is best described by a rotational Cauchy distribution (κ_c=0.06, dotted line).

Furthermore, the concentration parameter κ of the rotational Fisher-Bingham distribution correlates inversely with the variances of the wrapped normal distribution, i.e. the extent of the nodal plane clusters in Fig. 2.12a corresponds to the steepness of the ECDF in Fig. 2.11.

We conducted two stress tensor inversions, one, conventional inversion, using all events in the catalog of Northern Chile with an event depth of maximum 50 km. These shallow reverse faulting events are associated with interface activity. The second inversion uses the probabilities of the cluster subpopulations for reverse faulting as weights according to Eq. 2.52. These events are also associated mostly with interface activity. Fig. 5.10a shows the results of the conventional stress tensor inversion, i.e. all events are equally weighted. The plot in Fig. 5.10 shows the distribution of 20,000 bootstrapped results using a kernel density estimator with a von Mises-Fisher distribution (concentration $\kappa = 2500$). The orientations of the principal stresses are shown in a lower hemispheric plot. While the minimum stress S_3 (cyan) is well located and nearly vertical, the horizontal stresses S_1 (magenta) and S_2 (yellow)

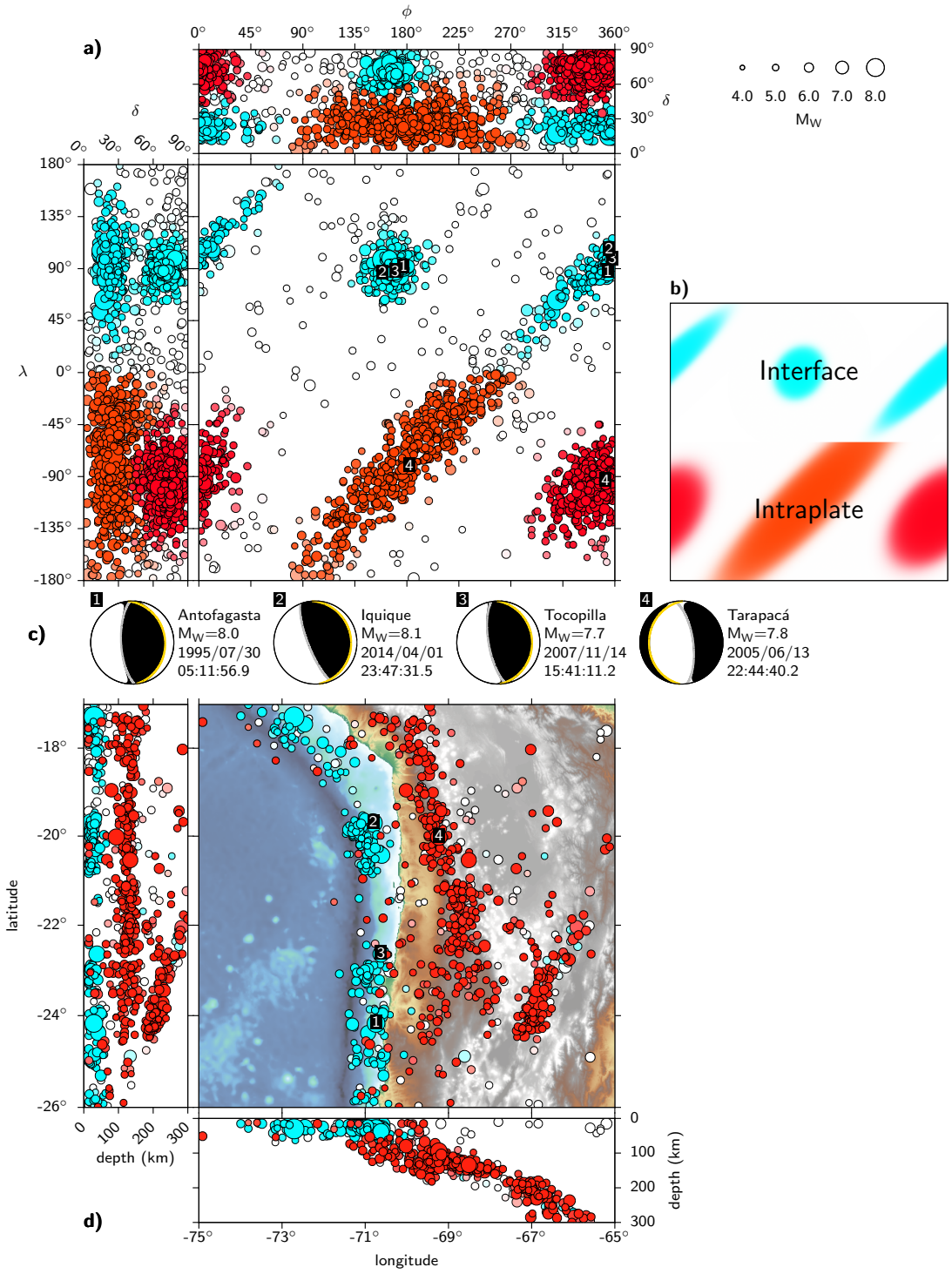

Figure 2.12: a) The optimal mixture model for the Northern Chile FMS data set. Two clusters for both normal and reverse faulting are identified. Both regimes show one (more or less) circular and one elongated cluster. b) Legend of the subpopulations. The reverse faulting clusters (cyan) are related to the interface of the colliding plates. The events in the normal faulting clusters (red) form the subpopulation associated with the subducting slab. FMS in the white area are unclassified. c) Four example beach ball plots of significant events in the region. The rupture plane and auxiliary planes are indicated as yellow and gray great-circles, respectively. d) Hypocentral locations of earthquakes from the GCMT catalog in Northern Chile. Nearly all reverse faulting events occur in the upper 50 km along the coast, while most normal faulting events are deeper in the slab. Few normal faulting events are close to surface along the shorelines. These events may be associated with the bending of the Nazca plate before being subducted. Many unclassified events are near the surface. These events are likely related to the thrusting of the Andes due to their locations, as well as their frequently positive rake values. Map data: ETOPO1 (Amante & Eakins, 2009).

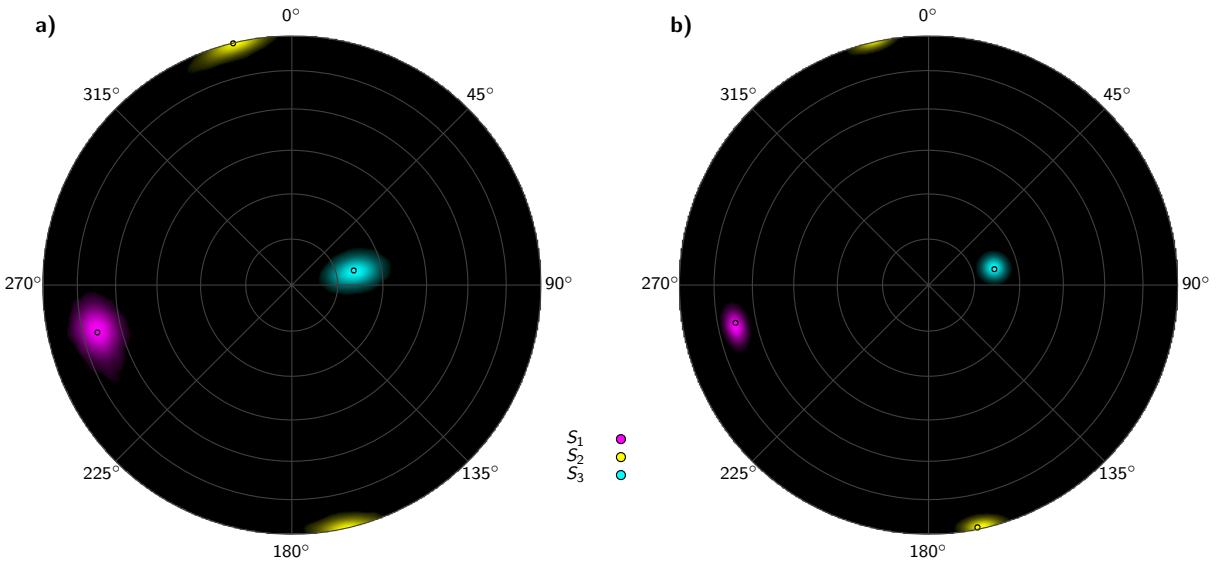

Figure 2.13: Results of conventional stress tensor inversion (a) and stress tensor inversion using weights based on ACE (b) for northern Chile. For the conventional inversion we used all events from the northern Chile (region extent in Figure 2.12d) with a maximum depth of 50 km. For the weighted inversion we used probabilities of the events belong to interface subpopulation (cyan colored in Fig. 2.12). The plots show the principal stress axes orientations (dots) in a lower hemisphere using the Lambert azimuthal equal-area projection (Schmidt net). Uncertainty distributions are estimated by bootstrapping (20,000 times) and are shown as a kernel density estimator based on the von Mises-Fisher distribution (κ=2500). Stress orientations are nearly identical for both inversions, though uncertainties are significantly reduced in the weighted inversion (b). This reduction is achieved by excluding events not associated with interface activity. Those excluded events are more likely associated with a different local stress field (e.g. Andes thrustbelt, reactivation of faults in the oceanic plate).

are less well constrained. Uncertainties are estimated by bootstrapping following Michael (1987) by selecting randomly events and randomly setting one nodal plane is rupture plane and one as auxiliary plane.

The inversion results based on ACE are shown in 5.10b. While principal stress orientations are comparable to the conventional solution in Fig. 5.10, uncertainties are significantly reduced. Uncertainties are estimated with same procedure as for the conventional inversion.

Based on the motion direction of the Nazca plate, the clusters for interface events are separable into a cluster consisting of rupture planes ($\phi \approx 0°$,$\delta \approx 15°$) and auxiliary planes ($\phi \approx 180°$,$\delta \approx 75°$). For the normal faulting subpopulation no such disambiguation is feasible due to two-sided fault activation. The lack of preferred rupture orientation has been confirmed by aftershock analysis and directivity analysis (e.g. Warren, 2014).

Furthermore, the event hypocenters in the Northern Chile region identified as reverse faulting are in the upper 50 km, a common threshold for the occurrence of reverse faulting in that region (e.g. Haendel et al., 2015) and all large magnitude reverse events occurred in shallower depths (Fig. 2.12c).

2.4.2 Nazca Plate

The second example covers the focal mechanisms of the GCMT catalog from 1976 - 2016 for the entire Nazca plate with eastward motion, thus this example does not cover data from the northern plate boundary due to the plate's north-south motion. As the previous example is a subset of this data set, we expect similar results for normal and reverse faulting. The bulk of the Nazca plate can be considered as a homogeneous block moving eastwards surrounded by the Cocos plate to the north, the Pacific plate to the west, the Antarctic Plate to the south and the South American Plate to the east. The catalog for this region contains 3528 events (7056 nodal planes) and the setup for ACE is as in the previous example.

The optimal mixture model (Fig. 5.11a) shows four clusters similar to those found for Northern Chile: two for reverse and normal faulting, respectively. In addition, eight clusters with rakes close to either $0°$ or $\pm 180°$ are identified as well, indicating strike-slip. In total, five subpopulations are identified: reverse, normal, two for strike-slip (right- and left-lateral), and one for unclassified events (Fig. 5.11a). The normal and reverse subpopulations appear similar in shape and location as in case of the Northern Chile data (which are a subset here), suggesting that the stress orientations remain fairly constant along the entire west coast of South America.

The rotation angle distributions for each event type subpopulation are shown in Fig. 2.14. The ECDF for reverse faulting events (cyan) is comparable to the one from Northern Chile in Fig. 2.11, though the concentration κ is lower. This is expected due to the much larger catalog of events spanning a larger area. The normal faulting subpopulation is less well described by a rotational Fisher-Bingham distribution and the ECDF deviates from the model. This can be explained by the large variety of

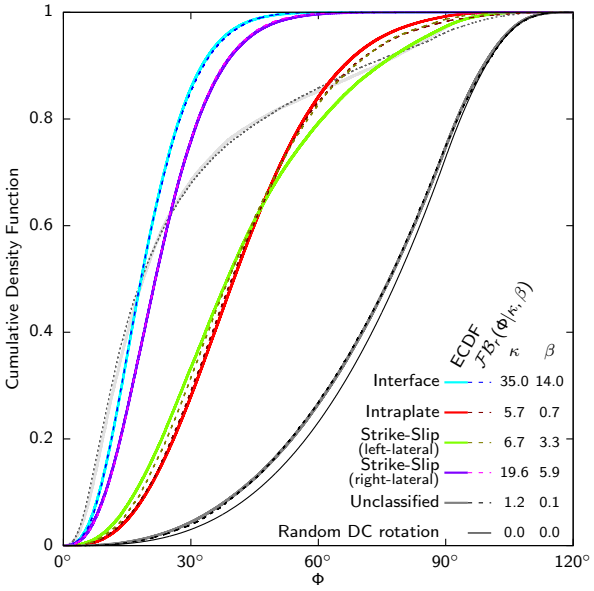

Figure 2.14: Cumulative distribution functions of the rotation angle between pairs of FMS for the Nazca Plate. The colored solid curves are estimated from the FMS data by using the subpopulation probabilities as weights. The empirical distributions are well described by rotational Fisher-Bingham distributions ($\mathcal{FB}_r$, dashed lines, parameters are in table). As for the northern Chile FMS (which are completely included in this data set), the angle distribution for unclassified FMS is nearly random and is very similar to the pure random DC distribution (thin black line). The solid light gray line shows the rotation angle distribution for pairs of FMS shallower than 100 km and with a hypocenters separated by less than 50 km. This unweighted distribution is best described by a rotational Cauchy distribution (κ_c=0.07, dotted line).

normal faulting events along the Nazca plate boundaries. While events to the East are mostly associated with intraslab activity, normal faulting events along the southern and western boundaries occur along the mid-ocean ridges.

A similar behavior of the rotation angle distribution is observed for strike-slip events (Fig. 2.14, green curve). This strike-slip subpopulation is associated with events along the East Pacific Rise (Fig. 5.11d, west boundary of the Nazca Plate) and events in this region are usually left-lateral. Yet another group in this subpopulation occurs along the Liquiñe-Ofqui fault in Chile (Fig. 5.11d, green colored events, southeastern corner). This fault on the South American Plate is subject to the continental stresses there and only indirectly connected to the Nazca Plate. These shallow events along this fault are right-lateral (Hauser et al., 1991). Therefore, this subpopulation is relatively diverse, which explains the relatively low concentration κ and the deviation from the rotational Fisher-Bingham distribution.

On the other hand, strike-slip events along the southern plate boundary to the Antarctic Plate are very similar to each other as shown by relatively small rotation angles (high concentration). These events are all left-lateral strike-slip. This applies also to the events further north

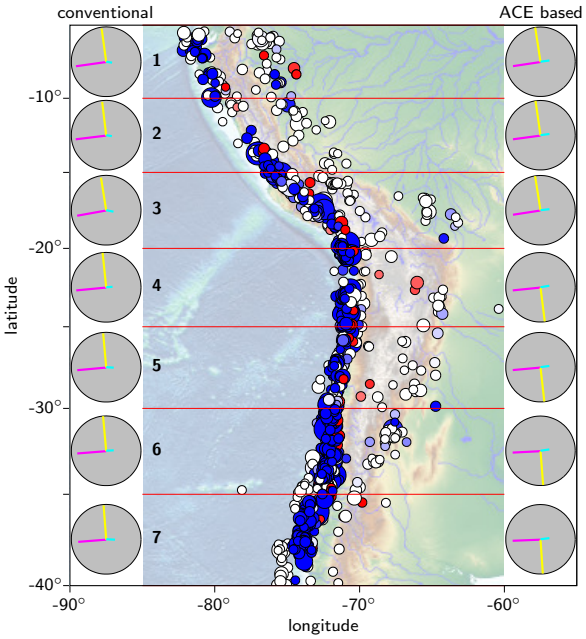

Figure 2.15: Results of conventional stress tensor inversion (left column) and stress tensor inversion using weights based on ACE (right column) by using SATSI for the South American west coast. Each tensor represents the stress in the map area next to it (areas separated along red lines). For the conventional inversion we used all events along the coast (region extent in map) with a maximum depth of 50 km. This encompasses all events in blue and white. For the ACE based inversions we used all events and the color saturation corresponds to the weight size: the more saturated, the larger the weight. The separation into blue and red colors is only necessary to indicate those events with depths less than 50 km (blue) and therefore also included in the conventional inversion (without weighting) and depths more than 50 km (red) and hence excluded from the conventional inversion. In case of the deeper events we show only events that highly probable of interface type. The stress orientation plots show principal stress orientations as lines (S_1 magenta, S_2 yellow, S_3 cyan). Projection is lower hemispheric Lambert azimuthal equal-area. Using the lower hemisphere only results in the flips of the S_2-axes (yellow) in the right column.

close to the East Pacific Rise.

The derived orientation of both strike-slip subpopulations is in agreement with the plate boundaries and the plate movement directions (Bird, 2003) (Fig. 5.11e).

The distribution of unweighted FMS (Fig. 2.14, light gray line) is determined as for the Northern Chile example: only events with hypocenters shallower than 100 km, and distances between hypocenters of less than 50 km. The resulting distribution is similar to the one for Northern Chile (Fig. 2.14, light gray line), yet less steep due to the much larger spatial extent of the region and therefore less similar events are more likely the catalog. As for Northern Chile, the rotational Cauchy distribution fits well to empirical distribution (Fig. 2.14, dotted gray line).

Due to the large extent of the region, we conducted stress tensor inversion with SATSI. As for northern Chile we focus on events associated with interface activity, i.e. with a depth of maximum 50 km. We subdivide the region between -85° and -60° longitude into seven strips of 5° width between latitudes -40° and -5°. Zones are shown as red horizontal lines in Fig. 5.12. We applied SATSI both conventionally without weighting and with ACE based weights. The dependency strength in Eq. 5.23 is set for both cases to $\epsilon = 0.2$ in order to minimize the trade-off between model length and variance. Results for both inversions are shown in Fig. 5.12. For each bin, we show the orientations of the principal stress axes in a lower hemispheric plot (large circles). The left column shows principal stresses for the conventional inversion and the right column for the ACE based inversion. All results are similar with the maximum principal stress S_1 pointing westward, the intermediate principal stress S_2 pointing northward (southward), and the minimum principal pointing downward and slightly eastward (depicted by the shortest arrow).

Results of the conventional inversion tend to be more tilted than results from the ACE based inversion. This is shown by the flipping of the northward/southward pointing stress axes in the ACE based inversion (Fig. 5.12, right column). These stress axes are nearly horizontal, hence they tend to flip from north to south for different tensor solution. This is not the case for the conventionally derived tensors, where all intermediate stress axes point northward.

Uncertainties are determined on the same basis as for northern Chile by bootstrapping. Uncertainties for each tensor between the conventional and ACE based inversion procedure are similar (Fig. 5.13). Individual solutions are shown by different shades of hue, with S_1 in red/purple, S_2 in orange/green, and S_3 in green/blue. However, the scatter of the tensor solutions themselves are larger for the conventional inversion. This is best demonstrated by the orientation of S_3: While for the conventional analysis each tensor uncertainty distribution is distinctively visible (Fig. 5.13a, green/blue areas), it is not the case for the ACE based inversion. Here all uncertainty distributions are in the same location (Fig. 5.13b, blue area). A similar behavior can also be observed for the maximum principal stress orientation (S_1, red/purple), and intermediate stress orientations (S_2, orange/green). For the intermediate stress orientations it also visible in Fig. 5.13 that orientations are closer to horizontal (i.e. at the edge of the plot) for the ACE based solutions than for the conventional inversion.

2.4.3 Kyūshū (SW Japan)

For the third example we investigated focal mechanisms of the NIED catalog from 1997 - 2016 for the island of Kyūshū and surroundings in southwestern Japan. Kyūshū is located on the Eurasian plate, west of the Philippine Plate. The island is traversed by the Futagawa and Hinagu fault systems from Southwest to Northeast. The April 2016 Kumamoto earthquake sequence (main shock: M_W 7.1) occurred on this fault system (Kubo et al., 2016). The catalog contains 1741 events (3482 nodal planes).

The optimal mixture model (Fig. 2.19a) identifies eleven clusters: one for unclassified faulting, two for reverse faulting, and four for normal and strike-slip faulting, respectively.

The two different types of normal faulting are also spatially separated (Fig. 2.19d). The subpopulation of normal faulting events with different mean dips of its two clusters (Fig. 2.19a, bright red) are mostly located in the slab of the subducted Philippine plate, while the other subpopulation of normal events is located in the crust of Kyūshū (Fig. 2.19a, dark red).

The rotation angle distribution are less concentrated compared to the results of the Nazca plate, even for reverse faulting (Fig. 2.18, cyan line). Though all subpopulations are well described by the rotational Fisher-Bingham distribution, both continental intraplate ((Fig. 2.18, dark red) and strike-slip (green line) events show deviations from the rotational Fisher-Bingham distribution and exhibit a slight jump at appr. 90°. This jump is similar to the rotational Cauchy distribution for large rotation angles, though the bump here is smaller in size. This fact and the relatively low concentration κ might be an indicator for a comparatively heterogeneous setting. The unclassified events are almost purely randomly distributed FMS.

The empirical distribution with unweighted data is determined as in the previous examples by considering only events shallower than 100 km and a maximum distance of 50 km between hypocenters. Similarly to the relatively low concentrations of the rotational Fisher-Bingham distributions, the unweighted rotation angle distribution demonstrates a heterogeneous setting for Kyūshū, as nearly half of the FMS pairs have rotation angles of more than 60° (Fig. 2.18, light gray line). Irrespective of the complexity, the rotation angle distribution is well described by the rotational Cauchy distribution (Fig. 2.18, dotted gray line).

2.5 Discussion & Conclusion

We introduced ACE as a purely data driven algorithm to identify clusters of earthquakes, solely based on a focal mechanism's strike, rake, and dip. The results ACE provides are in agreement with the general knowledge about the regions investigated. Within a region with relatively constant stress

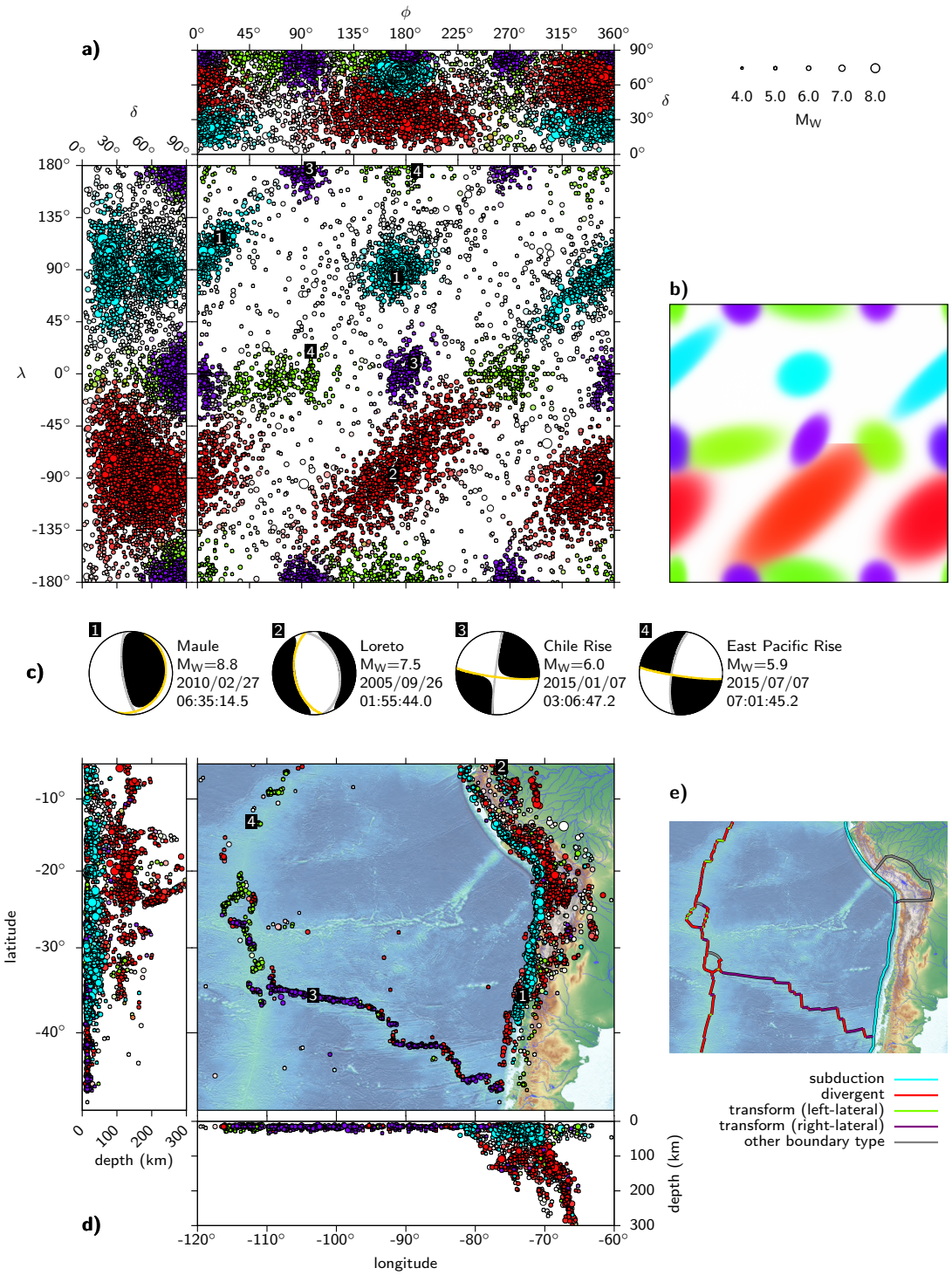

Figure 2.16: a) Optimal mixture model for FMS data from the Nazca plate from 1976-2016. The twelve identified clusters fall into four subpopulations: reverse (cyan), normal (red), strike-slip (chartreuse, violet). b) The reverse and normal faulting clusters are similar to the clusters shown in Fig. 2.12a,b and represent interface (cyan) and intraslab (red) events. In addition, the red clusters also include events along the mid-ocean ridges in the South and West of the Nazca Plate. Eight clusters for strike-slip are identified falling into two subpopulations. c) Four example beach ball plots for each SoF. The rupture plane and auxiliary planes are indicated as yellow and gray great-circles, respectively. The numbers correspond to the numbers in the strike-rake plane (a) and the map (d). d) Map of the Nazca plate showing the hypocenters of the GCMT catalog. Nearly all events are at the plate boundaries and the colored hypocenters of the near surface events delineate the plate boundaries as shown in (e) (Bird, 2003). Map data: ETOPO1 (Amante & Eakins, 2009). From the plate movement and plate boundaries it is possible to infer the strike-slip type: Nearly all strike-slip events along the Chile Rise (southern plate boundary with the Antarctic Plate) and along the southern East Pacific Rise form the subpopulation shown in violet. Due to the eastward motion of the Nazca Plate it is reasonable to assume these events as right-lateral. The strike-slip events shown in chartreuse are mostly along the East Pacific Rise and with left-lateral transform fault segments. A small group of this subpopulation is also located on the South American continent along the Chilean coast (lower right corner). These events are most likely associated with the right-lateral Liquiñe-Ofqui fault.

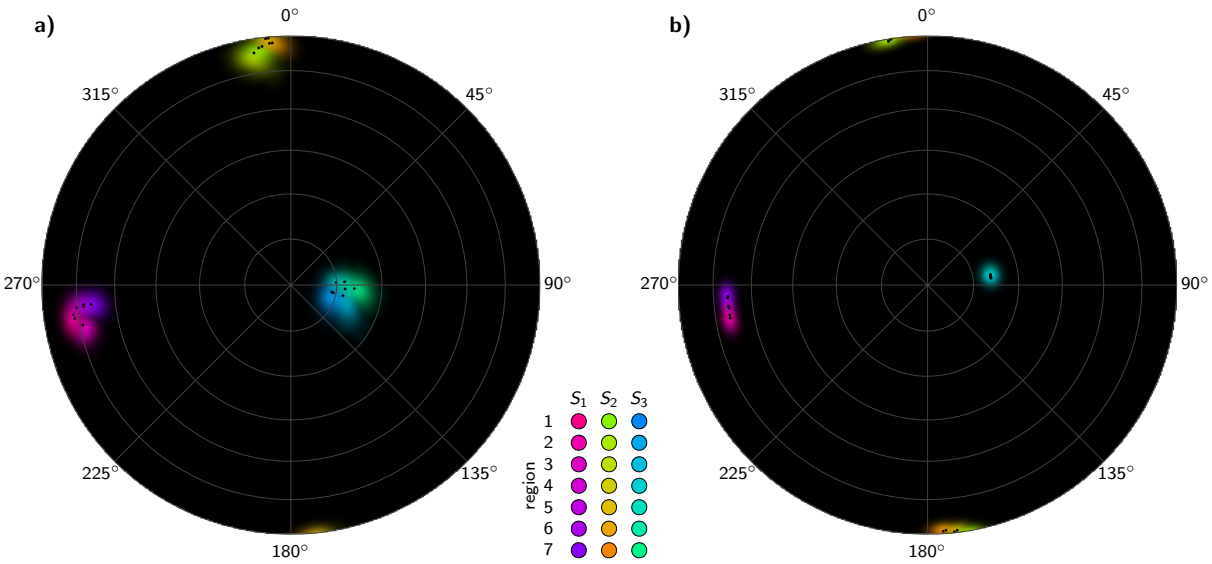

Figure 2.17: Same as Fig. 5.10 but for results in Fig. 5.12 (South American west coast) of SATSI based stress tensor inversion. The different shades for each stress axis distribution represent the different tensors for each region (base colors and numbers correspond to axes colors and numbers in Fig. 5.12). Uncertainties (shown as colored KDE) for each tensor are smaller for the ACE based inversion compared to the conventional weighting. In addition, results on the left are more scattered, e.g. S_1 orientations (black dots) show an unsorted "C" shaped pattern. On the hand, ACE based results show steady increase of the S_1 azimuth, while the dips remain constant. The orientation of the seven S_3-axes of the ACE based inversion (right) are within the uncertainties of each individual tensor, thus resulting in mixing the color shades in the plot. Also the S_2-axes are closer to horizontal for the ACE based inversion, resulting in distributions in the upper and lower half of the plot which explains the flip of the yellow axes in Fig. 5.12.

orientations, hypocenters are not directly required to classify the data. Therefore, classification errors are reduced, compared to classical deterministic classification schemes as presented by García et al. (2012). We also successfully demonstrated that the clusters improve estimates of stress tensors and can be further used for nodal plane disambiguation in the presence of geological/tectonic data.

Few strike-slip are also shown at larger depths (> 50 km, Fig. 5.11d, left and bottom). This misclassification can be caused by the fact, that certain more complex rupture processes are insufficiently represented by a FMS. Another explanation can be found by the fact of an insufficient amount of data. If a particular rupture process is represented by a small number of events, then it is unlikely that this particular process is assigned to its own cluster.

The automatic classification can be used for a wide range applications in the seismology and stress communities, e.g. for seismic hazard assessment, selection of existing ground motion prediction equations (GMPE's), selection of earthquakes to derive new GMPE's, SoF-specifc b-value estimation, selection of focal mechanism as stress indicators (World Stress Map Project) etc.

ACE - in conjunction with geological databases - can also be applied in rapid earthquake assessment to help identify the rupture plane of a newly calculated FMS. In this case, an existing FMS catalog is used as a training data set to derive a mixture model, which is representative for a region of interest. When a new FMS datum is available, the probability of the SoF can be calculated, and if additional geological data is available, the rupture plane orientation can be derived.

We showed the application of the mixture model probabilities of ACE as weights for the determination of the rotation angle distribution of focal mechanisms. The resulting weighted empirical distributions are well described by rotational Fisher-Bingham distributions even in tectonically complex settings. This provides an additional perspective on the distribution of FMS because the weighted distributions show high consistency even to spatially distant events. This effectively reduces the constraint of spatial closeness when considering unweighted data (Kagan, 1992; Kagan & Jackson, 2015). The investigation of the distributions of rotation angle between FMS pairs with ACE based weights also showed the separability of the data into rotationally consistent subsets and a nearly purely randomly orientated FMS subset (the noise/unclassified subpopulation). The former can be associated with large scale tectonic features (e.g. plate interface, subducting slab). The latter subset is only "nearly" purely random as it is not possible to separate those events from a consistent subpopulation (e.g. interface related) that are only by chance similar to the subpopulation's events. This is the main reason why the rotation angle distributions of the unclassified subpopulations are not completely following the random DC rotation.

Stress tensor inversion results with ACE based weighting of the FMS improve stress tensor uncertainties considerably. However, this reduction in uncertainties affects the precision of the results, not necessarily their accuracy. If only one plane of a conjugate fault system is activated (as usually is the case of subduction zones since subduction does not occur on conjugate planes), then the result-

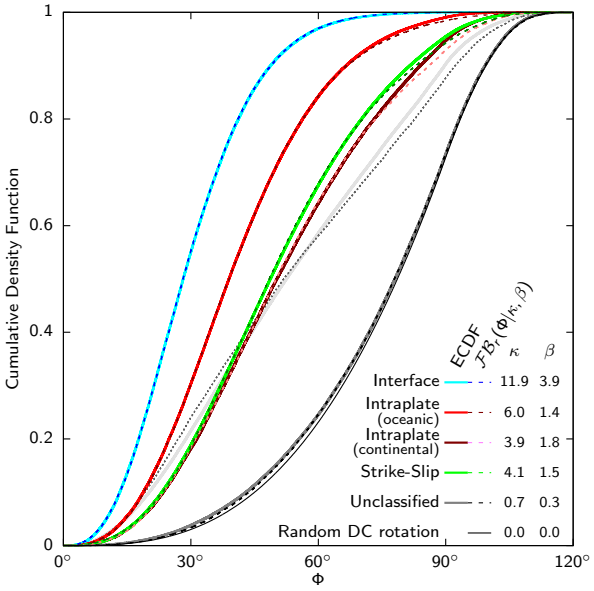

Figure 2.18: Cumulative distribution functions of the rotation angle between pairs of FMS from Kyūshū. The colored solid curves are estimated from the FMS data by using the subpopulation probabilities as weights. The empirical distributions are well described by rotational Fisher-Bingham distributions ($\mathcal{FB}_r$, dashed lines, parameters are in table). The angle distribution for unclassified FMS is nearly random since it is close to the pure random DC distribution (thin black line). The solid light gray line shows the rotation angle distribution for pairs of FMS shallower than 100 km and with a hypocenters separated by less than 50 km. This unweighted distribution is best described by a rotational Cauchy distribution (κ_c=0.23, dotted line). The distribution of the rotation angle indicates more tectonic heterogeneity compared to the previous examples from South America (Fig. 2.11, 2.14).

ing stress tensor can be biased. The bias affects the minimum and maximum principal stress directions and has a maximum magnitude of half the (usually unknown) angle of internal friction in the plane of the maximum and minimum stress orientations. If only one conjugate plane is activated, then the inversion will converge to solutions identical to the PBT axes. This convergence occurs irrespective of a priori knowledge of the rupture and auxiliary plane orientations.

The results of ACE based stress tensor inversion with nodal plane disambiguation are useful for rupture plane distance calculation (with magnitude-fault size relations from e.g. Strasser et al. (2010)), an important distance metric for ground motion prediction equations.

Acknowledgments

The authors would like to thank Moritz Ziegler, Dietrich Stromeyer, and Konrad Schellbach for helpful discussions on stress, mathematics and logic. Thanks to Anne Strader for constructive comments on the manuscript. The focal mechanism data used in this study are freely available at `http://www.globalcmt.org/` (GCMT), `http://geofon.gfz-potsdam.de/` (GEOFON), `http://earthquake.usgs.gov/earthquakes/search/` (USGS), `http://www.fnet.bosai.go.jp/event/search.php?LANG=en` (NIED), `https://wwweic.eri.u-tokyo.ac.jp/tseis/junecfm2/index.html` (JUNEC FM^2) and `http://www.bo.ingv.it/RCMT/` (RCMT). Most plots are generated with gnuplot (`http://gnuplot.sourceforge.net/`), Fig. 2.4 was generated with blender (`https://www.blender.org/`). Geographic maps are generated with GMT (Wessel et al., 2013), topographic data is based on ETOPO1 (Amante & Eakins, 2009). Sebastian Specht acknowledges support from the DFG research training group "Natural Hazards and Risks in a Changing World" (Grant No. GRK 2043/1).

2.6 Appendix: Mathematical concepts

2.6.1 Derivation of angular derivatives - Relations for rupture plane

The equations for the slip and normal vectors in terms of strike (ϕ), rake (λ) and dip (δ) are given by

$$\hat{\mathrm{n}} = \begin{pmatrix} -\sin\delta\sin\phi \\ -\sin\delta\cos\phi \\ \cos\delta \end{pmatrix} \tag{2.65}$$

$$\hat{\mathrm{d}} = \begin{pmatrix} \sin\lambda\cos\delta\sin\phi + \cos\lambda\cos\phi \\ \sin\lambda\cos\delta\cos\phi - \cos\lambda\sin\phi \\ \sin\lambda\sin\delta \end{pmatrix} \tag{2.66}$$

Let $\hat{\mathrm{d}}_2$ denote the slip vector of the auxiliary and $\hat{\mathrm{n}}_1$ the normal vector of the rupture plane. Since the nodal planes are orthogonal to each other, the vectors are identical (e.g. Stein & Wysession, 2003)

$$\hat{\mathrm{d}}_2 = \hat{\mathrm{n}}_1 \quad \text{or} \quad \hat{\mathrm{d}}_1 = \hat{\mathrm{n}}_2 \tag{2.67}$$

Following the Wallace-Bott hypopthesis, the slip and normal vectors are in the same plane as the maximum and minimum principal stress axes. This plane's normal vector is parallel to both the intermediate principal stress axis and the cross product of the slip and normal vector:

$$\hat{\mathrm{b}} = \hat{\mathrm{n}} \times \hat{\mathrm{d}} \tag{2.68}$$

$$= \begin{pmatrix} \cos\lambda\cos\delta\sin\phi - \sin\lambda\cos\phi \\ \cos\lambda\cos\delta\cos\phi + \sin\lambda\sin\phi \\ \cos\lambda\sin\delta \end{pmatrix}. \tag{2.69}$$

With the cross product (and intermediate stress axis) fixed, it follows

$$\hat{\mathrm{b}} = \text{const.} \tag{2.70}$$

Now, let the intermediate stress vector be defined as $\hat{\mathrm{b}}(\lambda(\phi,\delta),\delta,\phi)$ and

$$\frac{\partial\hat{\mathrm{b}}}{\partial\phi} = 0 \tag{2.71}$$

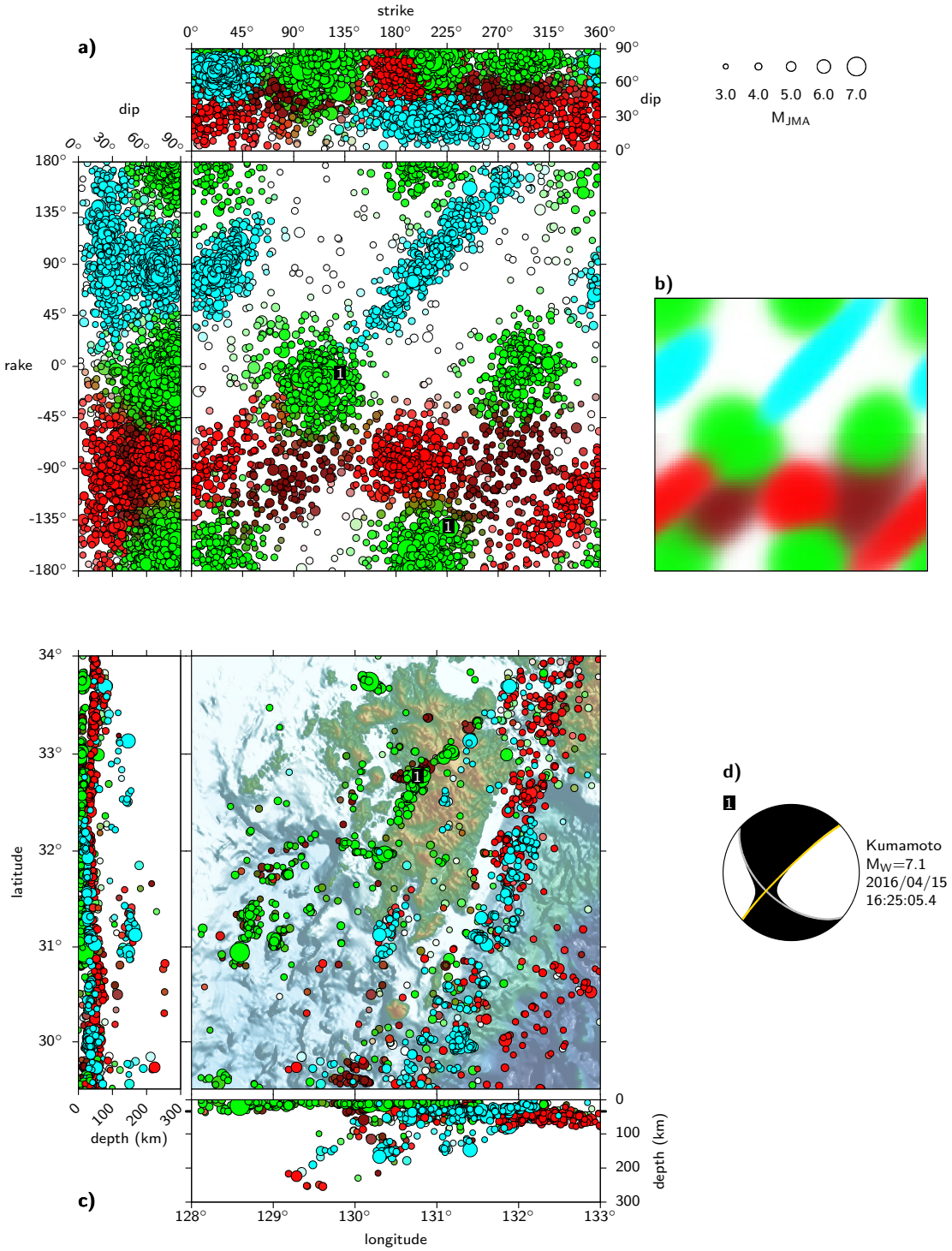

Figure 2.19: a) Optimal mixture model for FMS data from Kyūshū (Japan) from 1997-2016. The ten identified clusters fall into four subpopulations: reverse (cyan), two normal (red) and strike-slip (green). The two normal fault subpopulations show some differences: The clusters are separated by appr. 90° of strike, i.e. irrespective of the nodal plane, the rupture planes are perpendicular to each other. For the subpopulation shown in dark red the dips of both nodal plane clusters are appr. the same, while for the subpopulation in bright red the dips differ significantly for both clusters. The difference of dips in the clusters is also observable for the data from South America (Fig. 2.12a, 5.11a). c) Map of hypocenter locations shows most reverse faulting events along the eastern part of Kyūshū along the interface of the Philippine Plate which is subducted from East under the Eurasian Plate. Normal faulting FMS shown in bright red are close to interface related events and are associated with activity within the oceanic Philippine Plate. The normal faulting events in dark red are located further away from the subduction zone, relatively shallow and close to the strike-slip events. In central Kyūshū where the 2016 Kumamoto earthquake sequence occurred (moment tensor of main shock shown in (d)), events of normal and strike-slip subpopulations are spatially close. Events in this region may form a continuous transition from one SoF to another which is also indicated by the cluster alignment in (a).

And with Eq. 2.66:

$$0 = -\sin\lambda\frac{\partial\lambda}{\partial\phi}\cos\delta\sin\phi - \cos\lambda\cos\delta\cos\phi - \cos\lambda\frac{\partial\lambda}{\partial\phi}\cos\phi + \sin\lambda\sin\phi \tag{2.72}$$

$$0 = -\sin\lambda\frac{\partial\lambda}{\partial\phi}\cos\delta\cos\phi - \cos\lambda\cos\delta\sin\phi + \cos\lambda\frac{\partial\lambda}{\partial\phi}\sin\phi + \sin\lambda\cos\phi \tag{2.73}$$

Multiplying the first line with $\cos\phi$ and the second with $\sin\phi$ and subtracting the second from the first equation reduces to the relation

$$\frac{\partial\lambda}{\partial\phi} = \cos\delta \tag{2.74}$$

The derivative with respect to δ:

$$\frac{\partial\hat{\mathrm{b}}}{\partial\delta} = 0 \tag{2.75}$$

And with Eq. 2.66:

$$0 = -\sin\lambda\frac{\partial\lambda}{\partial\delta}\cos\delta\sin\phi - \cos\lambda\sin\delta\sin\phi - \cos\lambda\frac{\partial\lambda}{\partial\delta}\cos\phi \tag{2.76}$$

$$0 = -\sin\lambda\frac{\partial\lambda}{\partial\phi}\cos\delta\cos\phi - \cos\lambda\sin\delta\cos\phi + \cos\lambda\frac{\partial\lambda}{\partial\delta}\sin\phi \tag{2.77}$$

Again, multiplying the first line with $\cos\phi$ and the second with $\sin\phi$ and subtracting the second from the first equation reduces to the relation

$$\cos\lambda\frac{\partial\lambda}{\partial\delta} = 0 \tag{2.78}$$

The derivatives in Eq. 2.74 and 2.78 are also found by setting $\hat{\mathrm{d}} = \text{const}$.

2.6.2 Wrapped Normal Distribution

The bivariate normal distribution of a vector $\boldsymbol{\upsilon} = (\upsilon_1, \upsilon_2)$:

$$\mathcal{N}(\boldsymbol{\upsilon}|\boldsymbol{\mu}, \boldsymbol{\Sigma}) = \frac{1}{2\pi\sqrt{\det\boldsymbol{\Sigma}}}\exp\left(-\frac{1}{2}(\boldsymbol{\upsilon}-\boldsymbol{\mu})\boldsymbol{\Sigma}^{-1}(\boldsymbol{\upsilon}-\boldsymbol{\mu})^T\right) \tag{2.79}$$

where $\boldsymbol{\mu} = (\mu, \nu)$ is the mean vector and $\boldsymbol{\Sigma}$ the covariance matrix:

$$\boldsymbol{\Sigma} = \begin{pmatrix}\sigma^2 & \rho\sigma\tau \\ \rho\sigma\tau & \tau^2\end{pmatrix}, \tag{2.80}$$

with σ^2 and τ^2 as the variances and ρ is the (population) correlation coefficient.

The bivariate wrapped normal (WN) distribution is

$$\mathcal{N}_w(\phi, \lambda|\mu, \nu, \sigma^2, \tau^2, r) = \sum_{u,v\in\mathbb{Z}} \mathcal{N}(\phi + 2\pi u, \lambda + 2\pi v|\mu, \nu, \sigma^2, \tau^2, r) \tag{2.81}$$

The strike ϕ is in the range $[0, 2\pi]$ and has mean μ and variance σ^2. The rake λ is in the range $[-\pi, \pi]$ with mean ν and variance τ^2. The estimators of these parameters are found by maximum likelihood. Since the parameters of strike and rake have similar estimators, let $\boldsymbol{\theta} = (\phi, \lambda)$ represent the data, $\boldsymbol{\mu} = (\mu, \nu)$ the means and $\boldsymbol{\sigma} = (\sigma^2, \tau^2)$ the variances.

In order to address the circular property of $\boldsymbol{\theta}$, which is also inherent in the parameters of the WN distribution, a change of variable is performed:

$$\boldsymbol{\Theta} = e^{i\boldsymbol{\theta}}. \tag{2.82}$$

The mean is found by

$$\bar{\boldsymbol{\Theta}} = \frac{1}{N}\sum_{n=1}^{N}\boldsymbol{\Theta}_n, \tag{2.83}$$

and the maximum likelihood estimate of $\boldsymbol{\mu}$ of the WN distribution is

$$\hat{\boldsymbol{\mu}} = \arg\bar{\boldsymbol{\Theta}}. \tag{2.84}$$

The quadratic length of the mean vector, given by $\bar{\boldsymbol{\Theta}}\bar{\boldsymbol{\Theta}}^*$ ($*$ denotes complex conjugate), is used to estimate the variances of $\hat{\boldsymbol{\sigma}}$

$$\hat{\boldsymbol{\sigma}} = -\ln\left(\frac{N}{N-1}\left(\bar{\boldsymbol{\Theta}}\bar{\boldsymbol{\Theta}}^* - \frac{1}{N}\right)\right). \tag{2.85}$$

For large N it is sufficient to approximate the variance by

$$\hat{\boldsymbol{\sigma}} = -\ln(\bar{\boldsymbol{\Theta}}\bar{\boldsymbol{\Theta}}^*). \tag{2.86}$$

When applied within the expectation-maximization algorithm, this (biased) estimator must be used as the sample size is lost when the data are weighted according to the distribution functions.

With the mean estimated by Eq. 2.83, the circular sample correlation coefficient is calculated by

$$r = \frac{\sum_{n=1}^{N}\sin(\phi_n - \hat{\mu})\sin(\lambda_n - \hat{\nu})}{\sqrt{\sum_{n=1}^{N}\sin^2(\phi_n - \hat{\mu})}\sqrt{\sum_{n=1}^{N}\sin^2(\lambda_n - \hat{\nu})}}. \tag{2.87}$$

2.6.3 Beta Distribution

Similar to the wrapped normal distribution, the beta distribution is chosen for its wide range of shapes (other distributions are special/limiting cases of the beta distribution), its finite support, and the availability of simple parameter estimators.

The generalized beta distribution in an arbitrary interval (a, b) is given by

$$\mathcal{B}(x|\alpha, \beta, a, b) = \frac{(x-a)^{\alpha-1}(b-x)^{\beta-1}}{(b-a)^{\alpha+\beta-1}B(\alpha, \beta)}, \tag{2.88}$$

where α and β are the shape parameters. The beta function $B(\cdot, \cdot)$ is the normalization constant and is given by

$$B(\alpha, \beta) = \frac{\Gamma(\alpha)\Gamma(\beta)}{\Gamma(\alpha+\beta)}, \tag{2.89}$$

with $\Gamma(\cdot)$ as the gamma function. When programming the above equation, it as advisable to define it terms of its logarithms by using the log-gamma function (e.g. `lgamma` in C/C++, `gammaln` in MATLAB®are provided])/Python. As the gamma function increases to very large values even for small arguments, summing and subtracting the logarithms and exponentiation of the result at the end prevents arithmetic overflow.

The beta distribution has finite support in the range of (a, b), i.e. following the definition of Johnson et al. (1995), and leaves out the interval limits, due to the singularities at $\{0, 1\}$ for $0 < \alpha < 1$ or $0 < \beta < 1$. When applied to data, i.e. the dip angle δ, the interval limits must be defined to include all values. In case of the dip δ, the interval is set to $(-1°, 91°)$.

The estimators of the shape parameters are based on the method of moments. Only the mean m_δ and variance v_δ of the dip and their interval normalized counterparts m and v, respectively, are required:

$$m = \frac{m_\delta - a}{b - a} \qquad m_\delta = \frac{1}{N}\sum_{i=1}^{N}\delta_i \tag{2.90}$$

$$v = \frac{v_\delta}{(b-a)^2} \qquad v_\delta = \frac{1}{N-1}\sum_{i=1}^{N}(\delta_i - m_\delta)^2 \tag{2.91}$$

The shape parameters are found from the definitions of the moments in terms of the shape parameters

$$m = \frac{\alpha}{\alpha+\beta} \qquad v = \frac{\alpha\beta}{(\alpha+\beta)^2(\alpha+\beta+1)}, \tag{2.92}$$

and solving for the shape parameters results in

$$\hat{\alpha} = m\left(\frac{m(1-m)}{v} - 1\right) \tag{2.93}$$

$$\hat{\beta} = (1-m)\left(\frac{m(1-m)}{v} - 1\right). \tag{2.94}$$

These relations hold for $v < m(1-m)$. In few instances, this inequality may not hold within the EM-algorithm. In order to avoid discarding clusters with ill-conditioned shape parameters, we set $\hat{\alpha} = \hat{\beta} = 1$, i.e. the dip is then described by a uniform distribution. Note, that this overriding rule may become obsolete again as the iterations proceed and the distributions change.

2.6.4 Change of variable

The change of variables of a multivariate probability density function from x to y is given by

$$P(\mathrm{y}) = P(\mathrm{x})|\det \mathrm{J}|, \tag{2.95}$$

where J is the Jacobian matrix. The determinant of the Jacobian for the nodal plane angles is

$$\det(\mathrm{J}_\mathrm{I}) = \begin{vmatrix} \frac{\partial\phi_1}{\partial\phi_2} & \frac{\partial\phi_1}{\partial\lambda_2} & \frac{\partial\phi_1}{\partial\delta_2} \\ \frac{\partial\lambda_1}{\partial\phi_2} & \frac{\partial\lambda_1}{\partial\lambda_2} & \frac{\partial\lambda_1}{\partial\delta_2} \\ \frac{\partial\delta_1}{\partial\phi_2} & \frac{\partial\delta_1}{\partial\lambda_2} & \frac{\partial\delta_1}{\partial\delta_2} \end{vmatrix}. \tag{2.96}$$

Solving $\hat{\mathrm{d}_1} = \hat{\mathrm{n}_2}$ for ϕ_1, λ_1, and δ_1 in terms of ϕ_2, λ_2, and δ_2 (Eq. 2.65 and 2.66) gives following three equations:

$$\phi_1 = \phi_2 - \arcsin\left(\frac{\cos\lambda_2}{\sqrt{1-\sin^2\lambda_2\sin^2\delta_2}}\right) \tag{2.97}$$

$$\lambda_1 = \arcsin\left(\frac{\cos\delta_2}{\sqrt{1-\sin^2\lambda_2\sin^2\delta_2}}\right) \tag{2.98}$$

$$\delta_1 = \arcsin\sqrt{1-\sin^2\lambda_2\sin^2\delta_1} \tag{2.99}$$

From equations 2.97, 2.98 and 2.99, it can be readily seen that

$$\frac{\partial\phi_1}{\partial\phi_2} = 1,\ \frac{\partial\lambda_1}{\partial\phi_2} = 0,\ \text{and}\ \frac{\partial\delta_1}{\partial\phi_2} = 0, \tag{2.100}$$

and the determinant of the Jacobian matrix reduces to

$$\det(\mathrm{J}_\mathrm{I}) = \frac{\partial\lambda_1}{\partial\lambda_2}\frac{\partial\delta_1}{\partial\delta_2} - \frac{\partial\lambda_1}{\partial\delta_2}\frac{\partial\delta_1}{\partial\lambda_2}. \tag{2.101}$$

A common denominator of these derivatives is

$$\sqrt{1-\sin^2\lambda_2\sin^2\delta_2} = \sin\delta_1, \tag{2.102}$$

the right hand from Eq. 2.99 is used for brevity in the following equations. The derivatives are

$$\begin{aligned} \frac{\partial\lambda_1}{\partial\lambda_2} &= \frac{\cos\delta_2\sin\delta_2\sin\lambda_2}{\sin^2\delta_1} & \frac{\partial\lambda_1}{\partial\delta_2} &= -\frac{\cos\lambda_2}{\sin^2\delta_1} \\ \frac{\partial\delta_1}{\partial\lambda_2} &= \frac{\cos\lambda_2\sin\delta_2}{\sin\delta_1} & \frac{\partial\delta_1}{\partial\delta_2} &= \frac{\sin\lambda_2\cos\delta_2}{\sin\delta_1} \end{aligned} \tag{2.103}$$

and the determinant becomes

$$\det(\mathrm{J}_\mathrm{I}) = \frac{\sin\delta_2}{\sin^3\delta_1}\left(\sin^2\lambda_2\cos^2\delta_2 + \cos^2\lambda_2\right). \tag{2.104}$$

From the Pythagorean trigonometric identity follows

$$\det(\mathrm{J}_\mathrm{I}) = \frac{\sin\delta_2}{\sin^3\delta_1}\left(\sin^2\lambda_2\sin^2\delta_2 + 1\right), \tag{2.105}$$

and finally with Eq. 2.99, the determinant of the Jacobian is

$$\det(\mathrm{J}_\mathrm{I}) = -\frac{\sin\delta_2}{\sin\delta_1}. \tag{2.106}$$

The magnitude of the determinant is plugged into Eq. 2.95 and the change of variable from a distribution given in rupture plane angles to a distribution given in auxiliary plane angles is given by

$$P(\phi_2, \lambda_2, \delta_2) = P(\phi_1, \lambda_1, \delta_1)\frac{\sin\delta_2}{\sin\delta_1}. \tag{2.107}$$

2.6.5 Kernel Density Estimator (KDE)

The kernel density estimator (KDE) for the nodal plane data with variance σ^2_{KDE} for the strike (ϕ) and rake (λ) strike and rake, and bandwidth b_{KDE} for the dip is the product of a bivariate normal distribution with the wrapping property for strike and rake and beta distribution for

the dip. Therefore, this KDE is the non-parametric counterpart of the mixture model.

$$h(\phi,\lambda,\delta) = \frac{1}{2N\sigma_{\text{KDE}}\sqrt{2\pi}} \times \sum_{i=1}^{2N} \frac{\delta_i^{\alpha_i-1}\left(\frac{\pi}{2}-\delta_i\right)^{\beta_i-1}}{\left(\frac{\pi}{2}\right)^{\alpha_i+\beta_i-1}B(\alpha_i,\beta_i)} \sum_{u=-1}^{1}\sum_{v=-1}^{1} \exp\left\{-\frac{1}{2\sigma_{\text{KDE}}^2} \times \left[(\phi-\phi_i+2u\pi)^2+(\lambda-\lambda_i+2v\pi)^2\right]\right\} \quad (2.108)$$

The beta distribution KDE is based on Chen (1999). We modify the definition to apply the equation directly to the support interval $(0, \frac{\pi}{2})$. Furthermore, we exclude the support limits from the beta distribution as described in appendix 2.6.3. The parameters of the ith beta distribution, α_i and β_i, for the kernel with bandwidth b (subscript KDE dropped for brevity) in terms of dip δ_i are defined as:

$$\alpha_i = \begin{cases} \rho(\delta_i) & \text{if } \delta_i \in (0, 2b) \\ \frac{\delta_i}{b} & \text{if } \delta_i \in \left[2b, \frac{\pi}{2}\right) \end{cases} \quad (2.109)$$

$$\beta_i = \begin{cases} \frac{\frac{\pi}{2}-\delta_i}{b} & \text{if } \delta_i \in \left(0, \frac{\pi}{2}-2b\right] \\ \rho\left(\frac{\pi}{2}-\delta_i\right) & \text{if } \delta_i \in \left(\frac{\pi}{2}-2b, \frac{\pi}{2}\right) \end{cases} \quad (2.110)$$

where

$$\rho(x) = 2b^2 + \frac{5}{2} - \sqrt{4b^4+6b^2+\frac{5}{4}-x^2-\frac{x}{b}} \quad (2.111)$$

2.7 Supplementary: On updates of ACE

Since its first publication in 2016, the ACE algorithm was updated several times. In its current implementation, two major updates changed also some aspects of the underlying mathematics. While the impact on the results is small, it is necessary to state this changes here, as the ACE implementation used in ch. 5 and ch. 8 is based on the updated version of ACE. The changes affect the Style-of-Faulting-Index (SoFI) and the likelihood equation.

2.7.1 Changes on the Style-of-Faulting-Index (SoFI)

SoFI was initially introduced to classify events based on rake and dip (Eq. 2.22). The separation for the three faulting endmembers was set at a fixed value. The purpose of the separation was to avoid distributions where clusters with mostly reverse (normal) faulting events include also events of the opposite regime. The separation results in a truncated wrapped normal distribution with truncation along $\lambda = 0°$ and $\lambda = \pm 180°$.

However, from a stress perspective there is no physical reason why a cluster with mostly reverse faulting events (i.e. positive rakes) cannot include events with negative rakes as well, and vice versa. The rake—and thus SoFI—itself is insufficient for a meaninigful separation of mostly reverse faulting events and mostly normal faulting events. Furthermore, SoFI also forces a hard separation between reverse/normal and strike-slip faulting because distributions for strike-slip events are exempt from this SoFI-based separation as they always form clusters with positive and negative rake signs.

Based on the lack of physical meaning of SoFI, it is completely removed from the algorithm, thus no distribution truncation is applied. The paragraph about SoFI in section 2.2.2 can be skipped without any loss of information. Its only contribution on the algorithm was the truncated distribution, whose subscript was dropped for brevity at the end of the paragraph. Thus, any subsequent equations are not affected.

2.7.2 Changes in the likelihood

For the likelihood of Eq. 2.29 it is assumed that all data in the catalog are independent. Data here means all nodal planes, i.e. two nodal planes per earthquake. It is reasonable to assume that the focal mechanisms (FM) of two earthquakes are independent samples from the same distribution, i.e. they are i.i.d. (independently and identically distributed). The likelihood of i.i.d events is the product of all data probabilities. The i.i.d. argument does not hold for the two nodal planes of a single earthquake. These two data are on the contrary highly dependent on each other, given by their orthogonality. If one vector changes, the other vector changes almost surely as well.

In practice, however, the orthogonality of the two nodal planes effectively prevented nodal planes from one cluster to influence the other cluster, since the angular distance between corresponding clusters is usually several standard deviations. Thus, the likelihood of any nodal plane pair is vanishing small compared to the nodal plane probability within a single cluster. Based on this fact, the maximum likelihood estimates of the mixture distribution are very good proxies. On the downside, this means that broad clusters tend to have biased estimates related to the violation of independence of the data.

Although small in most real world cases, this bias is hard to assess and also for mathematical exactness it is reasonable to remove the violation of independence. Since the nodal planes are highly dependent on each other, it is sufficient to include only one of the two in the parameter estimations of the individual component distributions. Each component distribution has a mean vector as a function of strike, rake and dip. By using Eq. 2.6 the angles can be converted into the normal vectors of the clusters. When determining the probability densities for each component distribution and for each earthquake, only the nodal plane closer to the cluster mean is used. Closeness is defined by the dot product

$$c_{ijk} = \mathbf{x}_{ij} \cdot \bar{\mathbf{x}}_k \quad (2.112)$$

where $\mathbf{x}_{ij}$ is the jth nodal plane ($j = [1, 2]$) of the ith earthquake and $\bar{\mathbf{x}}_k$ is the mean vector of the kth component distribution, representing the kth cluster mean. By selecting only one nodal plane based on closeness c per earthquake, the data treatment of each focal mechanism is not anymore in violation of the independence assumption. Any subsequent computional step is not affected by this additional data selection step.

2.7.3 Comparisons

Differences between the computations with/without SoFI and with/without closeness selection are small. An example for parameter variability due to SoFI and closeness is given in Tab. 2.1) and shown in Fig. 2.20 for the Chile region—investigated in ch. 2, 4, 3, 5, 8. Focal mechanism classification can differ for events in clusters with mostly normal or reverse faulting type events if their are rakes close to $0°$ and $\pm 180°$. This difference is attributed to SoFI (or its lack of).

With closeness the component distributions are set to zero for the nodal planes further away, instead of having extremely small values (for the general case). These differences are of no importance for the earthquake classification and affect the likelihood estimation inconsequentially. Therefore, closeness selection has little impact on the results, highlighting its formal necessity over computational aspects.

Table 2.1: ACE parameters for different implementations of the algorithm:
line 1: with SoFI & without closeness
line 2: without SoFI & without closeness
line 3: without SoFI & with closeness
Note, that component V is the designated noise component which is only defined by weight w.

	component I	component II	component III	component IV	component V
μ [°]	174.83433 174.82398 174.82560	2.25023 2.58130 2.54507	179.27609 184.95978 184.13554	348.57179 348.79006 348.74845	–
ν [°]	87.37468 87.39680 87.39216	96.68298 96.94097 96.91150	−79.03901 −73.69400 −74.41855	−94.42576 −94.44088 −94.45539	–
σ [°]	10.66148 10.76866 10.74831	17.19676 16.35180 16.42311	40.94264 54.10582 52.41634	24.43683 24.98751 24.73133	–
τ [°]	7.79108 7.91208 7.88899	16.36581 15.61676 15.68399	41.11340 54.60027 53.53517	21.44381 21.92708 21.76086	–
ρ	0.35418 0.35538 0.35517	0.83193 0.81901 0.82011	0.85072 0.87054 0.87028	0.48684 0.48673 0.48779	–
α	20.55925 20.04359 20.14444	8.00100 7.99352 7.99392	3.00514 2.73908 2.76235	6.03354 5.88823 6.26795	–
β	7.05117 6.87822 6.91202	21.03628 21.01480 21.01435	5.69016 4.98911 5.05941	1.96280 1.93324 2.02309	–
w	0.20315 0.20479 0.20448	0.19507 0.19238 0.19266	0.16460 0.19951 0.19505	0.17574 0.17980 0.17745	0.26143 0.22351 0.23036

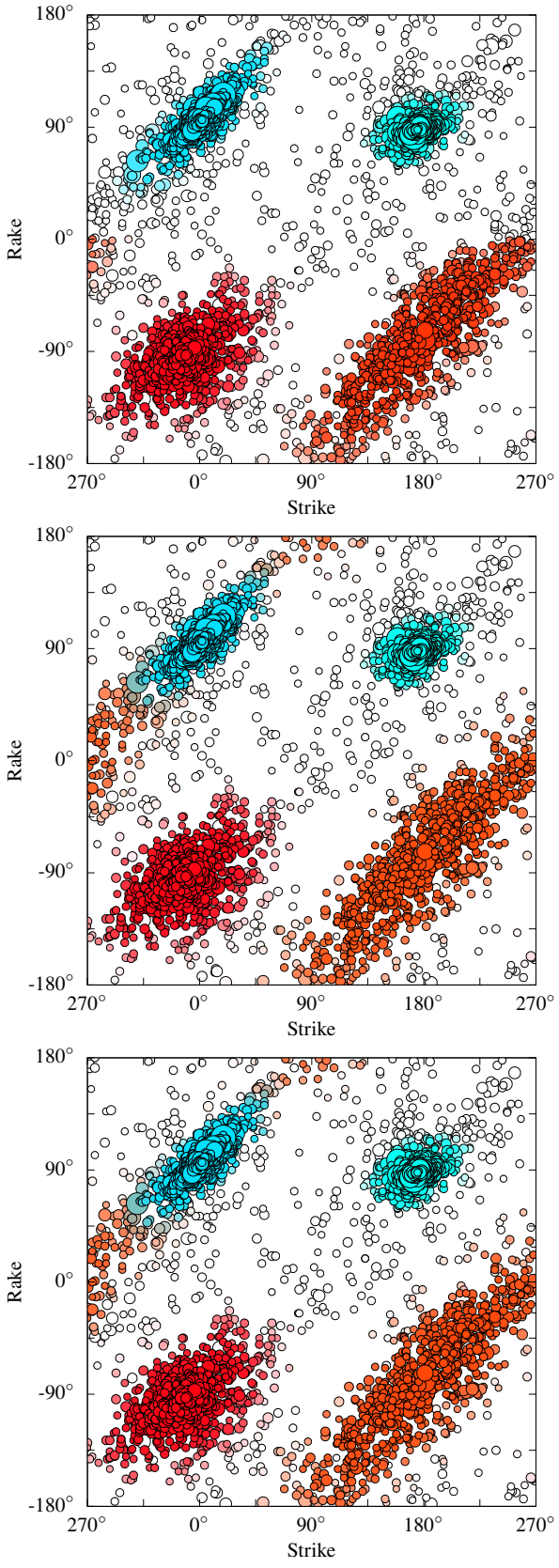

Figure 2.20: Cluster models for different implementations of the ACE algorithm for the parameters in Tab. 2.1. Top: with SoFI & without closeness (red parameters in Tab. 2.1), Middle: without SoFI & without closeness (blue parameters in Tab. 2.1), Bottom: without SoFI & with closeness (black parameters in Tab. 2.1). Notable differences exist only related to SoFI, the changes in the likelihood model with or without closeness are very small.

Chapter 3

Spatiotemporal Variations of Ground Motion in Northern Chile before and after the 2014 M_W 8.1 Iquique Megathrust Event

Abstract

To evaluate the spatiotemporal variations of ground motions in northern Chile, we built a high-quality rock seismic acceleration database and an interface earthquakes catalog. Two ground-motion prediction equation (GMPE) models for subduction zones have been tested and validated for the area. They were then used as backbone models to describe the time-space variations of earthquake frequency content (Fourier and response spectra). Consistent with previous studies of large subduction earthquakes, moderate interface earthquakes in northern Chile show an increase of the high-frequency energy released with depth. A regional variability of earthquake frequency content is also observed, which may be related to a lateral segmentation of the mechanical properties of the subduction interface. Finally, interface earthquakes show a temporal evolution of their frequency content in the earthquake sequence associated with the 2014 Iquique M_W 8.1 megathrust earthquake. Surprisingly, the change does not occur with the mainshock but is associated with an 8 month slow slip preceding the megathrust.[a]

[a] published as: Piña-Valdés, Jesús and Socquet, Anne and Cotton, Fabrice and Specht, Sebastian, 2018, Spatiotemporal Variations of Ground Motion in Northern Chile before and after the 2014 Mw 8.1 Iquique Megathrust Event, *Bulletin of the Seismological Society of America*, 108(2), 801–814

3.1 Introduction

A key issue of seismic hazard assessment and engineering seismology is the capability to perform predictions of ground motions (e.g., peak ground acceleration [PGA] and response spectra) that can be generated by an earthquake at a specific site. With this aim, ground-motion prediction equations (GMPEs) have been developed to describe seismic response spectra of an earthquake. These models are generally parameterized for magnitude, fault type, distance (e.g., to the rupture plane), and site conditions (e.g., soil type). The models are presented in terms of a median and a standard deviation (e.g. Strasser et al., 2009; Al Atik et al., 2010; Haendel et al., 2015). Several models have been derived for subduction zones (e.g Youngs et al., 1995, 1997; Zhao, 2006; Abrahamson et al., 2016). Because of the lack of data, most of these models have been developed using global databases that are mixing data from a couple of densely instrumented subduction zones (e.g., Japan, Alaska, Cascadia, Chile, and Mexico). The development of subduction ground-motion models then faces three main scientific challenges.

The first challenge is related to the regional variations of ground motions. Indeed, subduction zones are highly diverse in terms of mechanical behavior and geometry of the subduction interface (Kanamori, 1986; Astiz et al., 1988; Tichelaar & Ruff, 1993; Heuret et al., 2011). It is therefore necessary to evaluate regional variations of ground motions and test the robustness of global models for application to a given region. The second challenge is related to the impact of interface earthquake depths on ground shaking. Recent observations of seismological data from megathrust earthquakes have shown that the slip properties and spectral content of waves generated by major subduction events are highly depth dependent (e.g. Lay et al., 2012). These new observations challenge the ability of GMPEs to take into account the impact of depth on ground motions of interface earthquakes of moderate M_W, which are excluded from past subduction GMPE models. Such moderate earthquakes ($M_W < 5$) have a limited impact on seismic hazard assessment, which is mainly controlled by large earthquakes. They may however provide key information on the regional variations of the subduction interface properties and associated segmentation.

The third challenge relates to the impact of the processes at stake on the subduction interface during a seismic cycle on the generated ground motions. Recent major subduction earthquakes have also shown long (several years) preparation phases (Bouchon et al., 2013; Schurr et al., 2014) and postseismic phases (Ozawa et al., 2012; Mavrommatis et al., 2015; Yokota & Koketsu, 2015; Cesca et al., 2016; Kato et al., 2016). Variations of the frictional properties of the plate interface are likely associated with these preseismic and postseismic phases, and may cause ground-motion temporal variations. However, these ground-motion time dependencies have not yet been analyzed.

The northern Chile subduction (Fig. 3.1, left) provides a good case study to analyze regional, depth, and time dependencies of ground motions. The high convergence rate of 65–70 mm/yr between the Nazca and South American plates (Argus et al., 2011) generates observed seismicity associated with the interface plate convergence. This zone can be seen as a mature seismic gap between -23° and -18°S of latitude, as it has experienced only partial ruptures since the 1877 M_W 8.8 megathrust earthquake (Lomnitz, 2004). In 2007, the M_W 7.7 Tocopilla earthquake broke the deeper portion of subduction interface at the southern part of the gap (Delouis et al., 2009; Béjar-Pizarro et al., 2010; Motagh et al., 2010; Peyrat et al., 2010). In 2014, the M_W 8.1 Iquique earthquake partially ruptured an ≈150-km-long portion of the subduction interface centered at 20° S of latitude (Ruiz et al., 2014; Schurr et al., 2014; Gusman et al., 2015), with a coseismic moment release less than half of the moment deficit estimated in the area (Béjar-Pizarro et al., 2013; Métois et al., 2013, 2016; Hayes et al., 2014).

Because this region is identified as a high seismic hazard region, an important effort of seismological and geodetic monitoring has been performed since 2006 by several international agencies. In particular, 21 permanent multiparameter stations (including broadband seismometer, accelerometer, and Global Positioning System) have been installed in the frame of the Integrated Plate boundary Observatory Chile (IPOC) on relatively homogeneous rock geotechnical conditions. This network provided a substantial seismic catalog and associated high-quality rock-site conditions and strong-motion records, which are suitable to test GMPE models and also characterize the spatial and time variations of the earthquakes ground motion in this area. Thus, given this dataset, relevant GMPEs can be tested for their applicability to ground-motion estimates for the region.

3.2 Interface Earthquake Catalog

Having a reliable earthquake catalog is a critical point to analyze ground motions. Building a good catalog with a limited level of unknowns can potentially reduce the uncertainty of the ground motion predicted by the GMPEs. Indeed, earthquake catalogs provide most of the key parameters necessary to apply the GMPEs such as event location and magnitude. In addition, information about fault-plane orientation derived from earthquake focal mechanisms allow the style of faulting to be discriminated, key information to evaluate whether the event occurred on the subduction interface or within the subducted slab.

To compile a seismic catalog of interface seismicity appropriate for our purpose, we have searched events with $M_W \geq 4.0$ between January 2007 and June 2014, within the region between 18°–26° S and 69°–72° W of latitude–longitude range. We only considered events with a maximum depth of 90 km and with available focal mechanism solutions (FMS). Our catalog is a compilation of four different catalogs characterized by different accuracies and precisions of the hypocenter location, and different coverage in time and space (Fig. 3.1a,b). We selected data associated with each earthquake from the most accurate catalog. The four databases below are sorted from most to least accurate:

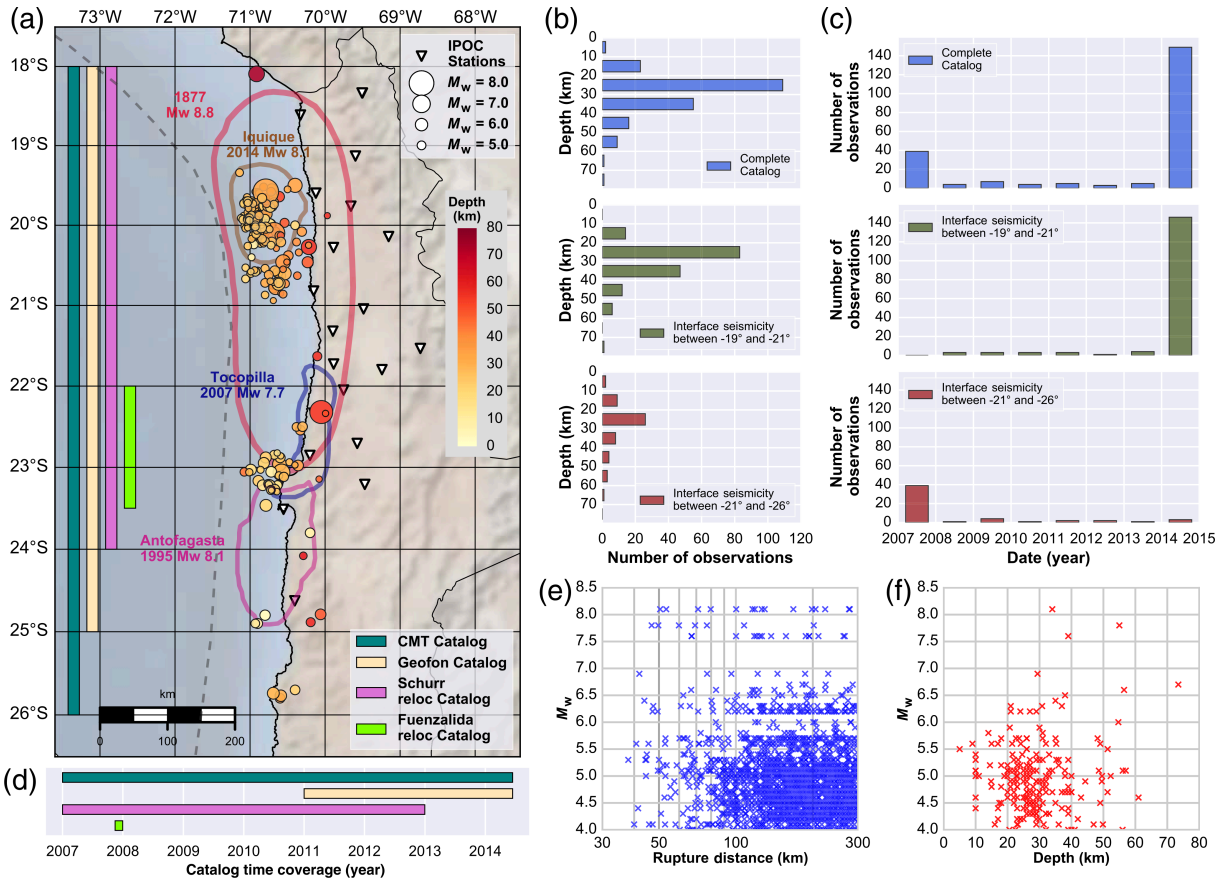

Figure 3.1: (a) Spatial distribution of the interface seismicity; the circles indicate the epicenter location, the fill indicates the depth, and the size indicates the magnitude. Contours of recent megathrust earthquakes ruptures are shown. Inverted triangles show the distribution of Integrated Plate boundary Observatory Chile (IPOC) multiparameter stations. Observed seismicity is concentrated in two clusters: the first one is centered at latitude -20° and the second one at -23°. The vertical bars on the left of the map indicate the latitudinal coverage of the catalogs included in the compilation used in this study. (b) Histograms of seismicity depth distribution and (c) histograms of seismicity temporal distribution, for whole catalog (upper), northern cluster (middle), and southern cluster (bottom). Most of the seismic activity occurs between 10 and 60 km depth. North cluster is mostly composed by the foreshock and aftershock sequences of the 2014 Iquique earthquake (M_W 8.1), and the southern cluster by the aftershock sequence of the 2007 Tocopilla earthquake (M_W 7.7). (d) Time coverage of the different catalogs. (e,f) Distribution of M_W as a function of rupture distance and depth, respectively.

1. High-resolution relocated catalog of the 2007 Tocopilla seismic event (Fuenzalida et al., 2013): magnitude, hypocentral location, and focal mechanism of 31 aftershocks, following the14 November 2007 M_W 7.7 Tocopilla earthquake. The catalog includes earthquakes located between 21° and 24° S, within 45 days after the mainshock.

2. Relocated catalog of north Chile (Schurr et al., 2012): magnitude and hypocentral location of 106 earthquakes from January 2007 to December 2012, within 18°–25° S and 69°–72° W, estimated from records of IPOC permanent stations.

3. GEOFON data center (GFZ) catalog (automatic estimates): magnitude, hypocentral location, and focal mechanism of 245 earthquakes from January 2011 to June 2014 within 18°–25° S and 69°–72° W, estimated from records of IPOC permanent stations.

4. Global Centroid Moment Tensor: magnitude, hypocentral location, and focal mechanism of 89 earthquakes from January 2007 to June 2014, within 18°–26° S and 69°–72° W.

The seismicity in the obtained catalog has been classified as either interface or intraplate earthquakes based on FMSs, using the Angular Classification with Expectation-Maximization cluster analysis (Specht et al., 2017), resulting in 216 identified interface earthquakes. We checked that this data-driven cluster analysis gave consistent classification results with the classical expert classification based on earthquake location and focal mechanisms used by Bastías & Montalva (2016). Additionally, 112 earthquakes that are not included in the catalog of Bastías & Montalva (2016) were identified, which correspond mainly to earthquakes of M_W between 4 and 5 that are not included in their work.

In the studied time period, the interface seismicity occurred in two main clusters (Fig. 3.1a). The cluster located south of the gap (≈23°S of latitude) is related to the

2007 M_W 7.7 Tocopilla earthquake. The cluster located between 19° and 21° S of latitude is related to the seismic event of the 2014 M_W 8.1 Iquique earthquake, and contains most of the seismicity included in our catalog. Both of them show depths between 10 and 60 km (Fig. 3.1b), and are highly concentrated in the years 2007 and 2014, respectively (Fig. 3.1c).

3.3 Acceleration Database and Data Processing

Multiple strong-motion databases are available in Chile (e.g. Arango et al., 2011; Bastías & Montalva, 2016). We have however chosen to use only the IPOC data to use homogeneous rock-site data to characterize the spatiotemporal variations of earthquakes frequency content, and also perform GMPE testing using an independent dataset.

Processing the acceleration dataset has been performed following the guidelines and recommendations of the COSMOS strong-motion record workshop (Boore & Bommer, 2005). We used horizontal acceleration records of interface events with a sampling frequency of 100 Hz. Records were cut 100 s before and 300 s after the reported event time. The raw data were deconvolved before applying a standard correction procedure. First, a baseline correction was performed by detrending and demeaning the acceleration time series to remove the instrument offset. Then, the records were manually picked to define the beginning and the end of the relevant seismic signal. Finally, the signal was tapered and zeros were padded at the beginning and the end of the waveform following Akkar et al. (2014).

The acceleration response spectra have been calculated over the north–south and east–west components, at 5% spectral damping ratio (Table S1, available in the electronic supplement to this article), using the method proposed by Nigam & Jennings (1969). The horizontal acceleration response spectru$M_W$as then obtained by calculating the geometric mean of the response spectra of both horizontal components for each oscillator of fundamental period T, as

$$\mathrm{SA}_{\mathrm{hor}}(T) = \sqrt{\mathrm{SA}_{\mathrm{NS}}(T)\mathrm{SA}_{\mathrm{EW}}(T)}, \qquad (3.1)$$

in which $\mathrm{SA}_{\mathrm{NS}}$ and $\mathrm{SA}_{\mathrm{EW}}$ correspond to the acceleration response spectra of the north–south and east–west acceleration components, and $\mathrm{SA}_{\mathrm{hor}}$ corresponds to the horizontal response spectra.

3.4 Evaluation of Ground-Motion Prediction Equations

We tested two GMPEs for subduction environments: the Abrahamson et al. (2016) model, which is a current GMPE model that has been calibrated with a worldwide database, and the Montalva et al. (2017) model that has been calibrated with a local ground-motion database of earthquakes of M_W higher than 5, exclusively occurring on the Chilean subduction

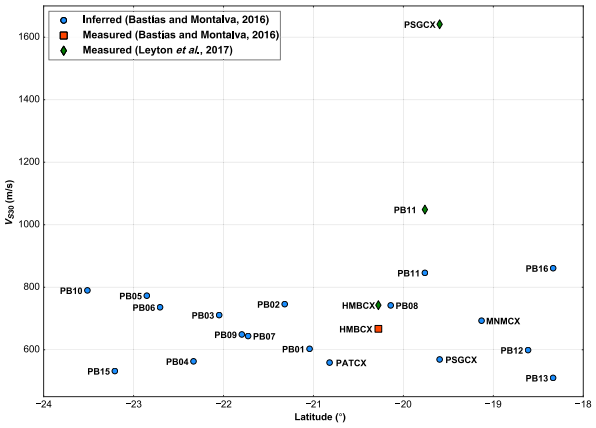

Figure 3.2: Average of the top 30 m shear-wave velocities (V_{S30}) of the CX-network stations with respect to the latitude. The square and circles indicate the measured and inferred V_{S30} values, respectively, taken from (Bastías & Montalva, 2016). Diamonds show the measured values taken from (Leyton et al., 2017). Note that the station PB13 has been replaced by the station PB16 (located near to the original site). This new station shows an inferred V_{S30} 69% higher than the PB13 site.

zone between -34° and -17° of latitude, including the records of the IPOC stations. Because we have no rupture plane models for the events, we estimate the rupture plane distance (R_{rup}), which is defined as the minimum distance between the rupture plane and a given site, by estimating the position and orientation of a rupture plane from the hypocentral depths and the dip and strike given by the focal mechanisms.

Because focal mechanisms have two nodal planes, we selected the nodal plane that is (near) parallel to the subduction interface as the rupture plane. As generally there is no information about the hypocenter position relative to the rupture plane, we assumed the hypocenters to be located at the center of the rupture planes and its geometry defined by the scaling relations of rupture source proposed by Strasser et al. (2010). Finally, a grid was defined on each rupture plane, to search the minimum distance between the nodes of the grid and the station site. When the minimum is localized, a refined grid is defined around the location of the minimum and the process is repeated again until no significant variations are observed (Haendel et al., 2015; Bastías & Montalva, 2016). The result of this procedure is summarized in Figure 3.1e that shows the magnitude–rupture distance distribution from 40 to 300 km for the whole range of magnitudes of the catalog.

Both selected GMPE models require the V_{S30} value to estimate indirectly the site effects on ground motions. There is no specific geotechnical information for the whole IPOC Network. Such lack of information has been supplied in previous works using proxy-based estimation on the predominant frequencies and the topographical slope (e.g. Bastías & Montalva, 2016). These inferred values are however lower than measured V_{S30} values obtained recently at the stations HMBX, PSGX, and PB11 by Leyton et al. (2017) (Fig. 3.2). Additionally, stations PB16 and PB13 (separated by a distance no larger than 500 m) show

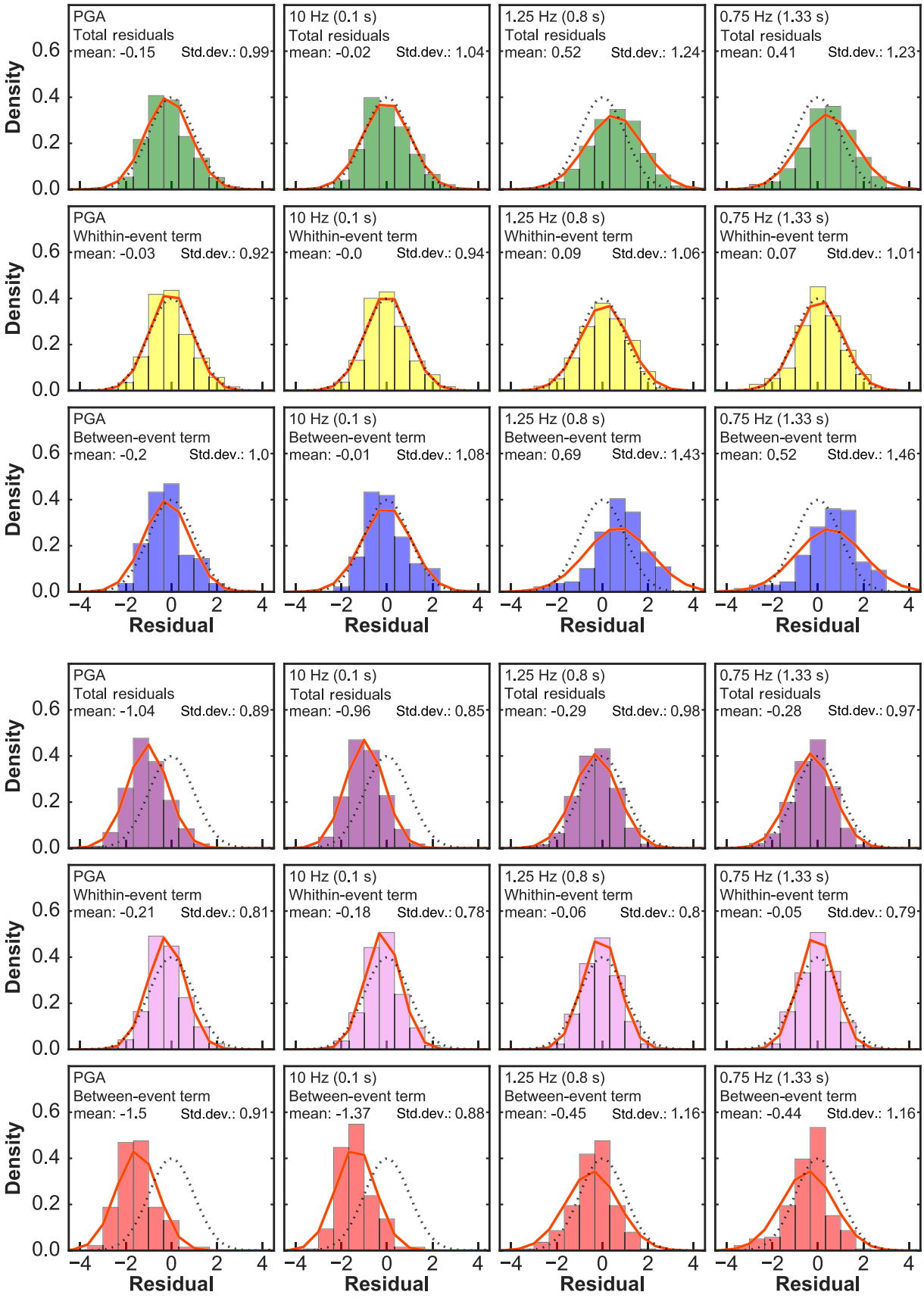

Figure 3.3: Residual histograms with respect to (top) Abrahamson et al. (2016) and (bottom) Montalva et al. (2017) ground-motion prediction equations (GMPEs). The dotted line represents the normal density function of the model and the solid line represents the normal density function of the dataset. Columns correspond to the residual distributions for different oscillator periods (peak ground acceleration [PGA], 10, 1.25, and 0.75 Hz), and rows to the total, within-event and between-event residuals.

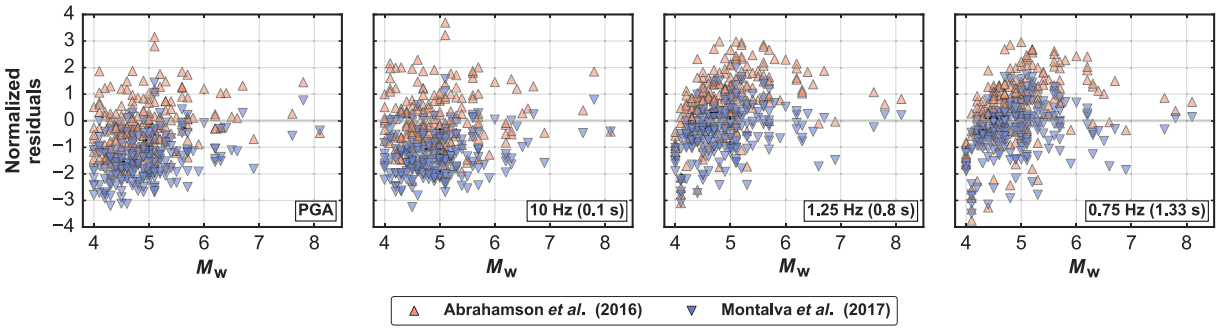

Figure 3.4: Distribution of computed between-event residuals at different frequencies (PGA, 10, 1.25, and 0.75 Hz) with respect to Montalva et al. (2017) (triangles) and Abrahamson et al. (2016) (inverted triangles) GMPEs. The residuals do not show any dependency with M_W.

significant differences of their inferred V_{S30} values. Such discrepancies between inferred and measured values confirm that a solid characterization of IPOC site conditions would lead to a significant improvement of the network.

Considering the discrepancy between inferred and measured values of V_{S30}, the homogeneity of geotechnical conditions of sites and the consistence between their geotechnical description and the measured values, a conservative value of V_{S30} of 850 m/s has been adopted for all stations of the network, similar to the value assumed by (Haendel et al., 2015). This assumption will be tested later in the article by the computation of site-specific stations terms and their comparisons with inferred V_{S30}.

Using this information and the data of the earthquake catalog, we calculated the predicted acceleration response spectra for each station–earthquake pair, for PGA and three different oscillator periods (0.1, 0.8, and 1.33 s). The respective values of the GMPEs were then compared with the observed horizontal accelerations response spectra for the given oscillator periods to compute the total normalized residuals as

$$Z_T^{ij}(T) = \frac{\log\left[\mathrm{SA}_{\mathrm{obs}}^{ij}(T)\right] - \log\left[\mathrm{SA}_{\mathrm{pred}}^{ij}(T)\right]}{\sigma(T)}, \quad (3.2)$$

in which $Z_T^{ij}(T)$ is the residual at site j for event i with oscillator period T, $\mathrm{SA}_{\mathrm{obs}}^{ij}(T)$ and $\mathrm{SA}_{\mathrm{pred}}^{ij}(T)$ correspond to the observed and predicted acceleration response spectra at site j for event i with oscillator period T, respectively, and $\sigma(T)$ is the total standard deviation of the model for oscillator period T. These residuals have been calculated only for the records with a rupture plane distance lower than 300 km, to stay in the distance validity range of the GMPEs. Additionally, to avoid bias, the records of the PB11 and PB15 stations have been removed, where possible site effects have been reported (D. Bindi, personal comm., 2015; F. Leyton, personal comm., 2016).

The total residual described above can be separated into between-event and within-event residuals. The first term represents the random effects between events that are not covered by the predictive model and reflects the variation of source factors such as the stress drop or the slip variability in space and time, that cannot be captured by the magnitude and the depth of the source. The within-event residual represents the variation of ground motion at a given distance to the source that comes from the azimuthal variation in the source, the path, and site effects derived from the complexity of the crustal structure, that are not captured by the distance to the source or the site classification (Abrahamson & Youngs, 1992; Strasser et al., 2009, 2010; Al Atik et al., 2010).

The normalized between-event residual of an earthquake

$$Z_B^i(T) = \frac{\tau(T)\sum_{j=1}^{n}\left[\log\left[\mathrm{SA}_{\mathrm{obs}}^{ij}(T)\right] - \log\left[\mathrm{SA}_{\mathrm{pred}}^{ij}(T)\right]\right]}{n\tau(T)^2 + \phi(T)^2}, \quad (3.3)$$

in which n is the number of records of the event i, $\tau(T))$ and $\phi(T)$ are the standard deviations of the between-event and the within-event residuals of the model for oscillator period T. To reduce the bias, we consider only those between-event residuals of the events that have more than four records with distances to the rupture lower than 300 km.

Consequently, the normalized within-event residuals, for the record j of earthquake i, are defined as

$$Z_W^{ij}(T) = \frac{\log\left[\mathrm{SA}_{\mathrm{obs}}^{ij}(T)\right] - \log\left[\mathrm{SA}_{\mathrm{pred}}^{ij}(T)\right] - Z_B^i(T)\tau(T)}{\phi(T)}. \quad (3.4)$$

To evaluate the fit of the models to the database, we have first plotted histograms of the distribution of the total, between-event, and within-event residuals with respect to the model ' s median for the PGA and the three oscillator periods considered (0.1, 0.8, and 1.33 s; Fig. 3.3). The difference between the standard deviation of the Abrahamson et al. (2016) GMPE model and the standard deviation of the residual database, as well as the difference between the median of the model and the median of the residual suggest that the model does not capture the whole variation of strong motions and underestimates their values for medium (0.8 s) and large (1.33 s) oscillator periods. On the other hand, the similar values between standard deviation in the Montalva et al. (2017) GMPE model and the standard deviation of the residual database show that this

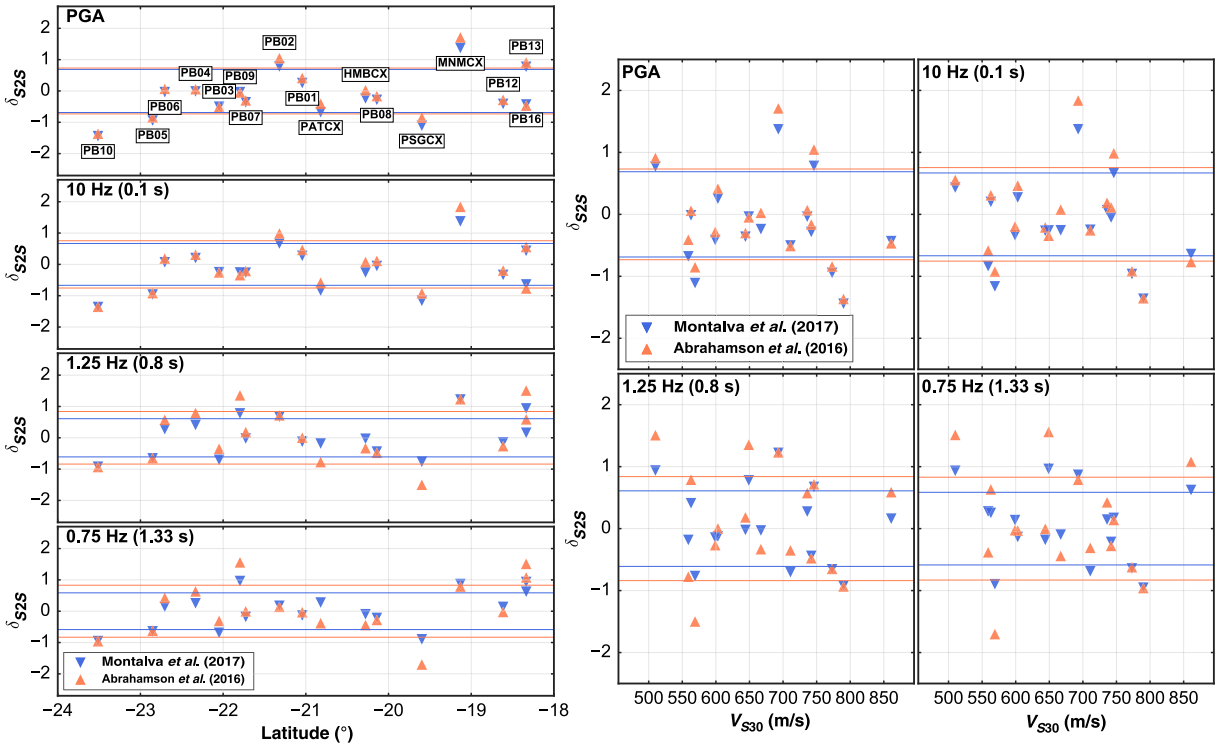

Figure 3.5: (Left) Stations site terms (δ_{S2S}) at different frequencies according to the Montalva et al. (2017) (inverted triangles) and Abrahamson et al. (2016) (triangles) GMPEs with respect to the latitude. (Right) Stations site terms (δ_{S2S}) with respect to the V_{S30} obtained by Bastías & Montalva (2016). The horizontal lines represent one standard deviation. No dependency is observed.

model describes well the variation for the all oscillator periods tested. However, the difference between the median of the model and the median of the residual indicates that the model overestimates the ground motion for low oscillator periods (PGA and 0.1 s).

The fit of the within-event residuals suggests that both models reasonably describe the variability of path and site effects.

The distribution of the between-event residuals suggests that the GMPE of Montalva et al. (2017) describes better the variation of source effects for PGA and the three tested oscillator periods. At periods of 0.8 and 1.33 s, the between-event residuals of the Abrahamson et al. (2016) model are more scattered than expected from the model.

The between-event residuals distribution does not indicate any magnitude dependency (Fig. 3.4). Therefore, these two GMPEs can be used as backbone models for the entire magnitude range from $M_W > 4$.

To evaluate the impact of the assumption of a unique value of V_{S30} for the whole network, the site terms (δ_{S2S}) have been computed at each station j for oscillator period T as the mean of the n within-event residuals recorded by the station:

$$\delta^j_{S2S}(T) \frac{1}{n} \sum_{i=1}^{n} \left[Z^{ij}_W(T) \right] . \tag{3.5}$$

The resulting site terms have been compared with inferred V_{S30} values given by Bastías & Montalva (2016). This comparison shows two interesting results: (1) site amplification at IPOC stations do not depend on the latitude (Fig. 3.5,left), and (2) the correlation between inferred V_{S30} and computed site terms is rather poor (Fig. 3.5, right). This lack of correlation is consistent with several studies (Chiou & Youngs, 2008; Derras et al., 2016), which have shown that GMPEs using inferred V_{S30} values show large within-event variabilities. These results give further encouragement to promote V_{S30} measurements of IPOC accelerometric stations and also indicate that the north–south variations of between- event residuals are not explained by a systematic regional variation of IPOC site conditions.

As a conclusion, the distribution of residuals suggests that the Montalva et al. (2017) model is the best suited for northern Chile and that it can therefore be used as a backbone model to study the spatiotemporal variations of ground motions in this area.

3.5 Depth and Regional Dependency of Ground Motions

The evolution of the between-event residual with respect to the depth shows a consistent and significant increase with depth of earthquake radiations at high frequency. This is clearly visible for both regional clusters at low oscillator periods (PGA and 0.1 s), whereas no tendency is observable at medium (0.8 s) or high (1.33 s) oscillator periods (Fig. 3.6). The distribution of between-event residuals along latitude and depth (Fig. 3.6, bottom row) shows that for PGA and an oscillator period of 0.1 s, the between-event residuals are clearly

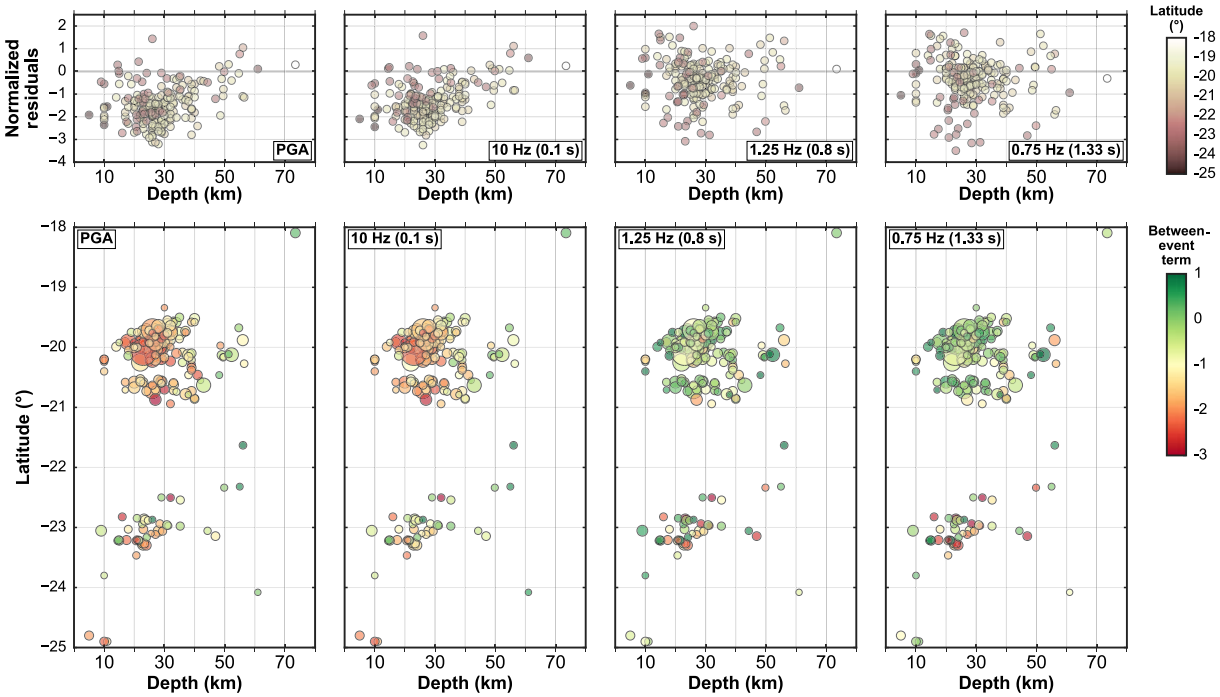

Figure 3.6: (Top row) Between-event residuals at different oscillator frequencies (PGA, 10, 1.25, and 0.75 Hz) with respect to the Montalva et al. (2017) GMPE as a function of the epicentral depth; the fill shows the latitude. An increase of between-event residuals with depth is observable for the PGA and low oscillator periods (0.1 s). (Bottom row) Between-event residuals as a function of epicenters latitude and depths.

differentiated at 40 km depth, where the residual dispersion decreases dramatically and concentrates on higher values. The figure also shows a regional dependency for the medium and high oscillator periods with a lower residual variability and slightly higher residuals values in the northern cluster for earthquakes shallower than 30 km.

To validate the depth dependency of the observed ground motions through between-event residual term distributions, the frequency content of earthquakes have been compared using a Fourier spectral ratio method. This approach has been used recently to compare the frequency content of two subduction earthquakes located at different depths (Lay et al., 2012). Following a similar methodology, we computed the spectral ratios between pairs of earthquakes, using the horizontal Fourier spectra of the acceleration records of the stations that recorded both events.

To apply the method, we used the processed horizontal waveforms to get the Fourier spectra. The Konno & Ohmachi (1998) smoothing function has been applied over each Fourier spectra and for each station record, both horizontal smoothed Fourier Spectra were then averaged to obtain the horizontal Fourier spectra at each station defined for each frequency f as

$$F_{\text{hor}}(f) = \sqrt{F_{\text{NS}}(f)^2 + F_{\text{EW}}(f)^2}, \tag{3.6}$$

in which F_{NS} and F_{EW} correspond to the smoothed Fourier spectra of the north–south and east–west acceleration components, respectively, and F_{hor} to the horizontal Fourier spectra. Then, all spectral ratios obtained at each station for a single pair of earthquakes were averaged with the geometric mean for each frequency; thus, the spectral ratio for each frequency f is defined as

$$\text{SR}_{AB}(f) = \sqrt[n]{\prod_{j=1}^{n} \frac{F_B^j(f)}{F_A^j(f)}}, \tag{3.7}$$

in which F_A^j and F_B^j are the horizontal Fourier spectra of events A and B, at the station j, and n is the number of stations that recorded both events.

Pairs of shallow and deep earthquakes with similar magnitudes ($\Delta M_W \leq 0.1$) and relative distance less than 100 km have been selected to compare their frequency contents. The selected pairs of earthquakes consist of one earthquake shallower than 25 km and one earthquake deeper than 40 km. We limited our analysis to earthquakes for which the theoretical hypocenter is located within a distance of 15 km from the subduction interface, as defined by Tassara & Echaurren (2012). We found four earthquakes pairs that meet these criteria. The spectral ratios were calculated as the division of the spectra of the deeper event divided by the spectra of the shallower event (Fig. 3.7). For all pairs, the spectra amplitude of the deep events is larger than the shallower event for frequencies larger than 1 Hz. This result is in agreement with the depth dependency observed in the GMPE residuals. The results of both methods presented here are consistent with each other and suggest that interface events below 40 km depth release more energy at high frequencies than shallow interface events for the whole region. In addition, shallow seismicity in the northern part of the seismic gap releases more energy at low frequencies than the seismicity in the southern part of the gap.

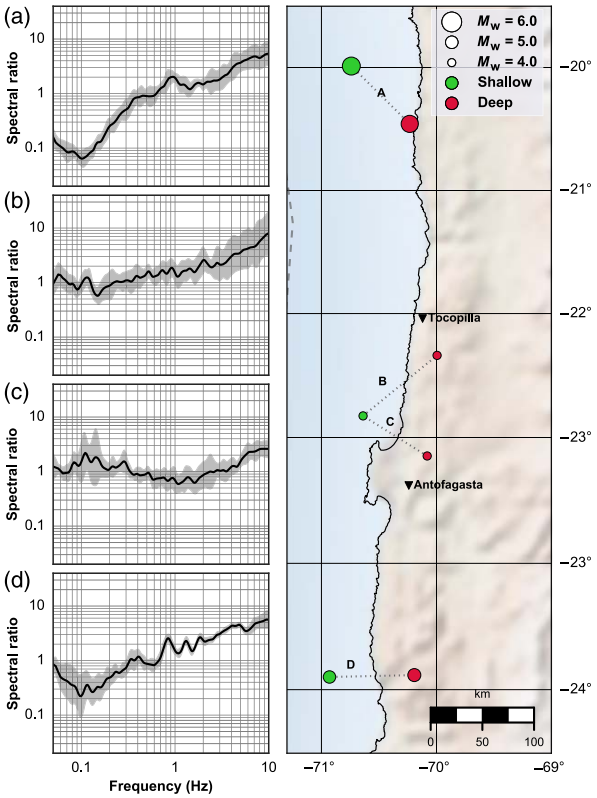

Figure 3.7: (Left) Spectral ratios computed for pairs of shallow and deep earthquakes. The gray bands show the standard deviation with respect to the geometric mean in the whole frequency band. (Right) Localization of shallow–deep couples. Deep earthquakes generate higher ground-motion amplitudes at frequencies larger than 1 Hz.

3.6 Time Dependency of Ground Motions

To evaluate the time variability of the between-event residuals, we focused our analysis on the northern seismicity cluster that is associated with the seismicity of the 2014 M_W 8.1 Iquique earthquake (Ruiz et al., 2014; Schurr et al., 2014; Cesca et al., 2016; Kato et al., 2016). We grouped the seismicity into three periods of the seismic cycle bracketing the Iquique earthquake (Schurr et al., 2014; Socquet et al., 2017):

1. interseismic: before August 2013
2. preseismic: August 2013–31 March 2014
3. postseismic: after 31 March 2014.

Between-event residual terms are compared in Figure 3.8 for the three time-period windows at PGA and the three oscillator frequencies selected (10, 1.25, and 0.75 Hz). For PGA and 10 Hz, the between-event residual term decreases from the interseismic to the postseimic period. At frequencies of 1.25 and 0.75 Hz, the between event does not show any important variation from interseismic to preseismic period, and a slight decrease is observed for the postseismic period.

To complement the analysis of the between-event residual variation, the spectral ratio method was again applied (equation 3.7). Selected pairs of earthquakes of similar magnitude ($\Delta M_W \leq 0.1$), with differences in depths smaller than 20 km and relative distance smaller than 25 km were selected; 425 pairs of earthquakes meet these criteria. The spectral ratios were computed as the division of the most recent event spectrum by the spectrum of the older one. Then, geometrical means of the spectral ratios are divided into three groups:

1. pairs of earthquakes within the interseismic period;
2. pairs of earthquakes belonging to preseismic and interseismic periods; and
3. pairs of earthquakes belonging to postseismic and interseismic periods.

The geometrical means of the spectral ratios over time (Fig. 3.9) show that at frequencies lower than 1 Hz, the earthquakes of the interseismic period show lower amplitudes than the earthquakes of the preseismic period. Instead, at frequencies higher than 1 Hz, the earthquakes that occur during the intersesimic period show higher amplitudes than the earthquakes that occur during the preseismic period. A similar pattern is also observable when comparing the earthquakes of the interseismic and postseismic periods, although with a lower intensity. The findings are consistent with the variations observed by the GMPEs residual analysis method (Fig. 3.8).

3.7 Discussion

The record of the 2007 Tocopilla and 2014 Iquique seismic sequences by the IPOC network provided a unique dataset in terms quality and quantity (more than 1000 records) to (1) test the performance of the most recent subduction GMPEs and to (2) observe the spatiotemporal variations of the ground motions in a region recognized as a mature seismic gap.

The comparison between the GMPE and the observations suggests that the two tested models are able to describe the ground motion 's within-event residuals, which are mainly controlled by site and propagation effects. The main discrepancies between the tested models and the observations are related to the between-event component of the ground-motion variability, which is mainly controlled by source effects.

A possible explanation for this misfit could be due to the limitations of the dataset used to calibrate the ground-motion models. Indeed, the Abrahamson et al. (2016) model is based on a global event catalog with a moment magnitude larger than 6, whereas the database used in this study includes earthquakes of smaller magnitude ($4 < M_W < 6$).

The Montalva et al. (2017) model has been developed from a seismic catalog with moment magnitudes larger than 5.0 along the entire Chilean trench. This model describes well the ground-motion variability of our dataset.

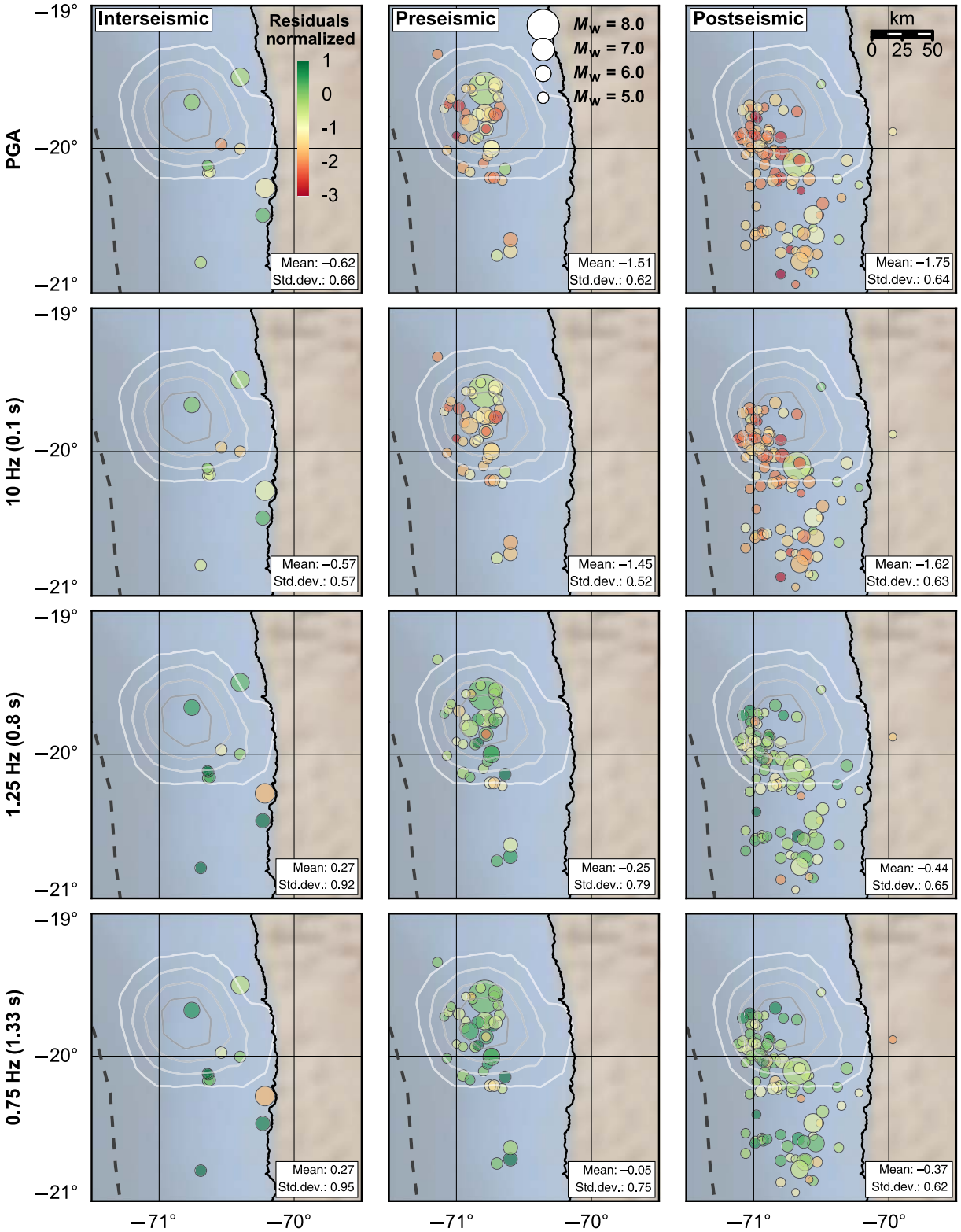

Figure 3.8: Time and space variability of residuals, at different frequencies (PGA, 10, 1.25, and 0.75 Hz), with respect to the Montalva et al. (2017) GMPE for earthquakes between -19° and -21°. Columns correspond to a given period of the seismic cycle period (interseismic before August 2013, preseismic between August 2013 and 31 March 2014, and postseismic after 1 April 2014). The mean and the standard deviation of the between-event residuals showed on each box are indicated in the right bottom corner. Contours lines correspond to the slip distribution of the 1 April 2014 M_W 8.1 Iquique earthquake. PGA and low oscillator period (high frequency, 10 Hz) residuals decrease from interseismic to preseismic time windows.

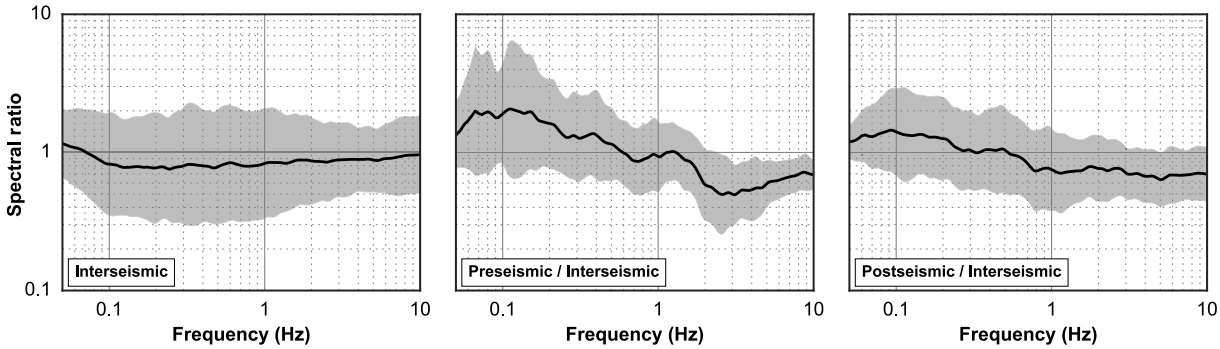

Figure 3.9: Spectral ratios of similar events ($\Delta M_W \leq 0.1$, interdistance ≤ 25 km), between -19° and -21° of latitude, for the interseismic, preseismic, and postseismic periods associated with the 1 April 2014 Iquique earthquake. The gray bands show the standard deviation (geometric mean) at each frequency.

The quality of the fit could then be explained by the inclusion of moderate earthquakes ($5 < M_W < 6$) to calibrate the model.

Our data analysis confirms that the energy radiation pattern of interface earthquakes varies with depth, in agreement with the proposal that the subduction interface is segmented down-dip with different frictional properties characterizing each segment (Lay et al., 2012; Lay, 2015). Such along-dip segmentation is not included so far in the GMPE models. Indeed, engineering ground-motion models predict ground motions for large earthquakes, which break the entire seismogenic zone from small to large (60 km) depths.

Our findings suggest that below 40 km depth, a significant change in the signature of the earthquake spectra exists. This change is coincident with the depth of the contact between the continental Moho and the subduction interface in this area (Patzwahl et al., 1999; Béjar-Pizarro et al., 2010). These two observations are also consistent with the segmentation along depth of the subduction interface and would correspond to the limit between the domains B and C proposed by Lay et al. (2012).

The Chilean subduction varies from north to south in terms of mechanical behavior and geometry of the interface (Clift & Vannuchi, 2004; Hoffmann-Rothe et al., 2006; Contreras-Reyes et al., 2010). There is also an influence on the coupling degree that is shown to vary along the trench (Béjar-Pizarro et al., 2010; Métois et al., 2012) and is coherent with the regional segmentation observed for the between-event residuals at medium and long oscillator periods for seismicity shallower than 40 km depth (Fig. 3.6, bottom row).

Several past crustal earthquakes studies (i.e. Abrahamson & Silva, 2008) have suggested that aftershocks generate weaker ground motions than the associated mainshock. Our results have shown that the ground motions have started to change several months before the occurrence of 2014 Iquique earthquake, with a progressive decrease of the released energy at high frequencies. This observation may indicate a change on the subduction interface that may be related to a long-term nucleation process of the megathrust earthquake (Socquet et al., 2017). The ground-motion temporal variation is consistent in time with aseismic slip around the rupture area of the 2014 Iquique earthquake and a slow migration of the foreshock activity (Kato & Nakagawa, 2014; Schurr et al., 2014; Kato et al., 2016; Socquet et al., 2017), similarly to what has been observed before the 2011 M_W 9.1 Tohoku-Oki earthquake (Mavrommatis et al., 2015; Yokota & Koketsu, 2015). This observation sheds light on the potential processes that occur on the subduction interface through the seismic cycle.

Stress-drop inversions have been used for years by the seismological community to analyze the physics of earthquakes. The stress drop, being proportional to the cube of the corner frequency, is sensitive to the uncertainty in the corner frequency (e.g. Cotton et al., 2013). Our study suggests that the analysis of GMPE between-event residuals could also be used not only for engineering purposes but also to analyze the source characteristics of earthquakes. Indeed, these residuals take into account both the magnitude effect and the propagation effect (through the functional form of the GMPE), and it has been shown that response between-event residuals are highly correlated with classical Fourier spectrum based stress drop (e.g. Bindi et al., 2007). Between-event residuals analysis may therefore constitute a new possibility to compare source effects of earthquakes with various magnitude and locations.

Finally, the consistency of the results with other studies opens the possibility to use parameters such as the between-event residuals, stress drop, earthquake spectra, and strong motion, as a proxy for the variability of the frictional properties of the subduction interface.

3.8 Conclusion

Testing the GMPEs models is a necessary contribution to seismic hazard assessment in areas that have been recently instrumented. For the specific case of northern Chile, the results presented in this study have shown that the combination of the Abrahamson et al. (2016) and Montalva et al. (2017) models show different strengths and weaknesses. These two models successfully predict the median values and capture the variability of the ground motions generated by the interface seismicity in different frequency bands, even for a dataset extended out of the validity range of M_W in both models. The results have shown that for a dataset including

earthquakes of M_W as low as 4.0, the Abrahamson et al. (2016) model fits observations better for low oscillator periods (0.8 and 1.33 s), whereas the Montalva et al. (2017) model is more suitable for medium and high oscillator periods (PGA and 0.1 s). Considering all frequencies and the magnitude range, which is important from a seismic hazard point of view ($M_W > 5$), the Montalva et al. (2017) model is the best suited for northern Chile.

The southern part of the north Chile seismic gap shows weaker ground motions at low frequencies than the northern part of the gap. This suggests a lateral segmentation of the subduction interface such an along-strike segmentation has also been shown by studies of interseismic coupling (Béjar-Pizarro et al., 2013; Métois et al., 2013; Li et al., 2015). This suggests a potential link between the state of coupling during the interseismic phase, the energy radiation characteristics of interface earthquakes, and the friction on the subduction interface that requires further investigations. In addition, using two different methods (GMPE residuals and the spectral ratios), we showed that the observed ground motions increase with hypocentral depth for interface subduction earthquakes. This suggests that the event depth must be considered in the development of future GMPE to include in the models interface subduction earthquakes of moderate magnitudes, which are not rupturing the entire seismogenic interface. This could extend the use of the GMPE as backbone ground motion to study the properties of the subduction interface. Also, this depth dependency confirms previous observations of along-dip segmentation of the subduction megathrust seen in the values of interseismic coupling (Béjar-Pizarro et al., 2010; Lay et al., 2012) and in the geometry because an abrupt change in the subduction angle has been documented in the area (Contreras-Reyes et al., 2012).

Ground motions have also been shown to vary through time by both methods presented in this work (GMPEs and spectral ratios). The time dependency can be related to the earthquake cycle and has been observed by studying in great details the seismic events associated with the 2014 Iquique megathrust earthquake. Although a significant change in the earthquake frequency content before and after the mainshock can be expected, this is not what we observe. Instead, the data show that the change occurs several months before the mainshock and is characterized by a progressive decrease of interface earthquake energy release at high frequencies. This change has been shown to concur with an eight-month slow-slip event on the subduction interface, and has been interpreted as the long-term nucleation process of the 2014 megathrust earthquake (Socquet et al., 2017).

Finally, the dependencies detected on the between-event term open the possibility to incorporate new factors to improve ground-motion models in the future. An important factor to improve the predictability of the GMPE models is to better take into account depth and regional variations.

Data and Resources

All strong-motion data used in this work have been recorded by the CX-network of the Integrated Plate boundary Observatory Chile (`http://www.ipoc-network.org`). These data are available to registered users at the GEOFON repository (`http://geofon.gfz-potsdam.de/waveform/archive/network.php?ncode=CX`). The Global Centroid Moment Tensor (CMT) and the moment tensor solutions are freely available (`http://www.globalcmt.org/CMTsearch.html`) as well the GEOFON bulletin information (`http://geofon.gfz-potsdam.de/eqinfo/eqinfo.php`). All of the above websites were last accessed on June 2016.

Acknowledgments

This work has been possible thanks to the contribution of the Integrated Plate boundary Observatory Chile (IPOC) consortium that has facilitated the access to the CX-network ground-motion data, of Bernd Schurr that has facilitated the focal mechanism catalog of GEOFON data center, of Dino Bindi and the two anonymous reviewers that contributed with their helpful comments on the article, and to the BecasChile scholarship program by the Chilean National Commission of Science and Technology (CONICYT).

Chapter 4

An 8 month slow slip event triggers progressive nucleation of the 2014 Chile megathrust

Abstract

The mechanisms leading to large earthquakes are poorly understood and documented. Here we characterize the long-term precursory phase of the 1 April 2014 M_W 8.1 North Chile megathrust. We show that a group of coastal GPS stations accelerated westward 8 months before the main shock, corresponding to a M_W 6.5 slow slip event on the subduction interface, 80 % of which was aseismic. Concurrent interface foreshocks underwent a diminution of their radiation at high frequency, as shown by the temporal evolution of Fourier spectra and residuals with respect to ground motions predicted by recent subduction models. Such ground motions change suggests that in response to the slow sliding of the subduction interface, seismic ruptures are progressively becoming smoother and/or slower. The gradual propagation of seismic ruptures beyond seismic asperities into surrounding metastable areas could explain these observations and might be the precursory mechanism eventually leading to the main shock.[a]

[a] published as: Socquet, A., J. P. Valdes, J. Jara, F. Cotton, A. Walpersdorf, N. Cotte, S. Specht, F. Ortega-Culaciati, D. Carrizo, and E. Norabuena (2017), An 8 month slow slip event triggers progressive nucleation of the 2014 Chile megathrust, *Geophysical Research Letters*, 44, 4046–4053

4.1 Introduction

Some earthquakes have been preceded by an intense foreshock activity (Bouchon et al., 2013; Schurr et al., 2014; Ruiz et al., 2014; Lay et al., 2014; Bedford et al., 2015; Cesca et al., 2016; Kato et al., 2016; Meng et al., 2015; Hasegawa & Yoshida, 2015; Kato et al., 2012; Ozawa et al., 2012; Sato et al., 2013; Bouchon et al., 2011) raising the possibility that earthquake forecasting may be achieved through a better understanding of precursory mechanisms. Two concurrent models have been proposed to explain the initiation of seismic rupture (Dodge et al., 1996). A first model assumes that the accelerated moment release observed before large earthquakes (Bowman & King, 2001) is triggered by a slow slip event on the fault interface (Bouchon et al., 2013; Ruiz et al., 2014; Dodge et al., 1996). Alternatively a slow cascade of failures eventually may trigger the main shock (Dodge et al., 1996).

The precursory phase of earthquakes is most usually studied using seismological data, which is readily available in some regions. Because of limited in situ monitoring combined with lower detection thresholds, geodetic data are less commonly used to study earthquake precursors. Therefore, the link between foreshock activity and associated deformation transients has never been directly established for periods exceeding a few weeks, although it has been observed and suggested (Obara & Kato, 2016, and references therein).

The M_W 8.1 2014 Iquique earthquake occurred within the North Chile seismic gap, which had not experienced a megathrust rupture since 1877 (Béjar-Pizarro et al., 2013; Métois et al., 2016). The earthquake ruptured an $\approx$ 150 km long portion of the subduction zone (Schurr et al., 2014; Ruiz et al., 2014), in an area that was partially locked before the earthquake (Béjar-Pizarro et al., 2013; Métois et al., 2016). The earthquake was preceded by a series of earthquake swarms beginning in July 2013 (Schurr et al., 2014; Ruiz et al., 2014).

Given the presence of detailed seismic and geodetic monitoring of the Chilean subduction zone, this earthquake is an excellent case to monitor the precursory seismic activity and associated deformation. Previous studies focused mostly on the 20 days immediately preceding the earthquake when a strong transient signal occurred (Schurr et al., 2014; Ruiz et al., 2014; Lay et al., 2014; Bedford et al., 2015; Cesca et al., 2016). Nevertheless, a debate remains on the mechanisms leading to this foreshock activity, notably on the existence or not of aseismic slip preceding the earthquake. Apart from the study of the foreshock sequence (Schurr et al., 2014; Ruiz et al., 2014; Lay et al., 2014; Bedford et al., 2015; Cesca et al., 2016; Kato et al., 2016; Meng et al., 2015), very little is known about any potential long-term precursors, in particular in terms of deformation.

Here we use geodetic and seismological observations to document the precursory deformation and foreshock frequency content for the 2 years preceding the Iquique earthquake.

4.2 Data and Methods

GPS data from several networks monitoring the North Chile subduction (IPOC, LIA Montessus de Ballore, ISTerre, Caltech Andean Observatory, IGS) have been processed in double differences, including tropospheric delays and gradients (Boehm et al., 2006), and mapped into the ITRF 2008 (Altamimi et al., 2011) (see supporting information for further details). The trend, as well as seasonal signals and common modes were removed from the time series. In order to study the long-term transient in our time series, we excluded data after 15 March 2014 (when a strong preseismic signal occurred) and then computed the average velocity variations, by fitting a linear regression in a 6 month sliding window of the detrended and denoised time series (Figure 4.1). In a second step, we compute the displacement during two preseismic periods (preseismic 1: July 2013 to 13 March 2014 and preseismic 2: 14 March 2014 to 31 March 2014), by taking as a reference the mean interseismic loading trend before July 2013 (Figures 4.S2 and 4.S3).

The surface deformation fields were then inverted to retrieve the distribution of slip on the subduction interface (Figure 4.2), by discretizing it as a series of dislocations buried in a layered elastic half space (Wang, 2003). A Laplacian smoothing has been applied; the best compromise between model roughness and data-model misfit has been chosen (Jónsson et al., 2002). The power of our data to constrain the slip on the interface (Loveless & Meade, 2011) is high from 15 km depth to more than 70 km depth in general (Figures 4.S4–4.S6). Although the details of slip distributions can vary from one inversion to the other, the estimated geodetic moment of preseismic slow slip events vary within less than 10% (Figure 4.S7).

To complement the geodetic analysis, we analyzed the frequency content of interface seismicity. The interface seismicity catalog (Figure 4.S9) was compiled using the GEOFON moment tensor catalog and the Global CMT catalog. We use a data driven algorithm to automatically determine focal mechanism clusters with similar style of faulting (strike, rake, and dip, Figure 4.S10).

The horizontal response and Fourier spectra of interface earthquakes were computed from the acceleration records of stations belonging to the IPOC network (Figure 4.S9). The raw acceleration records were demeaned and tapered, and a zero pad has been applied at the beginning and the end before being used to compute the spectra (Boore et al., 2012; Chiou & Youngs, 2008). The response spectra were also computed for each horizontal component of the records following the Nigam & Jennings (1969) method with a damping of 5%. Finally, both Fourier and response horizontal spectra were computed as the geometrical mean of the two horizontal response spectra at each station. Fourier source spectra depend on source, propagations, and site effects. Also, there is then a need to deconvolve the records from propagation and site properties to analyze earthquake source properties. In order to compare the shape of Fourier spectra during the different time span studied, we selected three IPOC stations located at equal distance from the earthquakes swarm to get rid

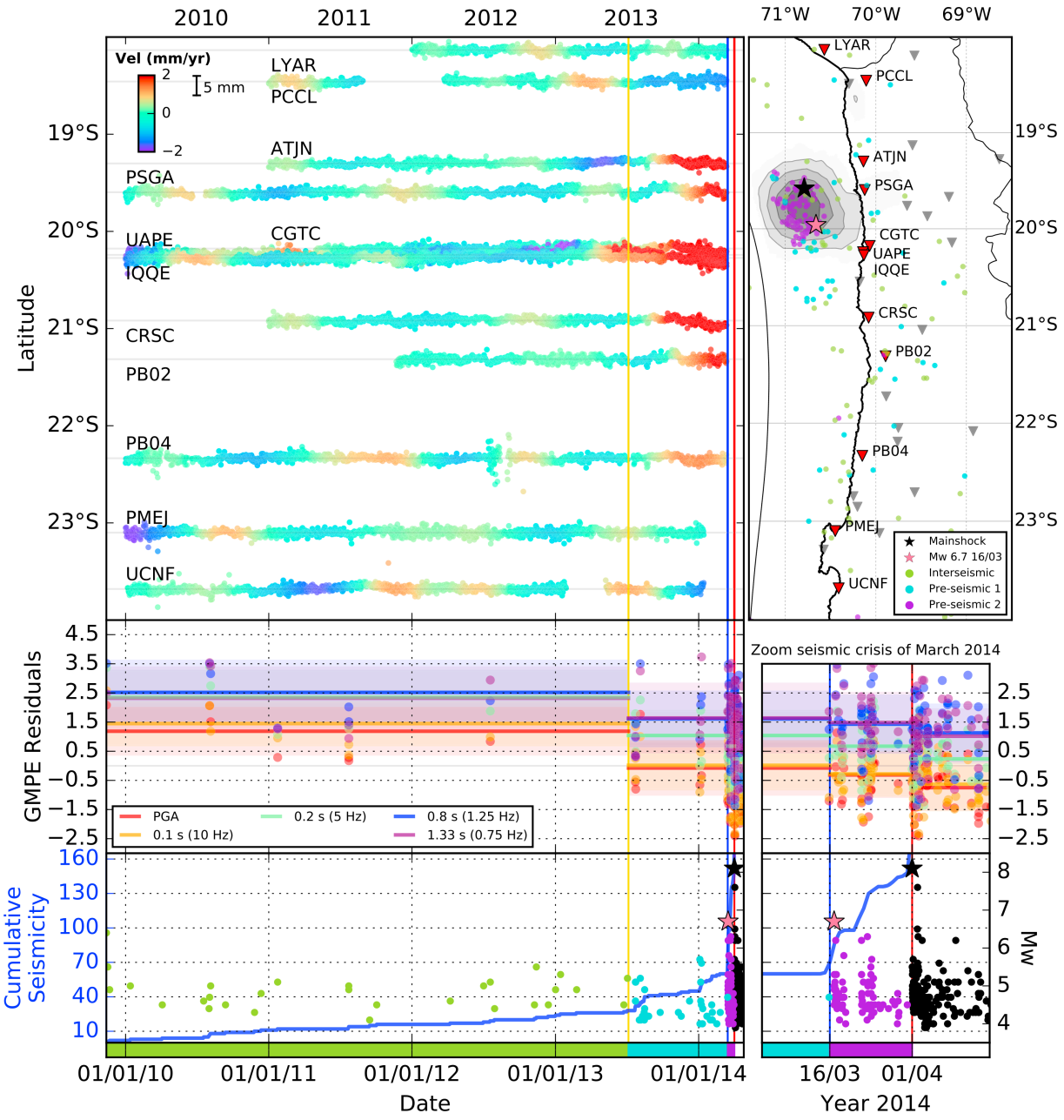

Figure 4.1: Preseismic ground deformation and foreshock frequency content over a 4 year period, before the 1 April 2014 megathrust in North Chile. (top right) Map of seismicity: foreshock activity color coded by periods, epicenters of M_W 8.1 main shock and M_W 6.7 foreshock are indicated by black and pink stars, M_W 8.1 slip distribution with 1 m contours. Triangles indicate the location of GPS stations, the red ones being stations whose time series are shown to the left. (top left) Trench perpendicular, detrended time series of coastal cGPS, sorted by latitude. Colors show the variation of average GPS velocities computed in 6 month sliding windows. (middle left) Frequency content evolution of interface foreshocks. Lines show average values of normalized residuals with respect to GMPE model (Abrahamson et al., 2016) at high (reddish) and low (bluish) frequencies computed for each time period. Standard deviation of the model is shown by shaded colors, while dots show single earthquakes residuals. (bottom left) Foreshock activity over time (dots). Blue curve shows the cumulative number of earthquakes. Red, blue, and yellow vertical lines separate the three preseismic periods and depict respectively the M_W 8.1 main shock on 1 April 2014, the M_W 6.7 foreshock of 16 March 2014 that is followed by an increase of seismicity rate 2 weeks before the main shock, and the July 2013 swarm.

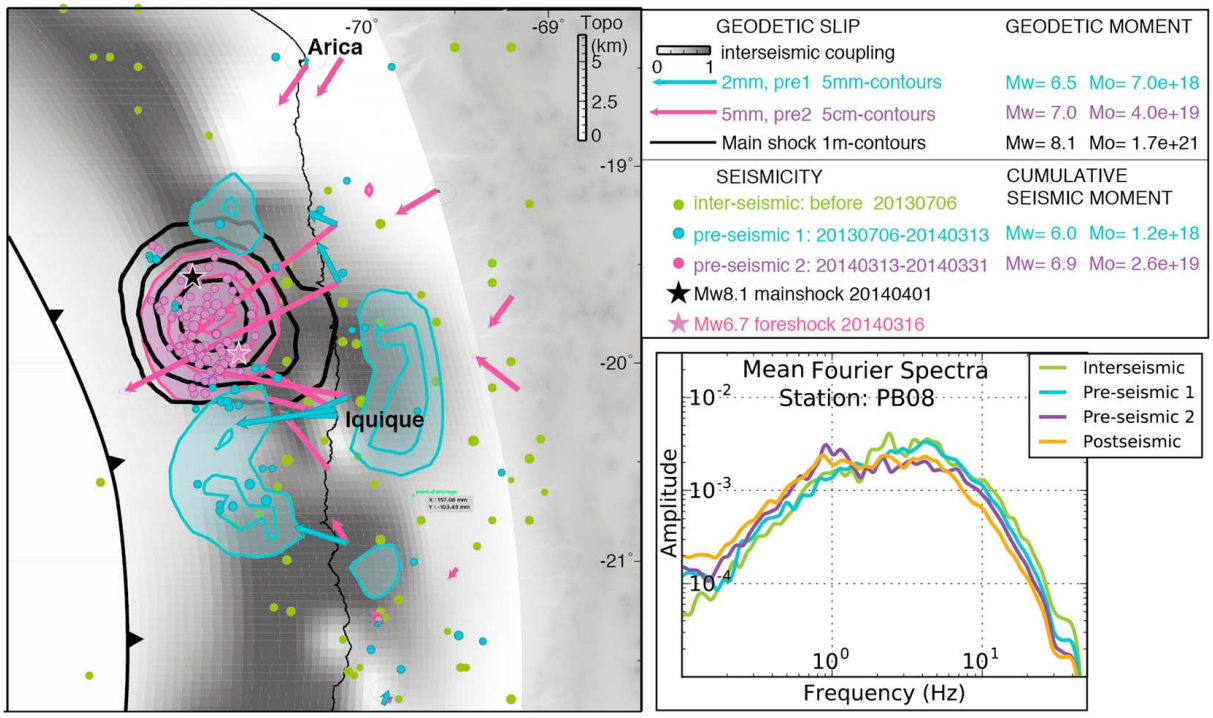

Figure 4.2: (left) Long- and short-term slip events (in blue and purple, respectively), preceding the M_W 8.1 main shock, superimposed on the interseismic coupling distribution (Métois et al., 2016) in gray, and the coseismic slip 1 m contours in black. Foreshock seismic activity for the same periods is also shown (in blue, purple, and green, $M_W > 4$). Epicenters of the main shock and the M_W 6.7 foreshock are shown as black and pink stars. (right inset) Mean Fourier spectra computed for interface earthquakes ($5.1 < M_W < 5.2$) grouped into four different time periods: interseismic in green, preseismic 1 in cyan, preseismic 2 in purple, and postseismic in orange. Station PB08 being located at an even distance of the earthquakes studied, the computed variations in Fourier spectra shapes should be unaffected by variations in attenuation but, instead, characterize earthquake ' s source.

of the attenuation effects and performed our analysis on earthquakes within a 0.1 magnitude range (Figures 4.S11 and 4.2 (right inset)).

Second, we compared the measured ground accelerations, at different frequencies, with the response spectra predicted by the recent Ground Motion Prediction Equation (GMPE) developed for subduction interface earthquakes by Abrahamson et al. (2016). Abrahamson et al. (2016) model is recognized as one of the leading models to predict ground motions in subduction areas and has been recently selected for the Global Earthquake Model (Stewart et al., 2015). The analysis of the obtained residuals confirmed that this model is well suited for our data set (see supporting information for details). Between-event residuals were computed, for each frequency (0.75 Hz, 1 Hz, 1.25 Hz, 5 Hz, 10 Hz, and PGA) and each earthquake, as the difference between the median of the observations of the given earthquake and the median of the model (Abrahamson & Youngs, 1992). The Ground Motion Prediction Equations is acting here as a backbone model which takes into account first-order magnitude and propagation effects. The analysis of relative time and spatial variations of between-event residuals allow us to compare the source effects of earthquakes with various magnitude and locations (Strasser et al., 2010; Al Atik et al., 2010; Youngs et al., 1995). It has been shown that response between-event residuals are fully correlated with "classical" Fourier stress drops (Bindi et al., 2007), so there is no information lost using response spectra and GMPEs compared to a more classical stress drop analysis. The between-event residuals were then organized as a function of time, space, and magnitude, in order to represent their variations and temporal evolution during the different periods before or after the main shock (Figures 4.3 and 4.S15).

4.3 Results

4.3.1 Precursory Slow Slip and Associated Seismicity

We detected a westward acceleration of some permanent GPS stations with respect to the average interseismic velocity (Figure 4.1). This acceleration begins $\approx$ 8 months before the main shock and affects mostly coastal stations located within an area 100 km south of the M_W 8.1 source, which was also affected by foreshock seismicity during the same period (Figure 4.1, blue dots). For comparison, during the preceding interseismic period, the seismicity is evenly distributed within the deeper part of the seismogenic zone (green dots in Figures 4.1 and 4.2). Inversion of these 8 month preseismic displacements (from July 2013 to mid-March 2014) suggests that a slow slip event occurred on the subduction interface (Figure 4.2, blue contours), surrounding the main

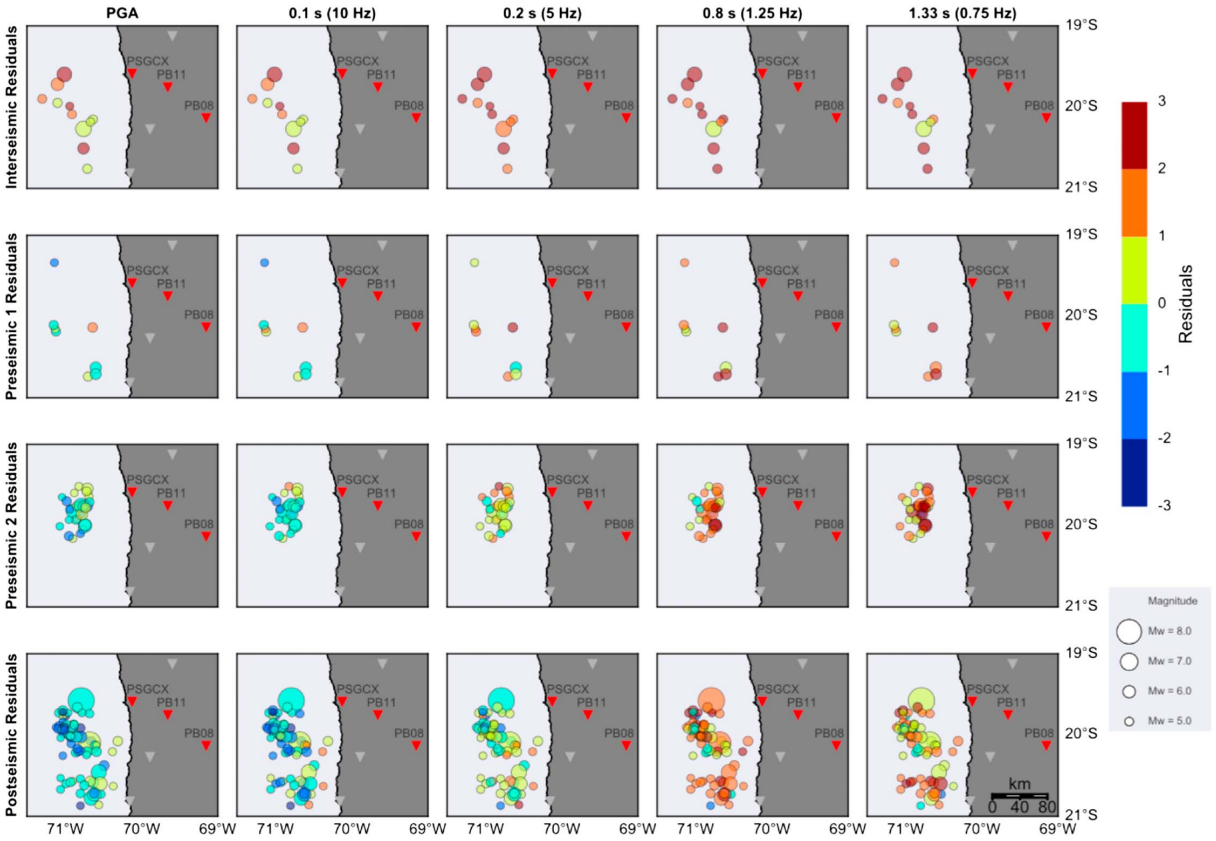

Figure 4.3: Time-space evolution of between-event residuals at the different frequency values shown in Figure 4.1 (middle row). Residuals are normalized by the standard deviation of the GMPE model. Therefore, average temporal changes can be considered significant from one standard deviation.

shock slip patch. South of the main shock, the slow slip occurs in a zone of low coupling during the interseismic period (Métois et al., 2016), while it rather affects areas characterized by intermediate locking downdip and north of the main shock. The geodetic precursor is collocated with long-term foreshock activity (Figure 4.2, blue dots). The comparison between geodesy and seismology shows that this long-term preseismic signal is at least 80% aseismic in nature; the cumulative seismic moment release ($1.2 \cdot 10^{18}$ Nm) representing 17 to 19% of the slip derived from GPS observations (6.4 to $7.0 \cdot 10^{18}$ Nm).

On 16 March 2014, a M_W 6.7 intraplate earthquake (Cesca et al., 2016) occurred 2 weeks before the main shock, north of the creeping area (pink star, Figure 4.2). This foreshock is the largest of the whole sequence. It is followed by an abrupt increase of the seismicity rate and associated b value (Schurr et al., 2014), some of them in the upper plate, and most of them on the subduction interface (Cesca et al., 2016), affecting the area that later ruptured during the M_W 8.1 megathrust. During this 15 day preseismic period, GPS stations were affected by a large deformation transient (Ruiz et al., 2014) (Figure 4.2). This preseismic slip measured by geodesy resembles the one released seismically: the location and shape of geodetic slip mimics the spatial distribution of epicenters (Figure 4.2, purple contours and dots) (Schurr et al., 2014), while the seismic moment is 65–67% of the geodetic moment (the remaining 33–35% is aseismic).

4.3.2 Evolution of Interface Earthquakes Ground Motions

To complement these findings, we analyzed the frequency content of interface seismicity (Specht et al., 2017; Strasser et al., 2009). Mean Fourier spectra at stations equidistant to the seismic crisis events show a consistent temporal decrease in high frequencies from interseismic to preseismic and, eventually, postseismic periods (Figures 4.2 and 4.S11).

The comparison of the measured accelerations for interface earthquakes with respect to the ground motion model (Abrahamson et al., 2016) provides an independent assessment of ground motion temporal variations (Haendel et al., 2015). The time, space, and magnitude dependencies of between-event residuals have been analyzed in order to search for a potential evolution of the source characteristic (Figures 4.3 and 4.S15). Measured residuals do not depend on earthquakes magnitude (as expected given the fact that the ground motion predictive equation acts as a backbone model correcting for magnitude and propagation effects). However, at frequencies of 5 Hz and above, a clear clustering of between-event residuals as a function of their time of occurrence is observed (Figure 4.S15), indicating a diminution of high-frequency energy release from interseismic period to preseismic period and later. Also, the temporal evolution of residuals differs from one frequency band to the other: at frequencies below 1.25 Hz residuals remain more or less constant with time, while

at higher frequencies (5 Hz and above) residuals decrease between interseismic period to preseismic and postseismic periods (Figures 4.1–4.3). During the second preseismic period (i.e., during the 15 days between the largest foreshock and the main shock) and the postseismic period, interface earthquakes show no significant change of their energy radiation. These two independent assessments of interface earthquake ground motions indicate a reduction of the high-frequency radiation, which is coincident with the preseismic acceleration in GPS velocities 8 months before the main shock.

4.4 Discussion

Our results indicate that a geodetic precursor occurred simultaneously with an identified increase in the seismicity rate (Figure 4.1, bottom row), and a decrease in the b value (Schurr et al., 2014). Such observations can be modeled as an aseismic slow slip on the subduction interface collocated with long-term foreshock activity (Figure 4.2, blue dots). This is consistent with the slow sliding of conditionally stable area on the subduction interface, spread out by sparse, small seismic asperities (Hetland & Simons, 2010), the seismic activity arising from the response of seismic asperities to the aseismic forcing.

Seismic radiation spectra of interface events have been proposed, on average, to be representative of the different frictional regimes of a subduction interface (Scholz, 1998; Lay et al., 2012); regions of unstable sliding can have large slip but generate modest amounts of short-period radiation upon failure, while smaller patchy regions of unstable sliding produce coherent short-period radiation when loaded to failure by creep of conditionally stable surrounding regions (Lay et al., 2012; Meng et al., 2015).

The reduction in high-frequency radiated energy often indicates a reduction in earthquake stress drop (i.e., a decrease of corner frequency). This phenomenon might be explained either by (a) smoother ruptures (Radiguet et al., 2009), (b) lower rupture velocities, or (c) increasing high-frequency attenuation. Given the foreshocks sequence does not migrate through time, a change in attenuation characteristics over such a short period of time seems unlikely. Rapid fluid migration within the fault zone may change the attenuation locally, within the few hundred meters of the damaged fault zone (high pore fluid pressures are accompanied by very low Q_S/Q_P ratios—0.1 to 0.4 for saturated basalt that are primarily due to increased shear attenuation (Tompkins & Christensen, 2001)). However, once integrated over the whole path followed by seismic waves through continental crust (a few hundred meters with increased attenuation versus tens of kilometers with no change), this local change in attenuation accounts for a minor part of the overall attenuation and only at large frequencies (higher than 15–20 Hz). It will be considered as part of the source, distance independent, high-frequency (kappa) attenuation. Therefore, the observed change of frequency content at 5–10 Hz rather seems related to a modification of the earthquake source parameters, such as a wider rupture area or slower rupture velocity. This is also compatible with the observed reduction in b value during the precursory time period, implying an increasing proportion of large to small earthquakes. Such a decrease in b value has been proposed as a precursor to major macrofailure (Smith & Adelfang, 1981). Our observations suggest that a slow aseismic forcing that started 8 months before the main shock triggerred an increased number of seismic events together with a modification of the earthquake frequency content, interpreted as a widening of rupture surfaces (Lay et al., 2012). This suggests a progressive expansion of failures into the conditionally stable areas surrounding small seismic asperities, in a mechanism that will eventually lead to the main rupture nucleation (Figure 4.4b). Two weeks before the main shock, the largest foreshock of the sequence triggered an increased deformation, seismicity, and b value. This seismicity, which is much more focused both spatially and temporally, might have been triggered by the M_W 6.7 foreshock that induced a significant increase of the Coulomb stress in the area. The seismicity and associated slow slip observed within the 15 days before the main shock may therefore result from a regular aftershock sequence and associated afterslip following the M_W 6.7 event, overprinting the preexisting slow aseismic slip (Figure 4.4c).

On 1 April 2014, the M_W 8.1 megathrust nucleates immediately north of the seismicity surge, in an area of increased stress resulting from adjacent preseismic slip. The maximum slip (Figure 4.2, black contours) occurs close to the area that started to slip before the main shock (pink), slightly downdip associated foreshock activity (pink dots), including repeating earthquakes (Meng et al., 2015). However, the rupture extends deeper to areas that were fully locked during the interseismic period (Métois et al., 2016). To the south, the rupture stops abruptly when it reaches the metastable areas affected by the long-term aseismic precursor (blue).

4.5 Conclusions

These observations confirm that a long-term aseismic slip of the subduction interface led to the nucleation of the M_W 8.1 Iquique megathrust earthquake. During the interseismic period, the seismicity was evenly distributed within the deeper part of the seismogenic zone (green dots on Figures 4.1 and 4.2) and ruptured small frictional asperities in response to deep interplate aseismic sliding (Figure 4.4). Eight months before the main shock, this slow sliding of plate interface started to accelerate within the seismogenic zone. South of the main shock this precursory creep occurs in an area characterized by little interseismic coupling, while downdip and north of the main shock, the slow slip affects more coupled areas (Figure 4.2) (Métois et al., 2016) and may be seen as the slow rupture of locked patches surrounding the main shock. Small seismic asperities scattered in this area ruptured repeatedly (Meng et al., 2015; Lay et al., 2012). The change in the earthquake frequency content during the foreshock sequence (a reduction of the stress drop) suggests that seismic failures widen progressively, decelerate, and start to extend into the slowly sliding, conditionally stable

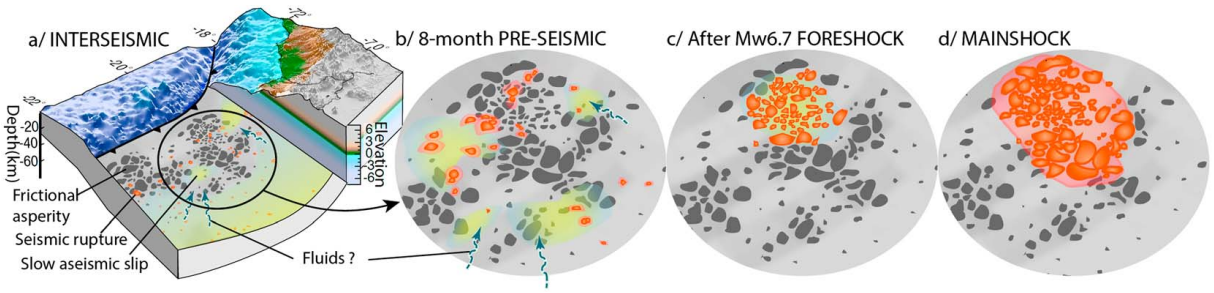

Figure 4.4: Schematic interpretation of the precursory phase of M_W 8.1 earthquake. (a) During the interseismic phase, the subduction interface slowly creeps (yellow) at depth and in low coupling areas, where frictional asperities are sparse. The rupture of small frictional asperities resisting this slow slip generates the background seismicity (red). (b) Eight months before the main shock, slow slip accelerates in the seismogenic zone (maybe facilitated by fluids migration), around the area ruptured by the main shock. Seismic ruptures start to propagate into the conditionally stable area surrounding the frictional asperities (light red). (c) After the largest foreshock on 16 March (M_W 6.7), slow slip goes on but is superimposed onto a rough seismic signal generated by the postseismic cascade. (d) On 1 April 2014, M_W 8.1 earthquake ruptures a large portion of the subduction interface, breaking both frictional asperities (red) and surrounding conditionally stable areas (light red).

areas surrounding frictional asperities. This process can be seen as the start of the precursory phase that will eventually lead to the megathrust rupture.

The simultaneous occurrence of slip acceleration, increased seismic activity, and the slow decrease of the high-frequency radiations of foreshocks may provide a way to detect the preparation of great earthquakes. Identifying aseismic slip combined with changes in associated earthquake spectra may therefore significantly help to mitigate seismic hazard at plate boundaries.

Acknowledgments

We are very grateful to Departamento de Geofísica de la Universidad de Chile (DGF) (`http://www.dgf.uchile.cl/`), Centro Sismológico Nacional de Chile (CSN) (`http://www.sismologia.cl`), International Plate Boundary Observatory Chile (IPOC) (`http://geofon.gfz-potsdam.de/waveform/`), LIA "Montessus de Ballore" International Laboratory (`http://www.lia-mb.net`), Central Andean Tectonic Observatory Geodetic Array (CAnTO) (`http://www.tectonics.caltech.edu/resources/continuous_gps.html`), and Instituto Geofísico del Perú for making raw GPS and strong motion data available. This work has been supported by PNTS-2014-08, LabeX OSUG@2020, SMINGUE, IRD AO-Sud, and INSU-Aléas grants. J.P.V. and J.J. acknowledge support provided by CONICYT through "Becas Chile" PhD fellowships. F.O. acknowledges support from Proyecto Fondecyt 1140904 (CONICYT). The authors warmly thank J.M. Nocquet for making PYACS software available. Thank you to J. Hollingsworth for editing the English writing. This work benefited from fruitful discussion with P.-Y. Bard, C. Beauval, D. Bindi, M. Bouchon, R. Bürgmann, M. Métois, G. Montalva, D. Marsan, and J. Ruiz among others.

4.6 Supporting Information for: An 8-month slow slip event triggers progressive nucleation of the 2014 Chile megathrust

This supporting information provides a general description of the methods and processing steps used and supplementary figures that support our findings.

4.6.1 cGPS data analysis & Daily cGPS processing

We used data from several cGPS networks spanning the whole central Andes subduction (IPOC, LIA Montessus de Ballore, ISTerre, and Caltech Andean Observatory), together with IGS stations. These cGPS data were analyzed in double differences, in two distinct regional subnetworks, plus a global network (Figure 4.S1). The fifty stations available during the period 2000–2014 were used to design the first regional subnetwork. The second regional subnetwork includes 50 stations running from 2007 to 2014, 33 stations overlapping with the first subnetwork in order to ensure consistency between the subnetworks. The global network includes 99 IGS sites worldwide, 22 of them in South America, with 49 stations overlapping with the two regional subnetworks. 24-hour sessions were reduced to daily estimates of station positions using the GAMIT 10.5 software, choosing the ionosphere-free combination, and fixing the ambiguities to integer values. We use precise orbits from the International GNSS Service for Geodynamics, precise EOPs from the IERS bulletin B, IGS tables to describe the phase centers of the antennas, FES2004 ocean-tidal loading corrections, as well as atmospheric loading corrections (tidal and non-tidal). We estimated one tropospheric zenith delay parameter every two hours and one couple of horizontal tropospheric gradients per 24h session, using the Vienna Mapping Function (VMF1) (Boehm et al., 2006), to map the tropospheric delay in zenithal direction, with a priori ZHD evaluated from pressure and temperature values from the VMF1 grids. Daily solutions are combined using the GLOBK software in a "regional stabilization" approach, and mapped it into the ITRF2008 reference frame (Altamimi et al., 2011) by adjusting selected stations coordinates to those defined in the ITRF in a least square iterative process. Time series analysis and identification of transient movements Annual and semi-annual signals were removed from the obtained daily time series, as well as the long-term constant deformation associated with interseismic loading, by fitting a linear regression together with a pair of sinusoids terms. The remaining noise has been reduced by removing the common-mode, obtained by selecting stations located within a distance range of 50-500km from the source region (SJUA, ATIC, CHRA, PTCL, LYAR, UTAR, PCCL, PB02, PB04, MLCA, PB05, PMEJ, JRGN, UCNF, NZCA, AREQ, TORA, TQPL, DANC, TRTA, PALC, PTRE, MNMI, COLC, CHMZ, PB11, PCHA, PB08, PB01, PB07, PB03, CDLC, RADO, PB06, CBAA, VLZL, CJNT) and by averaging their detrended signals. Then, in order to mitigate the residual loading signal present in our signal, we removed from each time series the mean annual residual seasonal movement computed between 2010 and 2013. This procedure reduced significantly the scatter in our time series. In order to study the long term transient in our time series, we excluded data after March 15th, 2014 (when a strong preseismic signal occurred), and then computed the average velocity variations, by fitting a linear regression in a six-month sliding window of the obtained detrended and de-noised time-series. The results indicate a velocity change in July 2013 (appr. eight months before the mainshock) at coastal stations located at 20.3°S close to the city of Iquique. This velocity change propagated bilaterally and reached stations located within a distance of appr. 100 km parallel to the strike of the subduction (parallel to the coastline). In a second step, we compute the average velocities by fitting a linear regression to the detrended cGPS time series on three different time periods before July 2013 (interseismic), July 2013–13th March 2014 (preseismic 1), 14th March 2014–March 31st 2014 (preseismic 2) (Figures 4.S2 and 4.S3). Uncertainties on linear regressions correspond to standard deviation of one for each linear regression. Displacements for both pre-seismic periods have been obtained by multiplying each station velocity by the time span. For the preseismic period 1, we selected only stations showing a continuous time series since 2012, to avoid artifacts associated with jumps or data holes in the time series. For both preseismic periods, we discarded noisy time series generating the largest uncertainties in the displacement computation.

4.6.2 Slip distribution inversion and resolution

The surface deformation fields associated with the coseismic and preseismic phases were modeled using a dislocation buried in a layered elastic half space (Wang, 2003), taking crust1.0 as a velocity model. The fault geometry was constrained by the trace of the trench at the surface. We assumed a uniform dip of 15° and a variable rake, so that the slip direction is parallel to the plate convergence (76°), and is taken constant at all patches. The fault was discretized into an array of 24×11 elements, measuring approximately 15×15km, although their size varies locally since the fault follows the trench geometry (Figures 4.S4, 4.S5 & 4.S6). To solve for the slip distribution along the 264 fault patches, we used a least squares minimization with a non-negativity constraint on the slip. Slip was forced to zero at the edges of the fault. To limit oscillations of the solution, we applied smoothing by minimizing the second-order derivative of the fault slip. We determined the optimal solution roughness (Jónsson et al., 2002) that was used in our final models searching for a compromise between the roughness and misfit of the solution. We estimate the sensitivity of our data set to unit displacements on each node of the grid by summing the horizontal deformation on the whole network after Loveless & Meade (2011). The power of our data to constrain the coupling on the interface is high from 15 km depth to more than 70 km depth in general. The coseismic offsets extracted

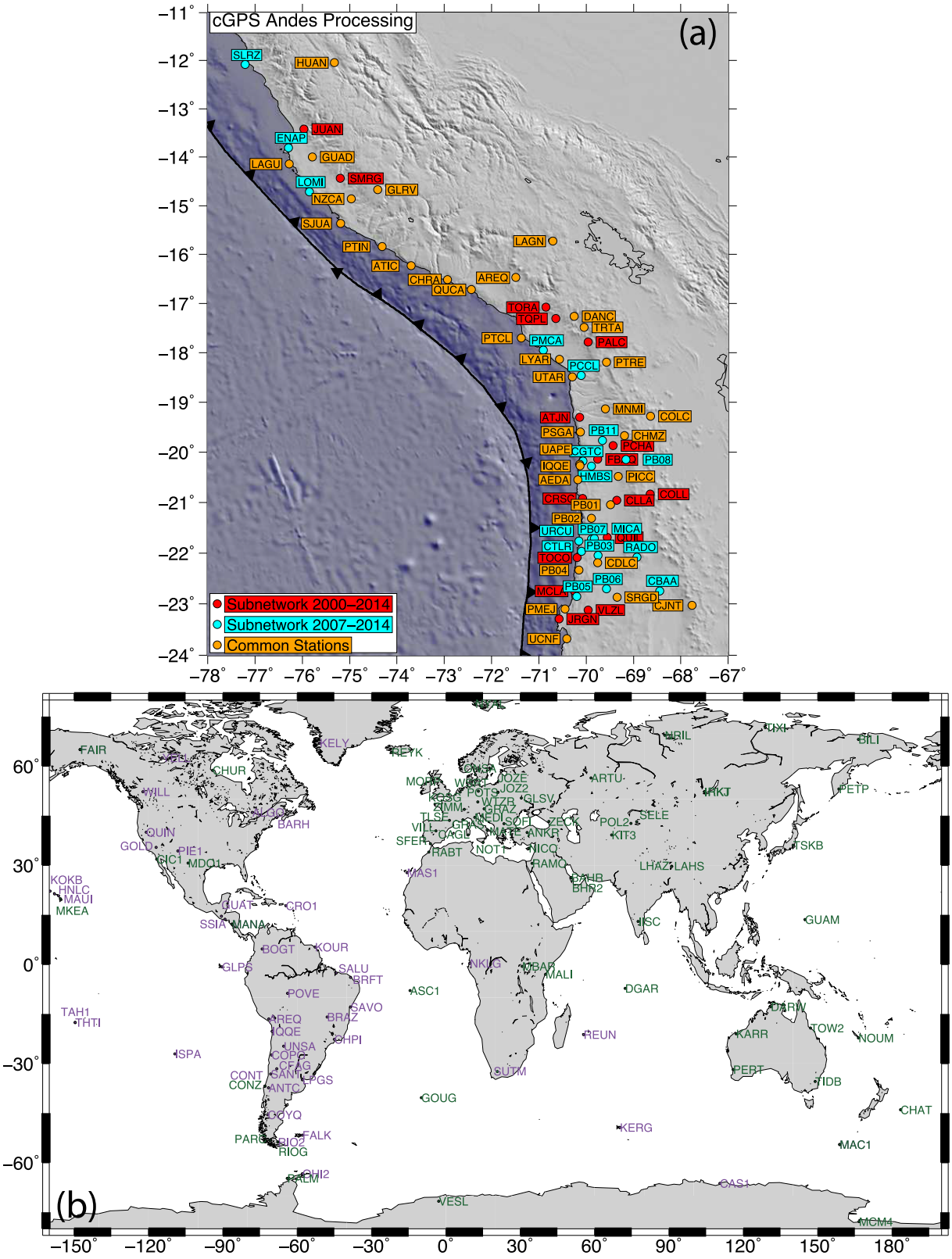

Figure 4.S1: Map of the network used in this study, showing the three subnetworks (Andes 2000–2014, Andes 2007–2014 (a) , and the Global Network (b)), as well as the stations used for the reference frame computation. Green color in (b) indicates IGS stations included for global processing, while purple indicates IGS stations overlapping with the Andes subtnetworks.

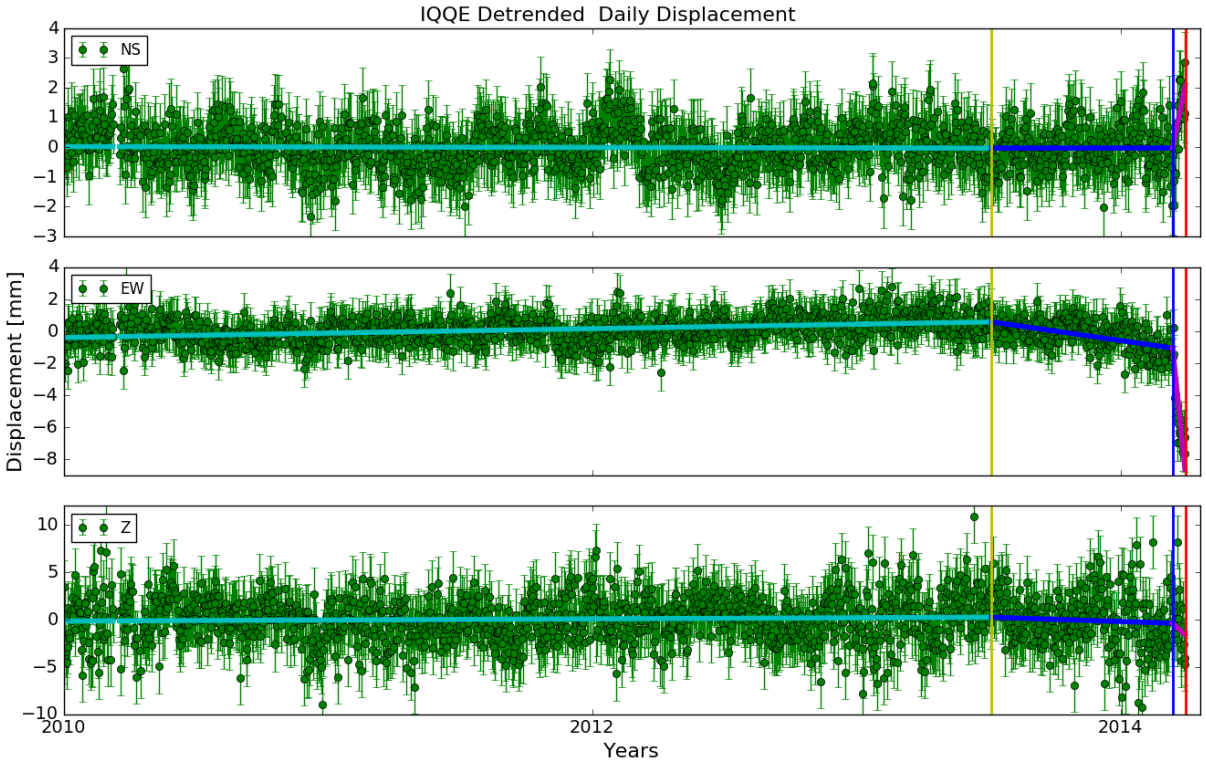

Figure 4.S2: N, E, U detrended daily displacements for IQQE station since 2010. Vertical lines indicate the dates of the swarm of July 2013 (yellow), the M_W 6.7 foreshock on March 16th 2014 (blue) and the M_W 8.1 main shock on April 1st 2014 (red). Linear regressions for the three preseismic periods are shown.

from cGPS time series were used to invert for the coseismic slip (Figure 4.S4). The roughness of the preferred coseismic distribution is 0.04 cm/km for a RMS (L_2-norm misfit) of 1.20 cm. The seismic moment is $1.7 \cdot 10^{21}$ Nm, and corresponds to a Magnitude 8.1. The inverted slip distribution for pre-seismic period 2 (Figure 4.S5) corresponds to a moment M_0 = $3.9 \cdot 10^{19}$ Nm (M_W = 7.0) and a fit to the data with RMS = 1.3 mm. The inverted slip distribution for pre-seismic period 1 (Figure 4.S6) corresponds to a moment M_0 = $7 \cdot 10^{18}$ Nm (M_W = 6.5) and a fit to the data with RMS = 0.5 mm (Figure 4.S7). Because we were able to estimate accurately the long term transient displacement on a subset of stations only, mostly located along the coast, the slip distribution for pre-seismic period 1 less well constrained than the co-seismic and pre-seismic period 2. However, the patches that are found to be slipping by our inversions are located in zones that are well constrained by our data (Figure 4.S6). Depending on the smoothing applied to the model, the estimate of the geodetic moment of pre-seismic slow slip events (for periods 1 and 2) vary within less than 10% (Figure 4.S7), and the main features of the slip distribution are quite stable whatever the smoothing applied (Figure 4.S8).

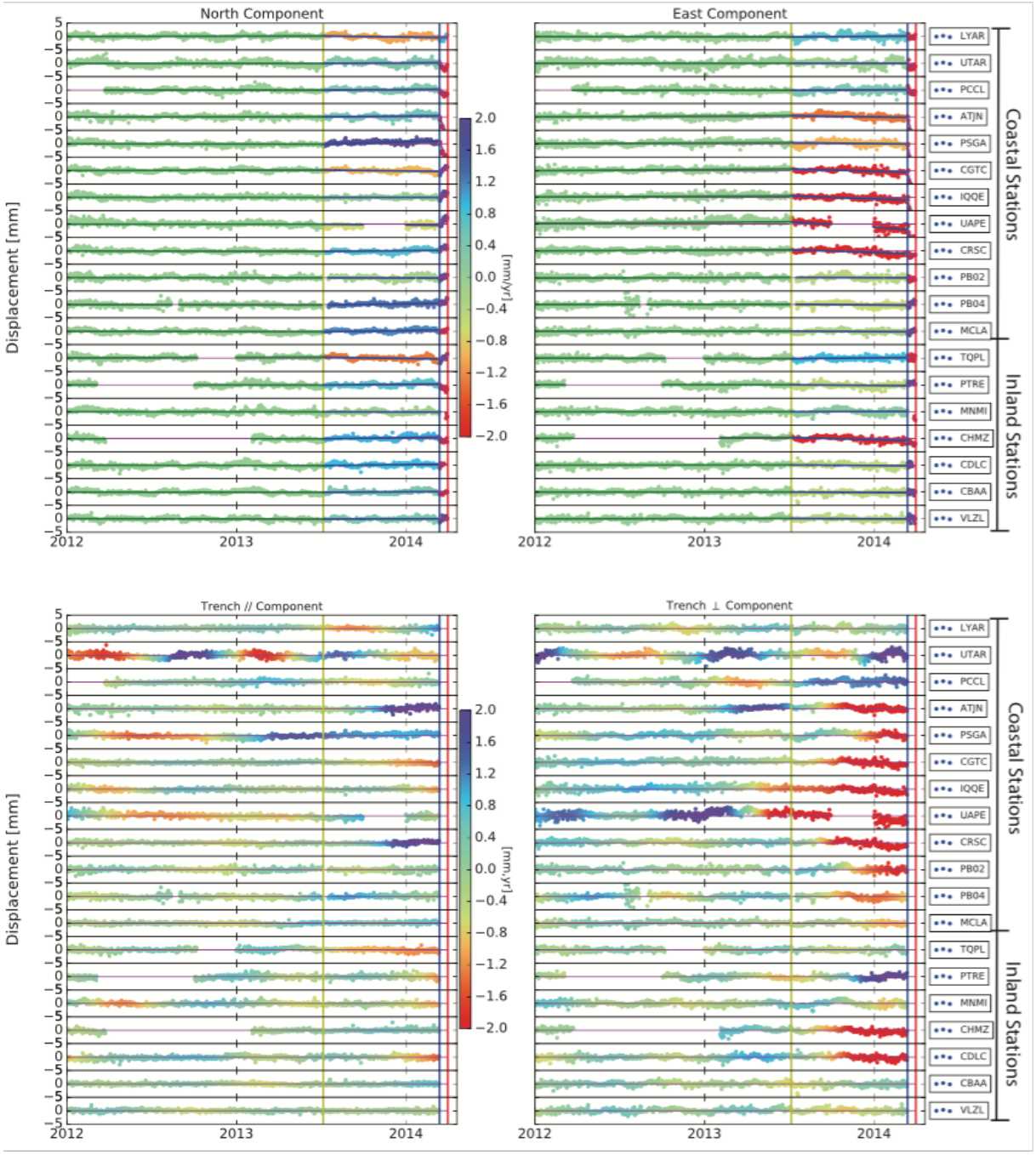

Figure 4.S3: Detrended displacement time series for a selection of stations along the coast and inland. Bottom 2 panels: Colors, indicate the trench parallel (left panels) and trench perpendicular (right panels) velocities obtained by computing the average velocity over a six-month sliding window. Top 2 panels: Colors, indicate the N–S (left panels) and E–W (right panels) velocities obtained by fitting a linear regression on the displacement time series for the three preseismic periods.

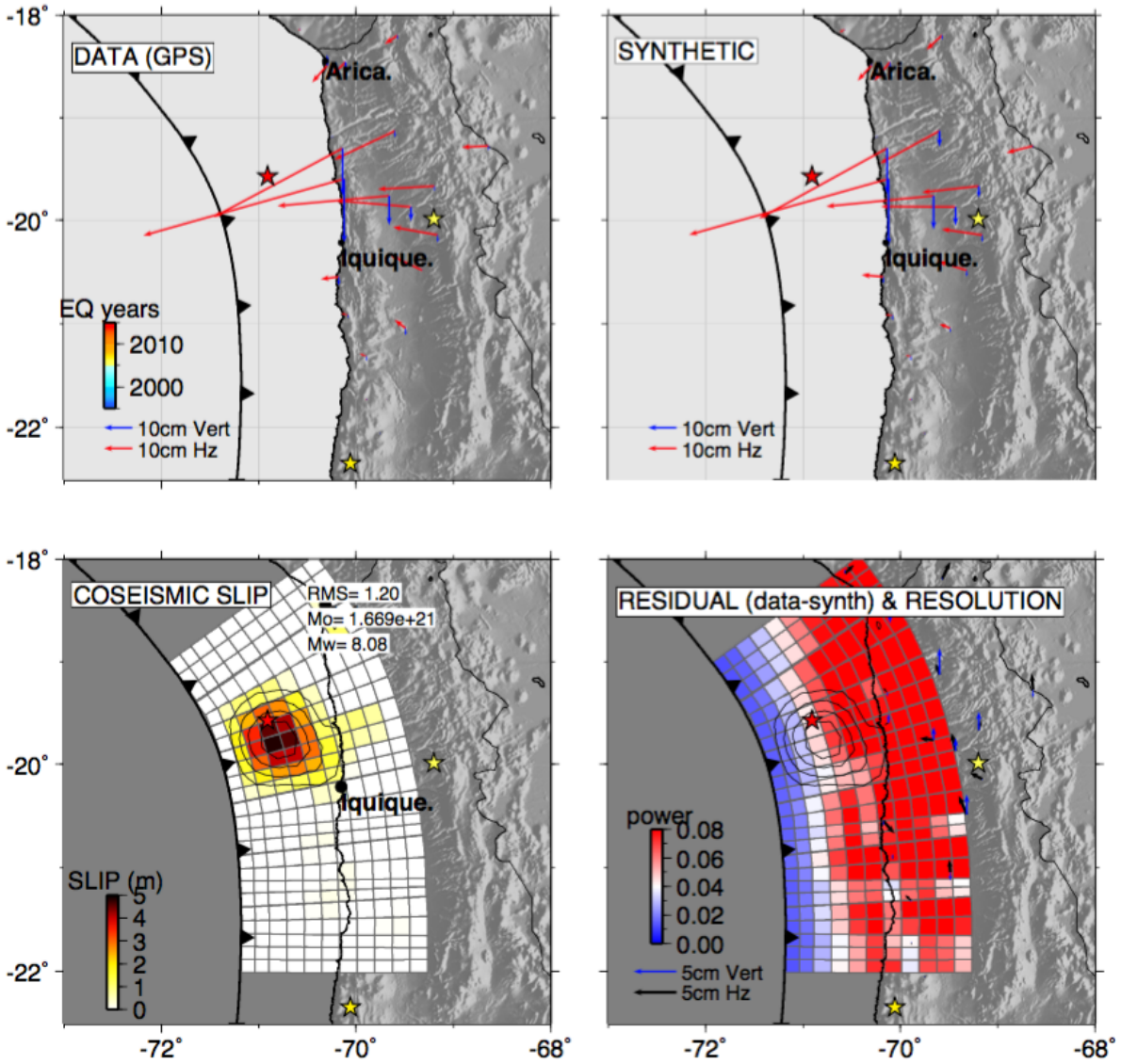

Figure 4.S4: Co-seismic displacements (observed : top left, and modeled: top right), co-seismic slip distribution inverted from surface displacements (bottom left), residuals and power of GPS stations to constrain plate interface behavior (i.e., sum of the partial derivatives relating GPS displacement to unit slip (Loveless & Meade, 2011)) (bottom right). One-meter contours are drawn.

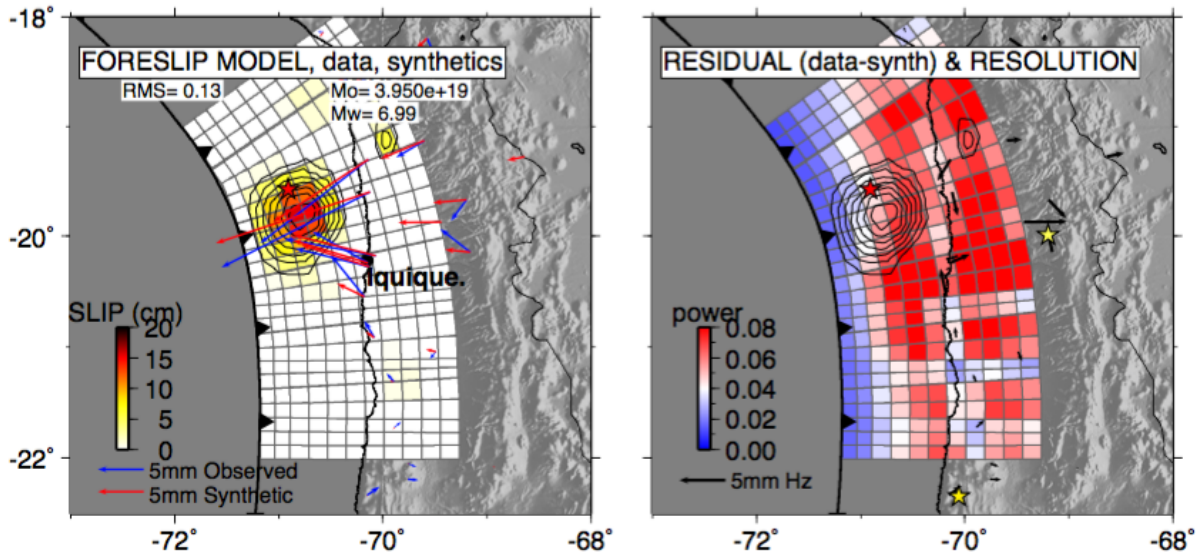

Figure 4.S5: Left: Displacements (observed: blue, modeled: red) during preseismic period 2 (March 14th 2014 to March 31st 2014) and preseismic slip distribution for the two weeks preceding the main shock inverted from surface displacements, Right: residuals and resolution. Two-cm contours are drawn.

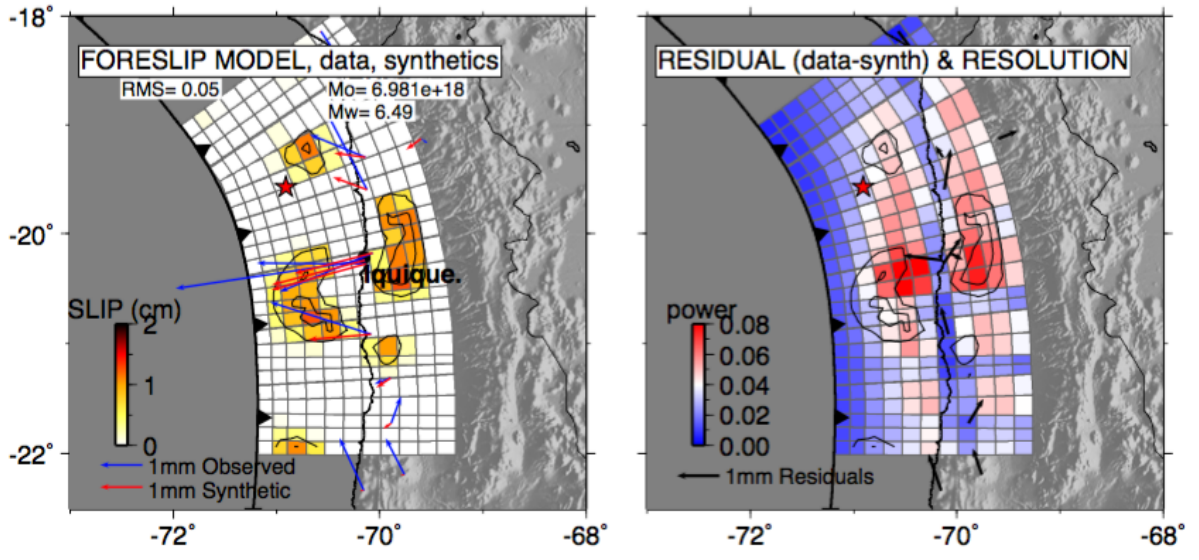

Figure 4.S6: Left: Displacements (observed: blue, modeled: red) during preseismic period 1 (July 6th 2013 to March 13th 2014) and preseismic slip distribution for the two weeks preceding the main shock inverted from surface displacements, Right: residuals and resolution. Five-mm contours are drawn.

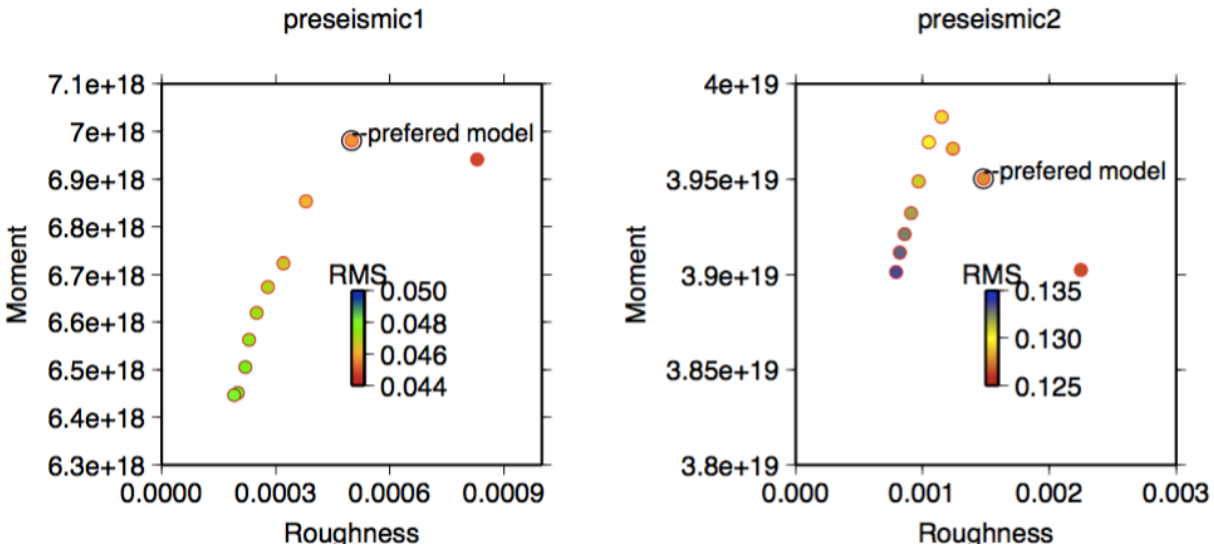

Figure 4.S7: Geodetic moment as a function of the model roughness, for both preseismic models. Dots are color coded with the model-data misfit. The preferred model is chosen as a compromise between smoothness and RMS.

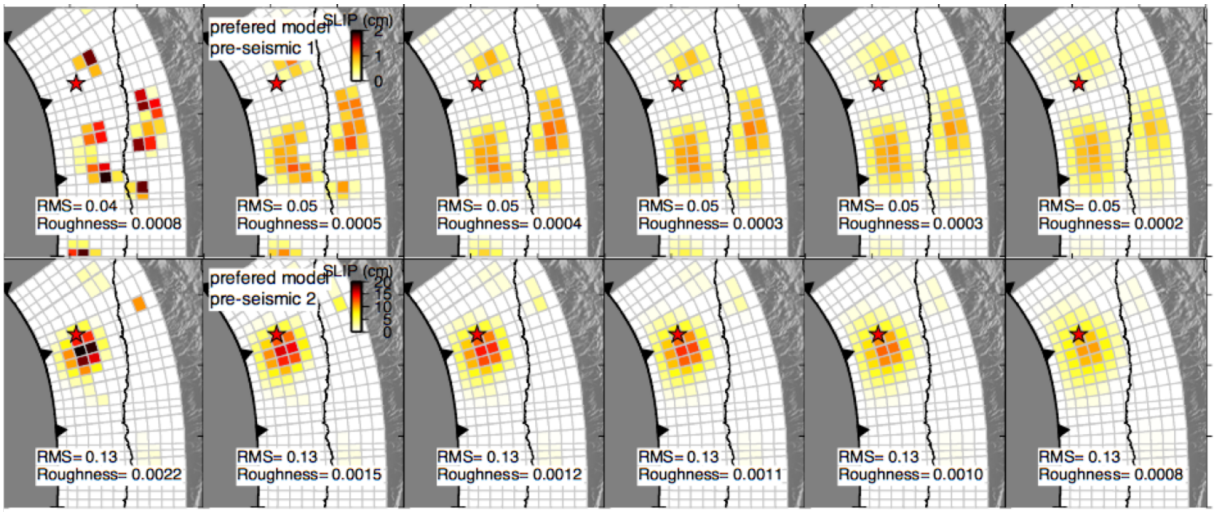

Figure 4.S8: Pre-seismic slip distribution for different model roughnesses. Top: 8 months preseismic (july 2013–mid-March 2014), Bottom: 15-day pre-seismic (Mid-March to End March 2014).

4.6.3 Interface Seismic Catalog

The interface seismicity catalog (Figure 4.S9) was compiled from the GEOFON moment tensor catalog (`http://geofon.gfz-potsdam.de/eqinfo/list.php?mode=mt`) and the Global CMT catalog (`http://www.globalcmt.org/CMTsearch.html`). We use ACE, a data driven algorithm to automatically determine focal mechanism clusters with similar Style-of-Faulting (strike, rake, and dip). The algorithm is also capable to identify the nodal planes as rupture and auxiliary planes, therefore allowing the computation of the rupture plane distance. Since the rupture plane size is unknown, we used a rupture plane scaling relation (Strasser et al., 2010). Hypocenters are not directly required to classify the data and therefore, classification errors are reduced, compared to classical deterministic classification scheme. We checked that this data-driven procedure was giving results consistent with a more classical classification and that the locations of the earthquakes identified as interface earthquakes were consistent with the known subduction fault plane geometry. This procedure allowed us to build a catalogue containing 125 interface earthquakes in North Chile between January 2008 and June 2014, from 19°S to 21°S and 72°W to 67°W, shallower than 80 km, with M_W equal or higher than 4.5 (Figures 4.S9 and 4.S10). Location and depth of earthquakes can be poorly constrained in the area (see the dispersion in the seismicity and the discrepancy with the trace of the slab in Figure 4.S10), demonstrating that the strategy of using the focal mechanisms to identify interface events is better adapted than a strategy based on earthquakes depth or location.

4.6.4 Validation of the Ground Motion Prediction Equations (GMPEs) for the studied seismic crisis

The prediction of ground motion was done using the Abrahamson et al. (2016) Prediction Model. GMPEs predict the Acceleration Response spectra, which correspond to the maximum acceleration experimented by an oscillator of a given mass with one degree of freedom (at different fundamental periods) for different input parameters (e.g. distance to the source, site conditions, magnitude). Abrahamson et al. (2016) model is recognized as one of the leading models to predict ground-motions in subduction areas and has been recently selected for the Global Earthquake Model (Stewart et al., 2015). To apply this model, V_{S30} = 850 m/s was assumed for all stations of the network based on the information that the stations are located on bedrock. The distance between each site and the rupture plane has been estimated directly from the hypocentral distances (Haendel et al., 2015). The fit of the model was tested for oscillators frequencies of 0.75 Hz, 1 Hz, 1.25 Hz, 5 Hz, 10 Hz and for PGA. Residuals have been computed and normalized by the standard deviation of the GMPE model. Therefore a residual value of one means that the observation is offset from the mean predicted value by one model standard deviation. The distribution of absolute residuals allows to evaluate how good is the predictive model in terms of consistency (i.e. do the residuals follow a similar probabilistic distribution than the random error of the model with respect to dataset used to calibrate the model?), precession and accuracy (i.e. are the observed normalized residuals centered on zero?). The obtained absolute residual distribution shows both a good residual distribution and a reasonable fit of the model, with a somewhat lower accuracy between 0.75 Hz and 5 Hz (Figure 4.S12).

GMPEs residuals can be separated in two residuals terms: between-event and within-event residuals (Abrahamson & Youngs, 1992). The within-event residuals correspond to the difference between each observation and the median of the observations. Its distribution provides an estimation of the variability of record specific factor as site amplification (i.e. variability in site conditions effects) (Strasser et al., 2009; Al Atik et al., 2010). The within-event residual distribution shows also a good fit, indicating that site effects variability is well estimated by the model (Figure 4.S13). The between-event residuals represent the difference between the median of the observations of a given event, with respect to the median of the model (Abrahamson & Youngs, 1992). The between-event residual distribution (Figure 4.S14) can be interpreted as the variability of wave radiation due to source parameters (e.g. stress-drop) that are not included in the prediction model (Al Atik et al., 2010; Youngs et al., 1995). Tests performed with other recent subductions GMPE ' s did not show a better global agreement and therefore the Abrahamson et al. (2016) model was chosen as the backbone model to predict ground-motions for the North Chile subduction area.

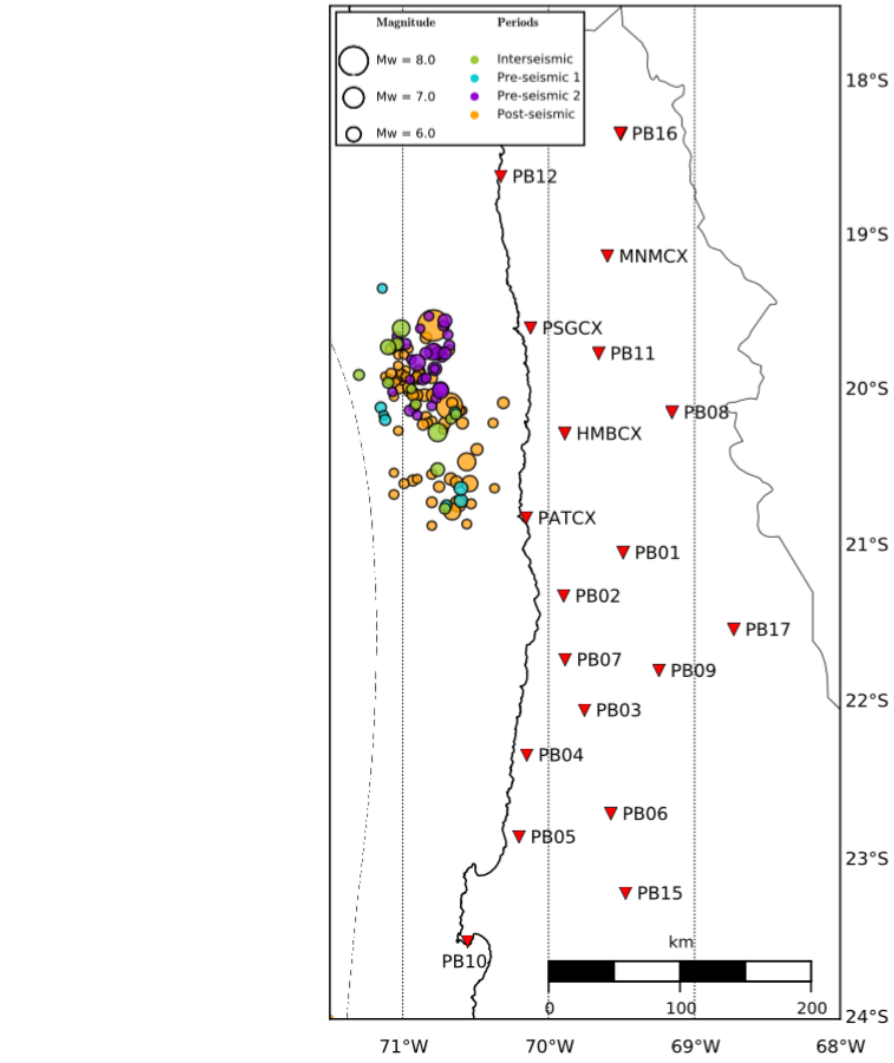

Figure 4.S9: Map of the interface seismicity data set (dots colored as a function of the 4 periods defined in the paper), and network of IPOC accelerometric stations (red inverted triangles) used to perform earthquakes frequency content analysis. All these stations are installed on bedrock. Most of them are also colocated with GPS stations used in this paper.

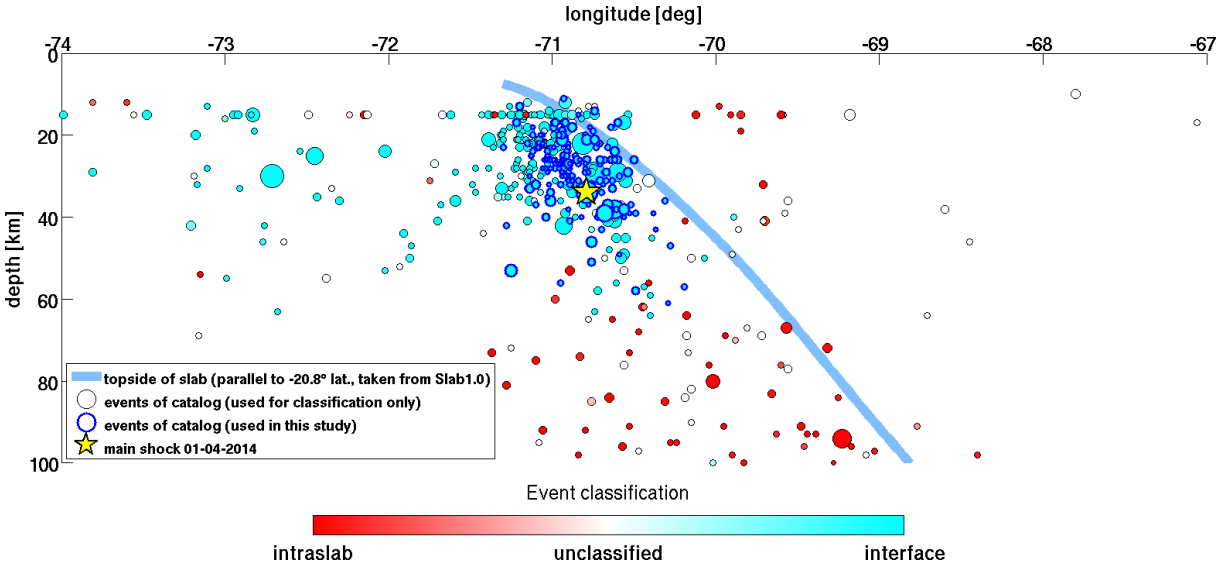

Figure 4.S10: Cross section of IPOC catalogue of earthquakes in North Chile. Colored dots represents the classification of earthquakes (interface, unclassified or intraplate) as a function of their focal mechanism. The blue line represents the Slab1.0 subduction interface. The events used in this study (contoured in blue) have been selected as being interface events that occurred between January 2008 and June 2014.

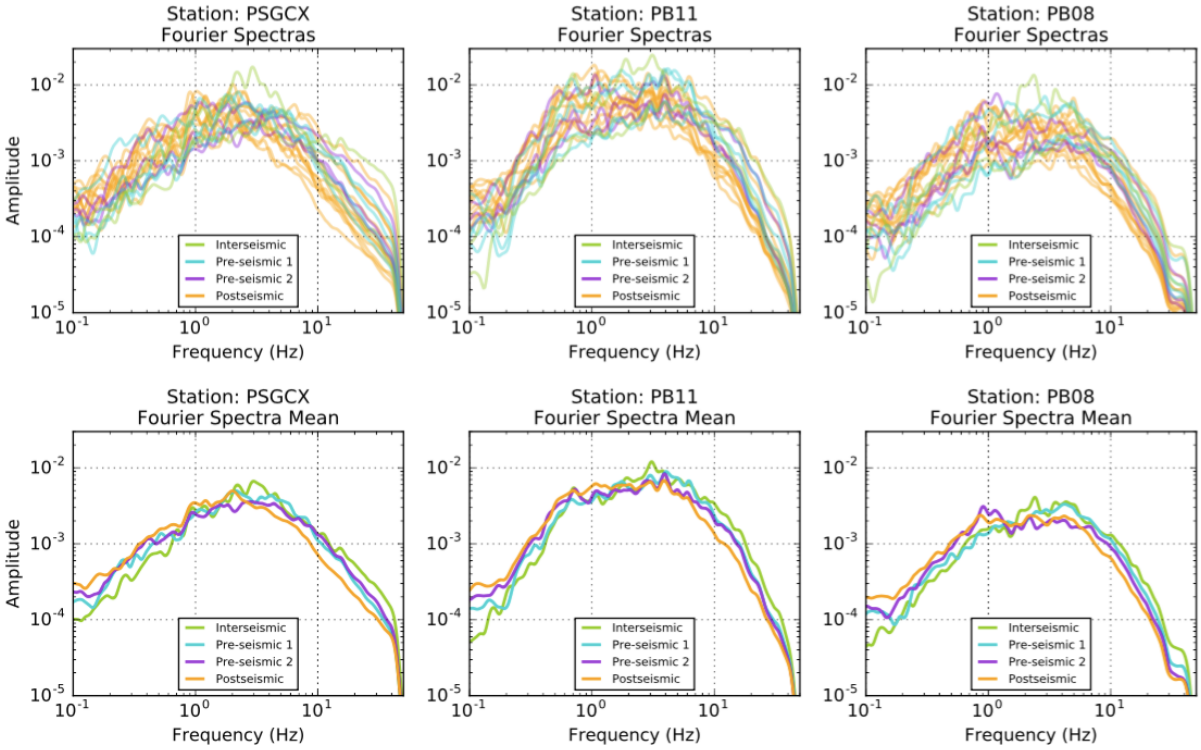

Figure 4.S11: Acceleration Fourier Spectra computed at stations PSGX, PB11 and PB08 (see Figure 4.S9 for location) for interface earthquake within 5.1–5.2 Magnitude range. Spectra are color-coded as function of the period when occured the earthquake (interseismic in green, pre-seismic 1 in cyan, pre-seismic 2 in purple, post-seismic in orange). Top line shows all individual spectra while bottom line shows the mean spectrum for each time period.

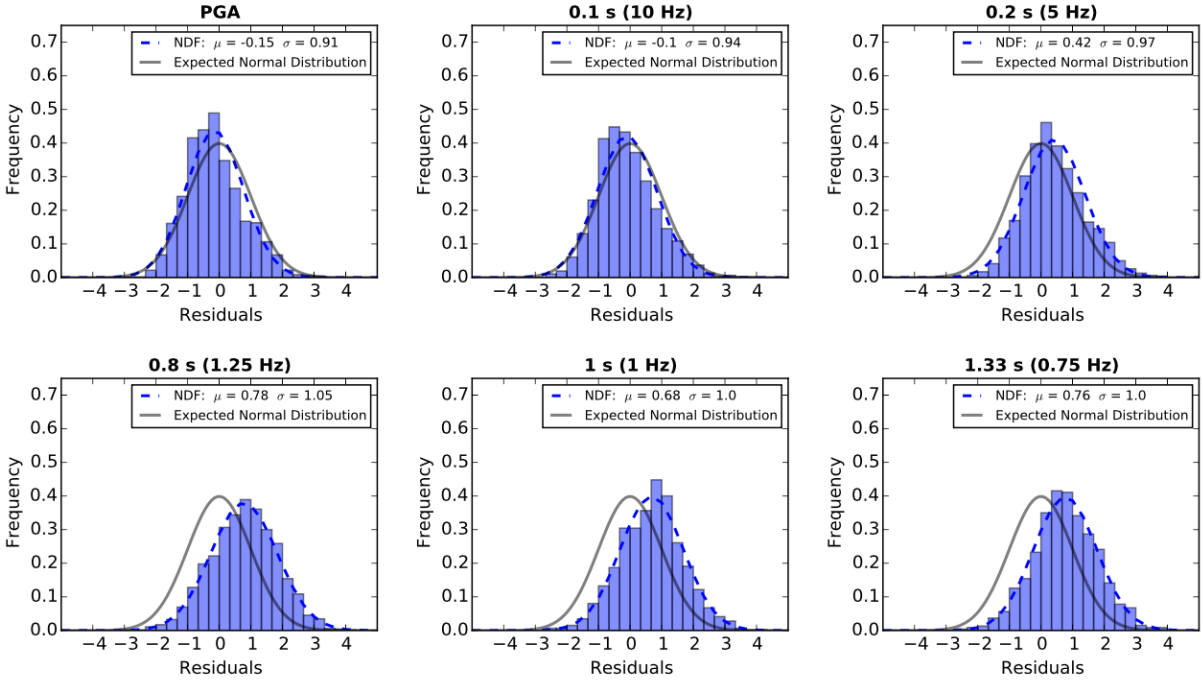

Figure 4.S12: Histograms of ground motion absolute residuals normalized with respect to the total standard deviation of the GMPE model (Abrahamson et al., 2016). The Normal Density Function (NDF) of the residuals is shown by the dashed lines and the expected normal distribution is represented by the gray lines.

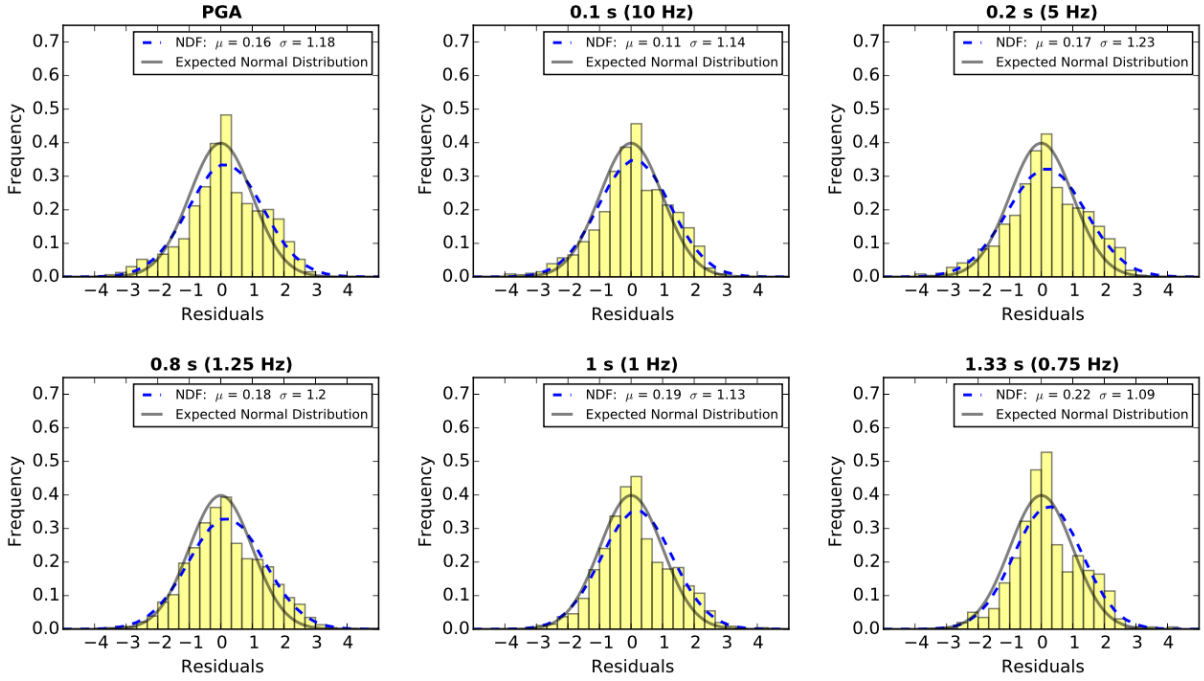

Figure 4.S13: Histograms of the Within-Events residuals normalized with respect to the Within-Event standard deviation of the model. The Normal Density Function (NDF) of the residuals is shown by dashed lines and the expected normal distribution by gray lines.

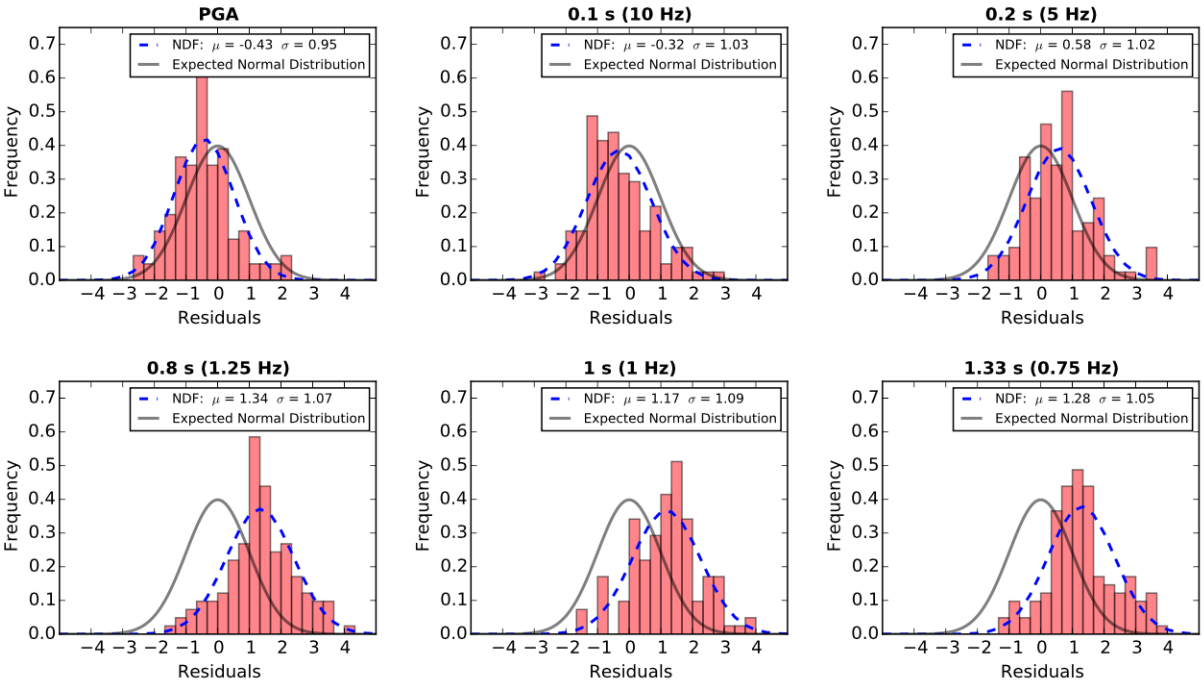

Figure 4.S14: Histograms of the Between-Event residuals normalized with respect to the Between-Event standard deviation of the model. The Normal Density Function (NDF) of the residuals is shown by dashed lines and the expected normal distribution by gray lines.

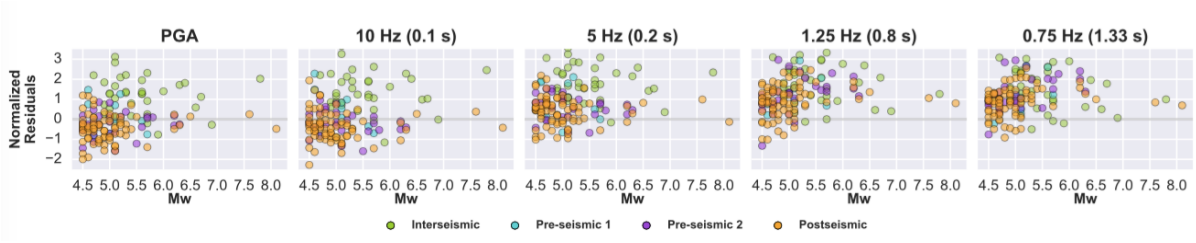

Figure 4.S15: Between-event residuals as a function of event magnitude at the different frequency values shown in figure 4.1 (mid-panel). At frequencies above 5 Hz, earthquakes occurring during the interseismic period exhibit significantly larger residuals than earthquakes belonging to preseismic and postseismic sequences. Instead, values of residuals are similar for all considered time periods at frequencies below 1.25Hz.

Chapter 5

Uncertainty reduction of stress tensor inversion with data-driven catalogue selection

Abstract

The selection of earthquake focal mechanisms (FMs) for stress tensor inversion (STI) is commonly done on a spatial basis, that is, hypocentres. However, this selection approach may include data that are undesired, for example, by mixing events that are caused by different stress tensors when for the STI a single stress tensor is assumed. Due to the significant increase ofFM data in the past decades, objective data-driven data selection is feasible, allowing more refined FM catalogues that avoid these issues and provide data weights for the STI routines. We present the application of angular classification with expectation-maximization (ACE) as a tool for data selection. ACE identifies clusters of F$M_W$ithout *a priori* information. The identified clusters can be used for the classification of the style-of-faulting and as weights of the FM data. We demonstrate that ACE effectively selects data that can be associated with a single stress tensor. Two application examples are given for weighted STI from South America. We use the resulting clusters and weights as *a priori* information for an STI for these regions and show that uncertainties of the stress tensor estimates are reduced significantly.[a]

[a] published as: von Specht, S., Heidbach, O., Cotton, F., Zang, A., 2018, Uncertainty reduction of stress tensor inversion with data-driven catalogue selection, *Geophysical Journal International*, 214(3), 2250–2263.

5.1 Introduction

UNDERSTANDING Earth's stress field provides insight into rupture mechanics of earthquakes and tectonic deformation processes in general. Stress itself cannot be observed directly and thus must be inferred from kinematic deformation. Earthquake focal mechanisms (FM) are of key importance to derive deformation within the Earth and thus allow inference of stress orientations.

Stress tensor inversion (STI) methods have been published since the 70's (Carey-Gailhardis & Brunier, 1974; Angelier, 1979; Armijo et al., 1982; Rivera & Cisternas, 1990). Due to their significance for stress tensor inference, several methods have been proposed to invert for the stress tensor from FM data alone. The three major routines used today are based on the works of Angelier (1979); Michael (1984); Gephart & Forsyth (1984). Maury et al. (2013) provide a comprehensive overview and comparison of these methods and summarize their common assumptions:

1. Slip orientation is parallel to the resolved shear stress orientation on the rupture plane. This assumption is known as the Wallace-Bott hypothesis (Wallace, 1951; Bott, 1959).

2. The medium in which the FM occurred is homogeneous, i.e. the stress is assumed to be constant in the entire volume and all ruptures are related to a single stress tensor.

3. Earthquakes are independent from each other. This assumption is linked to the previous assumption insofar, as a major earthquake temporarily alters the regional stress tensor. Aftershocks are therefore not only influenced by the background stress field, but also by the variation to it from the main shock.

The methods based on Angelier (1979) and Michael (1984) are based on the L_2-norm, i.e. least squares (LSQ). The large data variability in FMs lead Gephart & Forsyth (1984) to use an L_1-norm, i.e. least absolute deviation (LAD), to reduce the impact of outliers. Several advancements have been proposed on the basis of these three methods, including spatial variations (Hardebeck & Michael, 2006; Maury et al., 2013; Martínez-Garzón et al., 2016), identification of slip directions (e.g Lund & Slunga, 1999; Vavryčuk, 2011; Xu, 2004), inversion independent of nodal plane identification (Angelier, 2002), and uncertainty estimation (Hardebeck & Hauksson, 2001a).

Though advances have been made in the inversion routines, the basic aspect of data selection has not been addressed to a larger extent. The most common approach is to select data from spatial regions. The regional binning can be based on different criteria. Townend & Zoback (2001) used rectangular zones of different sizes, while Hardebeck & Michael (2004) defined stripes parallel to major fault zones (e.g. the San Andreas fault Hardebeck & Hauksson, 1999). Hardebeck & Hauksson (2001b) also used temporal binning. This kind of data binning is insofar a deterministic choice as it implies the same stress tensor for all FMs in a given bin. Data not following this assumption appear as outliers and enlarge the uncertainties of the inversion results. Hardebeck & Michael (2004) demonstrated large variations in stress tensor orientations due to different binning strategies. In addition to assumption of the constant stress tensor in a given bin, the FM data related to that stress tensor should be diverse to properly represent displacement associated with the given stress tensor (Hardebeck & Michael, 2004). This poses a tradeoff in any STI: To only include FM data that are related to a single stress tensor, the bin should be as small as possible. However, the same bin must be large enough to contain a variety of different FM to reduce the bias of the inversion.

Different approaches to the relaxation of the constant stress tensor assumption have been proposed, as spatial variations of the stress field have been documented even on local scale (Hardebeck & Hauksson, 1999). Michael (1991) superposes several stress tensors in a region; an approach similar to Armijo et al. (1982), where the data are grouped into different tectonic phases to minimize the stress ratio. Spatial subdivision has been proposed by Hardebeck & Michael (2006) by horizontally subdividing the region of interest into linearly dependent spatial bins. Maury et al. (2013) incorporated a linear variability of stress with depth.

In recent years, more advanced data selection criteria have been published. García et al. (2012) introduced a selection framework for the development of ground motion prediction equations which can be also applied to data selection for stress modeling. The data-driven binning technique by Martínez-Garzón et al. (2016) is based on Voronoi tessellation, which subdivides the region of interest into irregularly shaped convex subregions. In either case data selection is deterministic, as a datum is included in the set or not.

In this paper we present a non-deterministic data selection approach introducing data weighting. The general concept of data weighting in STI has already been proposed by Armijo et al. (1982) by incorporating the uncertainties of the data and the model. Due to the unknown model uncertainties, the data and model uncertainties are represented by a single ratio. This ratio is treated as a free parameter resulting in a damped least squares solution.

The data weights we use are based on ACE (Angular Classification with Expectation-Maximization); a probabilistic FM cluster analysis (Specht et al., 2017). ACE determines the FM cluster parameters and the number of FM clusters. The algorithm identifies FM clusters for both nodal planes. Clusters can be associated with different stress tensors (e.g. at a plate interface). Data which cannot be associated with any cluster are unclassified. The probabilities of each nodal plane pair (i.e. FM) to belong to a particular stress tensor can be directly used as weights. Event classification is not directly dependent on the event's hypocentre because ACE is based on the FM angles alone. Therefore, ACE also provides a binning strategy for data selection independent of the spatial distribution - the most common approach of data selection in STI.

The down-weighted data from ACE are demonstrated to be outliers which have a higher influence on the inversion outcome. If data originate from a region with several stress tensors, ambiguities arise when assigning FM to

a specific stress tensor. This ambiguity is important and needs to be considered when selecting data to accommodate the data diversity and reduce inversion bias.

The application of data-driven data selection has become feasible with the steady increase of FM catalogues over the last decades. During the pioneering times of STI - when data were scarce - and data picking was out of the question, every available datum was used in the inversion. However, with catalogues covering tens of thousands of FM the data selection in general can be improved as well as STI.

We briefly review the STI routine of Michael (1984) and its spatial extension (Hardebeck & Michael, 2006) and how data weighting is incorporated into both models (section 2). The applicability of data weighting and its impact on synthetic FM catalogues is shown in section 3. In section 4 we present two applications of the weighted STI by applying to data from South America.

5.2 Methods

In this section we first briefly review the theoretical framework of inverse theory which is the basis for all STI routines. We focus on data leverage in a model and its impact on inversion results and on how to mitigate the effects of highly self-sensitive data with data weighting. In the second subsection we review the STI routines of (Michael, 1984) and (Hardebeck & Michael, 2006) and how they can be augmented with data weighting.

5.2.1 Basics

The common approach to inferring the stress field is to align the stress tensor such that the differences of the observed displacement (e.g. in the form FMs) to the modeled displacement are overall minimized. This formulation can be expressed in its simplest from by the objective function

$$S = \sum_{i=1}^{n} |d_i - s_i|^p \tag{5.1}$$

where s and d are the observed and modeled data, respectively. The exponent p defines the weighting norm. The inversion routines by Angelier (1979); Michael (1984) use $p = 2$ (least squares), while Gephart & Forsyth (1984) uses $p = 1$ (least absolute deviation). The data type in the objective function differs for all routines, and is for generality not further specified here. The larger the p, the larger the impact of a large residual (i.e. outlier) on the objective function S and thus the outcome of the final model.

If $p = 2$ in Eq. 5.1 then the objective function can also be represented in matrix notation as

$$S = (\mathbf{s} - \mathbf{d})^{\mathrm{T}}(\mathbf{s} - \mathbf{d}) \tag{5.2}$$

$$= (\mathbf{s} - \mathbf{A}\mathbf{t})^{\mathrm{T}}(\mathbf{s} - \mathbf{A}\mathbf{t}) \tag{5.3}$$

The matrix A is the design matrix containing the independent variables of the model and the functional form relating the model parameters t to the data s. Data in s are therefore dependent variables. While the independent variables are assumed to be free of errors, the dependent variables are considered erroneous, i.e. uncertain.

The objective function in Eq. 5.3 can be generalized by (Menke, 2012; Tarantola, 2005; Armijo et al., 1982)

$$S = (\mathbf{s} - \mathbf{A}\mathbf{t})^{\mathrm{T}}\mathbf{C}^{-1}(\mathbf{s} - \mathbf{A}\mathbf{t}) \tag{5.4}$$

where the matrix is the data covariance matrix representing data uncertainties. The general least squares solution for t is given by

$$\mathbf{t} = (\mathbf{A}^{\mathrm{T}}\mathbf{C}^{-1}\mathbf{A})^{-1}\mathbf{A}^{\mathrm{T}}\mathbf{C}^{-1}\mathbf{d} \tag{5.5}$$

This relation expresses the model parameters in terms of the data. In the cases of the stress inversion routines by Angelier (1979); Michael (1984) it holds that $\mathbf{C}^{-1} = \mathbf{I}$ (the identity matrix). This is the ordinary least squares solution (Eq. 5.3) and implies that all data are equally reliable (erroneous). The method by Angelier (1979) includes a second constraint in Eq. 5.4 (see Xu (2004) for expressing this in matrix notation), as does the inversion routine of Armijo et al. (1982). The L_1-norm used by Gephart & Forsyth (1984) can be expressed by reweighting the data in $\mathbf{C}^{-1}$ (Hill & Holland, 1977; Holland & Welsch, 1977; Street et al., 1988); the data themselves are treated as in the cases for Angelier (1979); Michael (1984), i.e. equally reliable. In most cases the true uncertainties of the data are neither known nor included.

Because the model parameters are derived from all data, it is reasonable to investigate how the observed data d influence the outcome of the modeled data s (Cook, 1977; Hoaglin & Welsch, 1978; Cardinali et al., 2004; Menke, 2012). A relation between d and s results by using Eq. 5.5:

$$\mathbf{s} = \mathbf{A}\mathbf{t} \tag{5.6}$$

$$= \mathbf{A}(\mathbf{A}^{\mathrm{T}}\mathbf{C}^{-1}\mathbf{A})^{-1}\mathbf{A}^{\mathrm{T}}\mathbf{C}^{-1}\mathbf{d} \tag{5.7}$$

$$= \mathbf{N}\mathbf{d} \tag{5.8}$$

The matrix N is known under different names (hat matrix (Hoaglin & Welsch, 1978), data resolution matrix (Menke, 2012), influence matrix (Cardinali et al., 2004)). The elements of the data resolution matrix provides factors to express modeled data as a linear combination of observed data

$$s_i = \sum_{j=1}^{n} N_{ij} d_j \tag{5.9}$$

The elements of the main diagonal of N are called importance (Menke, 2012), self-influence / self-sensitivity (Cardinali et al., 2004), or leverage (Hoaglin & Welsch, 1978). The leverage expresses how much each observed datum contributes to its own prediction.

We define a relative leverage based on Eq. 5.9 as the ratio between the ith leverage and the sum of values of the ith row in the data resolution matrix.

$$N_i^{rel} = \frac{n N_{ii}}{\sum_{j=1}^{n} N_{ij}} \tag{5.10}$$

The relative leverage represents by how much more a datum influences its own prediction compared to the average

absolute contribution of the data. If $N_i^{rel} = 1$ then the datum's contribution is on average, if $N_i^{rel} > 1$ the contribution is larger, and if $N_i^{rel} < 1$ the contribution is less than the average.

The leverage of the observed data d is not necessarily uniform for a given model A, i.e. the model itself imposes different weighting on the data in the independent variables. Consider a simple line fit with least squares:

$$y = ax + b \tag{5.11}$$

Figure 5.1 shows two line data sets (15 observations) and their respective least square solutions. Both data sets include one datum with identical error, but at different locations. The first data set has the error in the first (leftmost) datum (Fig. 5.1a; circles), the second in the eighth (central) datum (Fig. 5.1b; circles). Despite their high similarities both data sets yield different inversion results (Fig. 5.1a,b; solid lines) not only in the parameters but also in the deviation from the true model. The reason for this difference is seen in the leverage of the data with respect to the model (Fig. 5.1c). In case of the simple line fit, leverage is lowest at the mean of the independent variables, ($\bar{x}$), and increases with distance to it. In this example, the outermost data points have more than three times higher influence on the model parameters than the data at the centre.

One way to mitigate the effects of outlying data and/or the high-leverage data is to introduce data weighting by using $^{-1}$ as a weight matrix, denoted by W:

$$S = (\mathrm{d} - \mathrm{s})^{\mathrm{T}}\mathrm{W}(\mathrm{d} - \mathrm{s}) \tag{5.12}$$

and

$$\mathrm{W} = \begin{pmatrix} w_1 & 0 & \cdots & 0 \\ 0 & w_2 & \cdots & 0 \\ \vdots & \vdots & \ddots & \vdots \\ 0 & 0 & \cdots & w_n \end{pmatrix} \tag{5.13}$$

This definition is the weighted least squares (WLSQ) solution (Menke, 2012). A reduction of the impact of outliers in the dependent variable is achieved by least absolute deviation (LAD) which can be realized with iteratively reweighted least squares (Hill & Holland, 1977; Holland & Welsch, 1977; Street et al., 1988). Effects of leverage can be mitigated by taking the data distribution into account. For the straight line example from above one could define a weight function based on the difference $x_i - \bar{x}$, i.e. the distance of an independent variable to the mean of the independent variable, e.g.

$$w_i = e^{-\left(\frac{x_i - \bar{x}}{b}\right)^2} \tag{5.14}$$

where b is some user-based scaling factor. This function weights data close to $\bar{x}$ highest and less with increasing distance to $\bar{x}$.

The effect of such a weighting function on the straight line data is shown in the right column of Fig. 5.1. The inversion for the data with the outlier in the outermost datum (Fig. 5.1 d) deviates less from the original model than in the unweighted case (Fig. 5.1 a). For data with the outlier in the central datum the deviation is slightly increased (Fig. 5.1 a). However, both results of the weighted

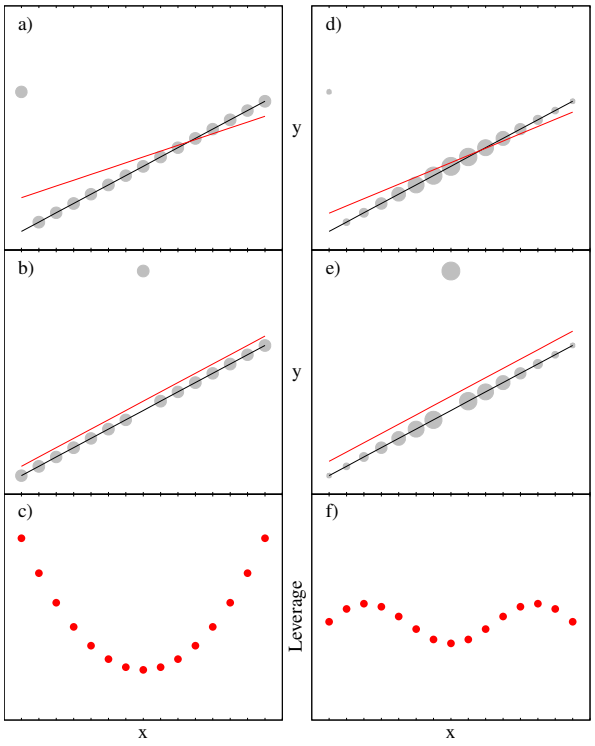

Figure 5.1: Comparison of ordinary LSQ (left column) to weighted LSQ (right column). In both cases the data originate from a straight line (black). In total 15 data points are sampled from this straight line (grey dots). In a) and d) an "error" is introduced in the first datum by shifting. In b) and e) the error is introduced in the eighth datum. The error is the same in all cases. The ordinary LSQ solution (red) in a) and b) differs not only from the truth (black) due to the introduced error but also both solutions differ from each other. This solution difference depends on the leverage of the data (c). In case of ordinary LSQ for the straight line problem leverage follows a parabola, thus the data at both ends influence the model more than data in the middle. Weighted LSQ can be used to redistribute leverage. In d) and e) the weights are represented by dot size and are the same in both cases. The straight line models in d) and e) differ less from each other than in the respective unweighted cases a) and b). While the model (red) in d) is closer to the truth (black) than in a), the model in e) deviates more from the truth than in b). Though the leverage of the weighted LSQ is more balanced (f) than for unweighted ordinary LSQ (c), i.e. each datum has a similar impact on the model in d) and e), the decreased leverage at the ends of the data (d) results in an increased leverage in the data in the middle (e). Weighted LSQ redistributes leverage and can therefore also be used to balance leverage.

inversions are more similar to each other than in the unweighted case, i.e. the leverage is more equally distributed due to the weighting. A weighting function redistributes leverage and can therefore be applied to balance the influence of data on the model parameters.

5.2.2 Stress Tensor Inversion (STI)

One of the most commonly used STI routines has been introduced by Michael (1984) which is a direct implementation of Eq. 5.5

$$\mathrm{s} = \mathrm{A}\mathrm{t} \tag{5.15}$$

where s represents the unit slip vectors, matrix A is based on the normal vectors n, and t is the deviatoric stress tensor in vector notation. This formulation implies that the slip magnitude is uniform in all directions as slip is represented by unit vectors and the relation to the 3×3 stress tensor $\boldsymbol{\sigma}$ is given by:

$$\mathrm{s} = \boldsymbol{\sigma}\mathrm{n} - (\boldsymbol{\sigma}\mathrm{n} \cdot \mathrm{n})\mathrm{n} \tag{5.16}$$

The difference of the deviatoric stress tensor to the stress tensor $\boldsymbol{\sigma}$ is the absence of an isotropic stress component (pressure p). The deviatoric stress tensor $\boldsymbol{\sigma}^{dev}$ is defined by

$$\boldsymbol{\sigma}^{dev} = \boldsymbol{\sigma} - p\mathrm{I} \tag{5.17}$$

where I is the identity matrix and pressure p is

$$p = \frac{\mathrm{tr}(\boldsymbol{\sigma})}{3} = \frac{\sigma_{11} + \sigma_{22} + \sigma_{33}}{3}, \tag{5.18}$$

thus follows $\boldsymbol{\sigma}^{dev}_{33} = \boldsymbol{\sigma}^{dev}_{11} + \boldsymbol{\sigma}^{dev}_{22}$, i.e. the deviatoric stress tensor has five independent components only. For convenience the stress tensor is expressed in Voigt notation

$$\mathrm{t} = \begin{pmatrix} t_1 \\ t_2 \\ t_3 \\ t_4 \\ t_5 \end{pmatrix} = \begin{pmatrix} \sigma^{dev}_{11} \\ \sigma^{dev}_{12} \\ \sigma^{dev}_{13} \\ \sigma^{dev}_{22} \\ \sigma^{dev}_{23} \end{pmatrix} = \begin{pmatrix} \sigma_{11} - p \\ \sigma_{12} - p \\ \sigma_{13} \\ \sigma_{22} \\ \sigma_{23} \end{pmatrix} \tag{5.19}$$

The eigenvectors of t represent the three principal stress orientations: S_1 for maximum, S_2 for intermediate, and S_3 for minimum principal stress.

The matrix A_i is based on the normal vector n_i (subscript i dropped in the following equation) and follows from Eq. 5.16

$$\mathrm{A} = \begin{pmatrix} n_1 - n_1^3 + n_1 n_3^2 & -n_2 n_1^2 + n_2 n_3^2 & -n_3 n_1^2 - n_3 + n_3^3 \\ n_2 - 2n_2 n_1^2 & n_1 - 2n_1 n_2^2 & -2n_1 n_2 n_3 \\ n_3 - 2n_3 n_1^2 & -2n_1 n_2 n_3 & n_1 - 2n_1 n_3^2 \\ -n_1 n_2^2 + n_1 n_3^2 & n_2 - n_2^3 + n_2 n_3^2 & -n_2^2 n_3 - n_3 + n_3^3 \\ -2n_1 n_2 n_3 & n_3 - 2n_3 n_2^2 & n_2 - 2n_2 n_3^3 \end{pmatrix}^T \tag{5.20}$$

The solution of t used by (Michael, 1984, 1987) is given by Eq. 5.5

$$\mathrm{t} = (\mathrm{A}^T\mathrm{A})^{-1}\mathrm{A}^T\mathrm{s} \tag{5.21}$$

and the weighted LSQ from Eq. 5.12 incorporates the weight matrix W and the solution for t is given by

$$\mathrm{t} = (\mathrm{A}^T\mathrm{W}\mathrm{A})^{-1}\mathrm{A}^T\mathrm{W}\mathrm{s} \tag{5.22}$$

For larger regions it is reasonable to invert for a set of tensors that are linearly dependent in space. Incorporating the weight matrix from Eq. 5.12 into Eq. 14 from Hardebeck & Michael (2006) results in weighted SATSI.

$$\mathrm{t}_a = (\mathrm{A}^T\mathrm{W}\mathrm{A} + \epsilon^2\mathrm{D}^T\mathrm{D})^{-1}\mathrm{A}^T\mathrm{W}\mathrm{s} \tag{5.23}$$

where D expresses the linear dependency of the neighboring stress tensors and ϵ is the dependency strength and t_a is the vector of all stress tensors.

$$\mathrm{t}_a = \begin{pmatrix} \mathrm{t}_1 \\ \mathrm{t}_2 \\ \vdots \\ \mathrm{t}_n \end{pmatrix} \tag{5.24}$$

The STI routine by Michael (1984) is more applicable to smaller regions where the stress tensor can be assumed to be constant. SATSI relaxes this constraint by assuming that the stress tensor is constant within a subregion only, therefore allowing STI to larger regions or tectonically more complex regions.

5.2.3 Confidence Intervals

Hardebeck & Hauksson (2001a) stated that the uncertainty estimates of stress tensor inversion are not always properly represented. In particular, Hardebeck & Hauksson (2001a) showed that with increasing data size, the inversion by Michael (1984) tends to underestimate uncertainties. Since we focus on improving the underlying inversion routine by Michael (1984), the uncertainty estimates are compared between the weighted and unweighted inversions. We estimate uncertainties for both unweighted and weighted inversions on the same synthetic data sets. The correct stress tensor is considered to be inside the x% confidence region if its rotation angle to the best-fit stress tensor is smaller than $(100 - x)$% of the bootstrapped stress tensor results. The rotation angle between two tensors is the Kagan angle, the smallest rotation angle between two three-axes systems (Kagan, 1991). Ideally, the amount of correct stress tensors within the x% confidence region should be approximately x%. If the confidence regions are too large or too small, the the amount of correct stress tensors will be above or below x%.

5.3 Data

This section examines the distribution of FMs and data with high leverage according to the model in Eq. 5.15. Based on synthetic data, we demonstrate the ambiguity of stress tensor identification for outlier data of a catalogue with FM caused by two different stress tensors. We then introduce data-driven weighting based on ACE to reduce the impact of these ambiguous outlier data in the STI.

The data in this study are both real world data and synthetic data. Real world data is provided by the global centroid moment tensor (GCMT) catalogue (Dziewonski et al., 1981; Ekström et al., 2012). The FM data are declustered (Zaliapin et al., 2008; Zaliapin & Ben-Zion, 2011) to investigate the background stress field and avoid effects of

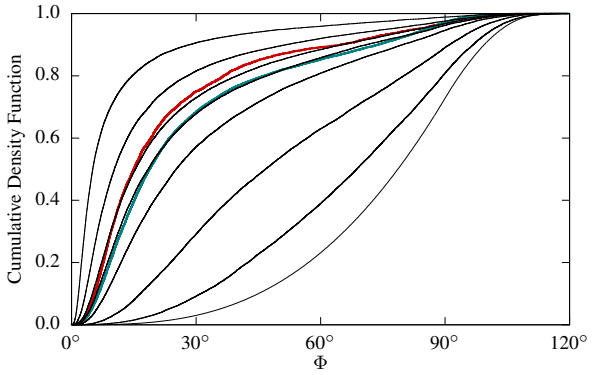

Figure 5.2: Cumulative DC rotational Cauchy distributions for different concentrations κ (grey lines - κ, from right to left: 1, 0.4, 0.2, 0.1, 0.07, 0.06, 0.04, 0.02). The Kagan angle Φ, the smallest rotation angle between two FM, follows this distribution. While rapidly increasing for small Φ, the distribution converges slowly to one for larger Φ - a typical behavior of right-skewed distributions. Data following this distribution therefore have a relatively large number of outliers. The colored curves represent empirical cumulative distribution functions (ECDF) of FM from GCMT for Chile (red, $\kappa = 0.06$) and the South American west coast (blue, $\kappa = 0.07$). The ECDF's are computed after Kagan (2013) for a reverse faulting events with maximum event distance of 50 km and a maximum event depth of 100 km.

local stress changes due to major earthquakes. Declustering is also necessary to allow compatibility to the synthetic data, since these are generated under the assumption of event independence and a single stress tensor.

5.3.1 Synthetic catalogue generation

The catalogue with synthetic data is compiled with several boundary conditions. The basis for the catalogue is a stress tensor with principal stresses $S_1 > S_2 > S_3$. Because we are interested in stress orientations only, neither magnitudes nor the stress ratio R are explicitly defined and used here. In addition, we assume a Mohr-Coulomb criterion with an angle of internal friction of $\phi_f = 30°$ (Fig. 5.3 a). The angle of internal friction is related to the coefficient of internal friction $\mu = \tan\phi_f$. According to Byerlee (1978) a common value in natural materials is $\mu \approx 0.6$ which corresponds approximately to $\phi_f = 30°$. In an unfractured homogeneous medium, this scenario can lead to two possible fractures which are symmetrically aligned around the principal stress axes with fracture angle α (Fig. 5.3 b). In case of the Mohr-Coulomb criterion for a newly formed fracture, the fracture angle α - as shown in Fig. 5.3 b - and the angle of internal friction are related by (e.g Zang & Stephansson, 2010)

$$\alpha = \frac{\pi}{2} - \frac{\phi_f}{2} \tag{5.25}$$

Both slip and normal vectors on the two conjugate fracture planes form the reference events for the generation of the synthetic catalog. The usage of two events (slip vectors) in conjunction with the Mohr-Coulomb criterion

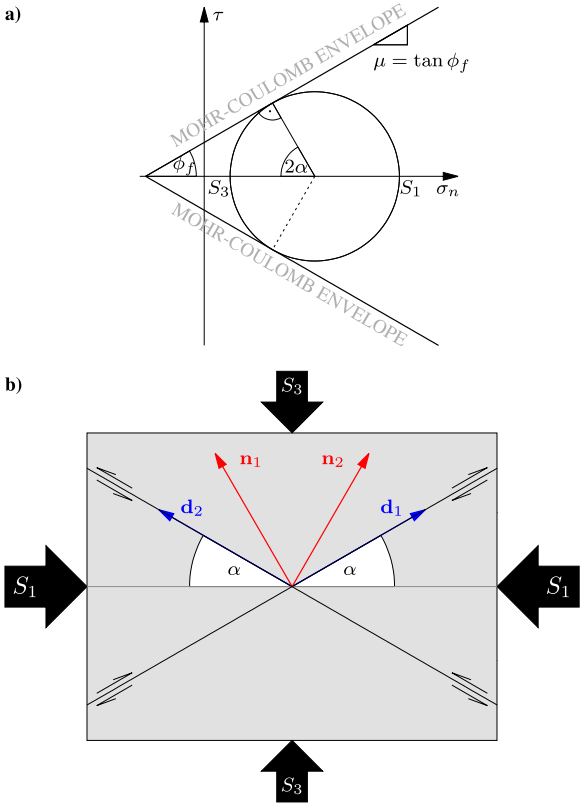

Figure 5.3: a) Mohr diagram for the Mohr-Coulomb failure criterion. The Mohr-Coulomb failure criterion is of form $\tau = C + \sigma_n \tan\phi_f$, where σ_n is the normal stress, τ the shear stress, C cohesion (offset at $\sigma_n = 0$), $\mu = \tan\phi_f$ the coefficient (angle) of internal friction. Furthermore, α is the fracture angle, S_1 the maximum and S_3 the minimum principal stress. For simplicity we do not show the intermediate principal stress S_2. Failure occurs where the Mohr circle reaches the failure envelope. The upper and lower envelopes relate to the conjugate fault planes as shown in b). b) Setting of the reference events for the generation of the synthetic catalog. The reference events originate as fractures in a homogenuous, unfractured medium. We consider a Mohr-Coulomb fracture criterion with a fracture angle $\phi_f = 30°$. As in a) S_1 is the maximum, S_3 the minimum principal stress. The intermediate principal stress S_2 is perpendicular to the S_1-S_3-plane. The fracture planes are described by the normal vector $\mathbf{n}_i$ and the slip with $\mathbf{d}_i$. Since both fractures are equally likely to occur as a result of the given stress conditions and friction angle, both are used as reference events equally. In addition, only with both conjugate fractures are the principal stress orientations of the stress tensor unambiguously represented by the slip orientations.

for newly formed fractures (represented by normal vectors) provides a one-to-one correspondence to the stress tensor, as a single event may not fully constrain the stress tensor (McKenzie, 1969). However, the magnitude of the slip is usually unknown and thus the full stress tensor cannot be inferred. Thus, given the definition of the STI of Michael (1984) in section 5.2.2 based on unit slip vectors, the two unit slip vectors - on faults related to each other by the Mohr-Coulomb fracture criterion - are sufficient to uniquely constrain the principal stress orientations of the deviatoric stress tensor t.

We assume the Wallace-Bott hypothesis for the slip orientation, i.e. the slip is parallel to the maximum resolved shear stress. For the reference events, this results in an orientation of the slip and normal vectors in the $S_1 - S_3$-plane. The null axis (the cross product of the slip and normal vector) is oriented parallel to S_2. No formal differentiation between the formation of a new fracture and the reactivation of a pre-existing fault is considered for the catalog, i.e. any event may represent either case.

To build the catalog, randomizations are applied to the two reference events. The randomization is introduced as rotation angles of the focal mechanisms. The rotation angle follows a DC (double couple) rotational Cauchy distribution (Kagan, 1992, 2013) and implies two assumptions:

> Variations in the rupture surfaces of earthquakes, as the surfaces may not be completely planar (Kagan & Knopoff, 1985; Kagan, 1990)
>
> The existence of random stresses due to unavoidable defects in the medium, preventing rupture surfaces from having the same orientation (Kagan, 1990).

The orientation of FM from a constant background stress tensor and the differences between FM pairs has been extensively studied and the DC rotational Cauchy distribution has been shown to adequately describe the distribution of FM orientations (Kagan, 1992, 2007, 2013). This distribution is characterized by a single parameter, the concentration κ, which determines the spread of the distribution. Examples of the DC rotational Cauchy distribution for different κ are shown in Fig. 5.2. The difference between two FM stated in NDB axes (i.e. axes parallel to fault normal vector, the slip vector and the null vector [orthogonal to the former two]) is expressed as the Kagan angle.

The randomization of the two reference events is applied in two steps. For each event in the synthetic catalog, we sample a Kagan angle from the DC rotational Cauchy distribution. In a second step, a rotation axis from a uniform distribution is sampled. The NDB-axes of the reference event are rotated around the rotation axis by the Kagan angle. For the first half of the catalog, we use the first reference event, for the second half, the second reference event.

The variability added by the DC rotational Cauchy distribution is only related to stress in a medium with random defects (Kagan, 1992). Effects of FM errors on stress inversions have been investigated by Hardebeck & Hauksson (2001a) and the distribution of FM errors in terms of the Kagan angle follows a von Mises-Fisher distribution (Kagan, 1992, 2000, 2013). The variability due to random defects considered in this study is much larger than the variability introduced by FM uncertainties (Kagan, 2000) and FM uncertainties are not further considered.

Kagan (1992) and the subsequent studies investigated the distribution of rotation angle between pairs of focal mechanisms without respect to a reference event. The Cauchy distribution and its derived distributions belong to the group of stable distributions (Kagan, 2000). A distribution is stable if a linear combination of independent random variables with that distribution results in the same distribution, only with a change of parameters. This property is also known infinite divisibilty. The scale (concentration) of the Cauchy distribution and its derivates is the linear combination of the individual scales (concentrations) of the individual Cauchy distributions. Since all samples in our catalogues are independently drawn from the same DC rotational Cauchy distribution, the distribution of all pairs follows again a DC rotational Cauchy distribution. The rotation angle between some event A and B can be seen as linear combination of the rotation between A and C, and a rotation between B and C. Event C is any other event, e.g. the reference event. It follows that for all pairs of focal mechanisms the DC rotational Cauchy distribution has its concentration doubled from the sampling distribution.

The introduction of a random component from the DC rotational Cauchy distribution results in a discrepancy to the Wallace-Bott hypothesis. However, Lisle (2013) investigated how strictly the Wallace-Bott hypothesis should be observed. Lisle (2013) remarked, that the resolved shear stress oriented $\approx 26^\circ$ off the orientation is at 90 % of the maximum resolved stress. This implies a range of 52° over which the shear stress varies only by 10 % and it has been pointed out that such variability should be considered in STI. The DC rotational Cauchy distribution is densest around its mean and has a relatively large positive skew if κ is sufficiently small, i.e. most applied rotations are only a few degrees. With only small rotations applied, the majority of the events in the synthetic catalogue still closely approximates the Wallace-Bott hypothesis.

5.3.2 Data Distribution

One common assumption for the STI is that all data are caused by the same stress tensor (Maury et al., 2013). When considering real-world data, several stress tensors might be present even on smaller scales. Figure 5.4a shows FM data from northern Chile and in comparison synthetic FM data are shown from a stress tensor corresponding to reverse and normal faulting, respectively. The distribution of random samples from the DC rotational Cauchy distribution is very similar to real-world data (e.g Kagan, 1992, 2013). In both cases data form dense clusters, but a significant number of outliers is also present.

Two different stress regimes prevail in Chile (and by extension most of South American west coast) (e.g. Pardo et al., 2002). At the plate boundary interface stresses result mostly in reverse faulting, while within the subducting slab stresses lead to normal faulting FM. The transition between the two regimes is continuous in space and addi-

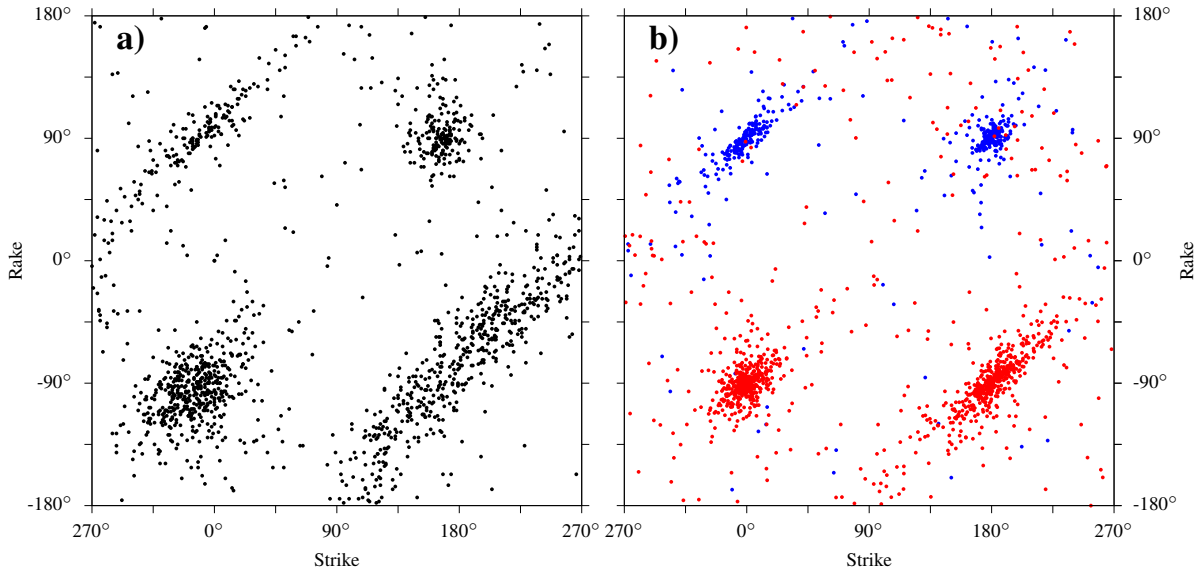

Figure 5.4: a) FM data from northern Chile in the strike-rake plane. The four notable clusters represent the two nodal planes for reverse faulting events (positive rakes) at the plate interface and normal faulting events (negative rakes) within the slab. b) Synthetic FM data sampled from two DC rotational Cauchy distributions with different stress tensors: reverse faulting (blue, $\kappa = 0.0625$) and normal faulting (red, ($\kappa = 0.125$). Although only based on the DC rotational Cauchy distribution and therefore only on stress orientations and no stress magnitudes, synthetic data yield a high similarity to the real data. The synthetic data show that each tensor can cause FM with virtually all strikes and rakes. Data following the heavy tailed DC rotational Cauchy distribution have a non-negligible number of severe outliers. Though the synthetic catalog is based on two reference events, only FM associated with the eastward dipping fault plane are shown.

tionally not well constrained due to FM hypocentre uncertainties.

When sampling from the DC rotational Cauchy distribution from two different stress tensors, we know which random datum originates from which stress tensor. This knowledge is unavailable for real world data and thus the synthetic data allows insight into its composition (Fig. 5.4b). While the dense clusters are dominated by FM of one stress tensor, the outlying data are composed of FMs of both stress tensors. This stress tensor overlap in the outlying regions limits the demand for FM diversity in STI, as a clear stress tensor assignment for real data is not feasible.

This limitation is even present if FM of one of the two stress tensors are less frequent. The synthetic catalogue, which is the basis for Fig. 5.6, contains 80 % reverse and 20 % normal faulting events. Still, regions off the cluster centres (shown by dots for either nodal plane and tensor type) are equally likely to contain FM from either tensor. Therefore, a clear distinction of tensors for those FM can neither be achieved from location alone nor from the FM in every case. The compiled FM catalogue for the STI will be most likely polluted by data of different stress tensors - especially in the outliers. If the presence of a single stress tensor is not given, it is necessary to downweight those FM that cannot be assigned to a particular stress tensor. This inadvertently reduces the data size of the outliers and thus the data variability, which has been shown to reduce the bias of STI (Hardebeck & Hauksson, 2001b). However, if the outliers originate from another stress tensor, increased data variability may not result in a decreased bias.

5.3.3 Data Leverage

As introduced in section 5.2.1, the leverage states how much an observed datum contributes to its own prediction. An example of the leverage of the inversion routine by Michael (1984) is shown in Fig. 5.5 for a synthetic data set of FM from a stress tensor with S_1 horizontally oriented and S_3 vertically, resulting predominantly in reverse faulting. The calculation of the leverage is similar to the STI routine as bootstrapping is applied to randomly select one nodal plane as the auxiliary plane. The final leverage is the average of all leverage calculations of the resampled data.

The distribution of the leverage follows approximately inversely the data density (Fig. 5.5). The less data are realized for a certain FM type, the higher the leverage, i.e. leverage increases with distance to the average FM. Thus, outliers are usually also high-leverage data.

In the previous section, we have shown that outliers cannot be assigned to a specific tensor in every case. However, the STI will give by design those ambiguous data a higher weighting due to their higher leverage. This contradicts the basic assumption that less reliable data should be down-weighted instead of up-weighted. Even if all data arose under a single stress tensor, an outlying datum will have a larger impact on the outcome then a datum that is close to the average.

5.3.4 Data Weighting

In section 5.2.2 the weight matrix W has been introduced into STI (Eq. 5.22). The weights we use are derived by ACE

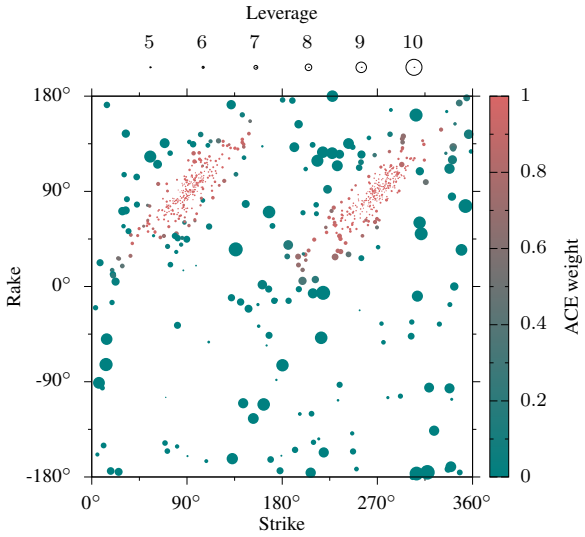

Figure 5.5: Leverage in the STI after Michael (1984) for a synthetic data set of FM drawn from DC rotational Cauchy distribution of a stress tensor associated with reverse faulting. While leverage is smallest in the two clusters for either nodal plane, leverage increases with distance to the clusters. The ACE based weights of this data set are indicated by color. The high-leverage data are all down-weighted to an extent that their impact is negligible in the STI.

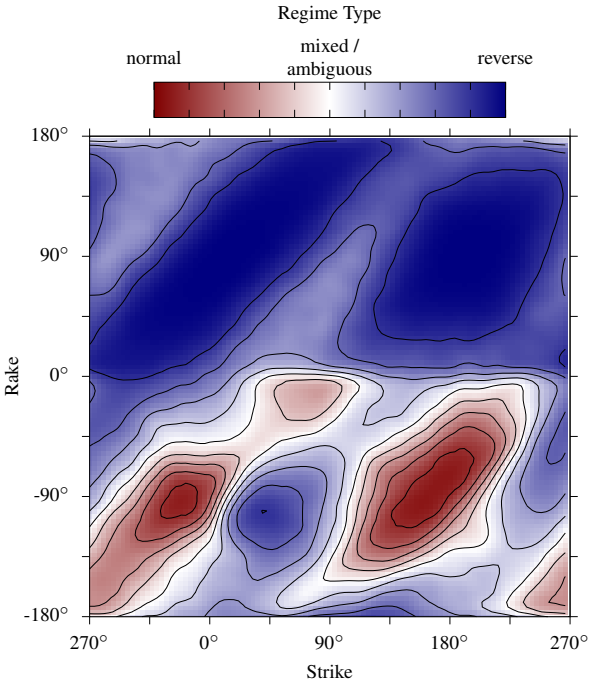

Figure 5.6: Relative Stress tensor prevalence in synthetic FM data similar to shallow seismicity of the upper 50 km in the Chile data with 80 % reverse and 20 % normal faulting with clusters similar to those from Fig. 5.4. Though normal faulting events are less common, in the regions off the cluster centres (pure blue and red regions), data of the extensional stress tensor may occur as reverse faulting events to such an extent that stress tensor assignment becomes ambiguous even for reverse faulting (less color saturated parts).

(Specht et al., 2017). In the previous section we demonstrated that the inversion tends to be more sensitive to outlying data which can be ambiguous in terms of stress tensor assignment which is crucial for data selection for STI.

The algorithm for Angular Classification with Expectation-Maximization (ACE) requires the same input as STI: FM data. Expectation-maximization (Dempster et al., 1977) is a widely used soft (fuzzy) clustering routine. Each FM is represented by two sets of angles (strike, rake, dip), each for one nodal plane. These angles are used to estimate probability distributions which describe the clusters of nodal planes. The functions are also called component distributions and the full set of the distributions form the mixture distribution. A cluster of nodal planes may be represented by a single component or several, depending on the shape complexity of the cluster. Each FM has a certain probability to belong to each distribution and thus to each cluster.

The values of the distributions are directly used as weights in the weight matrix of Eq. 5.22 and 5.23 (Specht et al., 2017). The clusters identified by ACE and described by the distributions can be associated with a stress tensor (e.g. at a plate interface). FM data not associated with any cluster remain unclassified. Unclassified data can be associated with data of increased leverage in the inversion (Fig. 5.5). If more than one stress tensor is present, the unclassified data fall into regions where stress tensor assignment is mixed/ambiguous (Fig. 5.6). It is only in the presence of several stress tensors necessary that the weights provided by ACE are used. If ACE identifies only FM clusters associated with e.g. reverse faulting at an interface, then the data weighting is not necessary as no ambiguities arise. Accordingly, ACE can also be used to determine, whether data weighting for STI is required.

5.3.5 Synthetic Data Test

We test the performance of both the unweighted and weighted STI routine on synthetic catalogues with known parameters. The synthetics are based on the DC rotational Cauchy distribution.

The synthetic catalogue is a sample of events drawn from a DC rotational Cauchy distribution with $\kappa = 0.06$ and the reference events are a pure reverse faulting events. The reference nodal planes have rakes of 90 degrees, the strikes are 90 and 270 degrees, and dips are 30 and 60 degrees. Most of the random events drawn from the DC rotational Cauchy distribution are distributed closely around the reference events. To estimate the differences between the unweighted and weighted STI results, we generated 10,000 synthetic catalogues each with 800 events. An example of such a catalogue is shown in Figure 5.4b. For each catalogue both types of STI were performed - unweighted and weighted - with weights determined by ACE for each catalogue.

The distribution of rotation angles of inverted stress orientations with respect to the stress orientation of the reference event indicate a reduction of 40 % in uncertain-

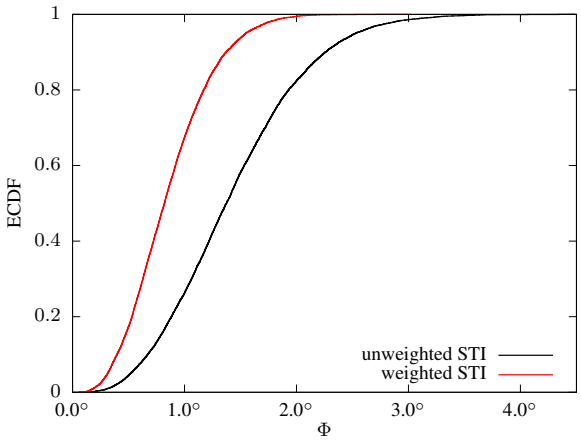

Figure 5.7: Empirical cumulative distribution function of the rotation angle between the stress axes of the inversion and the reference values of the synthetic catalogues. In total 20,000 synthetic FM catalogues were sampled from the DC rotational Cauchy distribution and inverted for the stress orientations with and without weights. The distributions show, that the rotation angles of the unweighted STI (black) are on average 40 % larger than for the weighted STI (red). Though 15 % of the data are down-weighted such that they are effectively removed from the data set, the weighted STI results in 40 % reduced error in comparison to the unweighted STI.

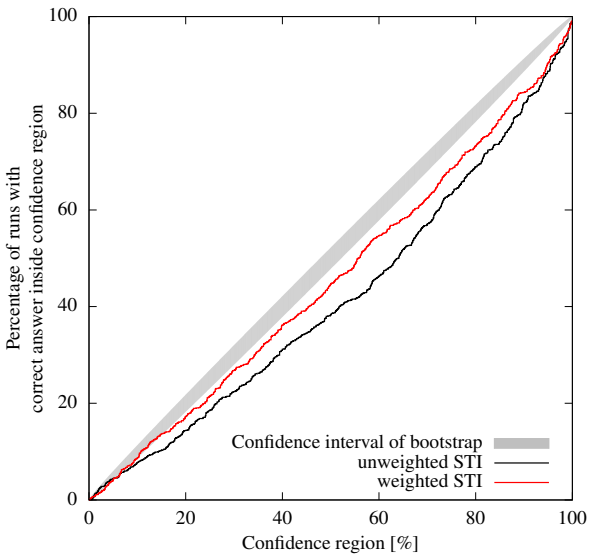

Figure 5.8: Confidence region appropriateness for both weighted and unweighted STI after Hardebeck & Hauksson (2001a). The amount of correct stress tensors within the x% confidence region is plotted as a function of x. If the confidence regions are appropriate, the amount of correct stress tensors falls in the grey area. Results from an experiment with perfect confidence regions would have a 95% probability of falling within the grey zone, which is the 95% confidence interval of the binomial probability distribution for 2000 trials with an x% probability of success each trial. As reported by Hardebeck & Hauksson (2001a), the uncertainties of STI after Michael (1984) for larger data sets are underestimated. However, the unweighted STI (black) underestimates uncertainties more than the weighted STI (red). This implies that the relative uncertainty reduction between both STI's of 40 % shown in Fig. 5.7 is larger, i.e. the weighting improves results by more than 40 %.

ties, while only 15 % of FM data has been down-weighted to an extent that the data are effectively removed from the data set. The removed/down-weighted data show comparatively large residuals, while data in the bulk remain unchanged. The data leverage shows that the removed data have an above average influence on the model result. Due to the removal of these high-leverage outlying data, the obtained stress tensor orientations are more robust, i.e. orientations are not affected but uncertainties are reduced.

The appropriateness of the uncertainty estimates for both weighted and unweighted STI are shown in Fig. 5.8. As found by Hardebeck & Hauksson (2001a), the uncertainty estimates of STI after Michael (1984) are too small for both weighted and unweighted routines. However, the weighted STI underestimates uncertainties to a lesser degree than the unweighted STI. The aforementioned relative uncertainty reduction of 40 % is therefore larger for when accounting for the different degrees of underestimation.

5.4 Examples

In this section, we present two case studies from South America. The first example is from northern Chile where in 2014 the Iquique earthquake occurred, and the second example covers the entire west coast of South America. The FM data are from the GCMT catalogue (Dziewonski et al., 1981; Ekström et al., 2012) from 1976 - 2017. FM clusters are identified with ACE and the probabilities of each event are used as weights in the weighted STI. We invert for stress tensor orientations with and without weights. For the STI and the derivation of the weights we use declustered catalogues (Zaliapin et al., 2008). Uncertainties are estimated by bootstrapping the data 10,000 times and, following Michael (1987), by randomly selecting nodal planes as rupture and auxiliary planes, respectively.

5.4.1 Northern Chile

Seismicity in northern Chile is dominated by plate interface and intraslab earthquakes. In the region considered here (26°S - 17°S, 75°W - 65°W) plate interface activity is mostly confined to the upper 50 km close to the coast, while most intraslab activity is below that depth. Crustal activity to the east of the coast is associated with orogenic processes. The catalogue contains 736 events after declustering.

In the unweighted estimation of the stress tensor at the plate interface, we only included events shallower than 50 km of the entire region (174 events). Results (Figure 5.10a) indicate that S_1-direction is westward, parallel to the movement orientation of the Nazca plate with respect to the South American plate (Bird, 2003), and dipping with

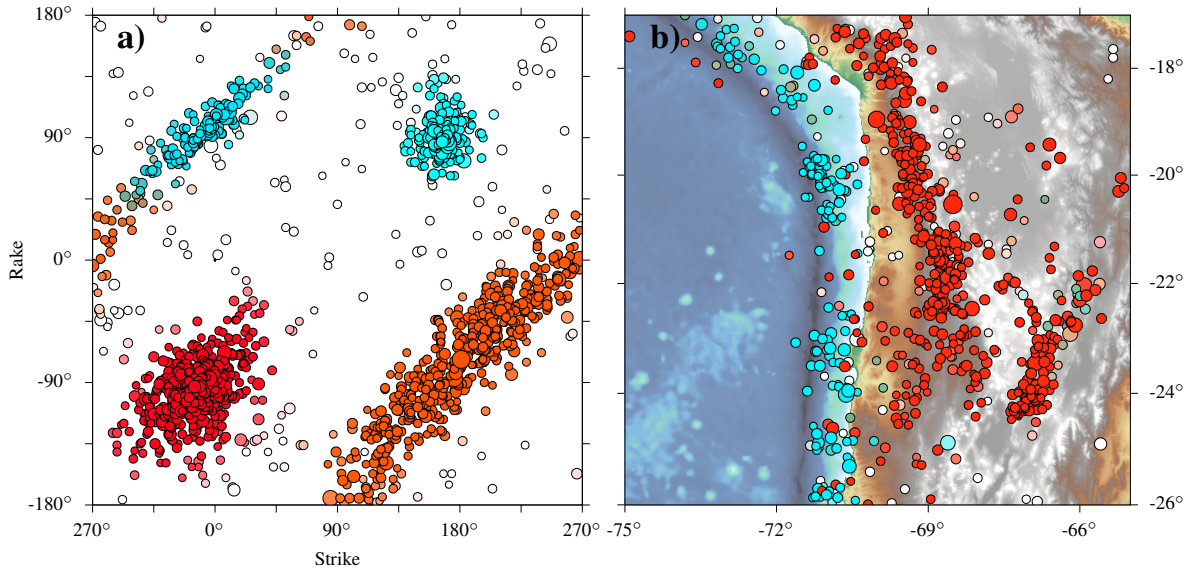

Figure 5.9: a) Strike-rake plot of GCMT FMs (both nodal planes) from northern Chile between 1976-2017 (26°S - 17°S, 75°W - 65°W). Clusters were identified with ACE with color saturation according to the probability of belonging to that cluster (cyan - plate interface,reverse faulting; red - intraslab, normal faulting; white - unclassified). The probabilities of the plate interface clusters correspond to the weights used in the weighted STI. The strike axis of the plot has been shifted by 90° to show all clusters continuously. b) Map of epicentres of GCMT FMs in a). Color scheme is identical to a). Since one FM consists of two nodal planes, the color for the epicentre is based on the average weight of both nodal planes. Most reverse events (cyan) are close to the trench and are associated with the plate interface, while normal faulting events (red) are further to the east and are associated with the subducted slab.

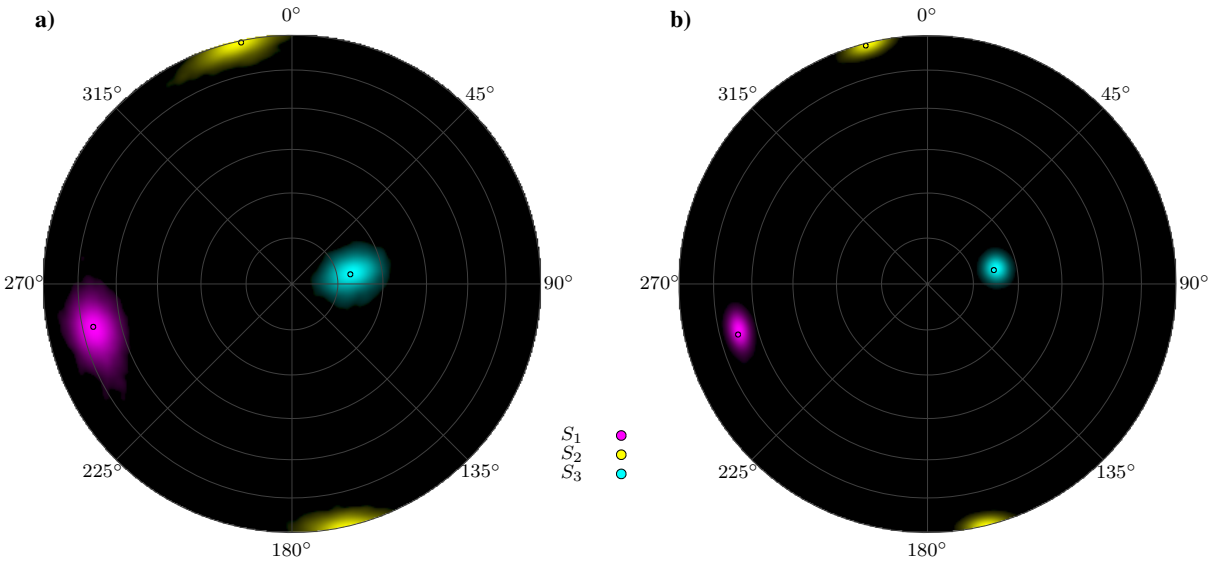

Figure 5.10: STI for northern Chile (a - unweighted, b - weighted). Principal stress axes are shown by small circles, uncertainty distributions by colored areas. Though only 15 % of the data are effectively removed (with near zero weights), uncertainties decrease by a larger margin.

Table 5.1: Principal Stress orientations for northern Chile of the conventional and weighted STI. Orientations are given as trend (tr.) and plunge (pl.), and uncertainties (one standard deviation) in italics below.

	Conventional		weighted STI	
	tr.	pl.	tr.	pl.
S_1	256.7	19.8	256.1	23.1
	4.0	*3.6*	*1.9*	*1.2*
S_2	347.1	1.1	346.3	0.4
	3.6	*2.6*	*1.6*	*1.5*
S_3	80.4	70.0	77.1	66.9
	7.2	*3.6*	*3.3*	*1.2*

appr. 20°. Uncertainties are represented in a Kernel density estimate with a von Mises-Fisher kernel.

For the weighted STI we apply ACE for the declustered GCMT catalogue of northern Chile with 736 events without any additional a priori information about the FM. Four clusters are identified (Fig. 5.9): Two of each (for either nodal plane) are associated with normal (intraslab) and reverse faulting (plate interface), respectively. The unclassified events are mostly near the surface and are associated with thrusting in the Andes. The weights are based on the probabilities of the two clusters associated with plate interface activity. The sum of the weights expressed as fractions is 19.4 % for plate interface, 65.4 % for intraslab and 15.2 % for unclassified. With respect to the total number of FM (736), 19.4 % is equivalent to 143 events which is comparable to the 174 events considered in the unweighted STI.

The three principal stress orientations differ only by a rotation angle of 3.9° between the unweighted and weighted STI. Differences are more prominent in the plunge than in the trend. In all cases uncertainties of the weighted STI estimates are reduced significantly (Table 5.1).

5.4.2 Nazca Plate

The second example covers the portion of the South American west coast between 40°S - 5°S. The longitudinal extent includes all major seismicity in the latitude range (85°W - 65°W, Fig. 5.11b). The catalogue of northern Chile in the first example is a subset of this data set, thus similar results for normal and reverse faulting are expected.

STI in this example is based on SATSI (Eq. 5.23) and focuses on plate interface activity with a maximum depth of 50 km. The region is subdivided between -85° and -60° longitude into seven stripes of 5° width between latitudes -40° and -5° (Fig. 5.12) SATSI is performed without weighting and with ACE based weights. The dependency in Eq. 5.23 is set in both cases to $\epsilon = 0.2$.

The catalogue for this region contains 1941 events and the set-up for ACE is as in the previous example. Four clusters similar to those found for northern Chile are identified: two for reverse and normal faulting, respectively (Fig. 5.11). Remaining data are unclassified. The clusters for normal and reverse faulting are similar in shape and location to the clusters from northern Chile. This similarity suggests that plate interface rupture processes are similar along the west coast of South America. The number of events per event type differs from northern Chile, as the sum of weights indicates 28.9 % as plate interface, 38 % as intraslab, and 33.1 % as unclassified. As in the case for northern Chile, only data with a depth of less than 50 km are used in unweighted STI (827 events). With 28.9 % of 1941 events weighted as plate interface results in 560 events for the weighted STI.

In Fig. 5.12, inversion results are shown for each for the unweighted (left column) and weighted inversions (right column). Principal stress orientations are similar to each other, with S_1 oriented westward, S_2 oriented northward (southward), and S_3 oriented downward and slightly eastward. S_2 orientations of the unweighted inversion are more tilted than orientations derived from the weighted inversion. All S_2 orientations are from the unweighted approach are northward, while in the weighted case the orientation flips between north and south, indicating that S_2 orientations are nearly horizontal (Fig. 5.12, right column).

Principal stress orientations with their uncertainties for both SATSI inversions are shown in Fig. 5.13 (a - unweighted, b - weighted). Individual solutions are shown by different shades of hue, with S_1 in red/purple, S_2 in orange/green, and S_3 in green/blue. The differences of principal stress orientations for all regions of the weighted and unweighted STI range between 4.7° and 10.8°. Trends and plunges and their respective uncertainties for all seven regions are summarized in Table 5.2. In case of the weighted inversion (Fig. 5.13b), uncertainties for each stress tensor are larger than the variance of the principal stress orientations for all regions, i.e. the results for each region are consistent with each other. In the unweighted STI, principal stress orientations of all regions are more scattered than in the weighted case. This difference of scattering is best illustrated in the orientations of S_3: While all bins in the weighted estimate have near identical S_3-orientations (Fig. 5.13b, blue/green region in the centre), S_3-orientations of the unweighted estimates are diverse to a level that they are mostly separate even with their uncertainties (Table 5.2). The orientation of S_1 of the unweighted inversion follows a horseshoe pattern (Fig. 5.13a, left) while in the weighted STI orientations are at a constant plunge. This horseshoe pattern is most likely caused by outlying data, as these are not identically distributed for each region due to the high variability in the occurrence of such more rare events. The rarity of these events is compensated in the STI by the increased leverage.

5.5 Discussion & Conclusion

The compilation of a FM catalogue for STI that strictly follows the assumptions of the stress inversion routine cannot be achieved by spatial and deterministic selection alone. We demonstrated that STI can be improved by applying data weighting based on ACE. Since the weights are not fully dependent of the event's hypocentre, they add an additional constraint to the otherwise purely spatially constrained extent of the data for the final catalogue. Furthermore, the weights are derived in a data-driven way, thus reducing effects from expert elicitation in the case of selecting spatial bins. Due

Table 5.2: Principal stress orientations for the seven regions of western South America as in Fig. 5.12 of the unweighted and weighted STI. Orientations are given as trend (tr.) and plunge (pl.) and uncertainties (one standard deviation) in italics below.

	unweighted STI						weighted STI					
	S_1		S_2		S_3		S_1		S_2		S_3	
	tr.	pl.	tr.	pl.	tr.	pl.	tr.	pl.	tr.	pl.	tr.	pl.
1	260.3 *1.8*	11.4 *2.0*	351.7 *1.8*	6.9 *2.6*	112.1 *10.6*	76.4 *2.2*	259.8 *1.0*	19.7 *0.6*	350.2 *0.9*	1.0 *0.7*	83.1 *1.8*	70.3 *0.6*
2	261.4 *1.6*	10.2 *1.8*	352.6 *1.7*	6.5 *2.4*	114.4 *10.6*	77.7 *2.0*	260.9 *1.0*	19.8 *0.6*	351.1 *0.9*	0.5 *0.7*	82.5 *1.8*	70.2 *0.6*
3	257.5 *1.8*	15.1 *2.0*	350.2 *1.9*	9.8 *3.0*	111.6 *8.5*	71.7 *2.4*	259.0 *1.2*	19.6 *0.6*	349.6 *1.0*	1.6 *0.8*	84.0 *2.1*	70.3 *0.6*
4	263.2 *1.3*	12.2 *1.6*	353.6 *1.3*	1.7 *1.6*	91.6 *7.5*	77.6 *1.6*	263.5 *1.0*	19.8 *0.6*	173.0 *0.9*	1.2 *0.6*	79.9 *1.7*	70.1 *0.6*
5	263.0 *1.6*	16.1 *2.0*	354.3 *1.7*	4.3 *2.5*	98.8 *8.5*	73.1 *2.1*	263.5 *1.1*	19.7 *0.6*	173.2 *1.0*	0.7 *0.7*	81.4 *2.0*	70.2 *0.6*
6	262.9 *1.2*	15.6 *1.7*	353.3 *1.2*	1.5 *1.8*	88.4 *6.6*	74.2 *1.8*	266.1 *0.9*	19.7 *0.6*	175.6 *0.8*	1.6 *0.6*	81.0 *1.5*	70.2 *0.6*
7	262.7 *1.4*	20.1 *2.2*	354.4 *1.5*	4.4 *2.4*	96.0 *6.6*	69.2 *2.3*	266.4 *0.9*	19.8 *0.5*	176.0 *0.8*	1.3 *0.6*	82.4 *1.6*	70.1 *0.5*

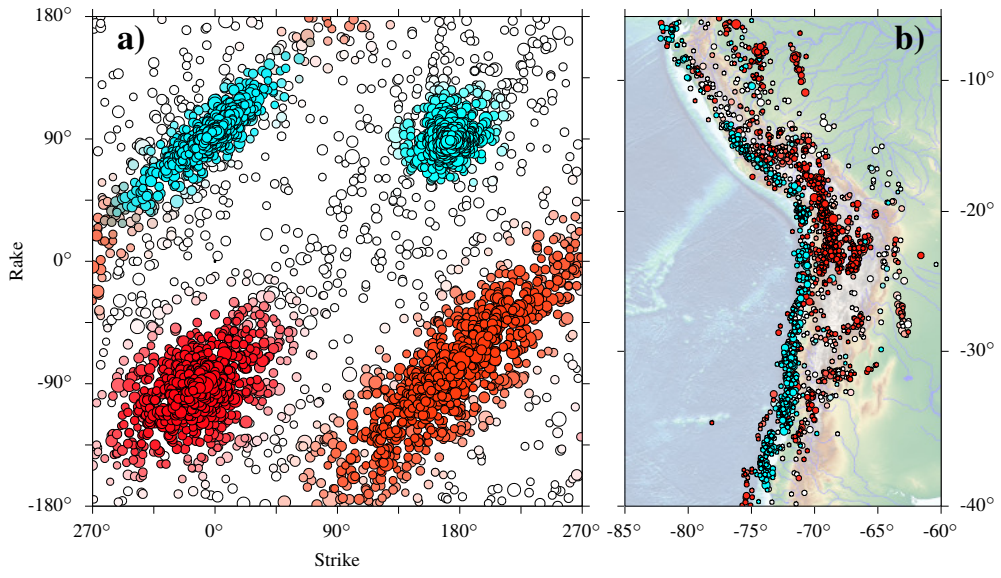

Figure 5.11: Same as Fig. 5.9, but for FM data from the South American coast between 1976-2017 (40°S-5°S, 80°W-60°W). Even though the region (b) has a much larger extent then northern Chile example, the identified clusters are similar to those of northern Chile.

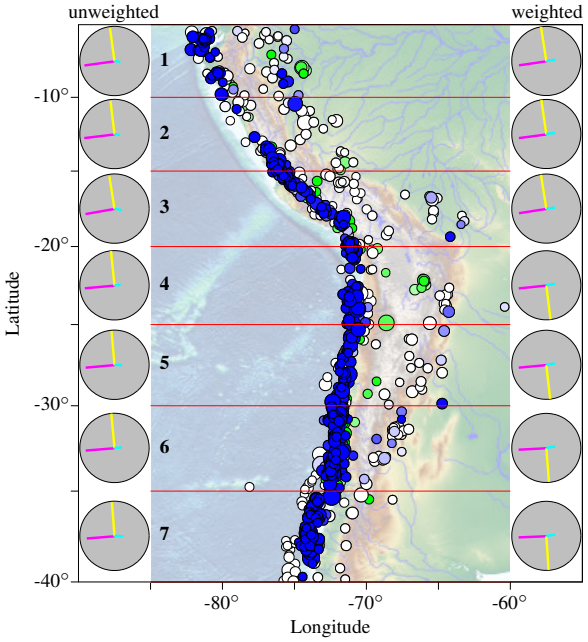

Figure 5.12: Subdivision of western South America for SATSI in regions 1-7 (red lines). Events in the map are used in both STI: All events shown have either an ACE weight $\geq$0.5 or have a depth of $\leq$50 km. Colour saturation corresponds to ACE weights for plate interface events (colour saturation is equivalent to the average saturation of the two plate interface / reverse faulting cluster in Fig. 5.11). Events in blue and white have a depth of $\leq$50 km and are used in the unweighted STI; events in blue and green are used in the weighted STI. Green events have an ACE weight of $\geq$0.5 and a depth of $>$50 km. In the weighted inversion all events are included, but events with weights below 0.5 are not shown in the figure. Principal stress orientations for each region are shown on either side of the map for unweighted (left) and weighted (right) STI. The S_2 orientations (yellow) fluctuate between north and south and the right column which is due to the usage of the lower hemispheric projection; all S_2 orientations are almost identical with near horizontal plunge and a north-south trend. Principal stress orientations are given in Table 5.2.

to the complexity of the FM distribution in the Earth, it is necessary to identify and remove / down-weight outliers if FM data originates from several stress tensors. The weighting not only improves the stress tensor solutions but also reduces uncertainties.

Outliers increase inadvertently data diversity, which has been shown by (Hardebeck & Hauksson, 2001b) is required for less biased stress tensor estimates. Outliers can originate either from different stress tensors or are extreme cases of the dominant stress tensor. However, the former case needs to be avoided from a physical point of view, the latter because these extreme value data influence the outcome of the inversion more than the close-to average data. The fewer data are used in an inversion, the larger the range of leverage. Under the assumption that angles between FM follow a DC rotational Cauchy distribution, FM outliers can occur at higher frequencies than expected from a normal distribution. A clear separation of both cases is not possible when two different stress tensors are in proximity to each other. Therefore, the reasons for the differences of stress orientations from weighted and unweighted STI in the examples cannot not be resolved as well.

Data selection in unweighted STI is highly dependent on the hypocentre location. However, the hypocentres are not always a good proxy whether events belong to a single stress tensor or not. Data weighting based on the distribution of the FM angles, as given by ACE, allows data selection independent of the hypocentres. The data selection is not only subject to the hypocentres but also to the properties of the focal mechanisms. Thus, STI is less sensitive to the spatial binning.

A major advantage of data weights is their implementation into any of the existing methods, as has been exemplified by the seamless incorporation of weights into the STI routine of Michael (1984) and Hardebeck & Michael (2006). The underlying routines remain unchanged and results have been shown to be consistent. However, uncertainties are considerably reduced by discarding only a small portion of the data set. ACE can also be used to determine whether data weighting is necessary, depending on the identified clusters. If the identified clusters are associated with multiple stress tensors (e.g. at a plate interface or in a subducting slab), then weighting is recommended. Furthermore, other types of data weighting can be added by expanding the weight matrix, e.g. by incorporating data uncertainties as in Armijo et al. (1982).

Data weighting can also be incorporated into more advanced methodologies for STI (e.g. Martínez-Garzón et al., 2016). As such, data-driven methods not only allow a refined analysis of the stress field but also open up other fields in stress field research, e.g. stress transients. Here, the reduction of uncertainties of stress tensor estimates is a necessary prerequisite for investigation of the spatio-temporal variability of the stress field.

Acknowledgments

FM data are accessible at `http://www.globalcmt.org/` (GCMT). Stress tensors according to Eq. 5.22

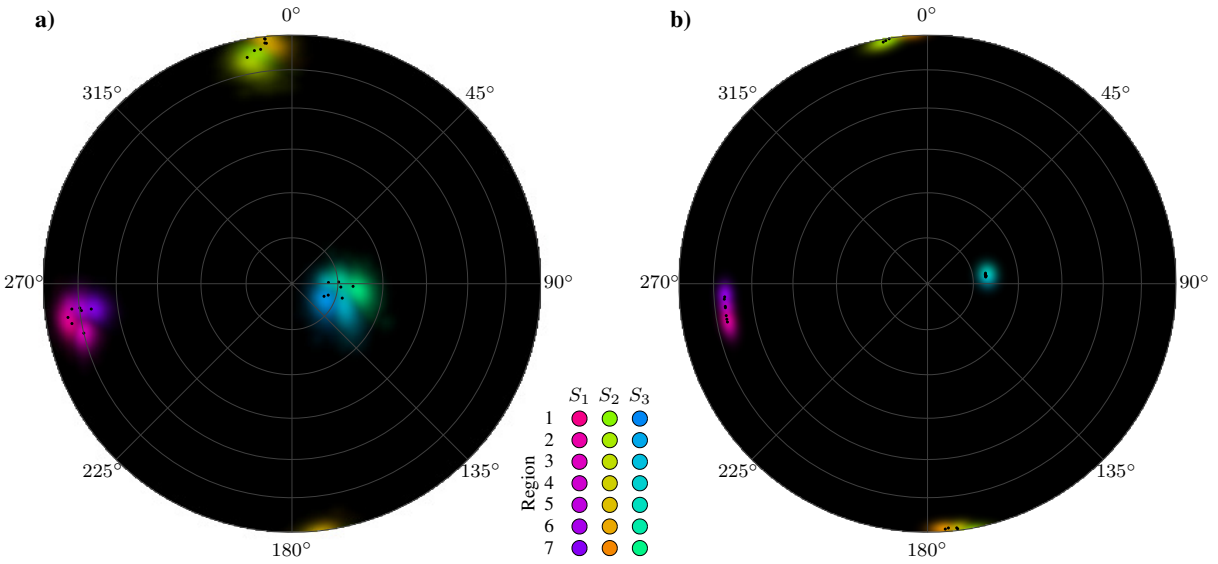

Figure 5.13: Principal stress orientations with SATSI (a - unweighted, b - weighted) for the South American coast (Fig. 5.12). Principal stress orientations are all over similar to those of Northern Chile (Fig. 5.10). The results of the unweighted STI not only show larger uncertainties per region (densities with same hue) to the weighted STI, but also between regions principal stress orientations are more diverse than those obtained from the weighted STI.

and 5.23 were computed with the armadillo library for C++ (`http://arma.sourceforge.net/`) (Sanderson & Curtin, 2016). Maps are generated with GMT (Wessel et al., 2013), and topographic data is based on ETOPO1 (Amante & Eakins, 2009). Sebastian von Specht acknowledges support from the DFG research training group "Natural Hazards and Risks in a Changing World" (Grant No. GRK 2043/1). We also like to thank Anne Strader and an anonymous reviewer for improving the manuscript.

Chapter 6

ICBM—Integrated Combined Baseline Modification: An algorithm for segmented baseline estimation

Abstract

Accelerograms are the primary source for characterizing strong ground motion. It is therefore of paramount interest to have high quality recordings free from any non-physical contamination. Frequently, accelerograms are affected by baseline jumps and drifts, either related to the instrument and/or a major earthquake. In this work, I propose a correction method for these undesired baseline drifts based on segmented linear least squares. The algorithm operates on the integrated waveforms and combines all three instrument components to estimate a model which modifies the baseline to be at zero continuously. The procedure consists of two steps: first a suite of models with variable numbers of discontinuities is derived for all three instrument-components. During this process, the number of discontinuities is reduced in a parsimoneous way, e.g. two very close discontinuities are merged into a single one. In the second step, the optimal model is selected on the basis of the Bayesian Information Criterion. I exemplify the application on synthetic waveforms with known discontinuities and on observed waveforms from a unified strong-motion database of the Japan Meteorological Agency (JMA) and the National Research Institute for Earth Science and Disaster Prevention (NIED, Japan) networks for the major events of the 2016 Kumamoto earthquakes. After the baseline jump correction, the waveforms are furthermore corrected for displacement according to Wang et al. (2011). The resulting displacements are comparable to the Interferometric Synthetic Aperture Radar-derived displacement estimates for the Kumamoto earthquake sequence[a].

[a] published as: von Specht, Sebastian, 2019, ICBM—Integrated Combined Baseline Modification: An algorithm for segmented baseline estimation, *Seismological Research Letters*, Early edition, doi: 10.1785/0220190134.

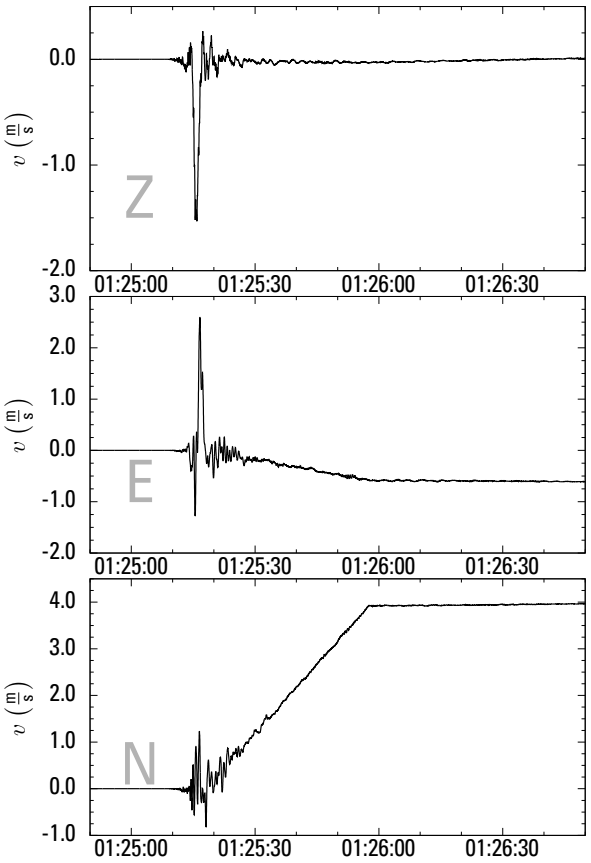

Figure 6.1: Result of acceleration baseline jumps in the integrated trace (velocity) at station 93048 (three component sensor from the Japanese municipal network). The waveform shown is from the Kumamoto 2016 earthquake. All segment shifts occur simultaneoulsy on the traces. While the first jump is probably related to the event itself, the second discontinuity after 60 s is most likely instrument related. Any further processing of this waveform will introduce a bias if left uncorrected.

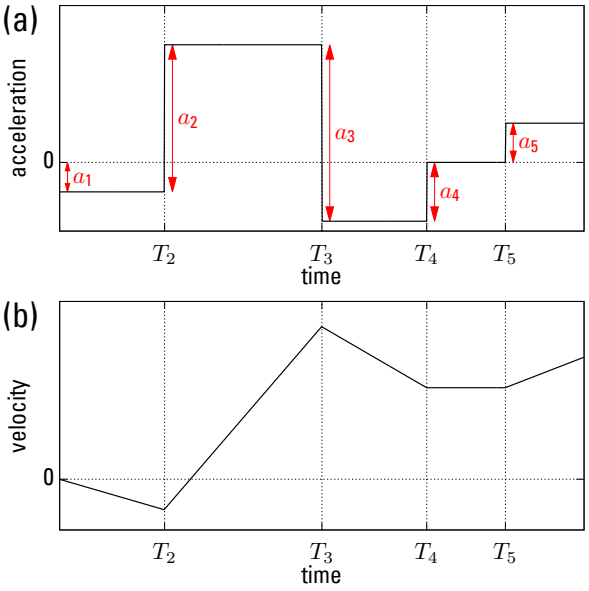

Figure 6.2: (a) Concept of several baseline jumps. Note that jump amplitudes are measured with respect to each other and not absolutely. (b) The same as in (a) but for velocity (i.e., the integral of (a)).

6.1 Introduction

Accelerometric waveform data are the basis of any ground-motion model (GMM). It is therefore of paramount importance to have clear recordings, free from errors. However, the presence of discontinuities in seismic data is ubiquitous and unavoidable. Discontinuities originate from natural (e.g., ground displacement and tilt (Graizer, 2006; Delorey et al., 2008; Vackar et al., 2015) or insufficient anchoring of the installation) or instrumental sources (e.g., self-noise, digitization noise (Wielandt & Streckeisen, 1982; Wilson et al., 2017).

In case of digitized analog record sections, improper splicing can introduce discontinuities in the time series (Douglas, 2003). Boore (2003) identified analog-to-digital conversion as another source of baseline drift in integrated acceleration recordings. Irrespective of their origins, in the preparation of seismic data for the development of GMMs these discontinuities must be removed (Boore & Bommer, 2005). The data discontinuities appear as step-like pulses in the acceleration records and result in considerable offsets when integrated to velocity and displacement. The baseline jumps in acceleration result in a segmented and shifted baseline (Fig. 6.1).

The manual removal of discontinuities (Boore & Bommer, 2005) becomes cumbersome for large data sets, in particular when instrument-related discontinuities appear regularly. In this article, I propose an inversion routine (integrated combined baseline modification [ICBM]), which not only identifies the timing and scale of the individual jump but also determines the number of jumps in the record. ICBM operates on the integrated acceleration traces (velocity) and combines all three instrument components to estimate baseline offsets and their timings. The best baseline correction model is selected with the Bayesian information criterion (BIC Schwarz, 1978), which not only takes the minimization of the residuals into account but also the number of parameters. Thus, the use of BIC safeguards against overfitting and the optimal model is selected in a parsimonious way. The method is applied to a synthetic data set and to waveform data from the 2016 Kumamoto (Japan) earthquake sequence. The baseline corrected waveforms are integrated to displacements after Wang et al. (2011) since displacements are most sensitive to baseline shifts and are compared to Interferometric Synthetic Aperture Radar (InSAR)-derived displacements by Jiang et al. (2017).

6.2 Method

A simple baseline jump in acceleration can be expressed as scaled and shifted Heaviside function:

$$a(t) = a_1 h(t - T_1), \tag{6.1}$$

in which a_1 is the jump amplitude and T_1 the time of the jump occurrence. The function $h(t)$ is the Heaviside func-

tion

$$h(t-T_1)=\begin{cases}1 & \text{if } t \geq T_1\\ 0 & \text{otherwise}\end{cases}. \tag{6.2}$$

Figure 6.2a visualizes the concept.

The previous concept can be easily extended to an arbitrary number of jumps M:

$$a(t)=\sum_{j=1}^{M} a_j h(t-T_j). \tag{6.3}$$

In this definition the jump amplitude a_{j+1} is the change with respect to the preceding jump a_j, i.e. subsequent jumps superpose each other. This relative change necessitates a definition which considers a jump that occurred before the record starts and its shift continues in the record. Because the jump time of the first datum is not retrievable, the jump is assumed to be present for the entire record duration:

$$a(t)=a_1+\sum_{j=2}^{M} a_j h(t-T_j) \tag{6.4}$$

In other words, a_1 is the baseline offset at the beginning of the record (Fig. 6.2 a).

The discontinuity jumps may be small and well below the signal level. However, because each jumps is a single unidirectional change in the record, they become very apparent on integrated traces as time-dependent offsets (Boore & Bommer, 2005). The integral of Eq. 6.4 is given by

$$\int_0^t a(\tau)d\tau = v(t) = a_0+a_1 t+\sum_{j=2}^{M} a_j(t-T_j)h(t-T_j), \tag{6.5}$$

in which a_0 is the constant of integration and has units of velocity, in contrast to $a_1, ..., a_M$ which have units of acceleration. The integral in Eq. 6.5 is visualized in Fig. 6.2 b.

The model proposed here is a nonlinear inverse problem with an unknown number of parameters, i.e. not only the parameters must be estimated but also the number of parameters must be determined. The model consists of two stages:

> a non-linear least-squares (NLSQ) parameter estimation for the baseline discontinuities and their times and
>
> information-based optimization of number of parameters.

6.2.1 Baseline parameter estimation

The parameter estimation in ICBM for a discrete time series over N time steps is based on least absolute deviation

$$S=\sum_{i=1}^{N}|\Delta v_i| \tag{6.6}$$

$$=\sum_{i=1}^{N}|v_i^{\text{obs}}-v_i^{\text{mod}}|, \tag{6.7}$$

in wjich v_i^{obs} and v_i^{mod} are the ith observed and modeled velocities. The minimization of S is achieved by NLSQ, generally stated as

$$\Delta \mathrm{v} = \mathrm{J}\Delta \mathrm{p}, \tag{6.8}$$

in which Δv is the vector of velocity residuals (may contain one or several seismic channels), J is the Jacobian matrix with the derivatives of the baseline model v with respect to its parameters, stated by vector p. The changes of the model parameters per iteration are given by Δp. The vector Δv represents the residuals between the observed and modelled data, i.e.

$$\Delta v_i = v_i^{\text{obs}} - \left(a_0+a_1 t_i+\sum_{j=2}^{M} a_j(t_i-T_j)h(t_i-T_j)\right). \tag{6.9}$$

The algoritm may be defined on single-component records and multi-component (commonly three) records. If baseline jumps appear simultaneously on all three components, then using all three components in the algorithm simultaneously mitigates overfitting and undesired removal (or alteration) of actual signals.

In the following, the more general three-component based routine is treated but can be easily changed to single-component by removing the respective entries (e.g. y and z) in the vectors and the Jacobian. Let v be a vector with N samples from all three components:

$$\mathrm{v}=\begin{pmatrix}\mathrm{v}_1\\ \mathrm{v}_2\\ \vdots\\ \mathrm{v}_i\\ \vdots\\ \mathrm{v}_N\end{pmatrix} \text{ with } \mathrm{v}_i=\begin{pmatrix}v_i^{(x)}\\ v_i^{(y)}\\ v_i^{(z)}\end{pmatrix}, \tag{6.10}$$

in which $\mathrm{v}_i = \left(v_i^{(x)},\ v_i^{(y)},\ v_i^{(z)}\right)^T$ are the three componets of the ith time sample.

The definition introduced here assumes that jump discontinuities are at same times on all three components, but have different amplitudes on each component. Therefore, baseline jumps are not necessarily correlated in time on all three traces, which is formally realized when one or two component amplitudes are zero. Under these assumptions, the parameter vector is defined as

$$\mathrm{p}=\begin{pmatrix}\mathrm{a}_0\\ \mathrm{a}_1\\ \mathrm{a}_2\\ T_2\\ \vdots\\ \mathrm{a}_j\\ T_j\\ \vdots\\ \mathrm{a}_M\\ T_M\end{pmatrix} \text{ with } \mathrm{a}_j=\begin{pmatrix}a_j^{(x)}\\ a_j^{(y)}\\ a_j^{(z)}\end{pmatrix}, \tag{6.11}$$

in which a_j are the amplitudes of the three components of the jth baseline jump and T_j is the time of the jth baseline

jump. As a consequence of Eq. 6.5 there are no T_0 and T_1. From a model point of view, a_0 represents the offset at the time of the first data sample (i.e. the intercept) and a_1 is the slope of the baseline in the beginning until time T_2 (Fig. 6.2). The three-component Jacobian with simultaneously occurring jumps on all three components is

$$\mathrm{J} = \frac{\partial \mathrm{v}}{\partial \mathrm{p}} = \begin{pmatrix} \frac{\partial \mathrm{v}_1}{\partial \mathrm{a}_0} & \frac{\partial \mathrm{v}_1}{\partial \mathrm{a}_1} & \dots & \frac{\partial \mathrm{v}_1}{\partial \mathrm{a}_j} & \frac{\partial \mathrm{v}_1}{\partial T_j} & \dots & \frac{\partial \mathrm{v}_1}{\partial \mathrm{a}_M} & \frac{\partial \mathrm{v}_1}{\partial T_M} \\ \frac{\partial \mathrm{v}_2}{\partial \mathrm{a}_0} & \frac{\partial \mathrm{v}_2}{\partial \mathrm{a}_1} & \dots & \frac{\partial \mathrm{v}_2}{\partial \mathrm{a}_j} & \frac{\partial \mathrm{v}_2}{\partial T_j} & \dots & \frac{\partial \mathrm{v}_2}{\partial \mathrm{a}_M} & \frac{\partial \mathrm{v}_2}{\partial T_M} \\ \vdots & \vdots & \ddots & \vdots & \vdots & \ddots & \vdots & \vdots \\ \frac{\partial \mathrm{v}_i}{\partial \mathrm{a}_0} & \frac{\partial \mathrm{v}_i}{\partial \mathrm{a}_1} & \dots & \frac{\partial \mathrm{v}_i}{\partial \mathrm{a}_j} & \frac{\partial \mathrm{v}_i}{\partial T_j} & \dots & \frac{\partial \mathrm{v}_i}{\partial \mathrm{a}_M} & \frac{\partial \mathrm{v}_i}{\partial T_M} \\ \vdots & \vdots & \ddots & \vdots & \vdots & \ddots & \vdots & \vdots \\ \frac{\partial \mathrm{v}_N}{\partial \mathrm{a}_0} & \frac{\partial \mathrm{v}_N}{\partial \mathrm{a}_1} & \dots & \frac{\partial \mathrm{v}_N}{\partial \mathrm{a}_j} & \frac{\partial \mathrm{v}_N}{\partial T_j} & \dots & \frac{\partial \mathrm{v}_N}{\partial \mathrm{a}_M} & \frac{\partial \mathrm{v}_N}{\partial T_M} \end{pmatrix} \tag{6.12}$$

And the derivatives are given by

$$\frac{\partial v_i^{(k)}}{\partial a_0^{(l)}} = \delta_{kl}, \tag{6.13}$$

$$\frac{\partial v_i^{(k)}}{\partial a_1^{(l)}} = t\delta_{kl}, \tag{6.14}$$

$$\frac{\partial v_i^{(k)}}{\partial a_j^{(l)}} = (t - T_j)h(t - T_j)\delta_{kl},\ \forall j \geq 2, \tag{6.15}$$

$$\frac{\partial v_i^{(k)}}{\partial T_j} = -a_j^{(k)}h(t - T_j),\ \forall j \geq 2, \tag{6.16}$$

in which the three seismic components are given by superscripts $k, l = \{x, y, z\}$, and δ_{kl} is the Kronecker delta.

The solution of Eq. 6.8 is based on least squares. For the least absolute deviation (Eq. 6.6) the NLSQ solution is iteratively reweighted:

$$\Delta\mathrm{p} = \left(\mathrm{J}^{\mathrm{T}}\mathrm{R}\mathrm{J}\right)^{-1}\mathrm{J}^{\mathrm{T}}\mathrm{R}\Delta\mathrm{v}. \tag{6.17}$$

The matrix R is a diagonal matrix, where ith diagonal element is given by

$$R_{ii} = \frac{1}{\max\left(\delta, |\Delta v_i|\right)}. \tag{6.18}$$

The maximum with threshold δ avoids singularities in R. The value for δ is application dependent and should reflect the average noise level of the record (pre-event and post-event). A reasonable value is $\delta = 10^{-4}\,\mathrm{m\cdot s^{-1}}$, representing a small velocity for acceleration records.

The incremental change of the parameter vector $\Delta\mathrm{p}$ requires initial values for $\mathrm{p}_{\text{initial}}$ and p is updated after each iteration (i)

$$\mathrm{p}^{(i+1)} = \mathrm{p}^{(i)} + \Delta\mathrm{p}^{(i)}. \tag{6.19}$$

There is no direct a priori information about the jump amplitudes available. For the amplitude parameters a_0 (offset at the record beginning) and a_1 (average slope of the entire record) initial values are estimated from an ordinary least squares fit to the entire record for all three channels. The remaining amplitude parameters a_{1+j} are set to zero, i.e. no baseline jumps are assumed initially. The initial values for the jump times T_j are equally distributed over the record length.

6.2.2 Spectral properties of a baseline jump

In Eq. 6.5 the baseline drift on the velocity traces is defined as a superposition of linear function. Although this functional form is practical for the inversion, it is not so for discussing some of its spectral properties. For an arbitrary velocity trace segment between times T_1 and T_2 with constant drift, the baseline model function for that segment

$$v(t) = (p + q(t - T_1))(h(t - T_1) - h(t - T_2)), \tag{6.20}$$

in which p is the offset at T_1 due to any previous discontinuities and q is drift due to the acceleration offset associated with time T_1, and at time T_2 is the subsequent acceleration offset. The Fourier transform of the velocity baseline segment is (for derivation, see appendix)

$$V(\omega) = \begin{cases} p(T_2 - T_1) + \frac{q}{2}(T_2 - T_1)^2 & \text{if } \omega = 0 \\ \frac{1}{\omega}\left\{\left[\frac{q}{\omega} + (q(T_2 - T_1) + p)\,i\right]e^{-i\omega T_2}\right. & \\ \qquad \left. - \left[\frac{q}{\omega} + ip\right]e^{-i\omega T_1}\right\} & \text{if } \omega \neq 0 \end{cases} \tag{6.21}$$

The spectrum is visualized in Fig. 6.3. An important feature is the main lobe of the spectrum around zero frequency. Its width is related to the length of the segment $\Delta T = T_2 - T_1$ and covers the frequency range below the frequency of the first local minimum of the spectrum at $f_0 = \frac{1}{\Delta T}$.

The spectrum of a series of baseline jumps results from the summation of spectra as defined in Eq. 6.21. When correcting baseline jumps it is important to consider the spectra of the baseline drift and of the actual signal. Interference between the signal spectrum and the correction function spectrum should be minimal, i.e. it is necessary to define a minimum time difference between baseline jumps for the correction model: ΔT_{min}.

The time threshold ΔT_{min} is related to the width of the main lobe. And as the main lobe contains most the baseline drift energy (Fig. 6.3), an estimate of ΔT_{min} can be derived from the spectral properties of the seismic signal by different means to reduce interference between the baseline spectrum main lobe and the seismic signal spectrum:

> Investigation of the usable bandwidth of the signal spectrum by computing the spectral ratio between signal and noise spectra. The lower frequency at which the spectral ratio exceeds a given amplitude threshold (e.g. 3) is used as the inverse of ΔT_{min}. This definition is most useful for records of seismic signals where background noise is of considerable influence.
>
> Inversion of parameters for a Brune spectrum model (Brune, 1970) (magnitude M, corner frequency f_c, along-path attenuation κ). Then one can set $\Delta T_{\text{min}} = f_c^{-1}$.
>
> Estimation of the signal duration, T_{dur} based on the running Arias intensity (e.g. Bommer et al., 2009) as

a proxy for threshold time difference. The signal duration is the time difference between e.g. the times where the running Arias intensity reaches 5 % and 95 % of the total Arias intensity of the seismic signal.

When setting $\Delta T_{\text{min}} \geq T_{\text{dur}}$, only a single baseline jump can occur within the baseline model. This safeguards against baseline overfitting in the actual seismic signal and restricts potential contamination of the signal spectrum to the frequency band below the corner frequency. The corner frequency f_c is related to the source duration, resulting in a lower (and thus less conservative) ΔT_{min} compared to usage of T_{dur}, which also includes path-related effects of wave guide propagation (Herrmann, 1985).

6.2.3 Redundancy of modeled jumps

During the iteration process some jump time T_m may become similar—or even identical for larger M—to another jump time T_n. Such overfit is undesired as it renders the model overly complicated and with increasing M, the baseline correction will approximate the actual waveform data. As described in the Spectral Properties of a Baseline Jump section, the baseline jump spectrum can contaminate the seismic spectrum, if the modeled baseline jumps are too frequent in time, in particular when subsequent jumps are less than the time threshold ΔT_{min}.

After each iteration of Eq. 6.17, all time intervals $|T_m - T_n|$ are examined to avoid unnecessary or redundant jumps in the baseline model. If for any two times it holds $|T_m - T_n| < \Delta T_{\text{min}}$, then the parameter sets are merged and the nth parameter set is updated:

$$\mathrm{a}_n^{\text{updated}} = \mathrm{a}_m + \mathrm{a}_n, \tag{6.22}$$

$$T_n^{\text{updated}} = \frac{1}{2}(T_m + T_n). \tag{6.23}$$

The mth parameter set is then removed. The 4 updated parameters are a combination of the original 8 parameters.

Another issue that may arise during the iteration is that some jump time T_m is out of data range, i.e. $T_m < 0$ or $T_m \geq T_N$. The jump parameters associated to the former case are equivalent to those in a_1, i.e. spanning the entire record. Therefore, the parameters a_m in the former case $T_m < 0$ are added to a_1:

$$\mathrm{a}_1^{\text{updated}} = \mathrm{a}_1 + \mathrm{a}_m, \tag{6.24}$$

and the jump amplitudes a_m and time T_m are removed from the parameters. In the latter case $T_m \geq T_N$ all parameters moved out of scope, such that neither the jump time T_m nor the amplitudes a_m have any impact on the model. Hence, these parameters are removed from the parameter vector.

Redundancy of parameter estimates may arise if the jump amplitudes a_m become very small. If it holds that

$$\bar{a} < \sum_{k=1}^{3} \left| a_m^{(k)} \right|, \tag{6.25}$$

then the parameters a_m and time T_m are removed. The value of $\bar{a}$ is application dependent, but when considering

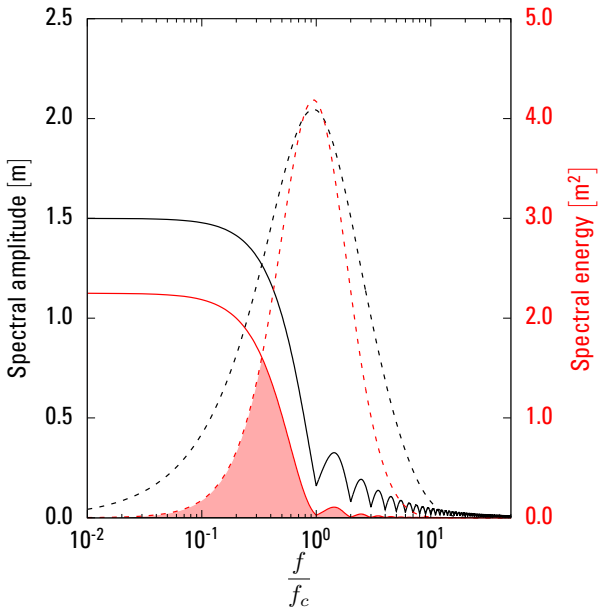

Figure 6.3: Theoretical spectra of a single baseline drift on a velocity trace (solid lines) and Brune source spectrum (dashed lines). The frequency axis is normalized to the main lobe width of the baseline spectrum and respectively to the corner frequency of the Brune source spectrum. Spectra in black are amplitude spectra, in red are energy spectra (squared amplitude spectra). The baseline segment spectrum is based on a 10 s segment with 0.1 $\text{m}\cdot\text{s}^{-1}$ initial offset and a velocity drift of 0.01 $\text{m}\cdot\text{s}^{-2}$. The Brune source spectrum has corner frequency f_c 0.1 Hz, M_W 7.0, along-path attenuation $\kappa = 680 f^{0.38}$, and a distance of 30 km; other parameters are taken from (Boore, 2003; Atkinson, 2000, Table 4). The light red area indicates the overlap of the baseline segment and Brune source energy spectra. When defining the minimum segment length in the baseline model, the earthquake spectra, on which the model is applied, should be taken into account. The source corner frequency is an adequate proxy for the definition of the minimum segment length (as the inverse of the corner frequency) at shorter distances. At longer distances—i.e. when the travel path duration adds substantially to the source duration—the total signal duration should be considered as a more conservative proxy.

strong-motion records, a value of $\bar{a} = 10^{-6}\,\mathrm{m \cdot s^{-2}}$ is sufficient to remove small jump amplitudes which have a negligible contribution on the entire inversion and are below the level of seismic background noise.

6.2.4 Optimization of number of baseline jumps

To determine the optimal number of jumps, the NLSQ inversion is performed P times with changing M. For each inversion the Bayesian Information criterion (BIC, Schwarz, 1978; Burnham & Anderson, 2002) is then calculated. The BIC is given by

$$BIC = N_p \ln N_d - 2 \ln \mathcal{L}, \tag{6.26}$$

in which N_p is the number of free parameters, N_d the number of data, and $\mathcal{L}$ the likelihood of the model. For (non-) linear least squares the assumption is that residuals are normally distributed, for the likelihood it then holds (Burnham & Anderson, 2002)

$$\mathcal{L} \sim \hat{\sigma}^2 = \frac{(\Delta \mathrm{v})^T (\Delta \mathrm{v})}{3N}. \tag{6.27}$$

The $3N$ arises from the number of data in all three components and Δv is the vector of residuals from Eq. 6.9. The number of free parameters N_p for the three-component baseline model in terms of the number of segments M is given by

$$N_p = 7 + 4(M - 1) \tag{6.28}$$

Note that the sum of the residuals is also a free parameter. Thus, the BIC for the baseline model is

$$BIC = (7 + 4(M-1)) \ln(3N) + 3N \ln \hat{\sigma}^2. \tag{6.29}$$

The optimal model of the P models is the one that minimizes BIC.

With the optimal model selected, the acceleration traces are corrected by

$$a^{\mathrm{corr}}(t) = a^{\mathrm{obs}}(t) - a(t). \tag{6.30}$$

6.3 Examples

6.3.1 Synthetic data

This section illustrates the baseline correction with synthetic data. The purpose of the synthetic data is to demonstrate the reliability of the inversion as the the number of jumps is set a priori and the times are known. Synthetic waveform data are generated from stochastic simulations for a magnitude 7 earthquake at 30 km distance using standard parameters from Boore (2003). Fig. 6.4 shows a synthetic three-component acceleration waveform with noise. Three baseline jumps with different amplitudes on each component are added at the same times. While the acceleration traces are negligibly affected, the integrated traces show strong baseline drifts if left uncorrected. Similarly, the effect of the baseline jumps in the amplitude spectra is more apparent in the velocity spectra where the baseline jump spectra dominate the low frequency range below the source corner frequency (Fig. 6.5a). Compared to the velocity spectra, the acceleration spectra are less affected by the baseline jumps, although at very low frequencies the baseline jump spectra show a strong effect (Fig. 6.5b). ICBM corrects the baseline shifts by identifying the jump amplitudes and times and the velocity baseline is around zero. Due to the usage of BIC, the correction model is selected in a parsimonious way.

6.3.2 The 2016 Kumamoto earthquake

On April 16 2016 central Kyushu (Japan) was hit by a M_W 7.1 strike-slip earthquake east of Kumamoto city. The rupture reached the surface and cause substantial surface displacements (Shirahama et al., 2016). Due to the rupture location within Kyushu, the event is well recorded on the dense seismological networks of Japan. Strong-motion data are available from NIED (K-Net, KiK-Net) and JMA (seismic stations used for the determination of the Japan Meteorological Agency seismic intensity [shindo]). Given the dense seismological network, the available waveform database is extensive with several hundreds of records for the mainshock, and large fore- and aftershocks. The database covers all events where data from NIED and JMA are available (Tab. 6.1).

All available JMA stations show baseline jumps on all three components (Fig. 6.6). These jumps would have implications on estimations of response spectra at low oscillatory periods, and a considerable impact on radiated seismic energy and peak ground velocity, and in particular static displacement and peak ground displacement. The static displacement estimation is most sensitive to baseline jumps due to the double integration of the accelerograms. The automated displacement estimation method of Wang et al. (2011) is applied to the waveform database. Their algorithm finds parameters to correct the waveform such that it best fits a step function. Since this algorithm expects one discontinuity only, it can fail to estimate static displacements in the presence of additional discontinuities (Fig. 6.7).

I compare the resulting cumulative static displacement of the major Kumamoto events with InSAR based displacement estimates by Jiang et al. (2017). InSAR (Interferometric Synthetic Aperture Radat) derived displacements perform similarly to the seismically inferred displacements and source parameters (Kobayashi, 2017; Weston et al., 2012). The pre-sequence InSAR imagery was acquired on April 8 and the post-sequence data on April 20, thus covering in addition to the mainshock all major fore- and aftershocks. The InSAR and accelerometer derived displacements correlate highly and displacements scale equally with both methods (Fig. 6.8). The functional relation between the two is

$$d_{\mathrm{InSAR}} = 0.89 d_{\mathrm{acc}} + 0.01, \tag{6.31}$$

where parameters were estimated by Deming regression (orthogonal least squares Deming, 1943), with a very high Pearson correlation $r = 0.932$.

Displacements are also in agreement with in-field measurements by Shirahama et al. (2016) in the vicinity of

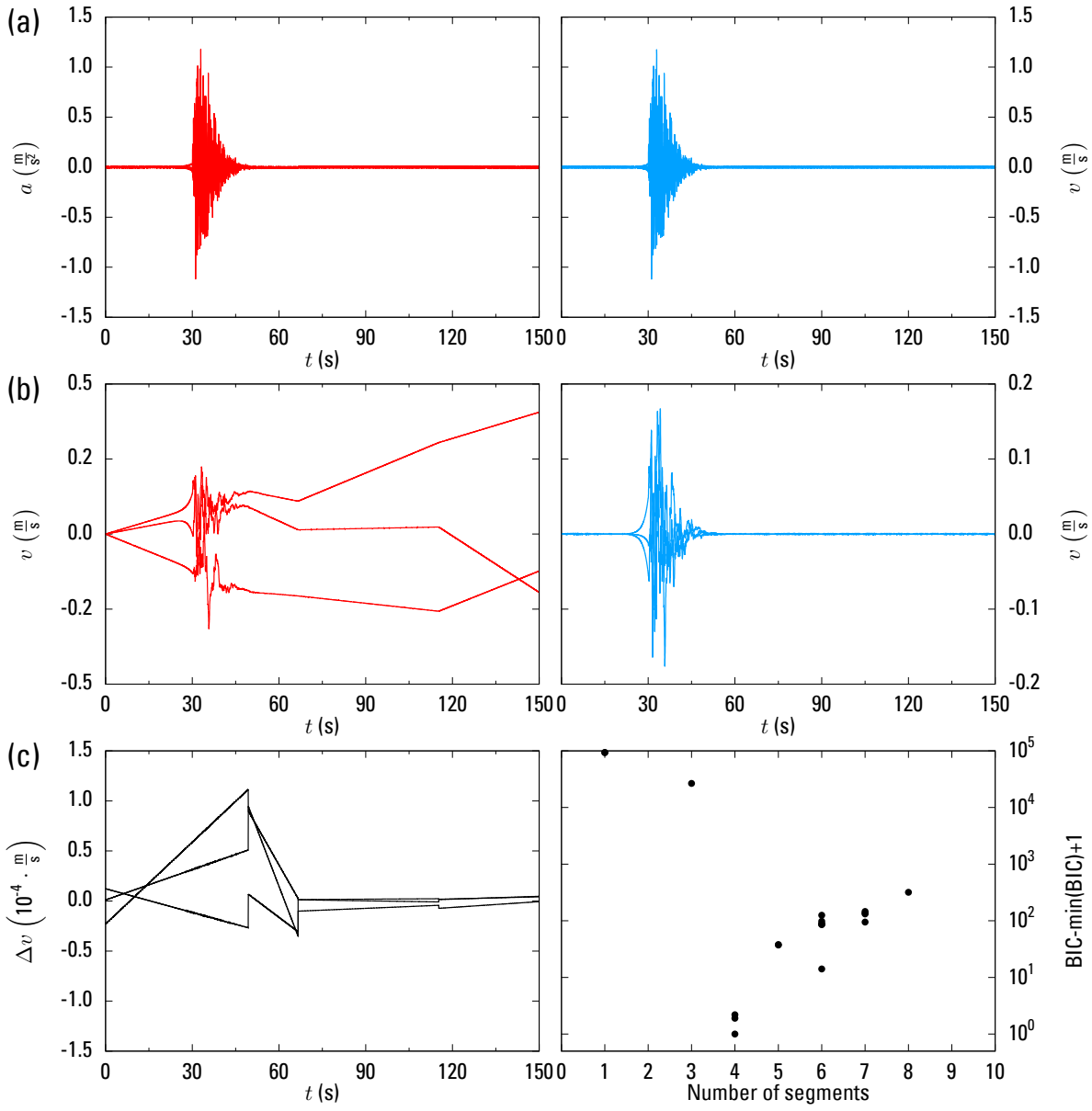

Figure 6.4: Comparison of 3-component acceleration waveform (top row) without baseline correction (left column, red waveforms) and the same waveforms with baseline correction (right column, blue waveforms). The synthetic waveforms are generated by the stochastic method after Boore (2003). Three random baseline jumps have been added at random times (resulting in four linear segments), which are covered by noise due to the jumps small amplitudes. The middle row shows the acceleration traces integrated to velocity and the uncorrected traces show now strong baseline drifts without correction (left), while the velocity baselines after correction are around zero (right). Bottom left: The residual of the baseline estimate of ICBM to the baseline shift function used to simulate the baseline jumps (i.e. ground truth). The deviation is minimal (note the y-axis scale), demonstrating that both amplitudes and times of the baseline jumps are sufficiently approximated. Bottom right: The Bayesian information criterion (BIC) against the number of baseline segments (equals baseline jumps plus one). The baseline correction used here was obtained after 20 runs with increasing number of segments (1-20). Since the algorithm can reduce the number of segments during the iteration process, some segment combinations have been eliminated before the BIC evaluation. The best models are correctly found with four segments.

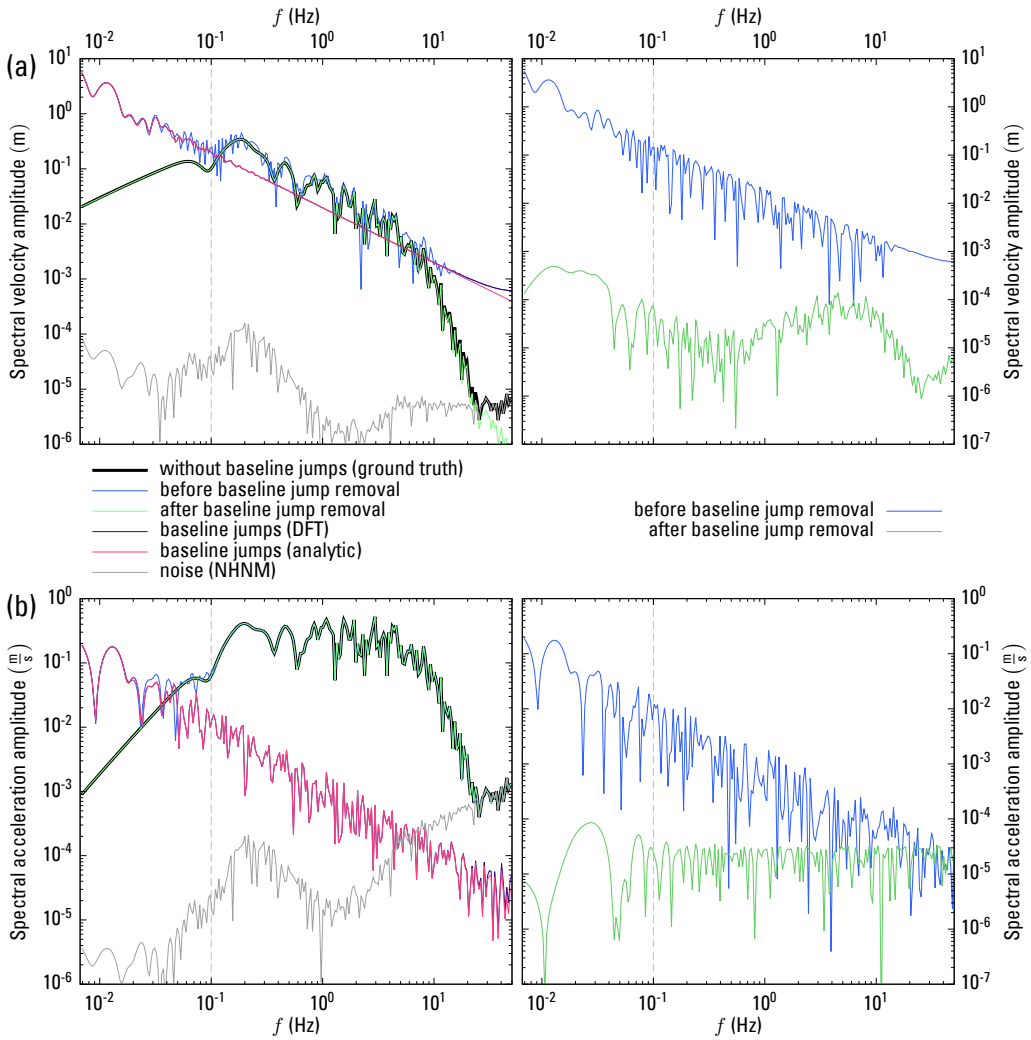

Figure 6.5: Waveform spectra of a component (lowest of the three) in Fig. 6.4 middle left. The source spectrum is designed after Boore (2003) with parameters from Atkinson (2000) for the Kumamoto earthquake with corner frequency f_c 0.1 Hz, M_W 7.0, along-path attenuation $\kappa = 680 f^{0.38}$ (see also Fig. 6.3). To the earthquake signal is a noise signal added based on the New High Noise Model (NHNM Peterson, 1993). Left column: Velocity (top) and Acceleration spectra (bottom). The spectrum of the waveforms with baseline drift (blue) is a superposition of the baseline drift spectrum (magenta) and the source spectrum (black). The baseline drift spectrum dominates at low frequencies, in particular below the source corner frequency (dashed line). The difference between the analytic expression of the baseline segment spectrum (magenta) and the discrete Fourier transform (DFT) of the baseline segment times series (dark purple) is negligible and increases relatively only slightly close to the Nyquist frequency at 50 Hz. After the removal the baseline drift, the corrected spectrum (green) recovers completely the uncontaminated spectrum (ground truth, black) The major difference between the velocity and acceleration trace is the relatively much smaller effect of the baseline shift at higher frequencies. Right column: Difference between spectra before (blue) and after (green) baseline correction with respect to the ground truth for velocity (top) and acceleration (bottom). The colors of the graphs correspond to the ones from the left column. The baseline correction removes the spectral contamination nearly completely with very little deviation from the ground truth for both velocity and acceleration.

Table 6.1: Events from the 2016 Kumamoto earthquake sequence used for displacement estimation. Date and Time is in local time (JST).

Date	Time	M_{JMA}	Lon. (°)	Lat. (°)	Depth (km)
2016-04-14	21:26:00	6.5	130.808	32.742	11
2016-04-14	22:07:00	5.8	130.848	32.775	8
2016-04-15	00:03:00	6.4	130.777	32.700	7
2016-04-16	01:25:00	7.3	130.762	32.753	12
2016-04-16	01:44:00	5.4	130.760	32.752	15
2016-04-16	03:55:00	5.8	131.190	33.025	11
2016-04-16	09:48:00	5.4	130.835	32.847	16

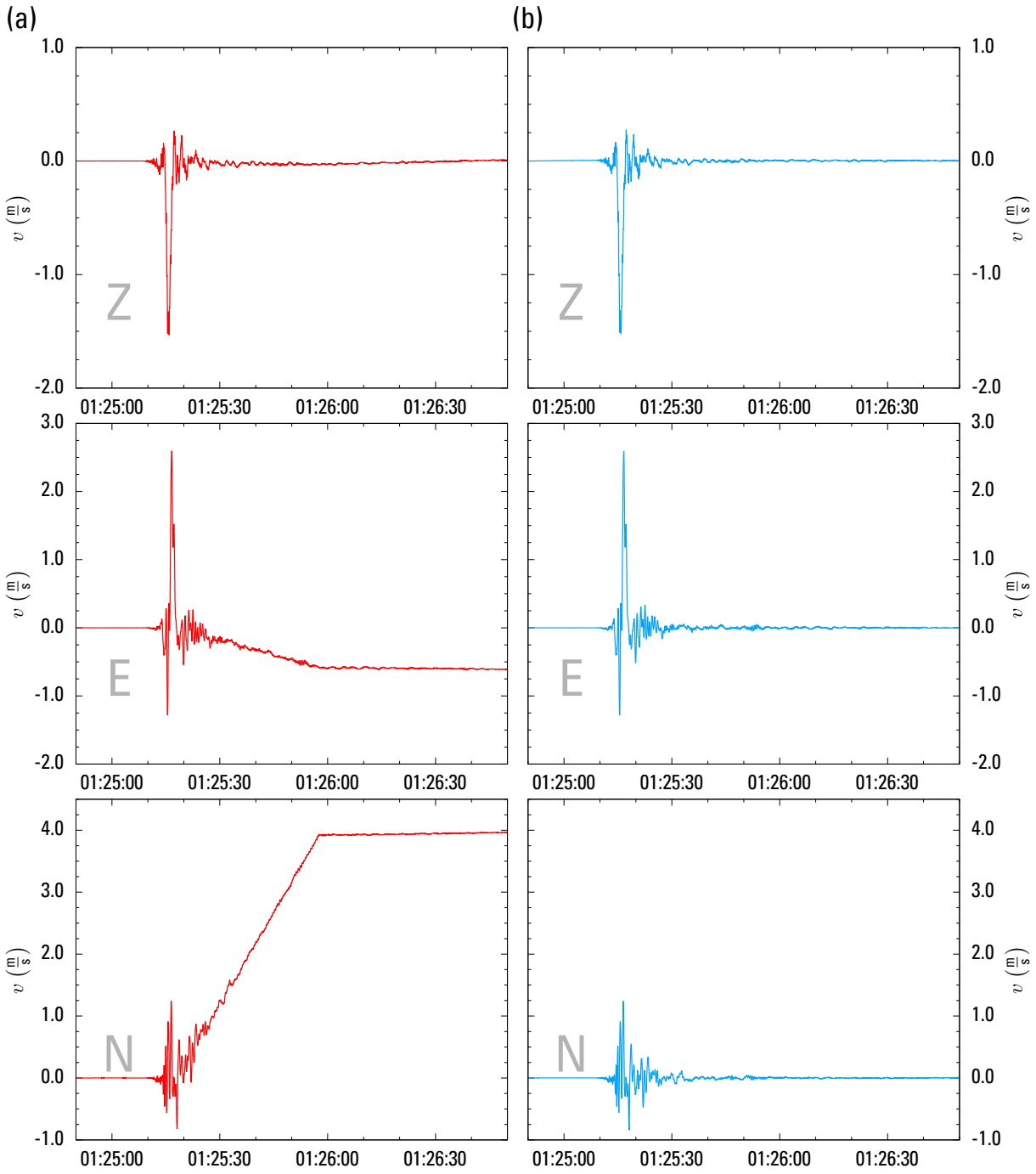

Figure 6.6: The example waveform of Fig. 6.1. Accelerations are integrated to velocities. Left column: raw velocity traces without baseline corrections. There are two notable discontinuities, one in the strong motion portion (most likely event related) and another 40 s later (most likely instrument related). Right column: velocities after baseline correction. All three velocity traces are now flat with both discontinuities removed.

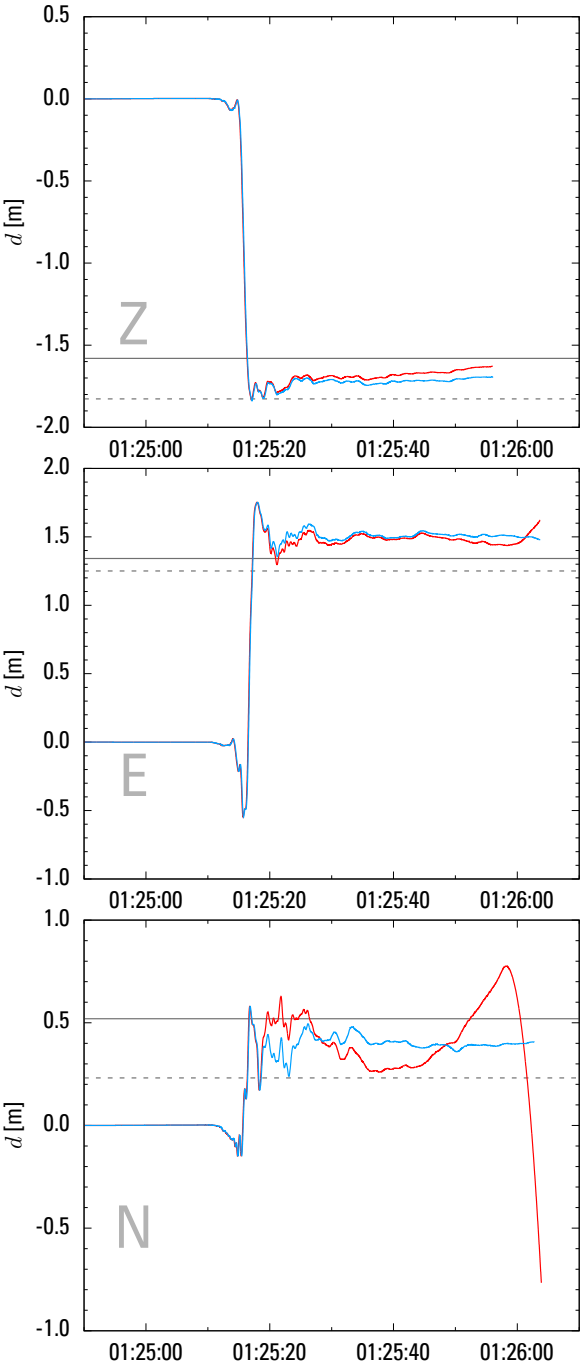

Figure 6.7: Static displacement estimation after Wang et al. (2011) for the waveforms in Fig. 6.6. Displacements without baseline correction are in red, with baseline correction in blue. The waveform length is cut according to Wang et al. (2011) to estimate the static displacements. While the Z– and N– components are less affected by the baseline jumps, the N–component is strongly affected. The solid gray lines are displacement estimates based on the high-resolution LiDAR model of Scott et al. (2018) at the accelerometer location. The dashed gray lines are displacements inferred by InSAR after Jiang et al. (2017) appr. 500 m away in NNW direction.

the surface rupture and displacements estimated from LiDAR measurements by (Scott et al., 2018). Major discrepancies appear only for few stations in the northern part of the caldera of Mt. Aso, northeast of the area with large static displacement (Fig. 6.8). The differences in displacements can be attributed to uncertainties of either displacement estimation method and might also be related to e.g. highly localized displacements at smaller surface ruptures in the rupture vicinity (Fujiwara et al., 2016).

6.4 Discussion & Conclusion

In this paper I introduced an automated baseline correction for three-component signals based on nonlinear least absolute deviation with model optimization related to the Bayesian Information Criterion. The method corrects for baseline jumps in accelerograms by identifying signal drifts and discontinuities in the velocity traces (time-integrated accelerograms). The correction function is a segmented linear function with an arbitrary number of segments. Since baseline jumps occur spuriously, several restrictions are imposed on the model to avoid overfitting (no clustering of jumps) and to stabilize the inversion process (jumps may occur simultaneously on all three components). Proxies for the minimum time length of the baseline segments are proposed that are related to the source corner frequency, usable spectral bandwidth, and the signal duration. These definitions ensure that the earthquake signal is not contaminated by to many baseline corrections which might arise due to overfitting. The Bayesian Information Criterion also selects the baseline model that best fits the baseline jumps in a parsimonious way.

Not only can the robust automated process handle large amounts of waveform data but the determination of the jump times is performed on up to three components simultaneously, improving the robustness of estimates even at noisier times, e.g. during an earthquake or when the jumps are in the coda. During the iteration of ICBM, all baseline jump estimates are improved concurrently, which contrasts with the approach by Boore & Bommer (2005) with a sequential fit of jumps. The concurrent estimation is an advantage, as estimation errors in ICBM are more evenly distributed over all jumps, while in the sequential fit errors from earlier jumps are propagated to later jumps, where estimates of later jumps can be overall more erroneous than earlier jumps.

The applicability of the method has been demonstrated on synthetic signals and real signals from the 2016 Kumamoto earthquake sequence. Comparison of the static displacements estimated from accelerograms with InSAR displacements by Jiang et al. (2017) highlight that the automated baseline correction can be used as a preprocessing routine for strong-motion records as described by Boore & Bommer (2005) and to improve static displacement estimation routines (Wang et al., 2011).

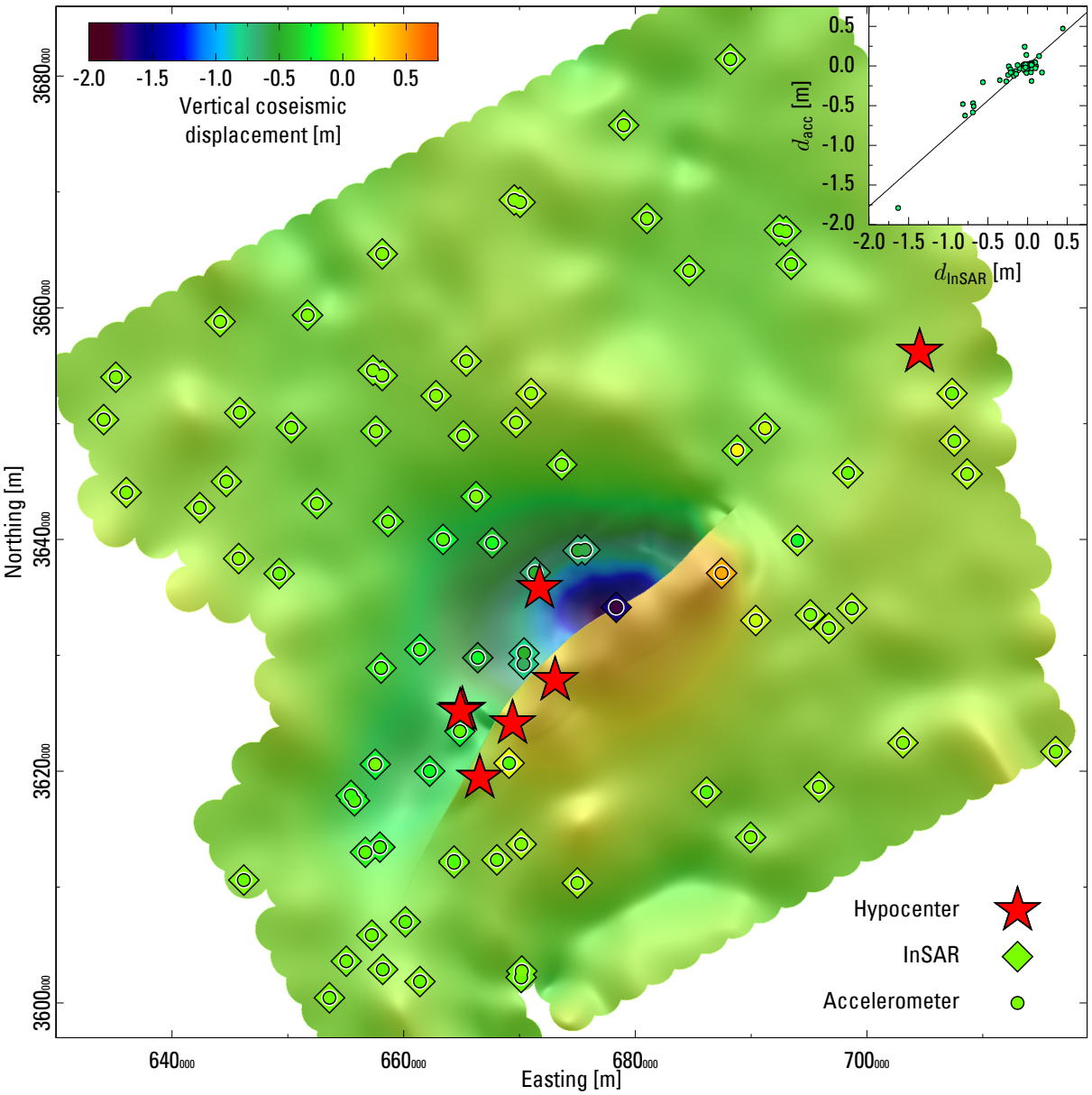

Figure 6.8: Map of the vertical coseismic displacement of the 2016 Kumamoto earthquake sequence derived from InSAR (Jiang et al., 2017). The surface rupture of the mainshock is indicated by the sudden displacement offset. Locations of major events (Tab. 6.1) are shown as stars. InSAR displacements at the accelerometer sites (diamonds) fit spatially to the accelerometer based displacements (circles in diamonds). The inset figure shows the comparison between accelerometer derived displacement (d_{acc}) and InSAR derived displacement (d_{InSAR}).

6.5 Data & Resources

The waveform data of the Kumamoto earthquake are obtained from K-Net/KiK-Net (http://www.kyoshin.bosai.go.jp/kyoshin/, last accessed May 2019) and from the Japanese Meteorological Agency (https://www.data.jma.go.jp/svd/eqev/data/kyoshin/jishin/index.html, last accessed May 2019). The InSAR data of Jiang et al. (2017) are avaialbale as electronical supplement at (https://agupubs.onlinelibrary.wiley.com/doi/10.1002/2016GL072253, last accessed May 2019). The Lidar data of Scott et al. (2018) are avaialbale as electronical supplement at (https://agupubs.onlinelibrary.wiley.com/doi/10.1029/2018JB015581, last accessed May 2019). I provide the code for ICBM as C++ header based on the linear algebra library Armadillo by Sanderson & Curtin (2016). The code is available at https://github.com/EmperorOfTheMoon/ICBM

Acknowledgements

Many thanks to Julian Bommer and Dave Boore for reviewing this paper which resulted in a very appreciable improvement of the article. Also, thanks to Fabrice Cotton for helping to improve the initial version of this paper.

6.6 Appendix: The Fourier transforms of a series of baseline jumps / drifts

The Fourier transform of

$$v(t) = (p + q(t - T_1))(h(t - T_1) - h(t - T_2)), \quad (6.32)$$

is

$$V(\omega) = \int_{-\infty}^{\infty} v(t) e^{-i\omega t} dt \quad (6.33)$$

and can be stated as

$$V(\omega) = \int_{T_1}^{T_2} (p + q(t - T_0)) e^{-i\omega t} dt \quad (6.34)$$

$$= p \int_{T_1}^{T_2} e^{-i\omega t} dt + q \int_{T_1}^{T_2} (t - T_1) e^{-i\omega t} dt \quad (6.35)$$

The left integral of Eq. 6.35 is readily given by

$$\int_{T_1}^{T_2} e^{-i\omega t} dt = \begin{cases} T_2 - T_1 & \text{if } \omega = 0 \\ \frac{i}{\omega} \left(e^{-i\omega T_2} - e^{-i\omega T_1} \right) & \text{if } \omega \neq 0 \end{cases} \quad (6.36)$$

Integration by parts gives the right integral of Eq. 6.35

$$\int_{T_1}^{T_2} (t - T_1) \frac{du}{dt} dt \quad (6.37)$$

with

$$\frac{du}{dt} = e^{-i\omega t} \text{ and } u = \frac{i}{\omega} e^{-i\omega t} \quad (6.38)$$

and thus

$$\int_{T_1}^{T_2} (t - T_1) e^{-i\omega t} dt$$

$$= \left[\frac{1}{2} (t^2 - T_1 t) u \right]_{T_1}^{T_2} - \int_{T_1}^{T_2} \frac{d(t - T_1)}{dt} u dt \quad (6.39)$$

$$= \begin{cases} \frac{1}{2} (T_2 - T_1)^2 & \text{if } \omega = 0 \\ \omega^{-1} (i(T_2 - T_1) + \omega^{-1}) e^{-i\omega T_2} & \\ \quad - \omega^{-2} e^{-i\omega T_1} & \text{if } \omega \neq 0 \end{cases} \quad (6.40)$$

Plugging Eq. 6.36 and Eq. 6.40 into Eq. 6.35 gives the Fourier transform of the baseline drift segment

$$V(\omega) =$$

$$\begin{cases} p(T_2 - T_1) + \frac{q}{2} (T_2 - T_1)^2 & \text{if } \omega = 0 \\ \frac{1}{\omega} \left\{ \left[\frac{q}{\omega} + (q(T_2 - T_1) + p) i \right] e^{-i\omega T_2} \right. & \\ \quad \left. - \left[\frac{q}{\omega} + ip \right] e^{-i\omega T_1} \right\} & \text{if } \omega \neq 0 \end{cases} \quad (6.41)$$

Due to the finiteness of the signal, the spectrum of the derivative of $v(t)$ is not simply $i\omega V(\omega)$. In addition the combined segments form a continuous function, while each segment alone is discontinuous. Therefore, the Fourier transform of a baseline jump segment comes from

$$a(t) = q(h(t - T_1) - h(t - T_2)). \quad (6.42)$$

The Fourier transform is as in Eq. 6.36

$$A(\omega) = q \int_{T_1}^{T_2} e^{-i\omega t} dt \quad (6.43)$$

$$= \begin{cases} q(T_2 - T_1) & \text{if } \omega = 0 \\ \frac{iq}{\omega} \left(e^{-i\omega T_2} - e^{-i\omega T_1} \right) & \text{if } \omega \neq 0 \end{cases} \quad (6.44)$$

”Jishin no Sakura” (Japanese: Cherry Blossoms of an Earthquake). The topographic data of Kyushu is overlaid with particle motion plots of the 2016 Kumamoto earthquake. Each time step is a petal, scaled and colored by the acceleration of the earthquake at each site.

Chapter 7

Effects of finite source rupture on landslide triggering: The 2016 M_W 7.1 Kumamoto earthquake

Abstract

The propagation of a seismic rupture on a fault introduces spatial variations in the seismic wave field surrounding the fault. This directivity effect results in larger shaking amplitudes in the rupture propagation direction. Its seismic radiation pattern also causes amplitude variations between the strike-normal and strike-parallel components of horizontal ground motion. We investigated the landslide response to these effects during the 2016 Kumamoto earthquake ($M_W 7.1$) in central Kyushu (Japan). Although the distribution of some 1,500 earthquake-triggered landslides as a function of rupture distance is consistent with the observed Arias intensity, the landslides were more concentrated to the northeast of the southwest–northeast striking rupture. We examined several landslide susceptibility factors: hillslope inclination, the median amplification factor (MAF) of ground shaking, lithology, land cover, and topographic wetness. None of these factors sufficiently explains the landslide distribution or orientation (aspect), although the landslide head scarps have an elevated hillslope inclination and MAF. We propose a new physics-based ground-motion model (GMM) that accounts for the seismic rupture effects, and we demonstrate that the low-frequency seismic radiation pattern is consistent with the overall landslide distribution. Its spatial pattern is influenced by the rupture directivity effect, whereas landslide aspect is influenced by amplitude variations between the fault-normal and fault-parallel motion at frequencies < 2 Hz. This azimuth dependence implies that comparable landslide concentrations can occur at different distances from the rupture. This quantitative link between the prevalent landslide aspect and the low-frequency seismic radiation pattern can improve coseismic landslide hazard assessment[a].

[a] von Specht, S., Ozturk, U., Veh, G., Cotton, F., and Korup, O.: Effects of finite source rupture on landslide triggering: the 2016 M_W 7.1 Kumamoto earthquake, *Solid Earth*, 10, 463–486, https://doi.org/10.5194/se-10-463-2019, 2019

7.1 Introduction

Landslides are one of the most obvious and hazardous consequences of earthquakes. Acceleration of seismic waves alters the force balance in hillslopes and temporarily exceeds shear strength (Newmark, 1965; Dang et al., 2016). Greatly increased landslide rates have been reported on hillslopes close to earthquake rupture, mostly tied to ground acceleration (Gorum et al., 2011) and lithology (Chigira & Yagi, 2006). Substantial geomorphological and seismological data sets are required to assess the response of landslides to ground motion, and a growing number of studies have shed light on the underlying links (e.g. Lee, 2013; Allstadt et al., 2018; Roback et al., 2018; Fan et al., 2018). Several seismic measures such as vertical and horizontal peak ground acceleration (PGA; Miles & Keefer, 2009), root-mean square (RMS) acceleration, or Arias intensity (I_A; Arias, 1970; Keefer, 1984; Harp & Wilson, 1995; Jibson et al., 2000; Jibson, 2007; Torgoev & Havenith, 2016), seismic source-moment release, hypocentral depth, and rupture extent and propagation (Newmark, 1965), correlate with landslide density (Meunier et al., 2007).

Landslides concentrate in the area of strongest ground acceleration (Meunier et al., 2007), whereas total landslide area decreases from the earthquake rupture with the attenuation of peak ground acceleration (Dadson et al., 2004; Taylor et al., 1986). This general pattern is modified by morphometrics (e.g. local hillslope inclination and curvature) and geological parameters (e.g. lithology, geological structure, land cover) (Gorum et al., 2011; Havenith et al., 2015) that influence landslide susceptibility (Pawluszek & Borkowski, 2017) on top of seismic amplification (Maufroy et al., 2015). For instance, Tang et al. (2018) found that lithology, PGA, and distance from the rupture plane are important in assessing the distribution of landslides triggered by the 2008 Wenchuan earthquake (M_W 7.9). Fan et al. (2018) found that hillslope aspect and slope were important determinants of the landslide distribution resulting from the 2017 Jiuzhaigou earthquake (M_W 6.5).

On April 16, 2016 at 16:25 UTC central Kyushu was hit by a M_W 7.1 earthquake (Fig. 7.1). The left-lateral dip-slip event ruptured along the Futagawa and Hinagu faults, striking NW–SE, with a hypocentral depth of 11 km (e.g. Kubo et al., 2016). The rupture propagated northeastward and stopped at Mt Aso. Fault source inversions show a northeast propagation of the rupture originating under Kumamoto City with highest slip near the surface at the western rim of the Aso caldera (e.g. Kubo et al., 2016; Asano & Iwata, 2016; Moore et al., 2017; Uchide et al., 2016; Yagi et al., 2016; Yoshida et al., 2017). The earthquake triggered approximately 1,500 landslides (National Research Institute for Earth Science and Disaster Prevention, 2016) that concentrated mainly inside the caldera and the flanks of Mt Aso on the Pleistocene and Holocene lava flow deposits (Paudel et al., 2008; Sidle & Chigira, 2004), although most of the terrain near the earthquake rupture is rugged (Fig. 7.1). Thus, we hypothesize that rupture directivity causes an asymmetric distribution of landslides around the rupture plane because of more severe ground motion along the propagating rupture (Somerville et al., 1997; Hovius & Meunier, 2012). Similarly asymmetric landslide distributions attributed to rupture directivity were reported for the 2002 Denali earthquake (M_W 7.9 Frankel, 2004; Gorum et al., 2014), and the 2015 Gorkha earthquake (M_W 7.8 Roback et al., 2018). In the case of the 1999 Chi-Chi earthquake, Lee (2013) speculated that the prevalent landslide aspects were correlated to the fault movement direction (Ji et al., 2003; Meunier et al., 2008). These observations indicate that the rupture process introduces variations on the incoming energy on hillslopes.

Here we link those dominant near-surface seismic characteristics relevant to the pattern and orientation of coseismic landslides. We investigate the geological conditions (lithology, aspect, hillslope inclination, topographic amplification, and soil wetness) in central Kyushu as well as seismic waveform records from 240 seismic stations within 150 km of the rupture (Fig. 7.1). The two most prominent seismic effects—well founded in seismological theory (e.g. Aki & Richards, 2002) and documented in empirical relationships (e.g. Somerville et al., 1997)—are the rupture directivity and amplitude variations in fault-normal and fault-parallel motion. We examine whether the geomorphic characteristics around the Aso caldera made this area more susceptible to landslides than the surrounding topography near the earthquake rupture or whether rupture effects control the asymmetric distribution of the landslides. We introduce a ground-motion metric related to azimuth-dependent seismic energy (i.e. seismic velocity) because these effects attenuate with increasing frequency and are less captured by acceleration-based metrics. We conclude by proposing a new ground-motion model (GMM) that is consistent with the observed coseismic landslide pattern.

7.2 Data

We combine data sets on the response of landslides to the earthquake, including topography, land cover, geology, seismic waveforms, velocity structure, near-surface characteristics, and landslide location and planform (Fig .7.2).

7.2.1 Topographic data

Most topographic data used in this study are provided by the Japan Aerospace Exploration Agency (JAXA) and its Advanced Land Observing Satellite (ALOS) project with a horizontal resolution of 1" ($\approx$ 30 m). This digital surface model (DSM) forms the basis for computing aspect, hillslope inclination, the median amplification factor (MAF; Maufroy et al., 2015), and the topographic wetness index (Böhner & Selige, 2006). The ALOS project also provides data on land cover including anthropogenic influence (sealing and agriculture) and vegetation, while data on major geological units are from the Seamless Digital Geological Map of Japan (scale of 1:200,000) by the Geological Survey of Japan.

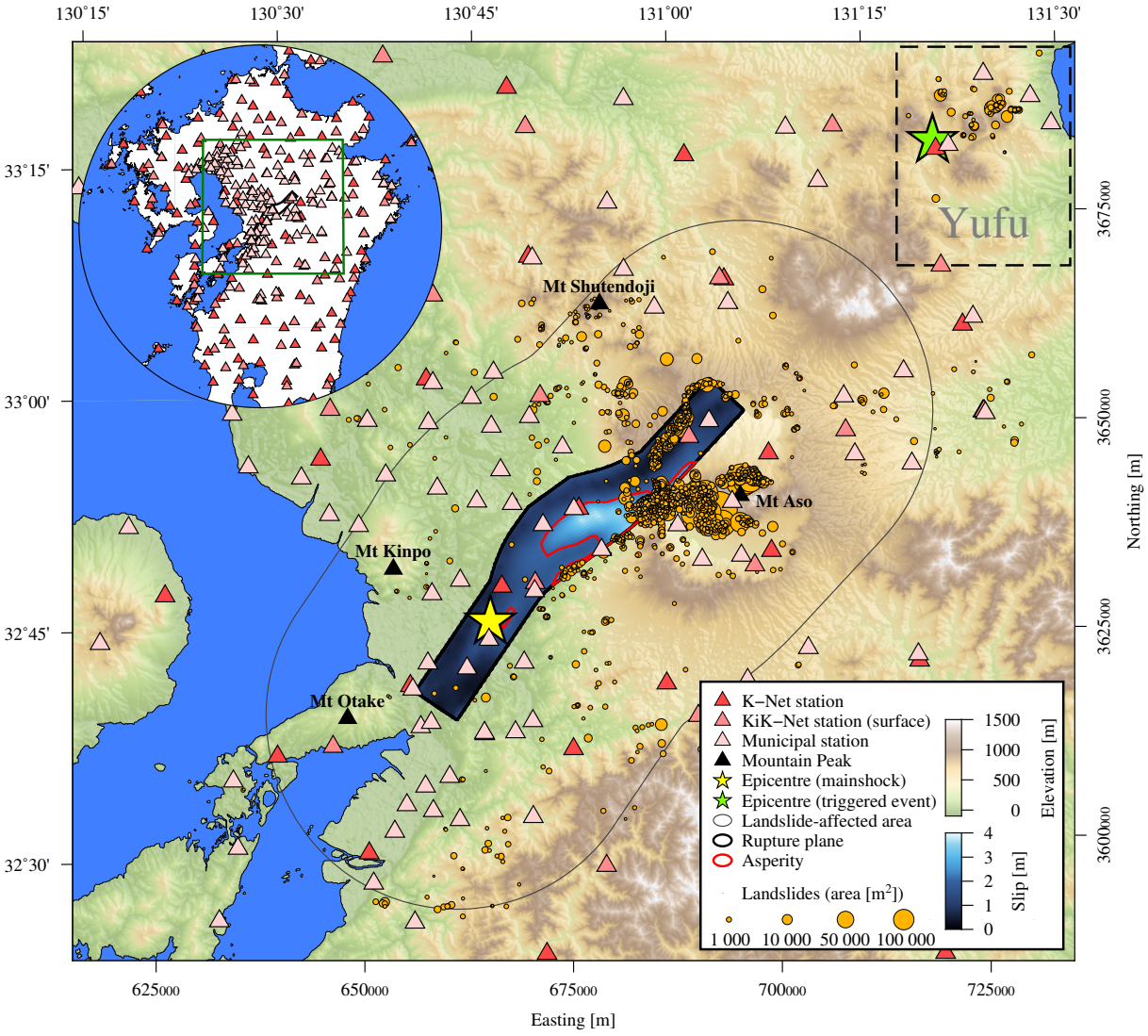

Figure 7.1: The area of Kyushu affected by coseismic landslides triggered by the 2016 M_W 7.1 Kumamoto earthquake. The coloured patch is the slip distribution of the rupture model by Kubo et al. (2016), and the dashed box encompasses landslides related to the triggered event in Yufu (epicentre location after Uchide et al. (2016)). The inset map shows the station network within 150 km of the rupture.

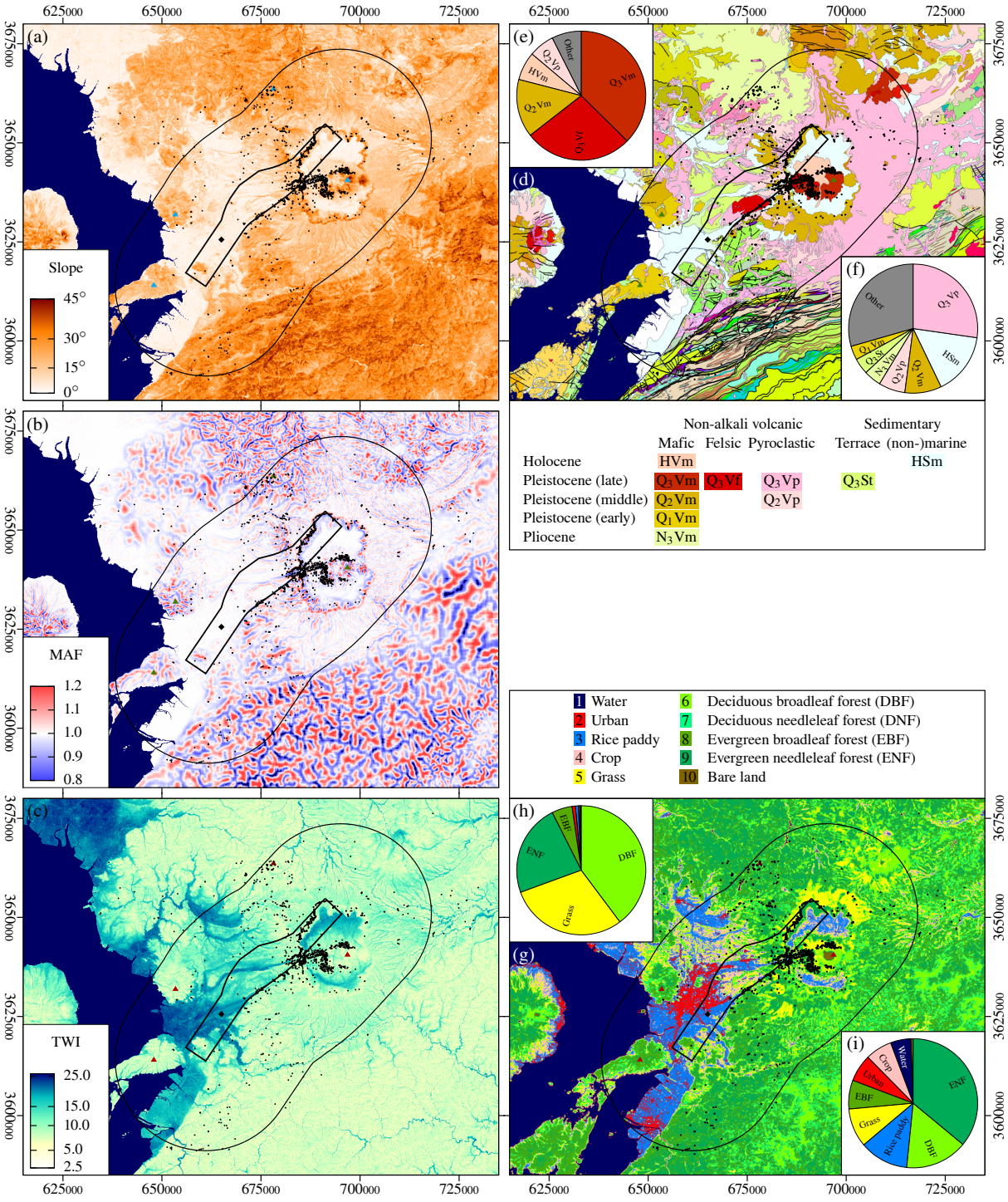

Figure 7.2: Topographic and geological features of central Kyushu with landslides (black dots), landslide-affected area (outer black line), rupture area (inner black line), hypocentre (black diamond), and mountain peaks from Fig 1 (triangles). (a) Hillslope inclination. (b) Median amplification factor (MAF). (c) Topographic wetness index (TWI). (d) Geology of central Kyushu. The most common geological units of the landslides are shown in (e). For the landslide-affected area the dominant geological units are in (f). (g) Land cover. Land cover in the landslide areas is shown in (h) and is shown for the entire landslide-affected area in (i).

7.2.2 Topographic amplification of ground motion

Topographic features, such as mountains and valleys, can amplify or attenuate seismic waves (Massa et al., 2014; Maufroy et al., 2012, 2015). The largest ground-motion variations occur on hillslopes and summits, whereas variations are intermediate on narrow ridges and low on valley floors. Maufroy et al. (2015) introduced proxies for these topographic site effects, of which we use the median amplification factor (MAF), based on the topographic curvature, and the S-wave velocity v_S travelling at frequency f:

$$MAF(f) = 8 \times 10^{-4} \frac{v_S}{f} C_S \left(\frac{v_S}{2f} \right) + 1 \qquad (7.1)$$

where $C_S \left(\frac{v_S}{2f} \right)$ is the topographic curvature convolved with a normalized smoothing kernel based on two 2D boxcar functions as a function of v_S and f.

The curvature is estimated from the DSM (Zevenbergen & Thorne, 1987; Maufroy et al., 2015), and the seismic velocity v_S is the average S-wave velocity of the uppermost 500 m from the model by Koketsu et al. (2012).

Another site effect that influences landslide potential is the local soil or groundwater content, which can be modelled for uniform conditions to the first order using the topographic wetness index (TWI) of Böhner & Selige (2006):

$$TWI = \log \frac{A_c}{\tan \beta}, \qquad (7.2)$$

where A_c is the upslope catchment area and β is the hillslope inclination derived from the DSM with filled sinks (Planchon & Darboux, 2001).

7.2.3 Ground-motion data

Ground-motion data are from the Kik-Net and K-Net of the National Research Institute for Earth Science and Disaster Prevention (NIED) of Japan. NIED operates both borehole and surface stations for Kik-Net, and we use the latter only. The Japan Meteorological Agency (JMA) also released seismic data from the municipal seismic network for the largest earthquakes of the Kumamoto sequence. In total, data from 240 stations in Kyushu are available with complete azimuthal coverage within 150 km of the earthquake rupture (Fig. 7.1).

The analysis of seismic waveforms is based on accelerometric data only. Both the NIED and JMA data are unprocessed, and we follow the strong motion processing guidelines of Boore & Bommer (2005). We use both acceleration and velocity in further processing and integrate the accelerograms to obtain velocity records. We correct the data with the automated baseline correction routine by Wang et al. (2011). The JMA accelerometric data further require a piecewise baseline correction prior to the displacement baseline correction due to abrupt (possibly instrument-related) jumps (Boore & Bommer, 2005; Yamada et al., 2007). We use the automated correction for baseline jumps by von Specht, 2018 (see Ch. 6).

An earthquake was triggered approximateley 80 km to the northeast in Yufu 32 s after the Kumamoto earthquake (Fig. 7.1 Uchide et al., 2016). Due to the close succession of the two events, waveforms of the triggered event interfere with the coda of the Kumamoto earthquake. We taper the data to reduce signal contributions by the triggered event. The taper position is based on theoretical travel time differences between the P wave ($v_P = 5700$ m s^{-1}) arrival of the Kumamoto earthquake and the S wave arrival ($v_S = 3300$ m s^{-1}) of the triggered event. The respective travel paths to the stations are measured from the hypocentres. Since fewer instruments are located to the northeast and the triggered event close to the sea, less than 10% of the data are strongly contaminated by the triggered event.

NIED hosts the rupture-plane model of Kubo et al. (2016), which describes the slip history on a curved rupture plane (based on the surface traces of the Futagawa and Hinagu faults) with a total length of 53.5 km and width of 24.0 km (Fig. 7.1). We use the extent and shape of the rupture plane to estimate the landslide-affected area and to define the rupture-plane distance r_{rup}, the shortest distance from the rupture plane. We follow the approach of Somerville et al. (1999) to identify the asperity from the rupture-plane model, which is is the area with more than 1.5 times the average slip.

The underground structure in terms of seismic velocities (v_P, v_S) and density (ρ) (Koketsu et al., 2012) is available for 23 layers down to the mantle in ≈ 0.1 degree resolution covering all of Japan; we only consider the layers of the upper 0.5 km to compute a velocity average for the MAF.

NIED provides data for the subsurface shear wave velocities (v_{S30}) as well as site amplification factors S_{amp}. Contrary to v_S by Koketsu et al. (2012), v_{S30} is derived for the upper 30 m only and is more suitable for energy estimates, which require velocities at the surface (recording station). The site amplification factor S_{amp} describes how much seismic waves are amplified by, independent of their frequency.

7.2.4 Landslide data

Detailed landslide data are provided by NIED as polygons (Fig. 7.1), mapped from aerial imagery with sub-metre resolution at different times after the Kumamoto earthquake. The first data set contains landslides that were identified between 16 and 20 April, though the area close to the summit of Mt Aso was not covered. A second data set was collected on April 29, 2016 and covers those parts of Mt Aso that remained unmapped. However, the second data set may contain rainfall-induced landslides, since the rainy season in Kyushu starts in May (Matsumoto, 1989), and there was rainfall after the Kumamoto earthquake and landslides triggered by volcanic activity. We selectively combine the two data sets for this study, using only those landslides from the second database, which are also partly present in the first data set. We exclude any rainfall triggered landslides with this approach, though possibly omitting seismically induced landslides exclusive to the second database. However, the area in question is comparatively small to the full extent of the study area, and the missing landslides are minor in terms of their area.

Several landslides cluster $\approx$ 80 km to the northeast of

the mainshock in the municipalities Yufu and Beppu (Fig. 7.1), which were hit by a triggered earthquake (Uchide et al., 2016). We hypothesize that the distant northeastern landslides were induced by this triggered event. This also explains the considerable gap in landslides ($\approx$ 50 km) between Yufu and Aso (Fig. 7.1) in otherwise steep topography. Hence we exclude the landslides near Yufu and Beppu (<10% of all landslides, <3% of total landslide area) from our database.

Apart from the special release of landslide data for the 2016 Kumamoto earthquake, NIED hosts a landslide database for all Japan (National Research Institute for Earth Science and Disaster Prevention, 2014). This database covers unspecified landslides of any origin. We extract a subset from this landslide database to compare it with the landslides triggered by the Kumamoto earthquake. Contrary to the special Kumamoto release, only the landslide deposits are mapped as polygons, whereas the scarps are mapped as lines. We manually define polygons representing the total landslide area bound by the scarp line and covering the deposit area to make both data sets comparable and because the landslide source area is generally not identical to the deposit area.

7.3 Total area affected by landsliding

We define the landslide-affected area, in which coseismic landsliding occurred, as the area spanned by the rupture-plane distance covering 97.5 % of the total landslide area (Harp & Wilson, 1995; Marc et al., 2017). Thus the total landslide-affected area is 3968.6 km^2 and is within 22.9 km distance from the rupture plane.

An M_W 7.1 event with a fault length of 53.5 km and an asperity length of 12.78 km (3 km) results in a landslide-affected area of 3914 km^2 (4406 km^2) using parameters proposed by Marc et al. (2016). We derived the event depth of 11.1 km as the moment weighted average of the rupture model of Kubo et al. (2016). Both estimates are consistent with our area estimate. Marc et al. (2016) introduced a topographic constant, A_{topo}, relating the total landslide area to the area that excludes basins and inundated areas. We estimate A_{topo} from the ALOS land cover, finding that 97 % of all landslides occurred in areas without anthropogenic influence, i.e. land with urban and agricultural use, and water bodies. We exclude water bodies, urban areas—predominantly the metropolitan area of Kumamoto City, and rice paddies from the topographic analysis, obtaining an affected area of 3037 km^2, i.e. $A_{\text{topo}} = 0.68$.

7.4 Total landslide area

Total landslide area is linked to several earthquake parameters, mostly magnitude and hypocentre or average rupture-plane depth (Keefer, 1984; Marc et al., 2016). We adopted the relation by Marc et al. (2016) to check for completeness of the total landslide area of 6.38 km^2. The actual total landslide failure plane is likely smaller, as the NIED data set provides the combined area of depletion and accumulation. The modal hillslope inclination is estimated at 15°. Instead of the earthquake magnitude scaling relation (Leonard, 2010) used by Marc et al. (2016), we use the rupture extent reported by Kubo et al. (2016). The area model requires the average length of the seismic asperities, which Marc et al. (2016) globally assumed to be 3 km. However, Somerville et al. (1999) derived a relationship of asperity sizes based on the seismic moment that results in an average asperity length of 12.78 km for the 2016 Kumamoto earthquake. This length is consistent with the asperity sizes found by Yoshida et al. (2017) for their finite rupture model. The estimated landslide area with an asperity length of 3 km results in a predicted total landslide area of 12.90 km^2, while with the magnitude scaled asperity size of Somerville et al. (1999), the landslide area is 3.03 km^2. The landslide area estimates with constant asperity length and moment-dependent asperity length differ by a factor of 2 and 0.5 from the NIED data set, respectively.

Landslide concentration is defined as landslide area per area at a given distance band (Meunier et al., 2007). For the seismic processing, we consider the rupture-plane distance r_{rup} based on the rupture model instead of the hypocentral distance (Meunier et al., 2007) or the Joyner–Boore distance (Harp & Wilson, 1995).

7.5 Ground motion and seismically induced landsliding

7.5.1 Coseismic landslide displacement

The sliding-block model of Newmark (1965) is widely used to estimate coseismic hillslope performance (e.g. Kramer, 1996; Jibson, 1993, 2007). The model estimates the permanent displacement on a hillslope affected by ground motion. Newmark (1965) established a relation for hillslope displacement in terms of the maximum velocity at the hillslope for a single rectangular pulse, v_{max} $\left(\text{m s}^{-1}\right)$

$$d_s = \frac{v_{\text{max}}^2}{2}\left(\frac{1}{A a_{\text{y}}} - \frac{1}{A}\right) \tag{7.3}$$

where A is the magnitude of the acceleration pulse and a_{y} $\left(\text{m s}^{-2}\right)$ the yield acceleration, which is the minimum pseudostatic acceleration required to produce instability. For downslope motion along a sliding plane, a_{y} is related to the angle of internal friction, ϕ_f and the hillslope inclination, δ, by

$$a_{\text{y}} = g\left(\frac{\tan\phi_f}{\tan\delta}\right)\sin\delta = g(\overline{FS} - 1)\sin\delta \tag{7.4}$$

with the average factor of safety $\overline{FS}$. Chen et al. (2017) characterized unstable hillslopes—related to both rainfall and earthquakes—by a safety factor of $FS < 1.5$.

An upper bound for the displacement, d_s, is based on two ground-motion parameters (Newmark, 1965; Kramer, 1996):

$$d_{\text{max}} = \frac{PGA}{a_{\text{y}}}\frac{PGV^2}{a_{\text{y}}}, \tag{7.5}$$

where PGA $\left(\mathrm{m\,s^{-2}}\right)$ and PGV $\left(\mathrm{m\,s^{-1}}\right)$ are the peak ground acceleration and velocity, respectively. Thus, the coseismic hillslope performance can be characterized by velocity and acceleration. In the following sections, we derive a ground-motion model based on the acceleration-related Arias intensity and the velocity-related radiated seismic energy.

7.5.2 Ground-motion metrics

Though PGA is the most widely used ground-motion metric in geotechnical engineering, the Arias intensity I_A (Arias, 1970) is widely used to characterize strong ground motion for landslides:

$$I_A = \frac{\pi}{2g} \int_{T_1}^{T_2} a(t)^2 dt, \tag{7.6}$$

where $g = 9.80665\ \mathrm{m\,s^{-2}}$ is standard gravity and T_1 and T_2 are the times where strong ground motion starts and cedes (the acceleration $a(t)$ has units of $\mathrm{m\,s^{-2}}$ and the Arias intensity has units of $\mathrm{m\,s^{-1}}$). The Arias intensity captures both the duration and amplitude of strong motion. Empirical relationships between I_A and d_s in terms of earthquake magnitude and epicentre distance have been developed (e.g. Jibson, 1993; Bray & Travasarou, 2007; Jibson, 2007).

Since PGA and I_A are related to each other (e.g. Romeo, 2000) and the hillslope displacement depends on both velocity and acceleration (Eq. (7.3), (7.5)), it is reasonable to characterize velocity similarly to Arias intensity. The velocity counterpart to I_A is $IV2$, the integrated squared velocity (Kanamori et al., 1993; Festa et al., 2008):

$$IV2 = \int_{T_1}^{T_2} v(t)^2 dt \tag{7.7}$$

The squared velocity is also used in radiated seismic energy estimates. The quantity j_E is the radiated energy flux of an earthquake and estimated by (Choy & Cormier, 1986; Kanamori et al., 1993; Newman & Okal, 1998)

$$j_\mathrm{E} = \frac{\rho c}{S_\mathrm{amp}^2} e^{-k r_\mathrm{rup}} IV2 \tag{7.8}$$

where ρ and c are the density and seismic wave velocity at the recording site and S_amp is the site specific amplification factor. The distance from the rupture is given by r_rup, and k is a term for path attenuation (Anderson & Richards, 1975) and effects of transmission and reflection (Kanamori et al., 1993). The attenuation constant k is also influenced by anisotropy and structure heterogeneity (Campillo & Plantet, 1991; Bora et al., 2015). The full definition of the energy flux includes two terms for compressional waves ($c = v_\mathrm{P}$) and shear waves ($c = v_\mathrm{S}$). The radiated energy of an earthquake, E_S, results from the integral over the wavefront surface:

$$E_\mathrm{S} = \iint j_\mathrm{E} dA, \tag{7.9}$$

where A is the area of the surface through which the wave passes at the recording station and represents the geometrical spreading.

The radiated seismic energy E_S describes the energy leaving the rupture area and is related to the seismic moment (Hanks & Kanamori, 1979):

$$E_\mathrm{S} = \frac{\Delta\sigma}{2\mu} M_0, \tag{7.10}$$

where $\Delta\sigma$ is the stress drop, μ the shear modulus, and M_0 the seismic moment. We make use of this relation, when considering the magnitude-related term in the ground-motion model. Since most seismic energy is released as shear waves, we apply the shear wave velocity at the recording site (v_S) to the entire waveform, i.e. we assume that all waves arrive with velocity v_S at a site. This assumption has the advantage that it does not require a separation of the record into P- and S-waveforms, simplifying the computation. In appendix 7.9.2 we show from a theoretical perspective that using a uniform v_S has only a small impact on the overall energy estimate. The site-specific correction term for the energy estimate $\hat{E}$ based on Eq. (7.8) and (7.9) becomes

$$\hat{E} = \frac{\hat{A}\rho v_\mathrm{S}}{S_\mathrm{amp}^2} e^{-k r_\mathrm{rup}} IV2. \tag{7.11}$$

While E_S is the radiated seismic energy at the source, $\hat{E}$ is estimated from the velocity records at a station and only approximates E_S. Therefore, $\hat{E}$ may differ from the true and unknown radiated energy E_S (Kanamori et al., 1993). Several assumptions characterize $\hat{E}$:

All energy is radiated as S-waves in an isotropic, homogeneous medium

Geometrical spreading is corrected for an isotropic, homogeneous medium

Since $IV2$ (Eq. (7.7)) depends on the radiation pattern, $\hat{E}$ depends on the azimuth

Attenuation is homogeneous

Surface waves are not considered

Site amplification is frequency-independent

Below, we investigate the azimuthal variation in the energy estimates to characterize the radiation pattern.

The estimated wavefront area $\hat{A}$ is related to the rupture extent and r_rup, and $\hat{A}$ corresponds to a simplified version of the wavefront area approximation by Schnabel & Bolton Seed (1973) and Shoja-Taheri & Anderson (1988):

$$\hat{A} = 2WL + \pi r_\mathrm{rup}(L + 2W) + 2\pi r_\mathrm{rup}^2. \tag{7.12}$$

The extent of the rupture is assumed to be rectangular with length L and width W. Equation (7.12) describes a cuboid with rounded corners and with only half of its surface considered, because no energy flux is assumed to be transmitted above ground.

While the geometrical spreading correction is expressed analytically as the wavefront area $\hat{A}$, we estimate the attenuation parameter k. Attenuation changes with distance, as a power law at short distances (< 150 km) (Anderson & Richards, 1975) and longer distances are not considered. An empirical attenuation relationship is

$$\ln Y = C + kr_{\text{rup}}, \tag{7.13}$$

where Y is

$$Y = \frac{\hat{A}\rho v_S}{S_{\text{amp}}^2} \int_{T_1}^{T_2} IV2, \tag{7.14}$$

i.e. the logarithm of the energy estimate without the attenuation term $e^{-kr_{\text{rup}}}$ from Eq. (7.11). The dummy variable C is only used for estimating k and not in the final correction for attenuation. A distance-independent form of the Arias intensity, i.e. corrected for geometrical spreading and attenuation, is defined by

$$I_{\text{A,A}} = \frac{\hat{A}}{S_{\text{amp}}^2} e^{-kr_{\text{rup}}} I_A, \tag{7.15}$$

where k is determined by Eq. (7.13) and setting $Y = I_A\hat{A}$. The corrected Arias intensity $I_{\text{A,A}}$ is the acceleration-based counterpart to $\hat{E}$.

Low-frequency effects, like directivity, are better captured with a velocity-based metric (e.g. azimuth-dependent energy estimate), than an acceleration-based metric (Arias intensity) alone.

In terms of the Fourier transform, the sensitivity of acceleration at higher frequencies becomes apparent, as the Fourier transform of the time derivative of any function is

$$\mathcal{F}(\dot{f}(t)) = i\omega\mathcal{F}(f(t)), \tag{7.16}$$

and thus scales with frequency in the spectrum. The frequency sensitivity of $IV2$ and I_A is related to the squared spectrum given the metrics. For example, in Fig. 7.3 we show the different spectral sensitivities of $IV2$ and I_A for a theoretical seismic source spectrum (Brune, 1970). $IV2$, and thus $\hat{E}$, has a higher sensitivity to lower frequencies than I_A. The low-frequency part of the spectrum can be accounted for by considering $IV2$ in a ground-motion model.

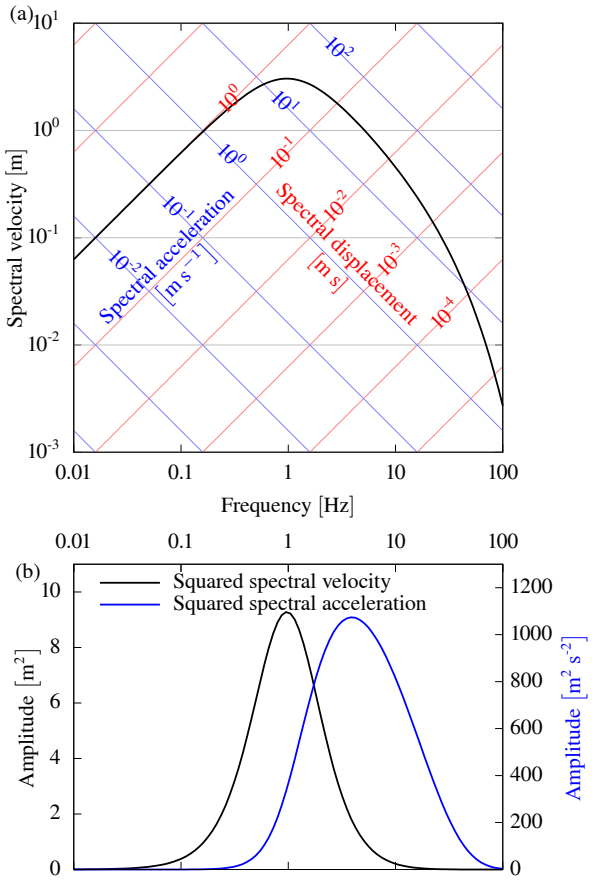

Figure 7.3: a) Far-field spectrum after Brune (1970). The spectrum can be read as displacement (red), velocity (black) and acceleration (blue). b) The squared Brune spectrum corresponds to the frequency sensitivity of velocity-based $IV2$ (blue) and the acceleration-based I_A (black).

7.5.3 Landslide-related ground-motion models

The basic form of landslide-related ground-motion models for Arias intensity is based on earthquake magnitude M and distance from the earthquake rupture r (e.g. Harp & Wilson, 1995).

$$\ln I_A = p_1 + p_2 M + p_3 \ln r \tag{7.17}$$

This form is widely used (Keefer, 1984; Harp & Wilson, 1995). In engineering seismology, ground-motion models usually have an additional distance term for anelastic attenuation:

$$\ln I_A = c_1 + c_2 M + c_3 r + (c_4 + c_5 M)\ln r. \tag{7.18}$$

This is a modified version of the model template by Kramer (1996). While Eq. 7.17 and Eq. 7.18 share some parameters (p_1, c_1 and p_2, c_2), the geometric spreading term includes not only distance dependence (p_3, c_4) but also has a magnitude-dependent component (c_5). In addition, anelastic attenuation is included as well (related to c_3) in Eq. 7.18. The template of Kramer (1996) relates to the majority of GMMs in engineering seismology. Models of this kind address strong motion in the context of landsliding (Travasarou et al., 2003; Bray & Rodriguez-Marek, 2004). The incorporation of anelastic attenuation is less common in landsliding GMMs and not mentioned in these studies but is included in more recent studies (Meunier et al., 2007, 2013; Yuan et al., 2013).

We exchange the magnitude term from Eq. (7.18) with a site-dependent energy term, assuming that landsliding is more related to the energy of incoming seismic waves than to the moment at the source. We replace moment magnitude by the logarithm of energy (Eq. (7.11)), since energy is proportional to the seismic moment M_0 (Eq. (7.10)). Based on the site-dependent energy estimate $\hat{E}$, we propose the model

$$\ln I_A = c_1 + c_2 \ln \hat{E} + c_3 r + (c_4 + c_5 \ln \hat{E}) \ln r \quad (7.19)$$

The five coefficients are inferred by non-linear least squares (e.g. Tarantola, 2005). We use the rupture-plane distance (r_{rup}), i.e. the shortest distance between a site and the rupture plane.

7.5.4 Rupture directivity model

In the NGA-west2 guidelines (Spudich et al., 2013), the directivity effect is modelled by isochrone theory (Bernard & Madariaga, 1984; Spudich & Chiou, 2008) or the azimuth between epicentre and site (Somerville et al., 1997). We use the latter approach and model directivity for estimated energy and corrected Arias intensity in a simplified way:

$$\ln \hat{E}_\theta = \ln \hat{E}_0 + a_{\text{E}} \cos(\theta - \theta_{\text{E}}) \quad (7.20)$$

$$\ln I_{\text{A,A},\theta} = \ln I_{\text{A,A,o}} + a_{\text{I}} \cos(\theta - \theta_{\text{I}}), \quad (7.21)$$

where $\hat{E}_0$ and $I_{\text{A,A,o}}$ are the offset (average), a_{E} and a_{I} the amplitude of variation with azimuth, and θ_{E} and θ_{I} are the azimuths of the maximum. The definition of θ is similar to that of Somerville et al. (1997) for the angle measured between the epicentre and the recording site with the difference of being measured clockwise from the north. The azimuths of the maximum, θ_{E} and θ_{I}, are free parameters because (1) the rupture is assumed to have occurred on two faults and has thus variable strike and (2) the event is not pure strike-slip and has a normal faulting component. We therefore do not expect a match between the rupture strike and θ_{E} and θ_{I}. The geometrical spreading is already incorporated in the energy estimate as a distance term (Somerville et al., 1997; Spudich et al., 2013).

7.5.5 Model for fault-normal-to-fault-parallel ratio

The ratio of the response spectra of the horizontal sensor components is a function of oscillatory frequency f_{osc}.

The north and east components (E, N) of the sensor are rotated to be fault-normal (FN) and fault-parallel (FP) with fault strike ϕ.

$$\text{FN} = E \cos\phi - N \sin\phi \quad (7.22)$$

$$\text{FP} = E \sin\phi + N \cos\phi \quad (7.23)$$

$$\text{FN/FP} = \frac{\text{SA}_{\text{FN}}(f_{\text{osc}})}{\text{SA}_{\text{FP}}(f_{\text{osc}})} \quad (7.24)$$

The response spectra are calculated from accelerograms after Weber (2002), with a damping of $\zeta = 0.05$.

The amplitudes of waves parallel to rupture propagation differ from waves normal to propagation on top of the directivity effect. This variation depends on the azimuth and is larger only at high periods. The fault-normal response amplitude is larger than the fault-parallel response if directed parallel or antiparallel to the rupture. We model the ratio similar to Somerville et al. (1997):

$$\ln(\text{FN/FP}) = (b_1 + b_2 f_{\text{osc}}^{b_3} \cos(2(\theta - \theta_R)) H(b_1 + b_2 f_{\text{osc}}^{b_3}), \quad (7.25)$$

where parameters b_i describe the relationship of the oscillatory frequency to the ratio, θ is the azimuth (Eq. (7.20)), and θ_R is the azimuth of the maximal ratio. The ratio azimuth is as subject to assumptions as is its counterpart θ_{E}. The Heaviside function $H(\cdot)$ avoids negative values in the model, which would be equivalent to an undesired phase shift in the cosine term.

We introduced a functional form for oscillatory frequency dependence with four parameters in Eq. (7.25). We did not introduce a distance term and apply the model only to data with $r_{\text{rup}} \leq 50$ km.

7.6 Results

7.6.1 Topographic analysis

Landslides occurred mostly in tephra layers (Fig. 7.2a,b) covered by forests (Fig. 7.2d,e) and predominantly along the NE rupture segment. Nearly all landslides concentrated on hillslopes with a steepness 15° and 45° and an MAF $\approx$ 1 (Fig. 7.4a,c). Hillslope inclination and the MAF were higher towards the landslide crown (Fig. 7.4b,d), indicating a progressive landslide failure starting from the crown, consistent with numerical simulations by Dang et al. (2016). The TWI is linked to land cover and is highest in areas with rice paddies (Fig. 7.2i). Terrain with landslides has a uniformly low TWI, thus we cannot evaluate the hydrological impact on the earthquake-related landslides (e.g. Tang et al., 2018).

Most landslides originated at locations with amplified ground accelerations and steep hillslopes and ran out on flatter areas with less amplified ground acceleration. Landslides—interpreted as shear failure—start as mode II (in-plane shear) failure at the scarp and mode III (anti-plane shear) failure at the flanks (McClung, 1981; Fleming & Johnson, 1989; Martel, 2004). At later stages of the landslide rupture, mode I (widening) failure can also occur in

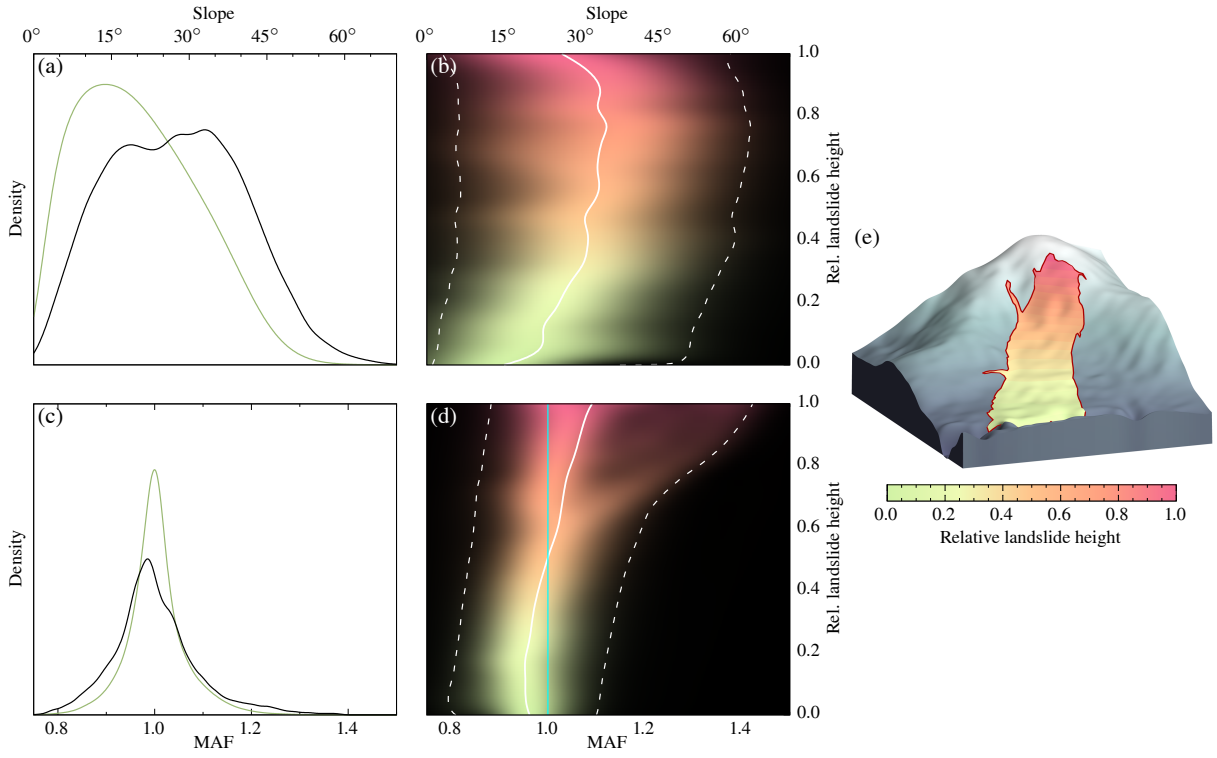

Figure 7.4: Distribution of hillslope inclination and MAF. The left column shows (a) hillslope inclinations and (c) MAF within the landslide-affected area (green), and within the landslide areas (black). The right column presents (b) hillslope inclinations and (d) MAF in different segments of the landslide areas which is expressed as relative height. Segments towards to the toe (relative height 0.0–0.5) are in green, and towards the crown are in red (relative height 0.5–1). The solid line is the mean, and the dashed lines enclose the 95 % uncertainty range. The concept of relative height is illustrated for the Aso Ohashi landslide in (e). MAF<1 indicates attenuation and MAF>1 amplification of seismic waves due to topography. The cyan line in (d) highlights MAF = 1, i.e. no amplification or attenuation.

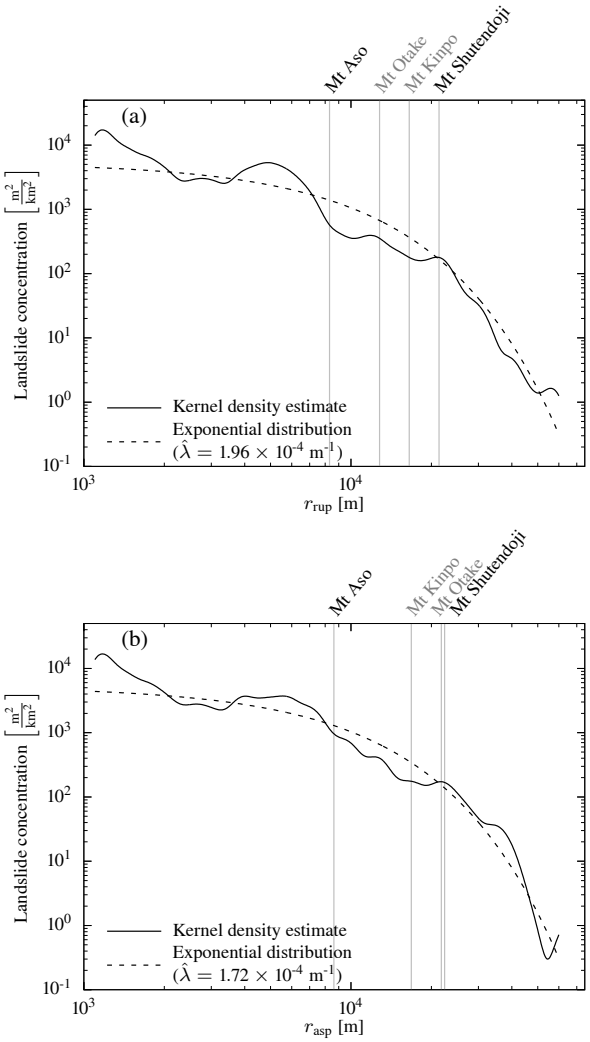

Figure 7.5: Landslide concentration with (a) rupture distance r_{rup} and (b) asperity distance $r_{asp}$of the Kumamoto earthquake landslides. The rate parameter of the exponentially decaying landslide concentration is estimated by maximum likelihood. The distances to the four peaks shown in Fig. 7.1 are given. Densities change little with distance metric, as highlighted by the similar kernel density estimates and the near-identical rate parameter estimates $\hat{\lambda}$. The landslide concentration for Mt Aso depends more on the distance metric than for the other three locations. The more distant mountains have very similar concentrations despite differences in distances (in particular Mt Otake). However, when compared to Fig. 7.7, Mt Shutendoji has a higher landslide concentration than Mt Kinpo and Mt Otake, despite being the farthest away.

the process (Martel, 2004). Simulations of elliptic landslides by Martel (2004) show that either the most compressive or the most tensile stresses are parallel to the major axis of the landslide, coinciding with the average landslide aspect. Yamada et al. (2013) and Yamada et al. (2018) show for several Japanese landslides that peak forces were aligned parallel to the long side of the landslides; Allstadt (2013) shows from waveform inversion for the Mt Meager landslide that force and acceleration were parallel to the long side of the landslide source area.

Mt Aso and its caldera and Mt Shutendoji had a high density of landslides (Fig. 7.5), whereas Mt Kinpo and Mt Otake had none, despite being closer to the epicentre and being comparably close to the rupture (Fig. 7.5). All these locations have comparable rock type, land cover, hillslope inclination, and MAFs. Hence, lithology, land cover, and topographic characteristics are insufficient in explaining the landslide distribution and concentration with respect to the hypocentre or the asperity.

The azimuthal density—with respect to the asperity centroid—of the unspecified landslides follows to some extent the distribution of hillslope inclinations $> 19^\circ$ in the landslide-affected area (Fig. 7.6b and c). This similarity shows that the abundance of unspecified landslides mimics the steepness of topography in the region. Densities are higher towards Mt Kinpo (W), Mt Otake (WSW), Mt Shutendoji (N), Mt Aso (E), and the Kyushu mountains (SE). The coseismic landslide distribution differs completely from the distributions of unspecified landslides and their surrounding topography (Fig. 7.6), respectively, as nearly all landslides happened to the northeast of the epicentre close to the rupture plane (Fig. 7.7). Chen et al. (2017) identified only 29 landslide reactivations during the Kumamoto earthquake. The contrast between the distributions of unspecified landslides and earthquake-related landslides indicates a contribution by the rupture process.

7.6.2 Impact of finite source on ground motion and landslides

The results of the seismic analysis are given for waveforms, the basis for $\hat{E}$ and I_A, and response spectra, used for FN/FP. To the northeast, signals with forward directivity are shorter in duration, with one or a few strong pulses (Fig. 7.8, top right). Waveforms with backward directivity to the southwest of the rupture are longer, with no dominant pulse (Fig. 7.8, bottom left). Waveforms parallel to the rupture have an intermediate duration. Waveforms in either forward or backward direction have stronger amplitudes in the fault-normal direction, whereas waveforms outside the directivity-affected regions have stronger amplitudes in the fault-parallel direction (Fig. 7.8, top left).

We estimated energies $\hat{E}$ from the three-component waveforms. For the Arias intensity, both horizontal components are used. The geometrical spreading A is calculated according to Eq. (7.12), with a rupture length of L =53.5 km and width of W =24.0 km. Any remaining distance dependence has been corrected for by estimating and applying the attenuation parameter k (Eq. (7.13))

After the determination of k, $\hat{E}$ and $I_{A,A}$ are consid-

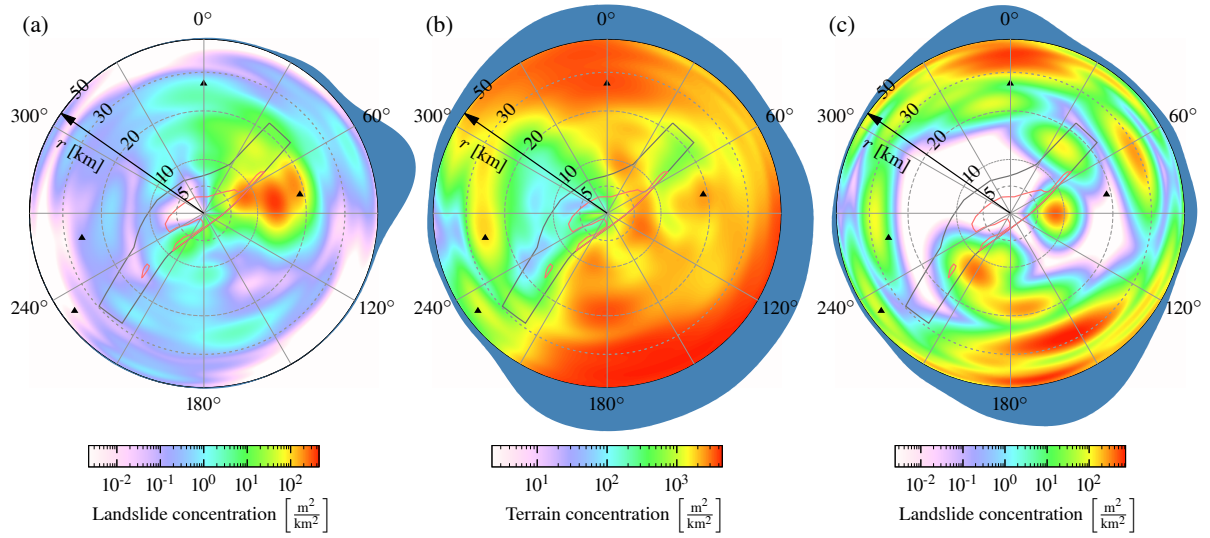

Figure 7.6: Kernel density estimates of azimuth and distance of (a) landslide concentration of the coseismic landslides, (b) concentration of landslide-susceptible terrain with hillslope inclinations >19°, and (c) landslide concentration of unspecified landslides. Azimuth and distance are with respect to the asperity centroid. The marginal densities with respect to azimuth are shown in blue as outer ring. The densities are normalized to their maxima.

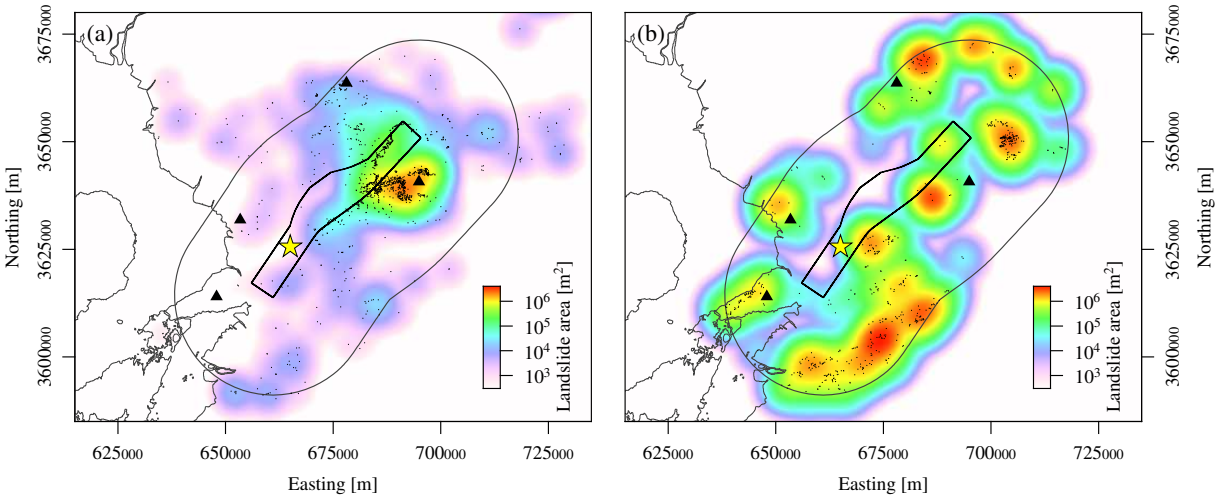

Figure 7.7: Spatial distribution of landslides. (a) Coseismic landslides. The total landslide area at a location is shown as a colour-coded smooth function in the background; (b) same as in (a) but for unspecified landslides within the landslide-affected area of the Kumamoto earthquake.

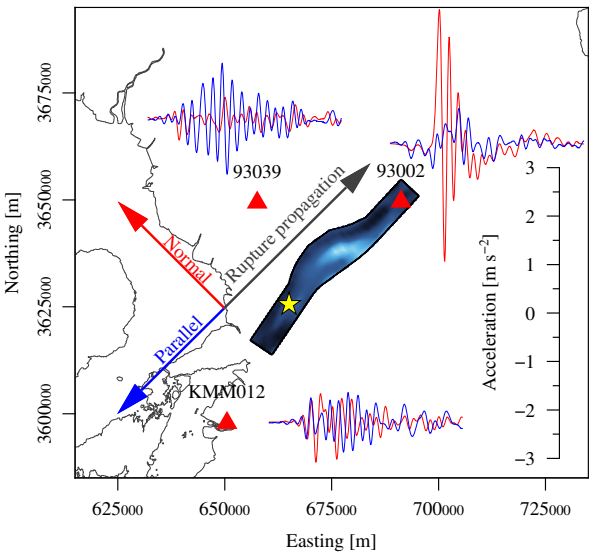

Figure 7.8: Characteristic waveforms observed in the vicinity of the rupture exhibiting rupture directivity effects. Station 93002 is in the forward-directivity region with a large amplitude pulse on the fault-normal component. Station 93039 is also in the forward-directivity region but with an offset to the rupture. In this region the fault-parallel component has higher amplitudes. The station KMM012 is in the backward-directivity region and waveforms have longer duration without large amplitudes. The waveforms are low-pass filtered at 1.2 Hz.

ered distance-independent and can be investigated for azimuthal variations. With a reference point for the azimuth at the epicentre, $\hat{E}$ shows oscillating variations in amplitude with azimuth (Fig. 7.9a), while $I_{A,A}$ exhibits a similar amplitude variations over the entire azimuthal range (Fig.7.9b). The running average based on a von Mises kernel ($\kappa_{vM} = 50$) of $\hat{E}$ and $I_{A,A}$ shows increased $\hat{E}$ between 45° and 135°, i.e. approximately parallel to the strike. Minimal values of $\hat{E}$ occur in the opposite direction (200°–300°). The running average of $I_{A,A}$ has several fluctuations, but these are not as wide and large as those of $\hat{E}$. The azimuthal variation in $\hat{E}$ indicates the rupture directivity, and the absence of large variations in $I_{A,A}$ indicates that the directivity effect is only evident at lower frequencies (compare with Fig. 7.3).

The azimuthal variation in $\hat{E}$ and $I_{A,A}$ is modelled according to Eq. (7.20). We estimate parameters for two scenarios:

directivity is assumed, resulting in azimuthal variations where a_E and a_I are free parameters,

directivity is not assumed, resulting in no azimuthal variations with $a_E = a_I = 0$.

The two models are compared with the Bayesian information criterion (BIC; Schwarz, 1978) for a least-squares fit:

$$BIC = n \ln N + N \ln \hat{\sigma}^2, \tag{7.26}$$

where n is the number of estimated parameters (n =4 for the first case, n =2 for the second case), N is the number of data, and $\hat{\sigma}^2$ is the variance of the model residuals. The model with the smaller BIC is preferable. The starting values of the parameters are the mean of $\hat{E}$ and $I_{A,A}$, no azimuthal variation (a_d =0), and the azimuths of the maximum of $\hat{E}_\theta$ and $I_{A,A,\theta}$ are set to the strike of the fault ($\theta_E = \theta_I = 225°$).

The directivity model for $\hat{E}$ follows the trend of the data and the running average closer than the model without directivity (Fig. 7.9a). According to BIC, the model with directivity is preferable ($BIC_{\text{directivity}}$ = -110, $BIC_{\text{no directivity}}$ = -11). In the case of the Arias intensity, the difference in BIC between the two models is less compared to the azimuth-dependent energy (Fig. 7.9b). Here, the model without directivity is the preferred one ($BIC_{\text{directivity}}$ = 30, $BIC_{\text{no directivity}}$ = 22). In consequence, azimuthal variations in wave amplitudes and energy related to the directivity effect occur at lower frequencies.

The forward-directivity waves contain a very strong low-frequency pulse (Fig. 7.8). The pulse amplitude depends on the ratio of rupture and shear wave velocity and the length of the rupture (Spudich & Chiou, 2008). The forward-directivity pulse is superimposed by high-frequency signals in acceleration traces but becomes more prominent in velocity traces (Baker, 2007) due to its low-frequency nature, i.e. below 1.6 Hz (Somerville et al., 1997).

The low-frequency azimuthal variations are also reflected in the spectral response of the waveforms. Spectral accelerations of stations with $r_{rup} \leq$50 km were computed from 0.1 Hz to 5 Hz at intervals of 0.01 Hz for the fault-normal and fault-parallel component. The distribution of FN/FP shows decreasing azimuthal variability with increasing oscillatory frequency (Fig. 7.11, Fig. 7.11). FN/FP is most variable with azimuth at low oscillatory frequencies (0.1 – 1 Hz; Fig. 7.11a); variations are much smaller between 1 and 2.5 Hz (Fig. 7.11b) and nearly absent above 2.5 Hz (Fig. 7.11c). This decrease with frequency is captured by the FN/FP model (Eq. (7.25); Fig. 7.10). Since our model is an average over the covered distance, with an average rupture distance of 25.06 km, we compare it to the FN/FP model of Somerville et al. (1997) at 25 km (Fig. 7.10, Fig. 7.11). Both models show a similar decay with frequency, with our model predicting a slightly higher FN/FP. Therefore, the wave polarity ratio related to rupture directivity is pronounced at lower frequencies and dissipates with increasing frequency, similar to the azimuthal variations observable in energy estimates (lower frequencies), but not in Arias intensity (higher frequencies).

The pattern of low-frequency ground motion is well reflected in that of the landslides. The azimuthal variation in $\hat{E}$ coincides with that of landslide concentration (Fig. 7.9). Both azimuth-dependent energy and landslide concentration have a similar trend, with the maximum being parallel to rupture direction and the minimum strike being antiparallel. The orientation of maximum FN/FP is also reflected in the landslide aspect. The northwest and east directions show higher landslide density (Fig. 7.12a). The highest density of landslides has a northwestern aspect in agreement with maximum FN/FP, both perpendicular to the strike. The eastward increased density is mostly due

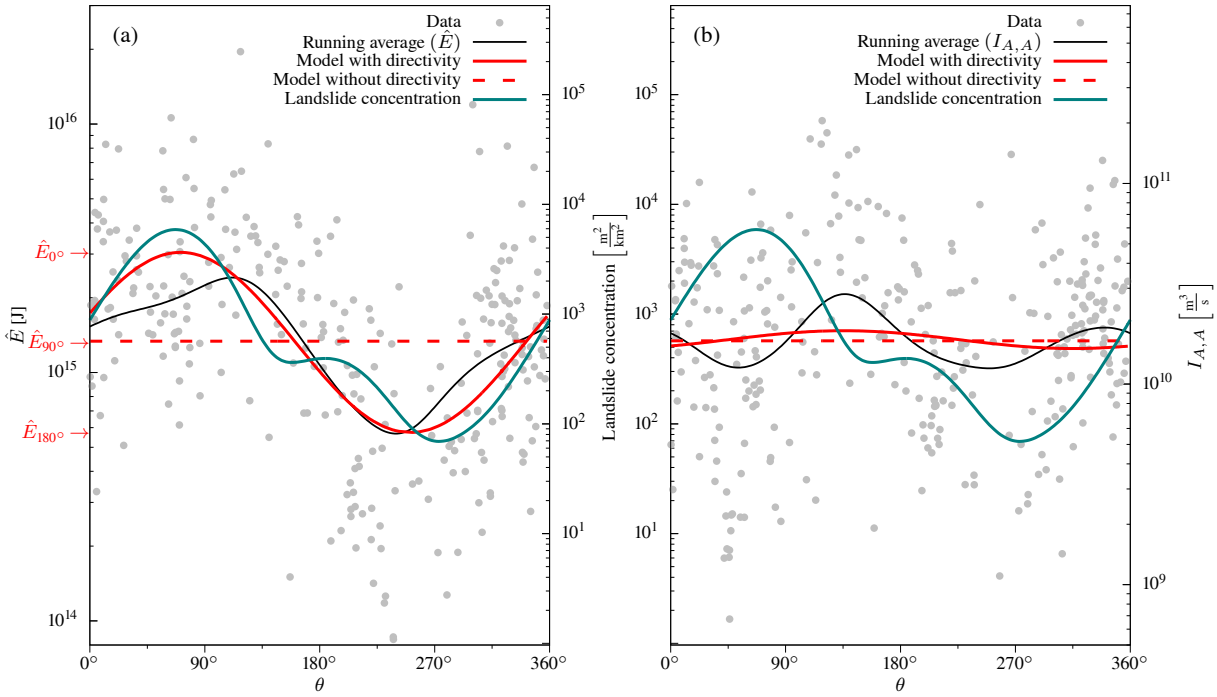

Figure 7.9: (a) Energy estimates ($\hat{E}$) over azimuth.; (b) same as in (a) but for Arias intensity with correction for geometrical spreading ($I_{A,A}$).

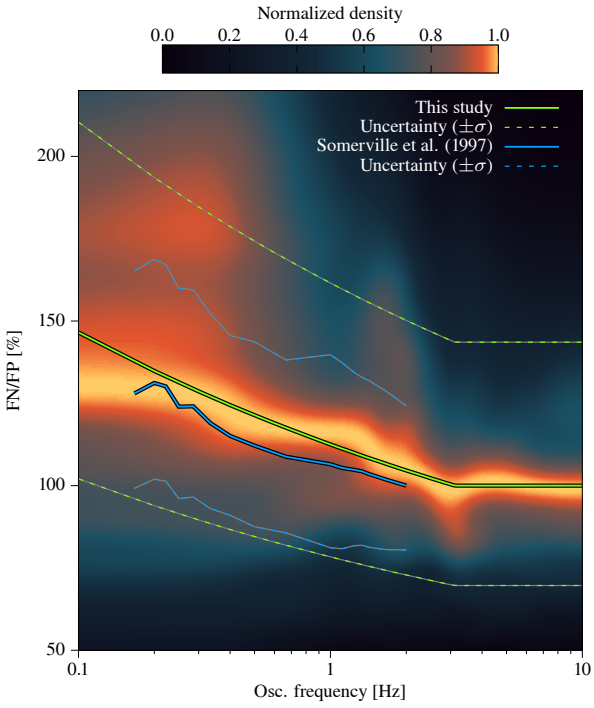

Figure 7.10: Kernel density estimate of the amplitude ratio of response spectra of fault-normal and fault-parallel components (FN/FP) with respect to oscillatory frequency. Beyond 2–3 Hz FN/FP variations cease, as highlighted by our model and the model by Somerville et al. (1997).

Table 7.1: Parameters for ground-motion models

	Model using M_W	Model using $\hat{E}$
c_1	4.083	1.453×10^{1}
c_2	1.991×10^{-1}	-2.682×10^{-1}
c_3	-2.899×10^{-5}	-3.059×10^{-5}
c_4	-4.343×10^{-1}	-3.287
c_5	-8.962×10^{-3}	8.114×10^{-2}

to landslides very close to the rupture. A look at different distances reveals that the increased density of landslides facing east by southeast is at very short distances ($r_{rup} \leq 2.5$ km; Fig. 7.14), while the northwest-facing landslides are further away (2.5 km $< r_{rup} \leq 6$ km). Only minor landslides are farther away with no specific pattern.

The distribution of aspect and hillslope inclination in the landslide-affected area varies little with aspect (Fig. 7.12b).. The distinct northwest and east orientation of landslides is not an artefact of the orientation of the topography in the landslide-affected area (7.12a,b). The unspecified landslides in the affected area have a near-northward aspect and deviate by $\approx$ 30° from the earthquake-triggered landslides (Fig. 7.12c). This highlights that the earthquake affects landslide locations (Fig. 7.6) and will force failure on specific slopes facing in the direction of ground motion (Fig. 7.12, 7.14).

7.6.3 Ground-motion model for Kumamoto

We derived two ground-motion models for Arias intensity from data with $r_{rup} \leq 150$ km (Tab. 7.1; Fig. 7.15). One model incorporates the azimuth-dependent seismic energy (Eq. (7.19)). The other is a conventional isotropic

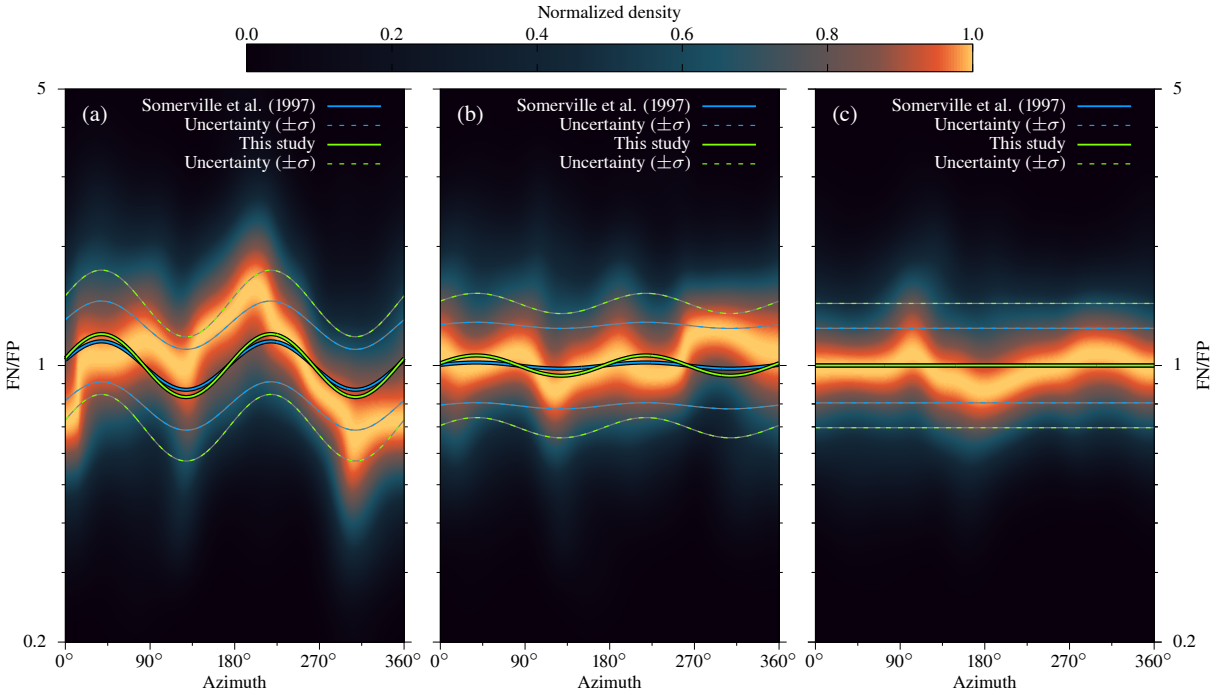

Figure 7.11: Kernel density estimate of FN/FP with azimuth obtained from response spectra for three different oscillatory frequency ranges: (a) 0.1–1 Hz, (b) 1.0–2.5 Hz, and (c) >2.5 Hz. For each plot, our FN/FP model and the model by Somerville et al. (1997) are shown for (a) 0.55 Hz, (b) 1.75 Hz, and (c) 4 Hz. As in Fig. 7.10, amplitudes decrease with increasing oscillatory frequency.

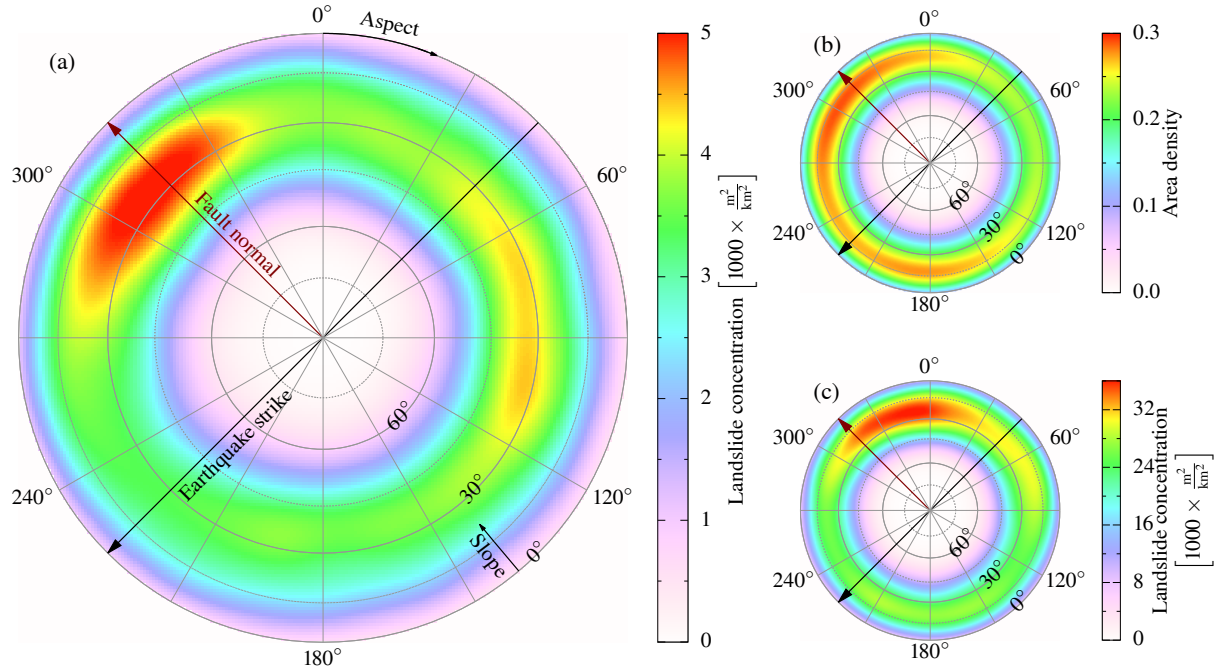

Figure 7.12: (a) Aspect and hillslope inclination distribution within areas of the earthquake-triggered landslides. This distribution is normalized by the distribution of the aspect of all hillslopes in the landslide-affected area. The black line denotes the strike of the Kumamoto earthquake (225°) (b) Distribution of aspect and hillslope inclination in the landslide-affected area. (c) same as in (a) but for unspecified landslides.

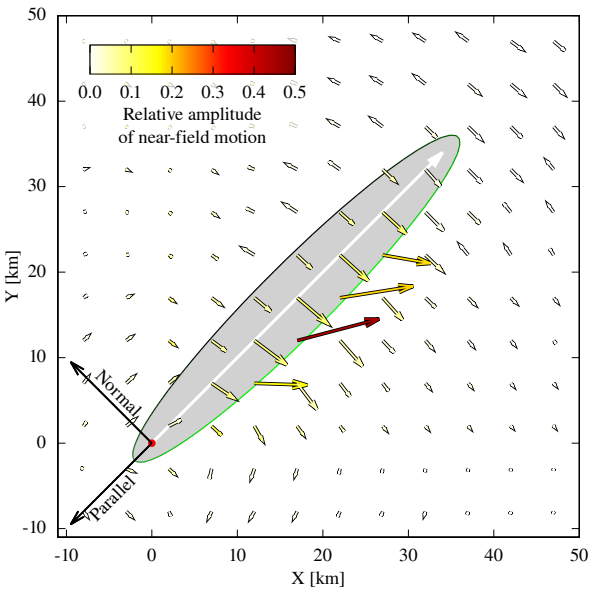

Figure 7.13: Orientation of horizontal peak ground acceleration for the simulated waveforms. The arrow length scales with magnitude of acceleration. The simulated rupture plane is oriented as the rupture plane of the Kumamoto earthquake (strike: 225°, dip: 70°) and of elliptic shape (grey). The upper side is denoted by the green line, and the lower half is denoted by black. The rupture process originated at the hypocentre (red dot) with circular propagation outwards (white arrow).

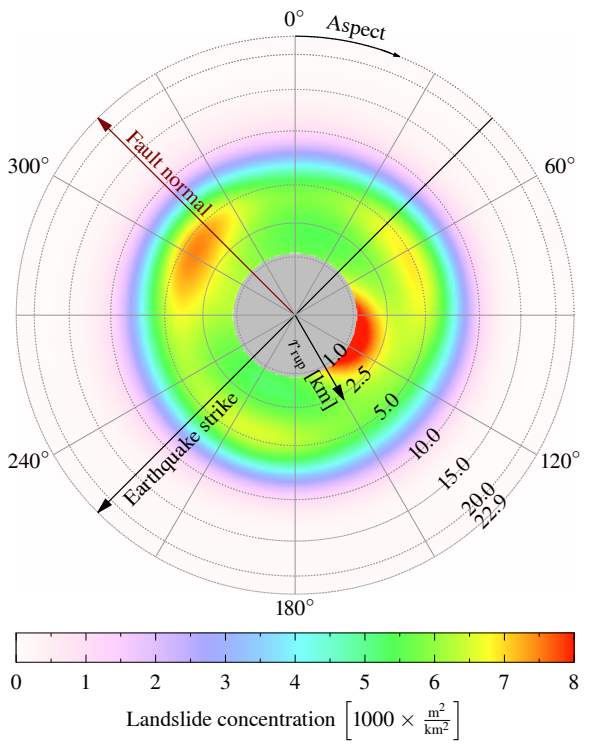

Figure 7.14: Distribution of landslides with aspect and rupture distance. The rupture distance is measured from the model by Kubo et al. (2016). This model does not completely reach the surface, truncating distances below 1 km. The distribution has been normalized by the distribution of aspect of the affected area.

moment magnitude-dependent model (Eq. (7.18)). The decay of Arias intensity with distance for both models fits the running average (anti)parallel and is proportional to the decrease in landslide density with distance. Variation in estimated energy is well covered by the model and spans more than two orders of magnitude, resulting in a variation in Arias intensity of nearly one order of magnitude.

The magnitude-based model is nearly equivalent to the energy-based model with $\hat{E} = 1.2 \times 10^{15}$ J. This value is close to the average energy estimate found from energy estimates of the directivity model from Eq. (7.20) ($\hat{E} = 1.3 \times 10^{15}$ J). The closeness of the two values implies that the magnitude-based model can be seen as an average over the azimuth of the energy-based model.

7.7 Discussion

We provide a framework for characterizing coseismic landslides with an integrated approach of geomorphology and seismology, emphasizing here the role of low-frequency seismic directivity and a finite source. Given the observations of ground motion of the Kumamoto earthquake, two questions arise:

1. How specific is the observed ground motion, i.e. is the Kumamoto rupture particularly distinct?

2. As a rupture very close to the surface, how much does seismic near-field motion contribute? The second question arises because many landslides occurred very close to the rupture plane.

However, it is not possible to separate the observed waveforms into near-, intermediate-, and far-field terms. To investigate both questions, we computed theoretical waveforms after Haskell (1964); Savage (1966); Aki & Richards (2002) from a circular rupture on an elliptic finite source with constant rupture velocity in a homogeneous, isotropic, and unbound medium (see Appendix).

Despite the simplified assumptions behind this waveform model, low-frequency ground motion captures the most prominent features of the observed waveforms. Simulated waveforms close to the rupture plane change in polarity orientation towards east–west, while a strong fault-normal polarity appears at larger distances. A decomposition into a near-field term and combined intermediate- and far-field term reveals that the former highly contributes to the ground motion at close distances. The impact of the near-field term may explain the dominance of east-facing landslides close to the rupture (Fig. 7.14).

The simulations also demonstrate the effect of directivity on estimates of radiated energy and Arias intensity. The azimuthal variations in simulated $\hat{E}$ are similar to the observed variations. The Arias intensity of the simulations also has azimuthal variations with the same characteristics as the energy estimate. These variations in Arias intensity are absent in the observed data, indicating that Arias intensity is more influenced by local heterogeneities and scattering than the energy estimates, as these are ignored in the simulations.

The results show that the Arias intensity is not as susceptible to the directivity effect and variations in fault-normal to fault-parallel amplitudes as the radiated energy; because of its higher sensitivity towards higher frequencies, these effects are masked by high-frequency effects such as wave scattering and a heterogeneous medium. We found that the radiation pattern related to the directivity effect is recoverable from energy estimates but not from Arias intensity. This low-frequency dependence is also seen in the response spectra ratios for FN/FP where directivity-related amplitude variations with azimuth have been identified only for frequencies <2 Hz, in agreement with previous work (Spudich et al., 2004; Somerville et al., 1997). We introduced a modified model for Arias intensity using site-dependent seismic energy estimates instead of the source-dependent seismic magnitude to better capture the effects of low-frequency ground motion.

The conventional magnitude-based isotropic model and the azimuth-dependent seismic energy model correlate with the landslide concentration over distance (Fig. 7.15). As in Meunier et al. (2007) it is therefore feasible to use the ground-motion model to model the landslide concentration, $P_{\text{ls}}(I_A)$, by a linear relationship:

$$\ln P_{\text{ls}}(I_A) = a_{\text{I}} + b_{\text{I}} \ln I_A \tag{7.27}$$

Azimuthal variations in landslide density correspond to azimuthal variations in seismic energy and can be described by a similar relationship:

$$\ln P_{\text{ls}}(E) = a_{\text{E}} + b_{\text{E}} \cos(\theta - \theta_{\text{E}}) \tag{7.28}$$

For the Kumamoto earthquake data, we estimate $a_{\text{I}} = 2.1$, $b_{\text{I}} = 2.6$, and $a_{\text{E}} = -31.5$, $b_{\text{E}} = 2.3$. The azimuth-dependent landslide concentration implies similar landslide concentrations at different distances from the rupture, thus partly explaining some of the deviation in Fig. 7.5 and Fig. 7.15.

Compared to the model of Harp & Wilson (1995) (Fig. 7.15) our model uses rupture-plane distance, as opposed to the Joyner–Boore distance (r_{JB}). When using the hypocentral depth as pseudo-depth, the model of Harp & Wilson (1995) overpredicts I_A both at shorter and longer distances—irrespective of the pseudo-depth at larger distances. This misestimate is most likely due to the lack of an additional distant-dependent attenuation term in their model (Eq. (7.17)).

The use of the MAF instead of curvature alone provides a proxy by how much a seismic wave is amplified (or attenuated) for a given wavelength and location. We show that both hillslope inclination and the MAF tend to be lower towards the landslide toe (Fig. 7.4). This effect is linked to the convention that landslide polygons cover both the zone of depletion and accumulation. (Sato et al., 2017) consider the tephra layers rich in halloysite to be the main sliding surfaces indicating shallow landslides (Song et al., 2017). When relating coseismic landsliding to the seismic rupture, only the failure plane of the landslide matters because this is the hillslope portion that failed under seismic acceleration. Chen et al. (2017) noted, for example, that landslide susceptibility and safety factor calculation depend on whether the entire landslide or only parts—scarp area or area of dislocated mass—are considered. The reconstruction of the landslide failure planes is limited to statistical assessments of landslide inventories (Domej et al., 2017; Marc et al., 2019). However, failure may have likely originated close to the crown and then progressively propagated downward the hillslope because MAF > 1 indicates an amplification of ground motion towards the crown of the landslides.

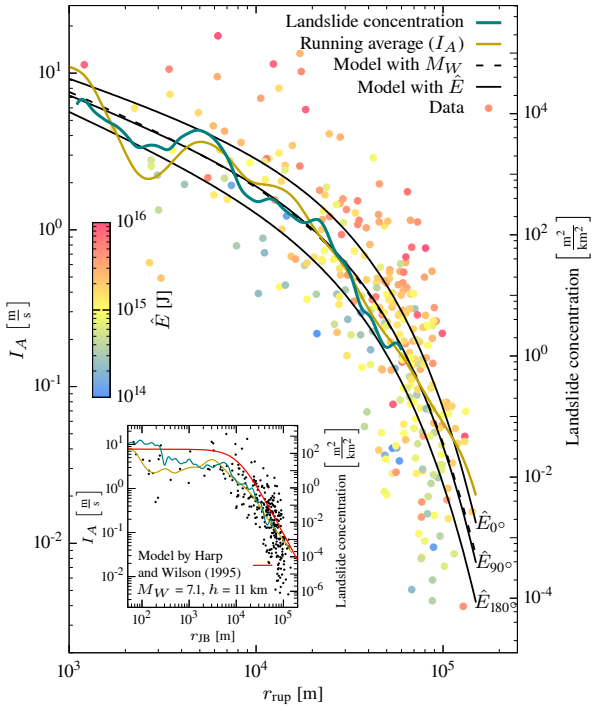

Figure 7.15: Ground-motion model for I_A. The solid lines are the model with energy estimates for three different energy levels as in Fig. 7.9a. The inset figure shows, for comparison, the ground-motion model of Harp & Wilson (1995) (green) and landslide concentration density (red).

Coseismic landslide locations have a uniformly low topographic wetness index, indicating that hydrology may have added little variability to the pattern of the earthquake-triggered landslides; at least we could not trace any clear impact of soil moisture on the coseismic landslide pattern (Tang et al., 2018).

7.8 Conclusions

We investigated seismic waveforms and resulting landslide distribution of the 2016 Kumamoto earthquake, Japan. We demonstrate that ground motion at higher frequencies controls the isotropic (azimuth-independent) distance dependence of Arias intensity with landslide concentration. In addition, ground motion at lower frequencies influences landslide location and hillslope failure orientation, due to directivity and increased amplitudes normal to the fault, respectively. Topographic controls (hillslope inclination and the MAF) are limited predictors of coseismic landslide occur-

rence because areas with similar topographic and geological properties at similar distances from the rupture had widely differing landslide activity (Havenith et al., 2016; Massey et al., 2018). Nonetheless landslides concentrated only to the northeast of the earthquake rupture, while unspecified landslides have been identified throughout the affected region.

We introduced a modified model for Arias intensity using site-dependent radiated seismic energy estimates instead of the source-dependent seismic magnitude to better model low-frequency ground motion in addition to the ground motion at higher frequencies covered by the Arias intensity.

Compared to previous models widely used in landslide-related ground-motion characterization our model is based on state-of-the-art ground-motion models used in engineering seismology, which have two different distance terms, one for geometrical spreading and one for along-path attenuation. The latter is rare in landslide studies (e.g. Meunier et al., 2007; Massey et al., 2018). Our results emphasize that the attenuation term should be considered in ground-motion models, as the landslide concentration with distance mirrors such ground-motion models.

The effect of the earthquake rupture on the rupture process of the landslides results in landslide movements parallel to the strongest ground motion. Due to the surface proximity of the earthquake rupture plane, near-field ground motion influences the aspect of close landslides to be east–southeast. The intermediate- and far-field motion of the earthquake promoted more landslides on northwestern exposed hillslopes, an effect that overrides those of steepness and orientation of hillslopes in the region.

We highlight that coseismic landslide hazard estimation requires an integrated approach of both detailed ground-motion and topographic characterization. While the latter is well established for landslide hazard, ground-motion characterization has been only incorporated by simple means, i.e. without any azimuth-dependent finite rupture effects. Our results for the Kumamoto earthquake demonstrate that seismic waveforms can be reproduced by established methods from seismology. We suggest that these methods can improve landslide hazard assessment by including models for finite rupture effects.

7.9 Appendix

7.9.1 Synthetic waveforms from displacement of a finite rupture

We illustrate the generation of ground displacement as a discontinuity across a rupture fault (e.g. Haskell, 1964, 1969; Anderson & Richards, 1975; Aki & Richards, 2002). The displacement for any point x at time t is given by

$$u_i(\mathrm{x},t) = \iint_\Sigma c_{jkpq} \frac{\partial G_{ip}(D_j(\boldsymbol{\xi},t))}{\partial x_q} n_k d\Sigma \qquad (7.29)$$

where c is the fourth-order elasticity tensor from Hooke's law, G is Green's function describing the response of the medium, $\mathrm{D}(\boldsymbol{\xi},t)$ is the displacement on the fault with area Σ and coordinates $\boldsymbol{\xi}$, and n is the fault-normal vector. Summation over i, j, p, and q is implied.

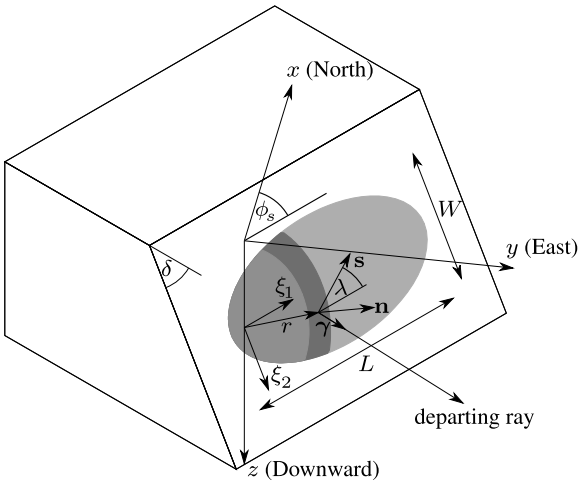

Figure 7.16: Set-up of the rupture model. Grey ellipse represents the rupture: light grey area is unruptured, medium grey area is slipping, and the dark grey area is after slip arrest.

While the surface integral is carried out numerically, the derivatives of Green's function for an isotropic, homogeneous, and unbound medium can be solved analytically:

$$\frac{\partial}{\partial x_q} G_{ip}(D_j(\boldsymbol{\xi},t)) = \qquad (7.30)$$

$$\frac{15\gamma_i\gamma_p\gamma_q - 3(\delta_{ip}\gamma_q + \delta_{iq}\gamma_p + \delta_{pq}\gamma_i)}{4\pi\rho r^4}$$

$$\cdot \int_{\frac{r}{\alpha}}^{\frac{r}{\beta}} D_j(\boldsymbol{\xi}, t-\tau)\tau d\tau \qquad (7.30a)$$

$$+ \frac{6\gamma_i\gamma_p\gamma_q - (\delta_{ip}\gamma_q + \delta_{iq}\gamma_p + \delta_{pq}\gamma_i)}{4\pi\rho\alpha^2 r^2} D_j\left(\boldsymbol{\xi}, t - \frac{r}{\alpha}\right) \qquad (7.30b)$$

$$- \frac{6\gamma_i\gamma_p\gamma_q - (2\delta_{ip}\gamma_q + \delta_{iq}\gamma_p + \delta_{pq}\gamma_i)}{4\pi\rho\beta^2 r^2} D_j\left(\boldsymbol{\xi}, t - \frac{r}{\beta}\right) \qquad (7.30c)$$

$$+ \frac{\gamma_i\gamma_p\gamma_q}{4\pi\rho\alpha^3 r} \dot{D}_j\left(\boldsymbol{\xi}, t - \frac{r}{\alpha}\right) \qquad (7.30d)$$

$$- \frac{\gamma_i\gamma_p\gamma_q - \delta_{ip}\gamma_q}{4\pi\rho\beta^3 r} \dot{D}_j\left(\boldsymbol{\xi}, t - \frac{r}{\beta}\right) \qquad (7.30e)$$

where

$$r = |\mathrm{x} - \boldsymbol{\xi}| \text{ and } \gamma_i = \frac{x_i - \xi_i}{r}, \qquad (7.31)$$

and δ_{ij} is Kronecker's delta. The terms in Eq. (7.30) are commonly separated into groups with respect to their distance r. In Eq. (7.30a) is the near-field (NF) term; as its amplitude decays with r^{-4}, it affects the immediate vicinity of a rupture only. Terms with a distance attenuation proportional to r^{-2} are called intermediate-field (IF) terms for P-waves (Eq. (7.30b)) and S-waves (Eq. (7.30c)). The remaining two terms are the far-field (FF) terms for P-waves (Eq. (7.30d)) and S-waves (Eq. (7.30e)) with a

decay proportional to r^{-1}. A major difference between the NF and IF terms and the FF terms is that the former depend on the slip on the rupture, and they are the cause for static and dynamic displacement, whereas the latter are functions of the time derivative of slip and result in dynamic displacement only.

The slip function in time is related to the Yoffe function Yoffe (1951) and Tinti et al. (2005) with rise time T. We use the slip distribution of Savage (1966) to describe the amplitude distribution of the slip on the rupture as well as the elliptical fault shape and rupture propagation from Savage (1966). The slip amplitude is given by

$$D(\boldsymbol{\xi}) = D_0 \sqrt{1 - \left(\frac{\xi_1 - p\epsilon\frac{L}{2}}{\frac{L}{2}}\right)^2 - \left(\frac{\xi_2}{\frac{W}{2}}\right)^2} \tag{7.32}$$

where D_0 is the maximum displacement at the centre of the fault, L and W are the length and width of the fault with eccentricity $\epsilon = \sqrt{1 - \left(\frac{W}{L}\right)^2}$, and p determines whether the rupture starts at the focus at the front of the rupture plane (strike-parallel, $p = 1$) or at the focus at the end (strike-antiparallel, $p = -1$). The rupture originates in one of the two foci and propagates radially away from the source with constant velocity ζ and terminates when it reaches the rupture boundary. The slip vector $\hat{\mathrm{s}}$ describes the orientation of the displacement $D(\boldsymbol{\xi})$ on the fault plane. We follow the definition of $\hat{\mathrm{n}}$ and $\hat{\mathrm{s}}$ in terms of fault strike ϕ_s, dip δ, and rake λ from Aki & Richards (2002):

$$\hat{\mathrm{n}} = \begin{pmatrix} -\sin\delta\sin\phi_s \\ \sin\delta\cos\phi_s \\ -\cos\delta \end{pmatrix}, \tag{7.33}$$

$$\hat{\mathrm{s}} = \begin{pmatrix} \cos\lambda\cos\phi_s + \cos\delta\sin\lambda\sin\phi_s \\ \cos\lambda\sin\phi_s - \cos\delta\sin\lambda\cos\phi_s \\ -\sin\lambda\sin\delta \end{pmatrix}. \tag{7.34}$$

The displacement vector D in Eq. (7.30) is given by

$$\mathrm{D} = D(\boldsymbol{\xi})\hat{\mathrm{s}} \tag{7.35}$$

We consider an isotropic medium, and the elasticity tensor c from Eq. (7.29) is

$$c_{jkpq} = \delta_{jk}\delta_{pq}\lambda_\mathrm{M} + (\delta_{jp}\delta_{kq} + \delta_{jq}\delta_{kp})\mu_\mathrm{M} \tag{7.36}$$

where λ_M and μ_M are the Lamé constants of the isotropic medium:

$$\lambda_\mathrm{M} = \rho(v_\mathrm{P}^2 + 2\mu_\mathrm{M}), \qquad \mu_\mathrm{M} = \rho v_\mathrm{S}^2. \tag{7.37}$$

We set $\lambda_\mathrm{M} = \mu_\mathrm{M}$, resulting in the widely observed relation $v_\mathrm{P} = v_\mathrm{S}\sqrt{3}$.

With the assumptions outlined above it is possible to calculate the displacement of an earthquake at location x with 12 parameters (Fig. 7.16):

fault size and orientation, including length L, width W, strike ϕ_s, and dip δ;

material: including 1st and 2nd Lamé constants λ_M and μ_M and density ρ (alternatively: compressional and shear wave velocities v_P and v_S and density ρ);

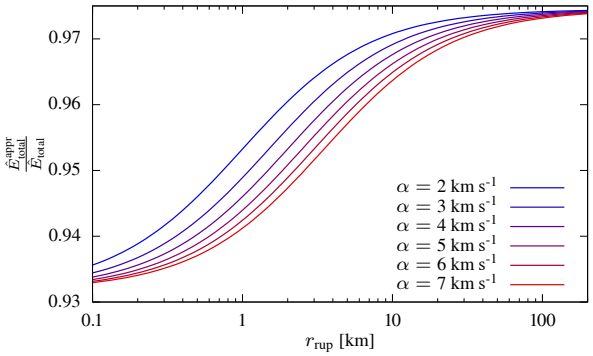

Figure 7.17: Ratio between the approximate and exact energy estimates for different P-wave velocities in the medium. The exact estimate assumes that P- and S-waves arrive at different velocities at the recording site, while the approximate estimate assumes that all waves arrive with shear wave velocity at the site. This approximation introduces only a minor underestimation, since most radiated energy is released as S-waves. The distance variation arises from the different distance and velocity dependencies of the intermediate-field terms and the far-field terms.

rupture and slip, including rupture velocity ζ, slip D_0, rise time T, rake λ and rupture orientation with respect to strike ϕ_s, and rupture orientation parameter p.

The fault size and displacement of earthquakes are correlated with each other and are scaled to the magnitude. The number of parameters reduces to ten (nine if the Lamé constants are equal) when scaling relations (e.g. Leonard, 2010; Strasser et al., 2010) are used in combination with the seismic moment M_0. The moment can be expressed as

$$M_0 = \mu_\mathrm{M} A \bar{D}, \tag{7.38}$$

with shear modulus (2nd Lamé constant) μ_M, the rupture area—here an ellipse—$A = \frac{\pi}{4}LW$, and average displacement $\bar{D}$, which follows from Eq. (7.32) as $\bar{D} = \frac{2}{3}D_0$.

The results are not strictly comparable to observed data due to the model simplicity. The computed amplitudes will be smaller than observed values because no free surface is assumed. Assuming a free surface would nearly double the amplitudes from wave reflection as well as the amplifications from wave transmissions (from high- to low-velocity zones). Only direct waves are computed, and effects of reflections of different layers are not covered due to the isotropy and homogeneity. Corresponding waveforms—in particular surface waves—are not exhibited. However, the purpose of this model is to show (1) the general behaviour of waveforms in the vicinity of a rupture, which is dominated by direct waves, and (2) how amplitudes distribute relatively in space.

7.9.2 Radiated seismic energy estimation

The exact calculation of radiated seismic energy is challenging. One simplifying assumption is that all waves arrive at the site with shear wave speed, which is a very good approximation for the far-field term. The reasoning can

be justified from a theoretical perspective: for most earth media the ratio between the P-wave velocity α and S-wave velocity β is

$$\frac{\alpha}{\beta} = \sqrt{3} \tag{7.39}$$

From this and Eq. 7.30d and 7.30e, it follows that the amplitude of compressional waves is $\approx \frac{1}{\sqrt{3}^3}$ of the shear wave amplitude. If we say that the P-wave train has a similar duration as the S-wave train, then the energy contribution of the P-waves with respect to the S-waves becomes $(\frac{1}{\sqrt{3}^3})^2 = \frac{1}{27}$. The total energy of a signal is (Rudnicki & Freund, 1981)

$$E_{\text{total}} = E_{\text{P}} + E_{\text{S}} \tag{7.40}$$

and can be estimated by

$$\hat{E}_{\text{total}} = \alpha_{\text{S}} a IV2_{\alpha} + \beta_{\text{S}} a IV2_{\beta}, \tag{7.41}$$

with the integrated squared velocity ($IV2$) for P- and S-waves from Eq. 7.7, the P- and S- wave velocities α_{P} and α_{S} at the recording site, and a constant a covering the remaining factors which are identical for both terms (compare with Eq. 7.8). If we express the energy contribution of P-waves in terms of S-waves, we can summarize the above relation to

$$\begin{aligned}
\hat{E}_{\text{total}} &= a IV2_{\beta} \left(\frac{\alpha_{\text{P}}}{27} + \beta_{\text{S}} \right) && (7.42)\\
&= a IV2_{\beta} \left(\frac{\beta_{\text{S}}\sqrt{3}}{27} + \beta_{\text{S}} \right) && (7.43)\\
&\approx a IV2_{\beta} \left(\frac{\beta_{\text{S}}}{27} + \beta_{\text{S}} \right). && (7.44)
\end{aligned}$$

The last expression is differs only by 2.6 % from the exact term. While slightly underestimating the energy, this approximate definition of using α_{S} instead of β_{S} does not require the identification of P- and S- waves. This is useful, since at short distances the S-wave train is usually inseparable from the P-wave train.

At shorter distances, the intermediate-field term needs also to be taken into consideration. The amplitude of the intermediate term decays with r^2 (Eq. 7.30b, 7.30c), while the far-field amplitude decays with r (Eq. 7.30d, 7.30e). That is, the amplitude scales by distance and velocities and thus the $IV2$ are

$$\begin{aligned}
IV2_{\alpha} &= \alpha^{-4} r^{-2} (r^{-1} + \alpha^{-1})^2, && (7.45)\\
IV2_{\beta} &= \beta^{-4} r^{-2} (r^{-1} + \beta^{-1})^2. && (7.46)
\end{aligned}$$

Again by replacing all P-wave terms by S-wave terms, the total energy becomes

$$\begin{aligned}
\hat{E}_{\text{total}} &= \alpha_{\text{S}} a IV2_{\alpha} + \beta_{\text{S}} a IV2_{\beta} && (7.47)\\
&= a r^{-2} \big(\alpha_{\text{S}} \alpha^{-4} (r^{-1} + \alpha^{-1})^2 \\
&\qquad + \beta_{\text{S}} \beta^{-4} (r^{-1} + \beta^{-1})^2 \big) && (7.48)\\
&= a r^{-2} \big(\sqrt{3}^{-3} \beta_{\text{S}} \beta^{-4} (r^{-1} + \sqrt{3}^{-1} \beta^{-1})^2 \\
&\qquad + \beta_{\text{S}} \beta^{-4} (r^{-1} + \beta^{-1})^2 \big). && (7.49)
\end{aligned}$$

With the assumption that $\alpha_{\text{S}} = \beta_{\text{S}}$, Eq. 7.48 becomes

$$\begin{aligned}
\hat{E}^{\text{appr}}_{\text{total}} &\approx a r^{-2} \big(\beta_{\text{S}} \alpha^{-4} (r^{-1} + \alpha^{-1})^2 \\
&\qquad + \beta_{\text{S}} \beta^{-4} (r^{-1} + \beta^{-1})^2 \big) && (7.50)\\
&= a r^{-2} \Big(\sqrt{3}^{-4} \beta_{\text{S}} \beta^{-4} (r^{-1} + \sqrt{3}^{-1} \beta^{-1})^2 \\
&\qquad + \beta_{\text{S}} \beta^{-4} (r^{-1} + \beta^{-1})^2 \Big). && (7.51)
\end{aligned}$$

The ratio between the approximation and the exact solution is

$$\frac{\hat{E}^{\text{appr}}_{\text{total}}}{\hat{E}_{\text{total}}} = \frac{\sqrt{3}^{-4} (r^{-1} + \sqrt{3}^{-1} \beta^{-1})^2 + (r^{-1} + \beta^{-1})^2}{\sqrt{3}^{-3} (r^{-1} + \sqrt{3}^{-1} \beta^{-1})^2 + (r^{-1} + \beta^{-1})^2}. \tag{7.52}$$

The two limits with respect to distance are

$$\begin{aligned}
\lim_{r \to 0} \frac{\hat{E}^{\text{appr}}_{\text{total}}}{\hat{E}_{\text{total}}} &= \frac{\sqrt{3}^{-4} + 1}{\sqrt{3}^{-3} + 1} && (7.53)\\
&\approx 0.932, && (7.54)\\
\lim_{r \to \infty} \frac{\hat{E}^{\text{appr}}_{\text{total}}}{\hat{E}_{\text{total}}} &= \frac{\sqrt{3}^{-5} + 1}{\sqrt{3}^{-6} + 1} && (7.55)\\
&\approx 0.974. && (7.56)
\end{aligned}$$

The second limit is identical to the far-field case derived above. The two limits show that even in the range of the intermediate-field term, the energy estimate deviates little when assuming that all waves arrive with β_{S} at the recording site. A comparison of the approximate energy estimate and the exact estimate as a function of distance and velocity is shown in Fig. 7.17.

Acknowledgements

We highly appreciate the help of Tomotaka Iwata and Kimiyuki Asano for providing links to additional seismic data from the municipal and NIED networks and for several helpful discussions on the specifics of the data. We are sincerely grateful to Takashi Oguchi, Yuichi Hayakawa, Hitoshi Saito and Yasutaka Haneda for the field trip to the Aso region and fruitful discussions. We also thank Hendy Setiawan, Tao Wang, and Qiang Xu for reviewing and helping to improve the paper. Thanks to Arno Zang, John Anderson, and Odin Marc for various discussions and comments.

Sebastian von Specht, Ugur Ozturk, and Georg Veh acknowledge support from the DFG research training group "Natural Hazards and Risks in a Changing World" (Grant No. GRK 2043/1). Ugur Ozturk is also supported by the Federal Ministry of Education and Research of Germany (BMBF) within the project CLIENT II–CaTeNA (FKZ 03G0878A).

The article processing charges for this open-access publication were covered by a Research Centre of the Helmholtz Association.

Review statement: This paper was edited by Ulrike Werban and reviewed by Hendy Setiawan, Tao Wang, and Qiang Xu.

Data availability: KiK-Net and K-Net data are accessible at http://www.kyoshin.bosai.go.jp/. The JMA special release seismic waveform data are accessible at http://www.data.jma.go.jp/svd/eqev/data/kyoshin/jishin/index.html. Coseismic landslide data are available at http://www.bosai.go.jp/mizu/dosha.html. Unspecified landslides are available at http://dil-opac.bosai.go.jp/publication/nied_tech_note/landslidemap/gis.html. The V_{S30} site amplification data are available at http://www.j-shis.bosai.go.jp/map/JSHIS2/download.html?lang=en. Seismic velocities and density after Koketsu et al. (2012) are available as part of the JIVSM data set at http://www.eri.u-tokyo.ac.jp/people/hiroe/link.html. The ALOS 30 m DSM is available at https://www.eorc.jaxa.jp/ALOS/en/aw3d30/index.htm. The ALOS land use data are available at https://www.eorc.jaxa.jp/ALOS/en/lulc/lulc_index.htm. The seamless geological map of Japan is available at https://gbank.gsj.jp/seamless/download/downloadIndex_e.html. All data are free of charge, and data sources were last accessed on 19 March 2019.

Chapter 8

A link between machine learning and optimization in ground-motion model development: Weighted mixed effect regression with data-driven probabilistic earthquake classification

Abstract

The steady increase of ground-motion data allows new possibilities but also comes with new challenges in ground-motion modeling and the development of ground-motion models. One challenge is data selection—not all data can be processed equally—and we introduce an extension of the widely used mixed effect model to incorporate data weighting. The parameter estimation of the mixed effects model, i.e. fixed effect coefficients of the ground-motion model and the random effect variances, are based on the weighted likelihood function. Furthermore, analytic uncertainty estimates of the weighted mixed-effect model parameters are provided. The data weighting allows for the possibility of data classification beyond the more classical, expert-driven, binary classification based e.g. on the depth of the event, distance to the trench, style-of-faulting and dip angle of the fault plane. We apply ACE - (A)ngular (C)lassification with (E)xpectation-maximization - a method to efficiently identify clusters of nodal planes from focal mechanisms to differentiate between interface and intraslab type events. Classification is continuous, i.e. no event belongs completely to one class and classification uncertainty is then evaluated and taken into account in the ground-motion modeling. As an example, we developed a ground-motion model from the strong motion database of Bastías & Montalva (2016) of appr. 2400 records from 319 events in the Chilean subduction zone. Our ground-motion model with the data-driven classification is comparable to the expert classification based model. Furthermore, the models show temporal variations of the between-event residuals before and after large earthquakes in the region[a].

[a] submitted as: A link between machine learning and optimization in ground-motion model development: von Specht S., Cotton F., Weighted mixed effect regression with data-driven probabilistic earthquake classification, *Bulletin of the Seismological Society of America.*

8.1 Introduction

The rapid progress and expansion of strong-motion networks result in a steady increase of available ground-motion data. The exponential growth of data and the need for reproducible, objective (i.e. independent of expert judgment) seismic hazard and ground-motion models make classical classification methods difficult to use. Indeed, current classifications used in seismic hazard or ground-motion modeling are deterministic in the sense that earthquakes or sites are unambiguously placed into a single category (e.g. intraplate or interface earthquake). With the exponential growth of data, properties and classifications of thousands of sites and earthquake cannot anymore be based on experts opinions and deterministic classification which are neglecting the uncertainties associated to the classification. Recently, the community is moving to data-driven and probabilistic classifications: e.g. for GMM regionalization (Chen et al., 2018) or site classification (Kotha et al., 2018). These classifications have the advantage to be fully data-driven, transparent and probabilistic (i.e uncertainties related to the classification are quantified). However, probabilistic classifications generate new challenges for ground-motion modelers since they require more generalized ground-motion regression which take into account both measurement errors (uncertainties of the ground motion values) but also new types of uncertainties resulting from machine-learning and data-driven classifications. These new uncertainty evaluations have to be incorporated in the regression methods used to develop ground-motion models but also to quantify correlations for the GMM coefficients and the various components of the aleatory variability (e.g. between-events, within-event, between-paths variabilities).

The limitations of classical earthquakes classifications and the need for new ground-motion models are particularly important for subduction areas since ground motion models (GMMs) for subduction zone earthquakes show large aleatory variability and epistemic uncertainties (Douglas, 2010). One of the key challenges of the development of new ground-shaking models for subduction zones relates to the event classification. Subduction zone ground-motion models differentiate between interface type events occurring at the coupled interface of the subducting and the overriding plate, and intraslab type events that take place within the down-going slab. The classification into different source types into interface and intraslab type events is performed manually and is based on the depth of an event, the distance to the trench, style-of-faulting and dip angle of the fault plane (e.g. Haendel et al., 2015; Abrahamson et al., 2016; Bastías & Montalva, 2016). These classifications are discrete, i.e. an event is unambiguously assigned to a single category ("intraplate" or "interface") neglecting any uncertainties.

In this study we couple an machine-learning based classification of earthquakes and a generalized ground-motion regression model. This new framework is tested and applied to the development of ground-motion models for the Chilean subduction zone. We first apply ACE - (A)ngular (C)lassification with (E)xpectation-maximization - a method to efficiently identify clusters of nodal planes from focal mechanisms (FM) as well as the style of faulting in one purely data-driven algorithm based on Expectation-Maximization with extensions in optimizing the number of clusters (Specht et al., 2017). ACE only requires the strike, rake, and dip of both nodal planes from focal mechanism catalogs to identify clusters belonging to different styles-of-faulting. Classification is continuous, i.e. no event belongs completely to one class and classification uncertainty is then evaluated. The method has been applied by (von Specht et al., 2018) to stress tensor inversion in northern Chile to reduce uncertainties of the stress tensor estimates by selecting events associated with one Style-of-Faulting for the inversion.

In a second step, the classifications uncertainties are incorporated into the ground-motion development. In this paper, the mixed effect model is reviewed from its theoretical foundation to incorporate data weights into the governing equations but also to provide a consistent work flow in the development of mixed effect based GMMs in general. The parameter estimators of the mixed effect model are derived from its basic assumptions and for different random effects (in ground-motion models namely the between event, between site, and between path/region variabilities) following the works of (Henderson et al., 1959; Harville, 1977; Lindstrom & Bates, 1988; Bates et al., 2015). Their work forms the basis of the state-of-the-art implementations of mixed-effect regression in general. The data weights (of any kind) are introduced into the model through the weighted likelihood (Field & Smith, 1994). The algorithmic formulation given here is a generalization of the linear mixed effects model of which the mixed effect model by Abrahamson & Youngs (1992) is a special case. Furthermore, the formulations of the mixed effect model used in this paper also form the basis for the derivation of analytic solutions of the parameter uncertainties and correlations for the GMM coefficients and the random effect variances. The analytic uncertainty estimates are based on the Fisher information matrix and the Cramér-Rao inequality. This allows to investigate the role and interactions of GMM parameters for a given model and its random effect variances.

We present results of the event classification for Chile showing the identification of clusters of thrust (associated with plate interface activity) and normal events (associated with intraslab seismicity). We then derive and compare ground-motion models with events selected by expert judgment and ACE as a data-driven method. We analyze the correlations among GMM parameters, variances but also between parameters and variances. Finally, we investigate the residuals and following Socquet et al. (2017); Piña Valdés et al. (2018); Bindi et al. (2018) we analyze the temporal variations of between-events residuals.

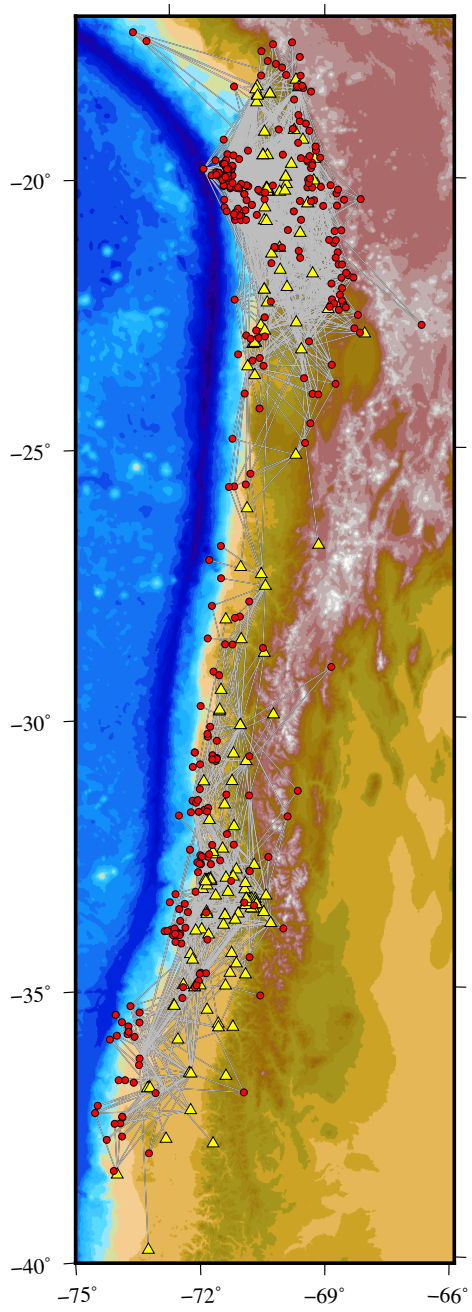

Figure 8.1: Map from Chile and adjacent regions showing events used in this study. The catalog from the flatfile we used contains 319 events (red dots) recorded at 176 stations (yellow triangles) with a total of 2443 records (black paths).

8.2 Method

8.2.1 The weighted mixed effects model

The general form of the linear mixed effect model is

$$\mathrm{y} = \mathrm{Ap} + \mathrm{Bq} + \epsilon \tag{8.1}$$

where Ap is the fixed effect model expressed as design matrix A and parameters p, and the random effects q with design matrix B. This model is stated under the assumption that the residuals of both the random and the fixed model are normally distributed, expressed by ϵ.

Furthermore, the random effects are normally distributed with $\mathrm{q} \sim \mathcal{N}(0, \sigma\mathrm{D})$, where $\sigma^2\mathrm{D}$ is the random effects covariance matrix. The data y conditioned on the random effects q are assumed to be $\mathrm{y}|\mathrm{q} \sim \mathcal{N}(\mathrm{Ap} + \mathrm{Bq}, \sigma^2\mathrm{C})$, where $\sigma^2\mathrm{C}$ is the data covariance matrix. From the theorem related to the partition of sums of squares follows that the sum of variance(s) associated with q (explained sum(s) of squares; random effect variances [between-event residuals, between-site residuals etc.]) and the variance of ϵ (residual sum of squares; within-event variance) is the total variance (total sum of squares) (e.g Sahai & Ageel, 2000).

The aim of the mixed effect regression is to maximize the likelihood of both the fixed effect and random effect models (Henderson et al., 1959; Harville, 1976). The joint probability is given by

$$P(\mathrm{y}, \mathrm{q}|\mathrm{Ap}, \sigma^2, \mathrm{C}, \mathrm{D}) = \frac{1}{\sqrt{(2\pi)^{N+M}|\sigma^2\mathrm{C}||\sigma^2\mathrm{D}|}} \times e^{-\frac{1}{2\sigma^2}\left((\mathrm{y}-\mathrm{Ap}-\mathrm{Bq})^{\mathrm{T}}\mathrm{C}^{-1}(\mathrm{y}-\mathrm{Ap}-\mathrm{Bq})+\mathrm{q}^{\mathrm{T}}\mathrm{D}^{-1}\mathrm{q}\right)} \tag{8.2}$$

The maximum likelihood (ML) estimation of its parameters is given by Henderson et al. (1959); Harville (1977); Lindstrom & Bates (1988); Bates et al. (2015).

At this point, we generalize the likelihood by introducing weights. A weighted likelihood (Field & Smith, 1994; Markatou et al., 1998, e.g.) is given by

$$\mathcal{L} = \prod_{i=1}^{N} P_i^{w_i} \tag{8.3}$$

and reduces to the ordinary likelihood, if $w_i = 1$. A generalized likelihood for mixed effects has been proposed by (e.g. Wolfinger & O'connell, 1993). This approach however has a very broad scope, e.g. modifying the assumption of normally distributed residuals. The penalized least squares approach for mixed effect by Bates & DebRoy (2004); Bates et al. (2015) accounts for weights by stating them explicitly in the covariance matrix C. This approach requires that the magnitude of the weights scales with the data, i.e. the weights are related to the data, e.g. the error measurements of the modeled quantity at hand. The weighted likelihood is less constrained on the relation between weights and data, as it does not weight the data but their probabilities. An illustrative example in terms of weighted mean and variance estimation for both weighting approaches is provided in appendix 8.8.1. This implies that the least squares

weights as used by Bates & DebRoy (2004) and the likelihood weights of Field & Smith (1994) are not mutually exclusive. On the contrary, both can be used simultaneously, each representing a different aspect of uncertainty, e.g. measurement error and degree of belief.

Here, we specifically introduce weights in the following way, illustrated with a set of earthquakes: The occurrence of an earthquake can be viewed as a random effect/event e_1, and it is recorded at N_1 random stations, i.e. we have N_1 records $\mathrm{y} = (y_1, y_2, \ldots, y_{N_i})^T$. If we observe E earthquakes, we have for the ith earthquake N_i records y_i. The number of records of an earthquake depends on several factors, e.g. earthquake location, magnitude, seismic station network and the record quality can vary with each event and to some extent also with each station. When developing a ground motion model from these E earthquakes, the records y are usually selected per earthquake. For GMMs, the selection of earthquakes often relates to the event type; particularly interface and intraslab events. Therefore, the seismologist (or some algorithm like ACE) applies a weighting per earthquake, i.e. the ith event gets weight w_i. This weighting represents the seismologist's (or ACE's) degree-of-belief whether an event is interface or intraslab (or something else). The main difference between the seismologist and ACE is, that the seismologist selects events on binary basis–an event is in or out–while ACE weights continuously based on a probabilistic model. To summarize: The seismologist wishes to develop a ground motion model from E earthquakes, where the ith earthquake is recorded at N_i stations, i.e. with the total number of records y of $N = \sum_{i=1}^{E} N_i$, and all records of the ith event are weighted with weight w_i. This exemplifying scenario is probably the mostly widely encountered in ground-motion modeling in terms of mixed-effect regression.

The variations between earthquakes and between stations are random. Let $\mathrm{e} = (e_1, e_2, \ldots, e_E)^T$ be the random effects of the earthquakes, and $\mathrm{s} = (s_1, s_2, \ldots, s_S)^T$ the random effects of all seismic stations, where S is the total number of stations. All random effects are assumed to have arisen from a normal distribution: $\mathrm{e} \sim \mathcal{N}(0, \sigma_E^2 \mathrm{D}_E)$ and $\mathrm{s} \sim \mathcal{N}(0, \sigma_S^2 \mathrm{D}_S)$. The random effects covariance matrices $\sigma_E^2 \mathrm{D}_E$, $\sigma_S^2 \mathrm{D}_S$ are diagonal matrix with $\mathrm{D_E} = \mathrm{I}_E$ and $\mathrm{D_S} = \mathrm{I}_S$ (I_X is a unit matrix of size $X \times X$), i.e. σ_E^2 is the variance between earthquakes (the variance associated with the between-event residuals) and σ_S^2 is the variance between stations (the station-to-station residuals). In line with these definitions, the covariance matrix $\sigma^2\mathrm{C}$—introduced in the beginning and Eq. 8.2—is set to $\sigma^2\mathrm{I}$. The variance σ^2 is therefore the variance of the data y conditioned on the random effects e and s; the remaining variance in the data after accounting for earthquake and station variations.

The K random effects $\mathrm{q}_1, \mathrm{q}_2, \ldots, \mathrm{q}_K$ can be summarized into a vector

$$\mathrm{q} = \begin{pmatrix} \mathrm{q}_1 \\ \mathrm{q}_2 \\ \vdots \\ \mathrm{q}_K \end{pmatrix} \tag{8.4}$$

and $M = N_{q_1} + N_{q_2} + \cdots + N_{q_K}$ is the total number of random effects. The summarized covariance matrix is a block diagonal matrix

$$\sigma^2\mathrm{D} = \sigma^2 \begin{pmatrix} \tau_1\mathrm{I} & 0 & \cdots & 0 \\ 0 & \tau_2\mathrm{I} & \cdots & 0 \\ \vdots & \vdots & \ddots & \vdots \\ 0 & 0 & \cdots & \tau_K\mathrm{I} \end{pmatrix}, \tag{8.5}$$

where the ith block matrix is of size $N_{q_i} \times N_{q_i}$. The elements τ_1, τ_2, …, τ_k are variance factors for the respective random effects; introduced for computational convenience. The ith random effect variance is given by $\sigma_i^2 = \sigma^2\tau_i$ The random effects design matrix is

$$\mathrm{B} = \begin{pmatrix} \mathrm{B}_1 & \mathrm{B}_2 & \cdots & \mathrm{B}_K \end{pmatrix} \tag{8.6}$$

where the ith design matrix is of size $N \times N_{q_i}$. With covariance matrices defined and the incorporation of weights according to Eq. 8.3, the event-weighted likelihood of Eq. 8.2 is

$$\begin{aligned} \mathcal{L}(\mathrm{Ap}, \sigma^2, \mathrm{C}, \mathrm{D}|\mathrm{y}, \mathrm{q}) = & \\ & \frac{1}{\sqrt{(2\pi)^M |\sigma^2\mathrm{D}|}} e^{-\frac{1}{2\sigma^2}\mathrm{q}^{\mathrm{T}}\mathrm{D}^{-1}\mathrm{q}} \\ & \times \prod_{i=1}^{E} \left[\frac{1}{\sqrt{(2\pi)^{N_i} |\sigma^2\mathrm{C_i}|}^{w_i}} \right. \\ & \left. \times e^{-\frac{1}{2\sigma^2}(\mathrm{V_i}(\mathrm{y_i} - \mathrm{A_i p}) - \mathrm{B_i q_i})^{\mathrm{T}} \mathrm{C_i}^{-1} (\mathrm{V_i}(\mathrm{y_i} - \mathrm{A_i p}) - \mathrm{B_i q_i})} \right], \end{aligned} \tag{8.7}$$

where the event-based weights are expressed in matrix form $\mathrm{V_i} = \sqrt{w_i}\mathrm{I}_{N_i}$. Note, that the random effects residuals $\mathrm{B_i q_i}$ are not weighted. The reason here is to obtain random effect predictions which do not scale with the weights. As shown in appendix 8.8.2, this condition is still in agreement with the definition of the weighted likelihood in Eq. 8.3.

The ML estimator for p and ML predictor q are derived from the derivatives of the log-likelihood in Eq. 8.7 (detailed derivation in appendix 8.8.2). The estimators for the GMM parameters are given as the fixed effect model parameters

$$\hat{\mathrm{p}} = \mathrm{X}\mathrm{y}, \tag{8.8}$$

with

$$\mathrm{X} = \left(\mathrm{A}^{\mathrm{T}}\mathrm{V}\mathrm{S}^{-1}\mathrm{V}\mathrm{A}\right)^{-1} \mathrm{A}^{\mathrm{T}}\mathrm{V}\mathrm{S}^{-1}\mathrm{V}, \tag{8.9}$$

which is the generalized least squares estimator with covariance matrix $\mathrm{V}\mathrm{S}^{-1}\mathrm{V}$ (Aitken, 1936), and the best linear unbiased estimator (Henderson, 1975).

The predictor for the random effects, q, is based on the fixed effect model parameters:

$$\hat{\mathrm{q}} = \mathrm{D}\mathrm{B}^{\mathrm{T}}\mathrm{S}^{-1}\mathrm{V}(\mathrm{y} - \mathrm{A}\hat{\mathrm{p}}), \tag{8.10}$$

which is the best linear unbiased predictor of q (Henderson, 1975).

The variance estimators of the mixed effect model dependent on the estimator $\hat{\mathrm{p}}$ and predictor $\hat{\mathrm{q}}$ of the fixed effect model. It is well established that ML variance estimates are biased downward by $\hat{\mathrm{p}}$ and $\hat{\mathrm{q}}$, i.e. variances

are underestimated Patterson & Thompson (e.g. 1971); Harville (e.g. 1974, 1976); Lindstrom & Bates (e.g. 1988); Bates & DebRoy (e.g. 2004); Bates et al. (e.g. 2015). To obtain unbiased variance estimates, the likelihood is defined in terms of error contrasts, resulting in the reduced maximum likelihood (RML). Details of the concept are described in full detail by Patterson & Thompson (1971); Harville (1976).

The RML estimator of the residual variance (within-event variance) σ^2 is found from the derivative of Eq. 8.72:

$$\hat{\sigma}^2 = \frac{\hat{\mathbf{r}}^{\mathrm{T}}\mathbf{V}\mathbf{S}^{-1}\mathbf{V}\hat{\mathbf{r}}}{\left(1 - \frac{P}{N}\right)\mathrm{tr}(\mathbf{V}\mathbf{V})}, \tag{8.11}$$

By normalizing the weights such that it holds, that

$$\mathrm{tr}(\mathbf{V}\mathbf{V}) = \sum_{i=1}^{N} V_{ii}^2 = N, \tag{8.12}$$

then the variance estimator can be stated as

$$\hat{\sigma}^2 = \frac{\hat{\mathbf{r}}^{\mathrm{T}}\mathbf{V}\mathbf{S}^{-1}\mathbf{V}\hat{\mathbf{r}}}{N - P} \tag{8.13}$$

This is the unbiased estimator of the variance and appears frequently with the denominator $N - 1$, i.e. for $P = 1$. The estimator corrects the bias for the loss of degree of freedoms which is equal to the number of parameters P in the GMM parameter estimator $\hat{\mathrm{p}}$. For generality the variance formulation in Eq. 8.75 is used in the following equations.

The RML estimators of the variance factors τ_k are linked to the variance $\hat{\sigma}^2$. There are no analytic solutions for the random effects variances and the likelihood must be maximized numerically, e.g. by gradient ascent based on the log-likelihood derivatives of the variance factors:

$$\begin{aligned}\frac{\partial \ln \mathcal{L}_w}{\partial \tau_k} = \frac{1}{2}\Bigg[&\mathrm{tr}\left(\mathbf{V}\mathbf{S}^{-1}\mathbf{B}_k\mathbf{B}_k^{\mathrm{T}}\mathbf{V}\right) \\ &+ \mathrm{tr}\left(\mathbf{X}\mathbf{B}_k\mathbf{B}_k^{\mathrm{T}}\mathbf{S}^{-1}\mathbf{A}\right)\frac{\mathrm{tr}(\mathbf{V}\mathbf{V})}{N} \\ &+ \frac{1}{\hat{\sigma}^2}\hat{\mathbf{r}}^{\mathrm{T}}\mathbf{V}\mathbf{S}^{-1}\mathbf{B}_k\mathbf{B}_k^{\mathrm{T}}\mathbf{S}^{-1}\mathbf{V}\hat{\mathbf{r}}\Bigg]\end{aligned} \tag{8.14}$$

The first and last term correspond to the basic ML estimator. The second term is the effect of the RML estimation, i.e. this term corrects for the bias of the ML estimator, if GMM parameters and random effects variances are derived from the data.

The variance factor estimates are found by iteration of

$$\boldsymbol{\tau}^{(i+1)} = \boldsymbol{\tau}^{(i)} + \gamma \nabla \mathcal{L}_w, \tag{8.15}$$

where $\boldsymbol{\tau}$ is the vector of variance factors, i.e. with Eq. 8.5 $\boldsymbol{\tau} = (\tau_1, \tau_2, \ldots, \tau_K)^T$. The factor γ is chosen such to guarantee convergence and is updated at each iteration (Barzilai & Borwein, 1988). The algorithm starts from some initial values and is repeated until sufficient convergence of the parameters is reached. At each iteration, $\hat{\sigma}^2$ and $\hat{\mathrm{p}}$ are updated before the factors $\boldsymbol{\tau}$ are updated. Finally, the maximum likelihood estimates of the variances are:

$$\hat{\boldsymbol{\upsilon}} = \hat{\sigma}^2\hat{\boldsymbol{\tau}} \tag{8.16}$$

8.2.2 Estimator uncertainties of GMM parameters & random effect variances

The mixed effect regression is based on the assumption that any kind of residuals are normally distributed. This property allows for the derivation of analytic expressions for parameter uncertainty estimates, i.e. computationally intensive methods like bootstrapping and jackknifing are not necessary. The (co)variance of a parameter is related to the Fisher information I of the parameters, expressed by the Cramér-Rao bound

$$\mathrm{cov}(\hat{\boldsymbol{\theta}}) \geq \mathrm{I}(\hat{\boldsymbol{\theta}})^{-1} \tag{8.17}$$

If the above relation becomes an equality, the estimator $\hat{\theta}$ is said to be an efficient estimator. Hartley & Rao (1967) showed for the mixed effects model that the parameter estimates $\hat{\mathrm{p}}$ are efficient and the variance estimators $\hat{\boldsymbol{\tau}}$ are asymptotically efficient, i.e. converge towards efficiency with increasing number of data. This (asymptotic) equality of the Cramér-Rao bound allows the derivation of parameter uncertainties from the Fisher information.

The Fisher information I of a parameter estimator $\hat{\boldsymbol{\theta}}$ is a matrix related to the likelihood $\mathcal{L}$. Its components are given by

$$I_{ij} = -\mathbb{E}\left[\frac{\partial^2 \ln \mathcal{L}}{\partial\hat{\theta}_i \partial\hat{\theta}_j}\right], \tag{8.18}$$

where $\mathbb{E}[\cdot]$ is the expected value operator. For the mixed effect model the Fisher information is given as 3×3 block matrix

$$\mathrm{I}(\hat{\mathrm{p}}, \hat{\sigma}^2, \hat{\boldsymbol{\upsilon}}) = -\mathbb{E}\begin{bmatrix} \frac{\partial^2 \ln \mathcal{L}_w}{\partial\hat{\mathrm{p}}\partial\hat{\mathrm{p}}} & \frac{\partial^2 \ln \mathcal{L}_w}{\partial\hat{\mathrm{p}}\partial\hat{\sigma}^2} & \frac{\partial^2 \ln \mathcal{L}_w}{\partial\hat{\mathrm{p}}\partial\hat{\boldsymbol{\upsilon}}} \\ \frac{\partial^2 \ln \mathcal{L}_w}{\partial\hat{\sigma}^2\partial\hat{\mathrm{p}}} & \frac{\partial^2 \ln \mathcal{L}_w}{\partial\hat{\sigma}^2\partial\hat{\sigma}^2} & \frac{\partial^2 \ln \mathcal{L}_w}{\partial\hat{\sigma}^2\partial\hat{\boldsymbol{\upsilon}}} \\ \frac{\partial^2 \ln \mathcal{L}_w}{\partial\hat{\boldsymbol{\upsilon}}\partial\hat{\mathrm{p}}} & \frac{\partial^2 \ln \mathcal{L}_w}{\partial\hat{\boldsymbol{\upsilon}}\partial\hat{\sigma}^2} & \frac{\partial^2 \ln \mathcal{L}_w}{\partial\hat{\boldsymbol{\upsilon}}\partial\hat{\boldsymbol{\upsilon}}} \end{bmatrix} \tag{8.19}$$

The inverse $\mathrm{I}(\hat{\mathrm{p}}, \hat{\sigma}^2, \hat{\boldsymbol{\upsilon}})^{-1}$ —which is asymptotically equivalent to the covariance matrix as $N \to \infty$—is stated as

$$\begin{aligned}&\mathrm{I}(\hat{\mathrm{p}}, \hat{\sigma}^2, \hat{\boldsymbol{\upsilon}})^{-1} \sim \mathrm{cov}(\hat{\mathrm{p}}, \hat{\sigma}^2, \hat{\boldsymbol{\upsilon}}) \\ &= \begin{pmatrix} \hat{\sigma}^2(\mathbf{A}^{\mathrm{T}}\mathbf{P}\mathbf{A})^{-1} & \circ & \circ \\ \circ & \frac{2\hat{\sigma}^4}{\mathrm{tr}(\mathbf{V}\mathbf{V})} + \mathbf{T}\mathbf{M}\mathbf{T}^{\mathrm{T}} & \mathbf{T}\mathbf{M} \\ \circ & \mathbf{M}\mathbf{T}^{\mathrm{T}} & \mathbf{M} \end{pmatrix}\end{aligned} \tag{8.20}$$

where P, T and M are matrices related to the random effect variances and the first and second derivatives of the mixed effect likelihood (See appendix 8.8.3 for the definitions and a detailed derivation of the covariance matrix). The terms related to the covariance for a single random effect without weighting reduces to the terms used by Abrahamson & Youngs (1992, Eq. 11,12,13). The covariance matrix shows that the covariance of the model parameters (upper left block) is independent of the covariance of the random effect variances (four lower right blocks), i.e. the

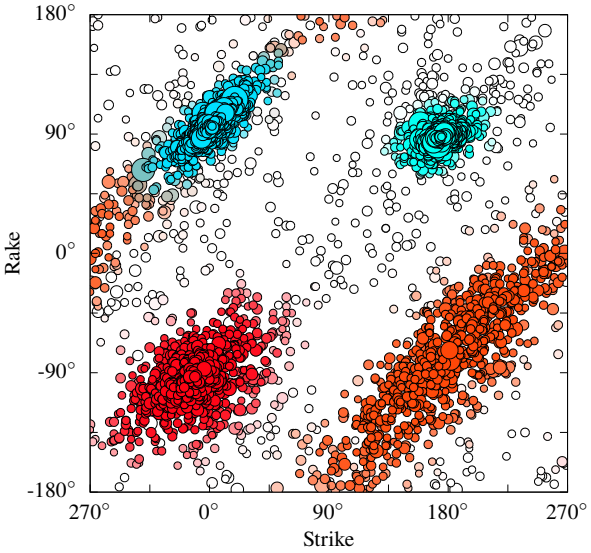

Figure 8.2: Distribution of nodal planes of FM for Chile from the GCMT catalog between 1976 - 2019. FM are represented in the strike-rake plane (lower right). The shape of the clusters depends on the dip, the shallower the dip, the more elongated the clusters. The model based on ACE identifies four clusters: Two for interface (blue shades) and intraslab (red shades), respectively. Data shown in white are unclassified. Those events have mainly hypocenters in the South American crust. The color saturation corresponds to the probability of a nodal plane to be in a certain cluster. For each event, the probabilities of both nodal planes are averaged and used as weights for the event classification used in ground motion modeling.

model parameters are independent of the variances. Furthermore, Eq. 8.20 shows that the variances of the random effect variances are not necessarily independent from each other as there are non-zero off-diagonal terms relating to the variances.

The correlations among the parameters (the off-diagonal elements) can be expressed by Pearson's correlation coefficient. The correlation between parameters θ_i and θ_j is given by

$$\rho_{\theta_i,\theta_j} = \frac{I^{-1}_{ij}}{\sqrt{I^{-1}_{ii} I^{-1}_{jj}}}, \tag{8.21}$$

where I^{-1}_{ij} is the ijth entry of the inverse of the Fisher information matrix. The Fisher information matrix provides therefore a powerful tool to assess the linear dependence of parameter and thus help with model design and evaluation and allows to check for the linear independence of the variance components.

8.3 Data

We use the strong motion flatfile for Chile published by Bastías & Montalva (2016). The flatfile contains in total 477 events range from M_W 4.6 to M_W 8.8 with 3572 three-component records, with distances measured from the rupture plane (r_{rup}). For each component PGA (peak ground acceleration) and spectral accelerations for oscillator periods between 0.01 - 10 s are available. Events are classified as interface, intraslab and crustal. Interface events are defined by a depth of less than 50 km and a maximum distance of 2.5° from the trench (260 km at 20°S and 210 km at 40°S). Intraslab events are all events deeper than 50 km. Crustal events are shallower than 50 km and have a distance more than 2.5° from the trench. Since ACE requires FM for classification, we use a subset of the flat-file events for which also GCMT ([Global Centroid Moment Tensor catalog]) solutions exist (Ekström et al., 2012). This subset contains 319 events with 2443 records with a magnitude range of M_W 4.9 - M_W 8.8 (Fig. 8.1).

8.4 Data-driven event classification

The weighted mixed effect regression introduced in this paper allows for a more general treatment of data selection. Besides the classical approach of deterministic selection, more sophisticated data selection is feasible with the weighted mixed effect regression. We use ACE (Angular Classification with Expectation-maximization) to classify earthquakes on the basis of their focal mechanisms (Specht et al., 2017; von Specht et al., 2018). ACE is based on expectation-maximization and fits a mixture distribution to the focal mechanism data in the strike-rake-dip domain. Since ACE considers both nodal planes, a separation into rupture and auxiliary plane is not required. The number of mixture components is optimized as part of the parameter estimation.

The underlying principle of ACE is the assumption that in a homogeneous background stress field only random variations in the stress field exist locally and focal mechanisms of a given Style-of-Faulting will tend to be similar to each other. Kagan (1991) showed that the minimal rotation angle between two FM in a homogeneous stress field follows a double couple rotational Cauchy distribution. FMs from regional catalogs tend to have small rotation angles, i.e. the FMs of a particular stress field form clusters in terms of their parameters (strike, dip, rake).

For the Chile region, ACE identifies three event types in five cluster: Two clusters for either nodal planes of interface and intraslab events, respectively, and one cluster for unclassified events (Fig. 8.2). The probability densities of the mixture distribution are used as weights in the development of the ground motion model and their square roots populate the matrix V.

Event classification of the Chile database based on expert judgment and ACE are shown in Fig. 8.3 a and b. Both event classifications are near-identical with few differences, and only 6 out of 319 events have opposite Style-of-Faulting assigned (Fig. 8.3 c).

8.5 Ground Motion Model

We apply the GMM of Haendel et al. (2015) to model strong motion data. The model has a similar functional form to the BC Hydro

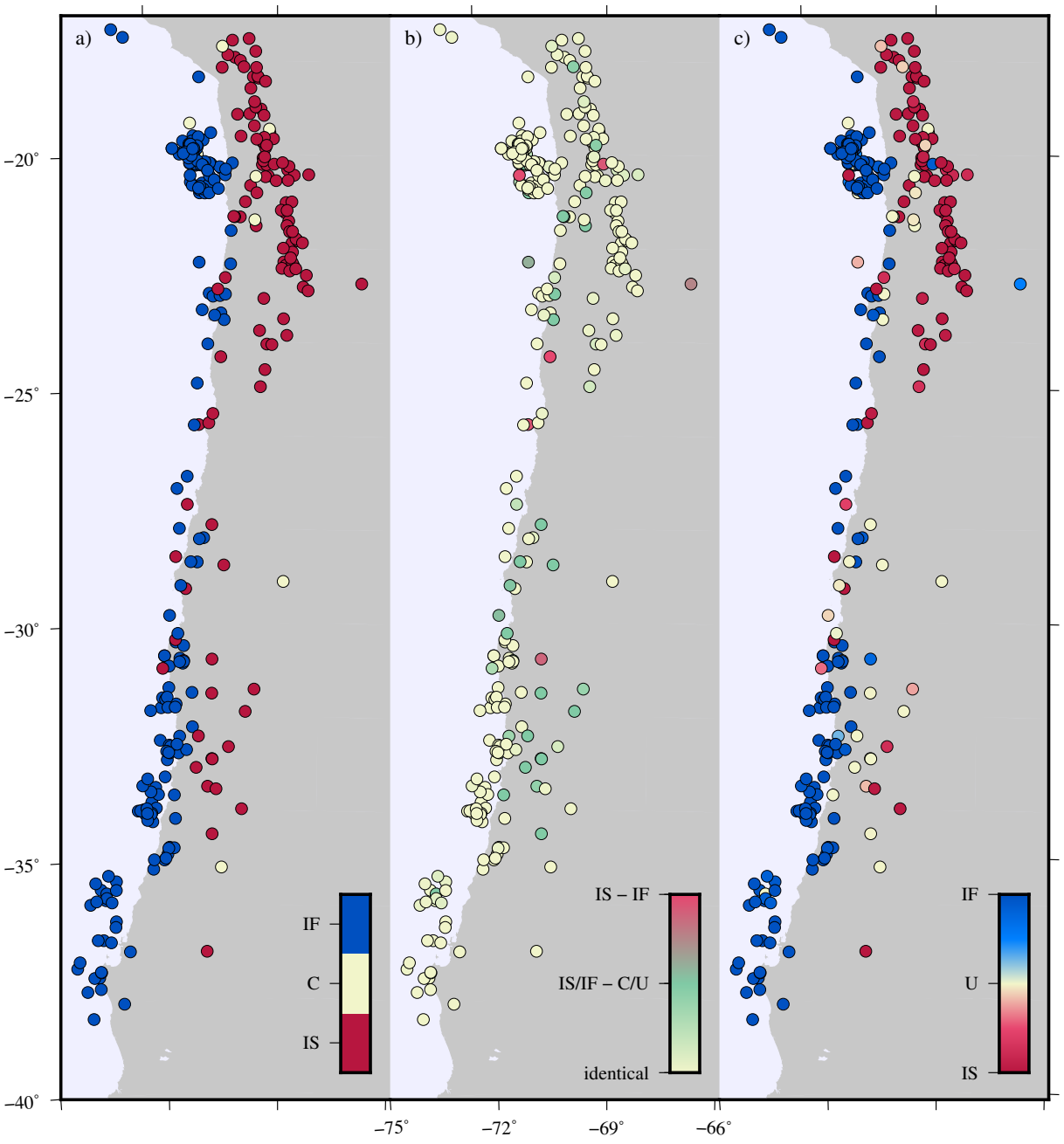

Figure 8.3: Left: (a) SoF-classification of events according to the flatfile (deterministic expert judgment): interface (IF), intraslab (IS), crustal (C). Right (c) Event classification based on ACE. SoF-Classification is continuous, i.e. no event belongs completely to one class. This is implemented by assigning weights to each event and shown as color saturation. Automated SoF assignments (interface (IF), intraslab (IS), unclassified (U)) are very similar to the expert based classification. Middle: b) Difference between expert based and ACE classifications. White - identical classification, yellow - interface/intraslab against unclassified/crustal, red - interface/intraslab against intraslab/interface.

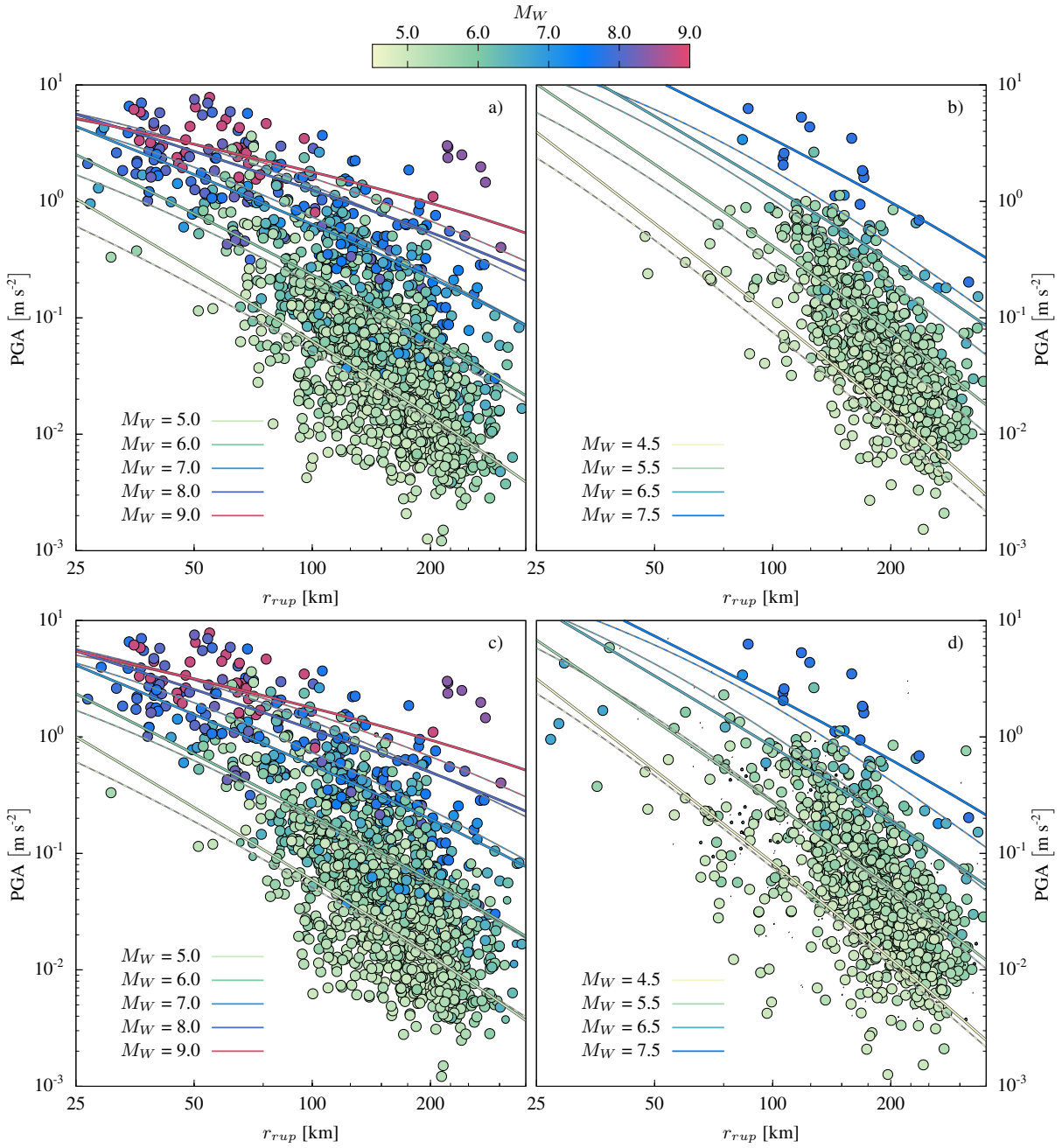

Figure 8.4: Top row: ground-motion model for Chile obtained for expert based data classification for interface (a) and intraslab (b). Only interface/intraslab events are used. Bottom row: ground motion model for Chile obtained for ACE based data classification for interface (c) and intraslab (d). All events are included with weights proportional to the color saturation in the map of Fig. 8.3 b. The size of the events corresponds to their weights (only visible in c) and d)).

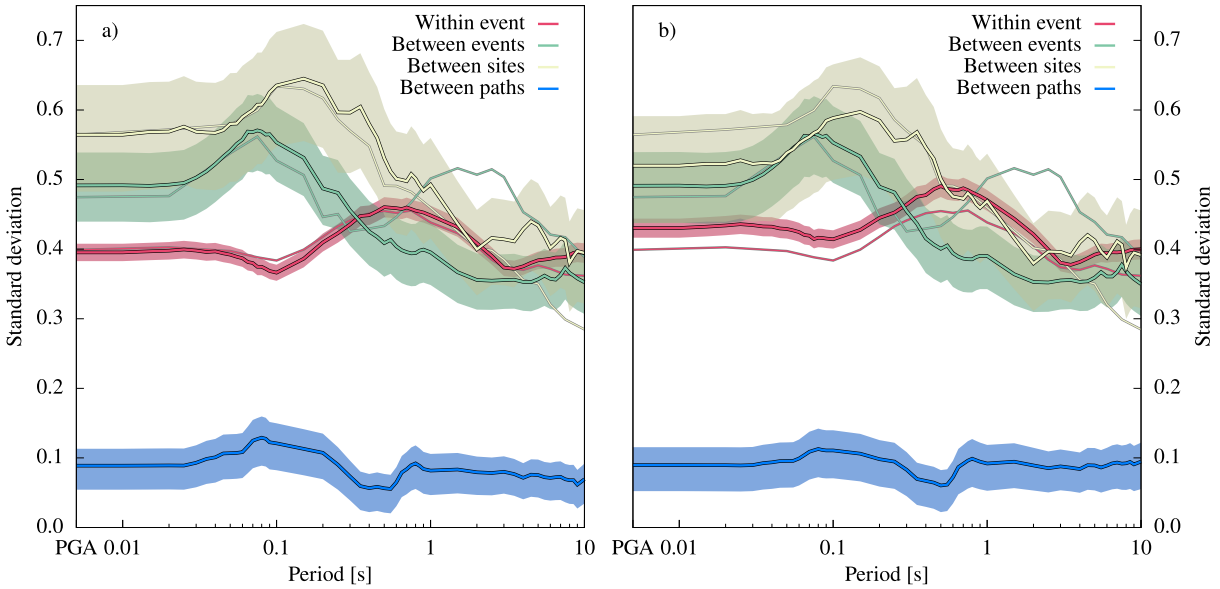

Figure 8.5: Model standard deviations (random effect variances + residual variance) with oscillatory period of the mixed effect regression with a) deterministic weights and b) probabilistic weights (ACE). Thick lines are standard deviations from this study with confidence regions shown as bands. Thin lines are the standard deviations of Montalva et al. (2017). Note, the path term is only in the models of this study.

model used by (Montalva et al., 2017), but with fewer parameters and is completely linear, simplifying parameter estimation.

$$
\begin{aligned}
y =& aM_W + br_{rup} - (c + dM_W)\ln r_{rup} \\
&+ e \begin{cases} z & \text{if } z \leq 125 \text{ km} \\ 125 & \text{otherwise} \end{cases} \\
&+ \begin{cases} w_i(q_i(M_W - 6.3)^2 + s_i) & \text{for IF} \\ w_s(q_s(M_W - 6.5)^2 + s_s + s_{sl}\ln r_{rup}) & \text{for IS} \end{cases} \\
&+ x \ln v_{S30}
\end{aligned}
\tag{8.22}
$$

where y is the logarithm of the geometric mean of the horizontal components of the accelerograms in [ms^{-2}], M_W the moment magnitude, r_{rup} is the rupture plane distance in [km], z the focal depth in [km], and v_{S30} the near-surface shear wave velocity in [ms^{-1}]. The model coefficients $\mathrm{p} = (a, b, c, d, e, q_i, s_i, q_s, s_s, s_{sl}, x)^T$ are the same as in Haendel et al. (2015). The parameters a, b, c, d are distance and magnitude related; e is related to depth. A second order magnitude term for interface and intraslab is given by q_i and q_s, respectively. Similarly, are the interface and intraslab specific offset terms s_i and s_s. For intraslab events an additional distance parameter s_{sl} accounts for the more complex travel paths of intraslab events. The parameter x characterizes the recording site conditions and is linked to v_{S30}.

The models subduction related parameters are weighted by w_i for interface events and for intraslab events by w_s. The choice of event type is straightforward in the expert classification by setting $w_i = 1$ for interface (IF) events, $w_s = 1$ for intraslab (IS) events and zero otherwise. For the ACE based classification, the event type weight is defined as the probability of an event being interface ($P(IF)$) or intraslab ($P(IS)$) conditioned on the probability of an event being related to subduction ($P(S) = P(IF) + P(IS)$, i.e. either interface or intraslab):

$$w_i = P(IF|S) = \frac{P(IF)}{P(IF) + P(IS)} \tag{8.23}$$

$$w_s = P(IS|S) = \frac{P(IS)}{P(IF) + P(IS)} \tag{8.24}$$

We augment the model with three random effects for between-event residuals, with standard deviation τ, between-station residuals, with standard deviation ϕ_{S2S}, and between-paths residuals, with standard deviation ϕ_{P2P}. The residual standard deviation is ϕ. The definition of the path related standard deviation is related to the spatial tiling approach of Dawood & Rodriguez-Marek (2013).

8.6 Results & Discussion

The ground motion models for Chile based on deterministic and ACE classifications (Fig. 8.3) show minor variations (Fig. 8.4). These two models are in agreement (Fig. 8.4) with the model of (Montalva et al., 2017) which is based on a more complex functional form.

The random effects variances of the new models are also comparable (Tab. 8.2) with variances of the (Montalva et al., 2017) model despite the fact that the new models are using a lower number of parameters. While the uncertainty estimates of the parameters are stable with frequency, the variance uncertainties are frequency dependent (Fig. 8.5). All random effect variances peak around 0.1 Hz. ACE based variance are however lower than the variances obtained using the classical deterministic classification. This result is important: PSHA (Probabilistic Seismic Hazard Analysis) is very sensitive to ground-motion mod-

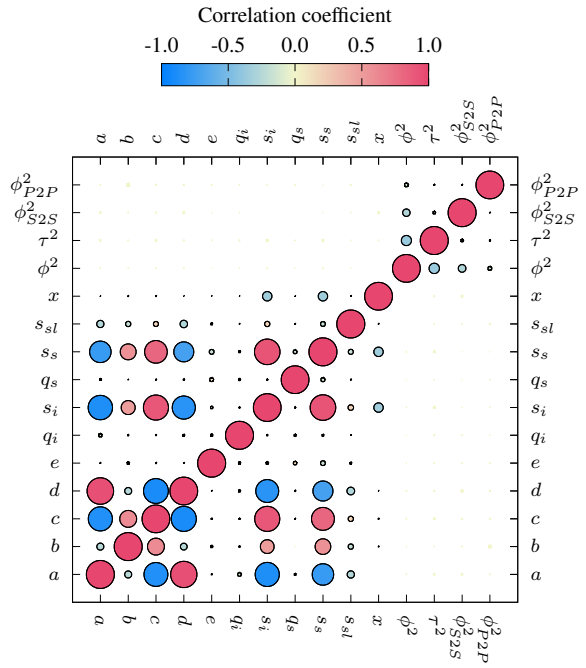

Figure 8.6: Correlation coefficients of the mixed effect regression for PGA for from the covariance matrix (Eq. 8.20). No correlations between the GMM parameters and the model variances exist by definition. Note, that many parameters of the GMM are correlated among each other, while some are not: the depth parameter e, the v_{S30} parameter x, and the interface and intraslab specific magnitude parameters q_i and q_s.

els variances; and, for the low annual exceedance frequencies, even small reductions in the model variance can bring appreciable benefits (Bommer & Abrahamson, 2006). This result then encourages the use of probabilistic earthquake classifications given the strong interest to decrease GMM variances among the engineering seismological community.

The new methods developed in this paper give also the opportunity to analyze the correlations among GMM parameters, variances but also between parameters and variances. The parameter covariance shows intricate correlations among GMM parameters, while virtually no correlations exist between the random effects variances (Figure 8.6). All random effect variances (τ^2, ϕ^2_{S2S}, ϕ^2_{P2P}) correlate with the residual variance ϕ^2, which is a consequence of Eq. 61. The correlation of random effects is usually assumed to be negligible but is rarely tested (e.g. Al Atik et al., 2010). For the model presented here, the random effects variances have negligible correlations. As can be seen from Eq. 8.20, the covariance matrix (and thus the correlation) is dependent on the data set and the ground-motion model, therefore systematic evaluation of the model covariance matrix is important. The GMM parameters and the variances have vanishing correlations, as implied by the covariance matrix in Eq. 8.20 and shown in Fig. 8.6. The correlation matrix indicates the trade-off between the models parameters and help to identify those that are poorly resolved. Ground motion parameters related to the magnitude scaling and near source ground-motion saturation (a, c and d) are strongly correlated as expected. The correlation matrix also confirms the fact that the site term (parameter x in Eq. 8.22) is weakly correlated with other parameters as suggested by Fourier spectra parameter inversion (e.g. Drouet et al., 2008).

Several past crustal earthquakes studies (e.g Abrahamson & Silva, 2008) have suggested that aftershocks generate weaker ground motions than the associated mainshock. Some recent analysis of ground-motion residuals have confirmed such lower shaking associated to aftershocks but have also suggested that ground motions residuals computed using a backbone model may change several months before large earthquakes (Piña Valdés et al., 2018). The detection and quantification of these time-dependencies are important since they may reveal changes in the signature of earthquake spectra, the long-term preparation phase of large earthquakes or postseismic healing processes (Socquet et al., 2017; Piña Valdés et al., 2018; Bindi et al., 2018). Because of this recent and stimulating literature, we have computed (Fig. 8.7) the time-dependencies of between-events residuals 15 years before the Maule earthquake and 5 years after. The results suggest a slight decrease of between-events before the mainshock which is consistent with the progressive decrease of the released energy at high frequencies observed before the Iquique Earthquake (Piña Valdés et al., 2018). These observations may indicate a change on the subduction interface that may be related to a long-term nucleation process of the megathrust earthquake (Socquet et al., 2017). Figure 8.7 show however that these pre-seismic changes are still poorly constrained because of the lack of data and the variability of the observed residuals.

One particular aspect usually neglected in mixed-effect regression within seismology is the scaling of the variances. When performing mixed-effect regression for both parameters and random effect variances, then the reduced maximum likelihood should be used to avoid an underestimation of the random effect variances by accounting for the reduction of degrees of freedom (Patterson & Thompson, 1971; Harville, 1974). The reduction of degrees of freedom depends on the number of free parameters in the model (e.g. Eq. 8.75); and probably the most famous example is the $N-1$ divisor in the unbiased estimate of the sample variance with unknown mean (the mean is the free parameter, hence the degrees of freedom are reduced by one). Thus when neglecting the reduced freedom of degrees, the underestimation decreases with increasing data size for a given number of model parameters. The introduction of the mixed effect model into the strong-motion seismological community is closely linked to the work by Abrahamson & Youngs (1992). Their widely cited mixed effect algorithm is based on Searle (1971, ch. 8 b, p. 462)). However, reduced maximum likelihood for mixed effects in a general definition has been introduced by Patterson & Thompson (1971), i.e. simultaneously to Searle (1971). Several works related to the reduced maximum likelihood for mixed effects followed Patterson & Thompson (1971) (Harville, 1974; Lindstrom & Bates, 1988, e.g.), and it is widely applied in many fields (Sahai & Ageel, 2000). Implementations of both types of likelihoods have

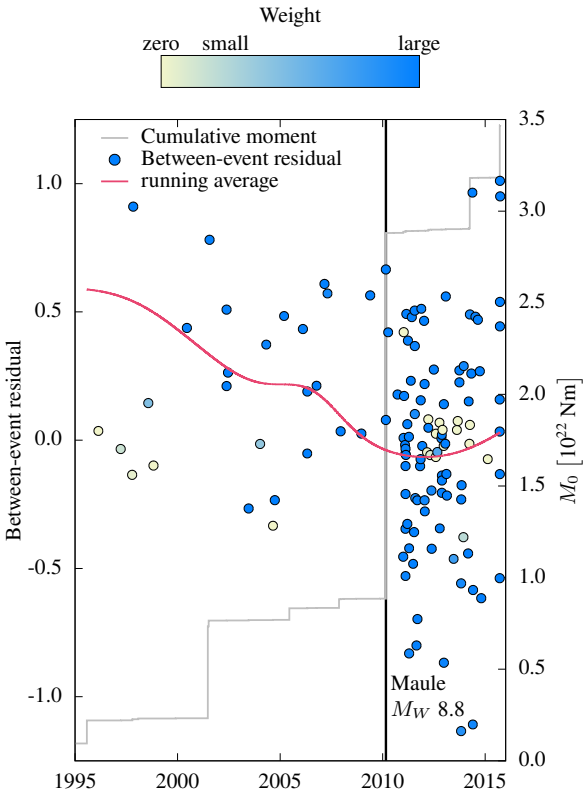

Figure 8.7: Temporal variations of the between-event residuals of the GMMs based on ACE weighted mixed-effect regression. The residuals follow the same trend and drop after major earthquakes, in particular after the 2010 Maule earthquake. The cumulative seismic moment of the earthquake catalog is shown in gray with the 2010 Maule earthquake having the single highest increase in released moment.

been realized in several software packages: `lme4` in R, `statsmodels` in python, `fitlme` in MATLAB to name a few. While the bias decreases with increasing data size, using the reduced maximum likelihood ensures better comparability between different GMMs.

8.7 Conclusion

This paper introduces the basis for a generalized mixed-effect regression by incorporating data weights through a weighted likelihood. The type of weights is more general and can be used in addition to data weights in the data covariance matrix. While the latter type of weights usually represents uncertainties related to the dependent variable, e.g. measurement errors (uncertainties of the ground motion values) or a different weighting of residuals (for e.g. robust regression), the former type of weights can represent not directly related uncertainties, e.g. degree-of-belief, event classification (either data-driven or expert judgment). With ACE-based data selection, as a data-driven and automatic determination of Style-of-Faulting classes, a fully machine-learning based GMM is provided here. The performance of the automatically derived GMM with regard to its parameters is comparable to (Montalva et al., 2017) with expert based judgment.

The cluster model of ACE can be directly implemented in modeling ground motion as weights for the events in the catalog. Once the mixture model has been learned from FM data set, new data can be classified instantly without a new cluster analysis. This opens the possibility to update ground-motions models in an automated way and can augment other updating routines as the Bayesian GMM approach of Stafford (2019).

We provide here a weight augmented mixed effects model which can be applied to both deterministic classification (expert judgment) and probabilistic classification (ACE). However, ACE treats data objectively and requires FM data alone, while expert judgment is subjective and requires additionally event location. Hypocenter uncertainties are usually not included and can be relatively large (e.g. depth). Furthermore, hypocenters may not be suitable to represent events with extensive rupture planes for a location dependent event classification.

The formulation used for the mixed-effect model is kept as general as possible and allows for an arbitrary number of random effects and is therefore suitable to design ground-motion models with a single framework. This facilitates hybrid models that partially incorporate mixed-effect regression (e.g Anderson & Brune, 1999; Sahakian et al., 2018). The incorporation of weights allows for smooth continuous spatial variations in regional GMMs—similar to the varying coefficient model by Landwehr et al. (2016)—thus opening the possibility for the development of nonergodic GMMs with mixed-effects regression.

Table 8.1: GMM coefficients with standard deviation in parentheses.

T [s]	a $[\times 10^{-1}]$	b $[\times 10^{-3}]$	c $[\times 10^{0}]$	d $[\times 10^{-1}]$	e $[\times 10^{-2}]$	x $[\times 10^{-1}]$
PGA	-3.7166 (*1.5993*)	-1.1993 (*0.7896*)	3.5219 (*0.2576*)	-3.0859 (*0.3097*)	0.9265 (*0.2013*)	-1.4190 (*0.4911*)
0.010	-3.7172 (*1.5993*)	-1.1992 (*0.7896*)	3.5220 (*0.2576*)	-3.0861 (*0.3097*)	0.9266 (*0.2014*)	-1.4190 (*0.4912*)
0.015	-3.7730 (*1.6050*)	-1.1697 (*0.7927*)	3.5295 (*0.2586*)	-3.0885 (*0.3109*)	0.9145 (*0.2012*)	-1.3738 (*0.4906*)
0.020	-3.6322 (*1.6101*)	-1.0437 (*0.7952*)	3.5379 (*0.2594*)	-3.0559 (*0.3120*)	0.9244 (*0.2017*)	-1.3727 (*0.4918*)
0.025	-3.6699 (*1.6177*)	-0.8489 (*0.7988*)	3.5854 (*0.2606*)	-3.0659 (*0.3134*)	0.9448 (*0.2027*)	-1.3927 (*0.4942*)
0.030	-3.6823 (*1.6155*)	-0.3844 (*0.7971*)	3.6730 (*0.2601*)	-3.0729 (*0.3126*)	0.9555 (*0.2045*)	-1.4506 (*0.4989*)
0.035	-4.3464 (*1.6154*)	0.0954 (*0.7966*)	3.8397 (*0.2599*)	-3.2056 (*0.3122*)	0.9818 (*0.2069*)	-1.4333 (*0.5053*)
0.040	-4.9187 (*1.6197*)	0.5480 (*0.7980*)	3.9977 (*0.2603*)	-3.3158 (*0.3126*)	1.0176 (*0.2099*)	-1.4215 (*0.5133*)
0.045	-5.0285 (*1.6186*)	0.8983 (*0.7966*)	4.0716 (*0.2598*)	-3.3296 (*0.3119*)	1.0453 (*0.2129*)	-1.4055 (*0.5210*)
0.050	-4.6772 (*1.6235*)	0.7513 (*0.7981*)	4.0285 (*0.2603*)	-3.2671 (*0.3124*)	1.0791 (*0.2161*)	-1.4232 (*0.5293*)
0.055	-4.7300 (*1.6228*)	0.6105 (*0.7967*)	4.0406 (*0.2598*)	-3.2770 (*0.3117*)	1.0995 (*0.2190*)	-1.4408 (*0.5369*)
0.060	-4.6084 (*1.6223*)	0.5426 (*0.7961*)	4.0442 (*0.2596*)	-3.2453 (*0.3112*)	1.1168 (*0.2210*)	-1.4810 (*0.5424*)
0.065	-4.3751 (*1.6192*)	0.4045 (*0.7938*)	3.9877 (*0.2588*)	-3.1981 (*0.3100*)	1.1183 (*0.2242*)	-1.4485 (*0.5511*)
0.070	-4.2310 (*1.6185*)	0.0816 (*0.7940*)	3.9055 (*0.2588*)	-3.1726 (*0.3099*)	1.1546 (*0.2239*)	-1.4201 (*0.5505*)
0.075	-4.2264 (*1.6090*)	-0.1632 (*0.7887*)	3.8654 (*0.2571*)	-3.1684 (*0.3077*)	1.1530 (*0.2250*)	-1.4138 (*0.5537*)
0.080	-4.6323 (*1.6144*)	-0.2865 (*0.7921*)	3.9114 (*0.2582*)	-3.2489 (*0.3090*)	1.1517 (*0.2244*)	-1.3764 (*0.5520*)
0.085	-4.6397 (*1.6127*)	-0.6732 (*0.7915*)	3.8586 (*0.2580*)	-3.2496 (*0.3088*)	1.1392 (*0.2234*)	-1.3548 (*0.5496*)
0.090	-4.1340 (*1.6120*)	-0.9253 (*0.7909*)	3.7544 (*0.2578*)	-3.1352 (*0.3085*)	1.1149 (*0.2240*)	-1.3569 (*0.5510*)
0.100	-2.9737 (*1.6051*)	-1.4707 (*0.7885*)	3.5272 (*0.2570*)	-2.8913 (*0.3077*)	1.1059 (*0.2207*)	-1.3834 (*0.5426*)
0.150	-1.4341 (*1.6341*)	-2.7746 (*0.8057*)	3.0988 (*0.2627*)	-2.5677 (*0.3149*)	0.9823 (*0.2153*)	-1.3374 (*0.5278*)
0.200	0.2029 (*1.6569*)	-3.2649 (*0.8211*)	2.6901 (*0.2678*)	-2.2864 (*0.3219*)	0.9233 (*0.2026*)	-1.2460 (*0.4937*)
0.250	0.1510 (*1.6681*)	-3.1038 (*0.8269*)	2.6981 (*0.2698*)	-2.3078 (*0.3246*)	0.7968 (*0.2005*)	-1.2498 (*0.4876*)
0.300	-0.0157 (*1.6809*)	-3.2203 (*0.8341*)	2.6672 (*0.2724*)	-2.3803 (*0.3284*)	0.6775 (*0.1927*)	-1.3767 (*0.4664*)
0.350	0.7806 (*1.6965*)	-2.9679 (*0.8409*)	2.5460 (*0.2750*)	-2.2480 (*0.3323*)	0.6083 (*0.1878*)	-1.2989 (*0.4524*)
0.400	0.8314 (*1.6869*)	-2.9095 (*0.8369*)	2.5388 (*0.2738*)	-2.2809 (*0.3311*)	0.6011 (*0.1812*)	-1.3974 (*0.4349*)
0.450	0.9034 (*1.7007*)	-2.0904 (*0.8437*)	2.6516 (*0.2762*)	-2.3084 (*0.3343*)	0.5219 (*0.1791*)	-1.4830 (*0.4288*)
0.500	0.9479 (*1.7007*)	-1.6843 (*0.8427*)	2.7277 (*0.2761*)	-2.3510 (*0.3344*)	0.5137 (*0.1774*)	-1.5829 (*0.4239*)
0.550	2.2388 (*1.6889*)	-1.5390 (*0.8366*)	2.5915 (*0.2740*)	-2.1716 (*0.3318*)	0.4733 (*0.1785*)	-1.6856 (*0.4268*)
0.600	3.0562 (*1.6861*)	-1.1653 (*0.8387*)	2.5370 (*0.2743*)	-2.0587 (*0.3319*)	0.4372 (*0.1750*)	-1.7868 (*0.4185*)
0.650	3.9233 (*1.6915*)	-1.3874 (*0.8446*)	2.3892 (*0.2758*)	-1.9316 (*0.3334*)	0.4141 (*0.1736*)	-1.8696 (*0.4156*)
0.700	4.6750 (*1.6995*)	-1.3918 (*0.8497*)	2.3022 (*0.2774*)	-1.8414 (*0.3352*)	0.3977 (*0.1730*)	-1.9198 (*0.4141*)
0.750	5.5926 (*1.6964*)	-1.5759 (*0.8488*)	2.1494 (*0.2771*)	-1.6886 (*0.3347*)	0.3486 (*0.1726*)	-1.9162 (*0.4134*)
0.800	5.8546 (*1.6874*)	-1.5832 (*0.8445*)	2.1050 (*0.2756*)	-1.6567 (*0.3329*)	0.2902 (*0.1722*)	-1.9135 (*0.4129*)
0.850	6.0168 (*1.6782*)	-1.4151 (*0.8390*)	2.1045 (*0.2739*)	-1.6590 (*0.3308*)	0.2432 (*0.1729*)	-1.9683 (*0.4147*)
0.900	6.2790 (*1.6693*)	-1.4797 (*0.8341*)	2.0661 (*0.2723*)	-1.6400 (*0.3289*)	0.2235 (*0.1731*)	-1.9853 (*0.4154*)
1.000	7.0070 (*1.6540*)	-1.2845 (*0.8260*)	2.0289 (*0.2697*)	-1.5656 (*0.3257*)	0.1645 (*0.1725*)	-2.0600 (*0.4142*)
1.500	7.2001 (*1.5592*)	-0.7853 (*0.7805*)	2.1935 (*0.2547*)	-1.7967 (*0.3074*)	0.0884 (*0.1615*)	-2.5235 (*0.3878*)
2.000	7.1013 (*1.4854*)	-0.8558 (*0.7429*)	2.3483 (*0.2423*)	-1.9775 (*0.2925*)	0.0896 (*0.1562*)	-2.6089 (*0.3778*)
2.500	5.7861 (*1.4309*)	-1.0977 (*0.7172*)	2.6464 (*0.2334*)	-2.3479 (*0.2813*)	0.1272 (*0.1541*)	-2.7653 (*0.3744*)
3.000	5.3336 (*1.3828*)	-0.4805 (*0.6923*)	2.8886 (*0.2252*)	-2.5348 (*0.2713*)	0.1272 (*0.1533*)	-3.0699 (*0.3739*)
3.500	4.0027 (*1.3824*)	0.4970 (*0.6953*)	3.2321 (*0.2254*)	-2.8827 (*0.2708*)	0.0898 (*0.1537*)	-3.1376 (*0.3755*)
4.000	2.7993 (*1.4809*)	0.4162 (*0.7624*)	3.4310 (*0.2479*)	-3.1876 (*0.2902*)	0.1287 (*0.1535*)	-3.2546 (*0.3755*)
4.500	2.0346 (*1.5110*)	0.5977 (*0.7770*)	3.5732 (*0.2535*)	-3.3735 (*0.2965*)	0.1619 (*0.1546*)	-3.2032 (*0.3786*)
5.000	1.6311 (*1.5348*)	0.8248 (*0.7923*)	3.6592 (*0.2578*)	-3.4672 (*0.3013*)	0.1395 (*0.1571*)	-3.1060 (*0.3844*)
5.500	2.3717 (*1.5602*)	1.0809 (*0.7996*)	3.5914 (*0.2615*)	-3.3145 (*0.3061*)	0.1198 (*0.1604*)	-2.9930 (*0.3924*)
6.000	1.2219 (*1.5748*)	2.0650 (*0.8127*)	3.8859 (*0.2657*)	-3.5943 (*0.3097*)	0.2107 (*0.1635*)	-2.9509 (*0.3894*)
6.500	1.6180 (*1.5903*)	2.5955 (*0.8221*)	3.9255 (*0.2686*)	-3.5531 (*0.3130*)	0.2035 (*0.1639*)	-2.9597 (*0.3905*)
7.000	2.8563 (*1.6024*)	2.6910 (*0.8273*)	3.7934 (*0.2706*)	-3.3268 (*0.3153*)	0.1826 (*0.1661*)	-2.9834 (*0.3961*)
7.500	3.4291 (*1.6174*)	2.6290 (*0.8327*)	3.7125 (*0.2733*)	-3.2269 (*0.3178*)	0.1640 (*0.1698*)	-2.9380 (*0.4050*)
8.000	4.1419 (*1.6474*)	2.9657 (*0.8689*)	3.6804 (*0.2803*)	-3.1293 (*0.3230*)	0.1466 (*0.1738*)	-2.9355 (*0.4014*)
8.500	3.7881 (*1.6705*)	3.0554 (*0.8799*)	3.7224 (*0.2853*)	-3.2065 (*0.3286*)	0.1606 (*0.1719*)	-2.8108 (*0.3974*)
9.000	3.7667 (*1.6732*)	2.8437 (*0.8846*)	3.6891 (*0.2861*)	-3.2116 (*0.3293*)	0.1577 (*0.1704*)	-2.7113 (*0.3941*)
10.000	4.1357 (*1.6848*)	2.6961 (*0.8902*)	3.6135 (*0.2888*)	-3.1457 (*0.3320*)	0.1677 (*0.1713*)	-2.5860 (*0.3894*)

Tab. 8.1 continued.

T [s]	q_i $[\times 10^1]$	s_i $[\times 10^{-2}]$	q_s $[\times 10^1]$	s_s $[\times 10^{-1}]$	s_{sl} $[\times 10^0]$
PGA	1.1247 (*0.1331*)	-4.7947 (*7.9464*)	1.3801 (*0.1358*)	-4.2801 (*0.9769*)	-1.1022 (*0.1708*)
0.010	1.1247 (*0.1331*)	-4.7908 (*7.9484*)	1.3800 (*0.1358*)	-4.2787 (*0.9768*)	-1.1019 (*0.1708*)
0.015	1.1453 (*0.1336*)	-5.4872 (*7.9383*)	1.4046 (*0.1363*)	-4.3491 (*0.9809*)	-1.1544 (*0.1716*)
0.020	1.1472 (*0.1340*)	-5.4562 (*7.9573*)	1.4057 (*0.1367*)	-4.3151 (*0.9843*)	-1.1442 (*0.1720*)
0.025	1.1540 (*0.1346*)	-4.8513 (*7.9960*)	1.4109 (*0.1373*)	-4.2731 (*0.9888*)	-1.0900 (*0.1730*)
0.030	1.1759 (*0.1344*)	-3.7051 (*8.0732*)	1.4254 (*0.1372*)	-4.0826 (*0.9865*)	-1.0322 (*0.1722*)
0.035	1.2393 (*0.1343*)	-3.0539 (*8.1759*)	1.4826 (*0.1372*)	-3.8958 (*0.9842*)	-0.9776 (*0.1720*)
0.040	1.3010 (*0.1346*)	-1.6202 (*8.3047*)	1.5376 (*0.1376*)	-3.7079 (*0.9853*)	-0.9273 (*0.1720*)
0.045	1.3340 (*0.1345*)	-2.8140 (*8.4293*)	1.5633 (*0.1376*)	-3.4617 (*0.9817*)	-0.9129 (*0.1719*)
0.050	1.3107 (*0.1350*)	-1.5681 (*8.5633*)	1.5120 (*0.1381*)	-2.8950 (*0.9820*)	-0.8928 (*0.1729*)
0.055	1.3062 (*0.1349*)	-0.6067 (*8.6851*)	1.4913 (*0.1382*)	-2.5597 (*0.9789*)	-0.8338 (*0.1729*)
0.060	1.3087 (*0.1349*)	-0.2816 (*8.7718*)	1.4563 (*0.1383*)	-1.8251 (*0.9755*)	-0.8087 (*0.1731*)
0.065	1.2822 (*0.1346*)	-0.6555 (*8.9114*)	1.4205 (*0.1381*)	-1.6211 (*0.9694*)	-0.7887 (*0.1727*)
0.070	1.2405 (*0.1346*)	-0.7930 (*8.8994*)	1.3669 (*0.1381*)	-1.4383 (*0.9678*)	-0.7536 (*0.1727*)
0.075	1.2354 (*0.1339*)	-0.8777 (*8.9488*)	1.3463 (*0.1375*)	-1.1435 (*0.9589*)	-0.7713 (*0.1719*)
0.080	1.2650 (*0.1344*)	-0.5271 (*8.9213*)	1.3546 (*0.1379*)	-0.7348 (*0.9628*)	-0.7716 (*0.1727*)
0.085	1.2543 (*0.1343*)	-0.4845 (*8.8808*)	1.3419 (*0.1378*)	-0.6754 (*0.9618*)	-0.7905 (*0.1731*)
0.090	1.2200 (*0.1343*)	-1.5327 (*8.9035*)	1.3013 (*0.1378*)	-0.5246 (*0.9603*)	-0.8091 (*0.1735*)
0.100	1.1113 (*0.1338*)	-3.4579 (*8.7667*)	1.1732 (*0.1373*)	-0.1735 (*0.9573*)	-0.7591 (*0.1734*)
0.150	1.0139 (*0.1364*)	-3.0704 (*8.5264*)	1.0611 (*0.1396*)	-0.2077 (*0.9827*)	-1.0111 (*0.1777*)
0.200	0.8805 (*0.1384*)	-7.9396 (*7.9798*)	1.0252 (*0.1411*)	-2.3283 (*1.0104*)	-1.2760 (*0.1807*)
0.250	0.9037 (*0.1391*)	-11.1371 (*7.8865*)	1.0639 (*0.1416*)	-2.6809 (*1.0230*)	-1.3723 (*0.1800*)
0.300	0.9256 (*0.1402*)	-14.1510 (*7.5516*)	1.1462 (*0.1424*)	-3.9282 (*1.0384*)	-1.5555 (*0.1825*)
0.350	0.8859 (*0.1416*)	-19.0944 (*7.3342*)	1.1746 (*0.1435*)	-5.2752 (*1.0530*)	-1.6979 (*0.1860*)
0.400	0.9011 (*0.1406*)	-21.4590 (*7.0575*)	1.2084 (*0.1424*)	-5.7341 (*1.0516*)	-1.8537 (*0.1840*)
0.450	0.9093 (*0.1416*)	-21.0934 (*6.9651*)	1.2369 (*0.1432*)	-6.1355 (*1.0640*)	-1.8015 (*0.1841*)
0.500	0.9028 (*0.1412*)	-22.3639 (*6.8948*)	1.2609 (*0.1428*)	-6.7351 (*1.0680*)	-1.7562 (*0.1816*)
0.550	0.7914 (*0.1401*)	-21.8836 (*6.9416*)	1.1844 (*0.1417*)	-7.4345 (*1.0610*)	-1.7274 (*0.1789*)
0.600	0.7294 (*0.1399*)	-22.9905 (*6.8028*)	1.1639 (*0.1414*)	-8.2297 (*1.0602*)	-1.7119 (*0.1775*)
0.650	0.6332 (*0.1404*)	-24.4540 (*6.7509*)	1.0793 (*0.1420*)	-8.4445 (*1.0626*)	-1.7030 (*0.1774*)
0.700	0.5605 (*0.1411*)	-22.4974 (*6.7259*)	1.0185 (*0.1426*)	-8.7566 (*1.0680*)	-1.6955 (*0.1778*)
0.750	0.4604 (*0.1410*)	-22.7678 (*6.7099*)	0.9175 (*0.1425*)	-8.7084 (*1.0642*)	-1.6560 (*0.1782*)
0.800	0.4124 (*0.1402*)	-23.5192 (*6.6993*)	0.8796 (*0.1417*)	-8.8377 (*1.0581*)	-1.6112 (*0.1767*)
0.850	0.3772 (*0.1393*)	-24.2886 (*6.7297*)	0.8582 (*0.1408*)	-9.0640 (*1.0526*)	-1.5561 (*0.1750*)
0.900	0.3204 (*0.1385*)	-24.2806 (*6.7412*)	0.8231 (*0.1401*)	-9.4775 (*1.0472*)	-1.4824 (*0.1737*)
1.000	0.2470 (*0.1374*)	-24.7474 (*6.7191*)	0.7516 (*0.1390*)	-9.4459 (*1.0359*)	-1.4211 (*0.1735*)
1.500	0.0298 (*0.1292*)	-28.6815 (*6.2908*)	0.5421 (*0.1307*)	-9.5254 (*0.9770*)	-0.8716 (*0.1611*)
2.000	-0.0211 (*0.1230*)	-29.6021 (*6.0843*)	0.4456 (*0.1243*)	-8.5730 (*0.9297*)	-0.7798 (*0.1514*)
2.500	0.0442 (*0.1189*)	-28.6204 (*6.0286*)	0.4559 (*0.1206*)	-7.5541 (*0.8931*)	-0.7315 (*0.1504*)
3.000	0.0906 (*0.1150*)	-29.2423 (*6.0100*)	0.5123 (*0.1168*)	-7.8012 (*0.8582*)	-0.7101 (*0.1461*)
3.500	0.1964 (*0.1150*)	-29.4751 (*6.0203*)	0.6455 (*0.1168*)	-8.2958 (*0.8540*)	-0.7129 (*0.1455*)
4.000	0.2660 (*0.1252*)	-28.1366 (*6.0103*)	0.7107 (*0.1280*)	-8.2689 (*0.8662*)	-0.7616 (*0.1493*)
4.500	0.3117 (*0.1279*)	-26.1627 (*6.0662*)	0.7533 (*0.1307*)	-8.2819 (*0.8834*)	-0.8038 (*0.1523*)
5.000	0.3308 (*0.1301*)	-24.9374 (*6.1713*)	0.7843 (*0.1330*)	-8.5051 (*0.9014*)	-0.8126 (*0.1557*)
5.500	0.3026 (*0.1319*)	-24.2165 (*6.3368*)	0.7625 (*0.1349*)	-8.5918 (*0.9178*)	-0.9021 (*0.1563*)
6.000	0.3985 (*0.1335*)	-23.3495 (*6.3023*)	0.8451 (*0.1363*)	-8.4787 (*0.9253*)	-0.9038 (*0.1565*)
6.500	0.3795 (*0.1351*)	-20.7371 (*6.3271*)	0.8230 (*0.1379*)	-8.4775 (*0.9372*)	-0.8793 (*0.1592*)
7.000	0.2825 (*0.1362*)	-19.1086 (*6.4181*)	0.7316 (*0.1391*)	-8.6150 (*0.9449*)	-0.8328 (*0.1611*)
7.500	0.2236 (*0.1374*)	-18.4469 (*6.5690*)	0.6904 (*0.1403*)	-8.9694 (*0.9495*)	-0.8134 (*0.1612*)
8.000	0.1596 (*0.1408*)	-18.4366 (*6.5888*)	0.6463 (*0.1456*)	-9.3905 (*0.9974*)	-0.7479 (*0.1632*)
8.500	0.1671 (*0.1430*)	-15.3929 (*6.5299*)	0.6630 (*0.1475*)	-9.6733 (*1.0066*)	-0.7455 (*0.1660*)
9.000	0.1471 (*0.1436*)	-13.9506 (*6.4685*)	0.6378 (*0.1481*)	-9.6086 (*1.0100*)	-0.7532 (*0.1676*)
10.000	0.0975 (*0.1448*)	-11.0084 (*6.4159*)	0.6027 (*0.1490*)	-9.9641 (*1.0212*)	-0.7702 (*0.1689*)

Table 8.2: GMM random effect standard deviations with standard deviation in parentheses.

T [s]	ϕ	τ	ϕ_{S2S}	σ_{P2P}
PGA	0.4303 (*0.0060*)	0.4911 (*0.0254*)	0.5199 (*0.0404*)	0.0896 (*0.0027*)
0.010	0.4303 (*0.0060*)	0.4913 (*0.0254*)	0.5199 (*0.0404*)	0.0896 (*0.0027*)
0.015	0.4323 (*0.0061*)	0.4901 (*0.0253*)	0.5225 (*0.0408*)	0.0895 (*0.0027*)
0.020	0.4340 (*0.0061*)	0.4912 (*0.0254*)	0.5224 (*0.0408*)	0.0895 (*0.0027*)
0.025	0.4359 (*0.0062*)	0.4936 (*0.0257*)	0.5277 (*0.0415*)	0.0893 (*0.0027*)
0.030	0.4345 (*0.0061*)	0.4996 (*0.0262*)	0.5224 (*0.0408*)	0.0898 (*0.0027*)
0.035	0.4325 (*0.0061*)	0.5074 (*0.0269*)	0.5238 (*0.0410*)	0.0924 (*0.0028*)
0.040	0.4323 (*0.0061*)	0.5169 (*0.0278*)	0.5229 (*0.0409*)	0.0937 (*0.0029*)
0.045	0.4297 (*0.0060*)	0.5265 (*0.0286*)	0.5277 (*0.0414*)	0.0954 (*0.0030*)
0.050	0.4291 (*0.0060*)	0.5364 (*0.0296*)	0.5384 (*0.0428*)	0.0955 (*0.0030*)
0.055	0.4269 (*0.0059*)	0.5456 (*0.0304*)	0.5436 (*0.0435*)	0.0958 (*0.0030*)
0.060	0.4245 (*0.0059*)	0.5522 (*0.0310*)	0.5525 (*0.0446*)	0.0991 (*0.0031*)
0.065	0.4204 (*0.0058*)	0.5629 (*0.0320*)	0.5576 (*0.0452*)	0.1040 (*0.0034*)
0.070	0.4193 (*0.0057*)	0.5620 (*0.0319*)	0.5615 (*0.0457*)	0.1088 (*0.0036*)
0.075	0.4146 (*0.0056*)	0.5664 (*0.0323*)	0.5670 (*0.0463*)	0.1109 (*0.0037*)
0.080	0.4163 (*0.0057*)	0.5639 (*0.0321*)	0.5698 (*0.0468*)	0.1128 (*0.0038*)
0.085	0.4160 (*0.0056*)	0.5610 (*0.0318*)	0.5768 (*0.0477*)	0.1115 (*0.0038*)
0.090	0.4151 (*0.0056*)	0.5628 (*0.0319*)	0.5844 (*0.0488*)	0.1107 (*0.0037*)
0.100	0.4141 (*0.0056*)	0.5530 (*0.0309*)	0.5884 (*0.0493*)	0.1107 (*0.0037*)
0.150	0.4276 (*0.0060*)	0.5330 (*0.0292*)	0.5972 (*0.0509*)	0.1061 (*0.0035*)
0.200	0.4448 (*0.0064*)	0.4897 (*0.0255*)	0.5846 (*0.0496*)	0.0981 (*0.0031*)
0.250	0.4526 (*0.0067*)	0.4815 (*0.0249*)	0.5557 (*0.0458*)	0.0947 (*0.0030*)
0.300	0.4640 (*0.0070*)	0.4546 (*0.0227*)	0.5574 (*0.0463*)	0.0829 (*0.0025*)
0.350	0.4752 (*0.0073*)	0.4365 (*0.0214*)	0.5683 (*0.0481*)	0.0697 (*0.0019*)
0.400	0.4777 (*0.0074*)	0.4153 (*0.0197*)	0.5460 (*0.0450*)	0.0669 (*0.0018*)
0.450	0.4860 (*0.0076*)	0.4065 (*0.0192*)	0.5299 (*0.0431*)	0.0645 (*0.0018*)
0.500	0.4906 (*0.0078*)	0.4006 (*0.0188*)	0.5008 (*0.0394*)	0.0603 (*0.0016*)
0.550	0.4865 (*0.0076*)	0.4052 (*0.0191*)	0.4848 (*0.0373*)	0.0615 (*0.0016*)
0.600	0.4854 (*0.0076*)	0.3941 (*0.0183*)	0.4756 (*0.0361*)	0.0721 (*0.0020*)
0.650	0.4849 (*0.0076*)	0.3892 (*0.0179*)	0.4740 (*0.0360*)	0.0867 (*0.0027*)
0.700	0.4874 (*0.0077*)	0.3863 (*0.0177*)	0.4722 (*0.0359*)	0.0916 (*0.0029*)
0.750	0.4847 (*0.0076*)	0.3854 (*0.0176*)	0.4806 (*0.0368*)	0.0961 (*0.0031*)
0.800	0.4814 (*0.0075*)	0.3854 (*0.0176*)	0.4741 (*0.0359*)	0.0989 (*0.0033*)
0.850	0.4787 (*0.0074*)	0.3886 (*0.0178*)	0.4645 (*0.0347*)	0.0966 (*0.0031*)
0.900	0.4761 (*0.0073*)	0.3903 (*0.0179*)	0.4593 (*0.0340*)	0.0945 (*0.0030*)
1.000	0.4702 (*0.0072*)	0.3901 (*0.0178*)	0.4690 (*0.0350*)	0.0919 (*0.0029*)
1.500	0.4436 (*0.0064*)	0.3639 (*0.0155*)	0.4157 (*0.0283*)	0.0945 (*0.0029*)
2.000	0.4212 (*0.0058*)	0.3527 (*0.0145*)	0.3795 (*0.0241*)	0.0892 (*0.0026*)
2.500	0.3992 (*0.0052*)	0.3521 (*0.0143*)	0.3966 (*0.0254*)	0.0851 (*0.0024*)
3.000	0.3806 (*0.0048*)	0.3549 (*0.0142*)	0.3960 (*0.0250*)	0.0878 (*0.0025*)
3.500	0.3775 (*0.0047*)	0.3557 (*0.0143*)	0.3908 (*0.0246*)	0.0859 (*0.0024*)
4.000	0.3816 (*0.0048*)	0.3529 (*0.0142*)	0.4097 (*0.0269*)	0.0840 (*0.0023*)
4.500	0.3868 (*0.0050*)	0.3537 (*0.0144*)	0.4202 (*0.0283*)	0.0895 (*0.0026*)
5.000	0.3921 (*0.0052*)	0.3590 (*0.0149*)	0.4125 (*0.0279*)	0.0891 (*0.0026*)
5.500	0.3949 (*0.0053*)	0.3671 (*0.0156*)	0.3966 (*0.0265*)	0.0863 (*0.0025*)
6.000	0.3941 (*0.0054*)	0.3607 (*0.0153*)	0.3880 (*0.0258*)	0.0891 (*0.0026*)
6.500	0.3955 (*0.0054*)	0.3607 (*0.0153*)	0.4004 (*0.0273*)	0.0922 (*0.0028*)
7.000	0.3953 (*0.0055*)	0.3671 (*0.0158*)	0.4112 (*0.0286*)	0.0933 (*0.0029*)
7.500	0.3961 (*0.0055*)	0.3775 (*0.0166*)	0.4060 (*0.0282*)	0.0918 (*0.0028*)
8.000	0.3964 (*0.0057*)	0.3683 (*0.0164*)	0.3735 (*0.0254*)	0.0923 (*0.0029*)
8.500	0.3984 (*0.0058*)	0.3620 (*0.0160*)	0.3875 (*0.0271*)	0.0943 (*0.0030*)
9.000	0.3993 (*0.0058*)	0.3571 (*0.0157*)	0.3949 (*0.0280*)	0.0908 (*0.0028*)
10.000	0.3998 (*0.0059*)	0.3498 (*0.0153*)	0.3915 (*0.0277*)	0.0947 (*0.0030*)

8.8 Appendix

8.8.1 Effect of different weighting methods

To show the difference between generalized (weighted) least squares and weighted likelihood estimators, both types of estimators for the mean and variance are derived, respectively. The weighted least squares estimator of a parameter minimizes the log-likelihood for N independent and identically distributed samples each with probability p_i:

$$\ln \mathcal{L} = \sum_{i=1}^{N} \ln p_i. \tag{8.25}$$

Least squares is based on the assumption of normally distributed variates and the log-likelihood is

$$\ln \mathcal{L} = -\frac{N}{2} \ln(2\pi\sigma^2) - \frac{1}{2\sigma^2} (\mathrm{x}-\mu)^T \mathrm{W} (\mathrm{x}-\mu). \tag{8.26}$$

The minimum of the log-likelihood is attained when the derivatives with respect to mean and variance vanish:

$$\frac{\partial \ln \mathcal{L}}{\partial \mu} = 0 \tag{8.27}$$

$$= W(\mathrm{y} - \mu), \tag{8.28}$$

and

$$\frac{\partial \ln \mathcal{L}}{\partial \sigma^2} = 0 \tag{8.29}$$

$$= -\frac{N}{\sigma^2} + \frac{1}{2\sigma^4} (\mathrm{x} - \mu)^T \mathrm{W} (\mathrm{x} - \mu). \tag{8.30}$$

Using sum representation, the weighted mean follows

$$\hat{\mu} = \frac{\sum_{i=1}^{N} w_i x_i}{\sum_{i=1}^{N} w_i}, \tag{8.31}$$

and the weighted variance

$$\hat{\sigma}^2 = \frac{1}{N} \sum_{i=1}^{N} w_i (x_i - \hat{\mu})^2. \tag{8.32}$$

While the weighted mean is normalized by the weights, the weighted variance is not.

Now we derive the estimators from weighted likelihood:

$$\ln \mathcal{L}_w = \sum_{i=1}^{N} w_i \ln p_i. \tag{8.33}$$

For the normal distribution holds

$$\ln \mathcal{L}_w = -\frac{1}{2} \sum_{i=1}^{N} w_i \left(\ln(2\pi\sigma^2) + \frac{(x_i - \mu)^2}{\sigma^2} \right). \tag{8.34}$$

The minimum of the log-likelihood is attained when the derivative vanishes

$$\frac{\partial \ln \mathcal{L}_w}{\partial \mu} = 0 \tag{8.35}$$

$$= \sum_{i=1}^{N} w_i (x_i - \mu), \tag{8.36}$$

and

$$\frac{\partial \ln \mathcal{L}_w}{\partial \sigma^2} = 0 \tag{8.37}$$

$$= \sum_{i=1}^{N} w_i \left(\frac{1}{\sigma^2} - \frac{(x_i - \mu)^2}{\sigma^4} \right). \tag{8.38}$$

The weighted mean follows as

$$\hat{\mu} = \frac{\sum_{i=1}^{N} w_i x_i}{\sum_{i=1}^{N} w_i}, \tag{8.39}$$

and the weighted variance

$$\hat{\sigma}^2 = \frac{\sum_{i=1}^{N} w_i (x_i - \hat{\mu})^2}{\sum_{i=1}^{N} w_i}. \tag{8.40}$$

The weighted mean is identical for both approaches, while only the weighted likelihood variance is (properly) scaled by the sum of weights and not by the number of samples.

8.8.2 Derivation of the coefficients of the mixed effects model based on weighted likelihood

The estimators for the GMM parameters p and predictors for the random effects q

The ML estimator for p and ML predictor q are derived from the derivatives of the log-likelihood in Eq. 8.7 (detailed derivation in appendix 8.8.2). Replacing the constant factors independent of p and q by c, and summarizing all weight matrices $\mathrm{V} = \mathrm{diag}\,(\mathrm{V}_1, \mathrm{V}_2, \ldots, \mathrm{V}_E)$ the log-likelihood is

$$\ln \mathcal{L} = c - \frac{1}{2\sigma^2} \Big(\mathrm{q}^T \mathrm{D}^{-1} \mathrm{q} + (\mathrm{V}(\mathrm{y} - \mathrm{Ap}) - \mathrm{Bq})^T \mathrm{C}^{-1} (\mathrm{V}(\mathrm{y} - \mathrm{Ap}) - \mathrm{Bq}) \Big). \tag{8.41}$$

The derivatives are given by

$$\frac{\partial \ln \mathcal{L}}{\partial \mathrm{p}} = \frac{1}{\sigma^2} \mathrm{A}^T \mathrm{V} \mathrm{C}^{-1} (\mathrm{V}(\mathrm{y} - \mathrm{Ap}) - \mathrm{Bq}) \tag{8.42}$$

$$\frac{\partial \ln \mathcal{L}}{\partial \mathrm{q}} = \frac{1}{\sigma^2} \left(\mathrm{B}^T \mathrm{C}^{-1} (\mathrm{V}(\mathrm{y} - \mathrm{Ap}) - \mathrm{Bq}) - \mathrm{D}^{-1} \mathrm{q} \right) \tag{8.43}$$

Setting both derivatives to zero, leads to the equations for the weighted mixed effects model

$$\begin{pmatrix} \mathrm{A}^T \mathrm{V} \mathrm{C}^{-1} \mathrm{V} \mathrm{y} \\ \mathrm{B}^T \mathrm{C}^{-1} \mathrm{V} \mathrm{y} \end{pmatrix} = \begin{pmatrix} \mathrm{A}^T \mathrm{V} \mathrm{C}^{-1} \mathrm{V} \mathrm{A} & \mathrm{A}^T \mathrm{V} \mathrm{C}^{-1} \mathrm{B} \\ \mathrm{B}^T \mathrm{C}^{-1} \mathrm{V} \mathrm{A} & \mathrm{B}^T \mathrm{C}^{-1} \mathrm{B} + \mathrm{D}^{-1} \end{pmatrix} \begin{pmatrix} \hat{\mathrm{p}} \\ \hat{\mathrm{q}} \end{pmatrix} \tag{8.44}$$

Solving the second row for the ML predictor of the random effects

$$\hat{\mathrm{q}} = \left(\mathrm{B}^T \mathrm{C}^{-1} \mathrm{B} + \mathrm{D}^{-1} \right)^{-1} \mathrm{B}^T \mathrm{C}^{-1} \mathrm{V} (\mathrm{y} - \mathrm{A}\hat{\mathrm{p}}) \tag{8.45}$$

The following matrix substitution is given by Henderson & Searle (1981)

$$\left(\mathrm{B}^T \mathrm{C}^{-1} \mathrm{B} + \mathrm{D}^{-1} \right)^{-1} \mathrm{B}^T \mathrm{C}^{-1} = \mathrm{D} \mathrm{B}^T \left(\mathrm{C} + \mathrm{B} \mathrm{D} \mathrm{B}^T \right)^{-1}, \tag{8.46}$$

and with

$$S := C + BDB^T \tag{8.47}$$

the predictor for q is

$$\hat{q} = DB^T S^{-1} V(y - A\hat{p}) \tag{8.48}$$

which is the best linear unbiased predictor of q (Henderson, 1975). Substituting $\hat{q}$ in the first row of Eq. 8.44:

$$A^T V C^{-1} \left(I - BDB^T S^{-1}\right) V(y - A\hat{p}) = 0 \tag{8.49}$$

$$A^T V C^{-1} \left(S - BDB^T\right) S^{-1} V(y - A\hat{p}) = 0$$

$$A^T V C^{-1} C S^{-1} V(y - A\hat{p}) = 0$$

$$A^T V S^{-1} V(y - A\hat{p}) = 0, \tag{8.50}$$

and solving for the parameters of the fixed effect model

$$\hat{p} = \left(A^T V S^{-1} V A\right)^{-1} A^T V S^{-1} V y, \tag{8.51}$$

which is the generalized least squares estimator with covariance matrix $VS^{-1}V$ (Aitken, 1936), and the best linear unbiased estimator (Henderson, 1975).

In Eq. 8.7 no weighting for the random effects is included. To show that Eq. 8.7 is consistent with the definition of the weighted likelihood in Eq. 8.3, the random effects predictor $\hat{q}$ of Eq. 8.48 is back-substituted (showing only the relevant part of the equation):

$$\begin{aligned} V(y - Ap) - B\hat{q} &= V(y - Ap) - BDB^T S^{-1} V(y - Ap) \\ &= V(y - Ap) - VBDB^T S^{-1}(y - Ap) \\ &= V(y - Ap - BDB^T S^{-1}(y - Ap)) \\ &= V(y - Ap - B\hat{q}_u). \end{aligned}$$

The matrices BDB^T and S^{-1} commute with V, because they are simultaneously diagonalizable, respectively. The predictor $\hat{q}_u = DB^T S^{-1}(y - Ap)$ is the unweighted random effects predictor. Therefore, the definition of the weighted likelihood in Eq. 8.7 agrees with Eq. 8.3 in addition for the random effects to be unweighted.

The difference between $\hat{q}$ and $\hat{q}_u$ is the weight matrix V, i.e. the square root of the weights w Let V and U be random variables and their respective outcomes are some weights $V = V$ and some unweighted residuals $U = Bq_u$. The underlying probability distributions of V and U are not further specified; it is only necessary that their expected values, $\mathbb{E}[V]$ and $\mathbb{E}[U]$, exist. According to the law of large numbers, the sample averages converge to the expected value

$$\bar{V} \to \mathbb{E}[V] \text{ and } \bar{U} \to \mathbb{E}[U] \text{ for } N \to \infty, \tag{8.52}$$

where the samples averages are

$$\bar{V} = \frac{1}{N}\sum_{i=1}^{N} V_i \text{ and } \bar{U} = \frac{1}{N}\sum_{i=1}^{N} B_i q. \tag{8.53}$$

Furthermore, the weight V is independent of the residual U, i.e. their covariance is zero, $\mathrm{Cov}(V, U) = 0$. From this follows, that the weighted residual, i.e. $VU = VBq_u = Bq$, has the expected value

$$\mathbb{E}[VU] = \mathbb{E}[V]\mathbb{E}[U]. \tag{8.54}$$

In other words, if the expected value of the square roots of the weights is unity, $\mathbb{E}[V] = 1$, then the expected values of the weighted and unweighted residuals are identical. Therefore, the weights are scaled by $\mathbb{E}[V]$ which is asymptotically equivalent to their sample average:

$$w_i = \frac{w_i^{(\text{unscaled})}}{\mathbb{E}(V)} \sim \frac{N}{\sum_{j=1}^{N} \sqrt{w_j^{(\text{unscaled})}}} w_i^{(\text{unscaled})}. \tag{8.55}$$

The variance estimators

The variance estimators of the mixed effect model dependent on the estimator $\hat{p}$ and predictor $\hat{q}$ of the fixed effect model. It is well established that ML variance estimates are biased downward by $\hat{p}$ and $\hat{q}$, i.e. variances are underestimated Patterson & Thompson (e.g. 1971); Harville (e.g. 1974, 1976); Lindstrom & Bates (e.g. 1988); Bates & DebRoy (e.g. 2004); Bates et al. (e.g. 2015). To obtain unbiased variance estimates, the likelihood is defined in terms of error contrasts. Details of the concept are described in full detail by Patterson & Thompson (1971); Harville (1976).

The basis for the variance estimators is to marginalize out the random effects q of the probability function from Eq. 8.2. First, completing the square for q in the exponential part. For brevity, the residuals are given by

$$r = y - Ap. \tag{8.56}$$

And

$$\begin{aligned} (r - Bq)^T C^{-1}(r - Bq) + q^T D^{-1} q \\ = (q - u)^T P(q - u) + v \end{aligned} \tag{8.57}$$

with

$$\begin{aligned} P &= B^T C^{-1} B + D^{-1} \\ u &= P^{-1} B^T C^{-1} r \\ v &= r^T C^{-1} r - r^T C^{-1} B P^{-1} B^T C^{-1} r. \end{aligned}$$

The integral over q is given by

$$\int_{\mathbb{R}^M} e^{-\frac{1}{2}(q-u)^T P(q-u)} dq = \left(\frac{2\pi}{|P|}\right)^{\frac{M}{2}}, \tag{8.58}$$

and the marginal probability of Eq. 8.2 is

$$\begin{aligned} P(y|Ap, \sigma^2, C, D) = \\ \frac{1}{\sqrt{(2\pi)^N |\sigma^2 C||\sigma^2 D||\sigma^{-2}\left(B^T C^{-1} B + D^{-1}\right)|}} \\ \times e^{-\frac{1}{2\sigma^2} r^T \left(C^{-1} - C^{-1}B\left(B^T C^{-1} B + D^{-1}\right)^{-1} B^T C^{-1}\right) r}. \end{aligned} \tag{8.59}$$

By using the identities in Eq. 8.46, Eq. 8.47, as well as Eq.8.49 - Eq.8.50, the matrix expression in the exponential term reduces to S^{-1}. With the generalized matrix determinant lemma (e.g. Harville, 1997, Theorem 13.3.8) and the identity $|kM| = k^n |M|$ (where M is of size $n \times n$), the determinant is restated as

$$|\sigma^2 C||\sigma^2 D||\sigma^{-2}\left(B^T C^{-1} B + D^{-1}\right)| \tag{8.60}$$

$$= \sigma^{2N} |C||DB^T C^{-1} B + I| \tag{8.61}$$

$$= \sigma^{2N} |C + BDB^T| \tag{8.62}$$

$$= \sigma^{2N} |S|. \tag{8.63}$$

Thus, the marginal probability is

$$P(\mathrm{y}|\mathrm{Ap},\sigma^2,\mathrm{S}) = \frac{1}{\sqrt{(2\pi\sigma^2)^N|\mathrm{S}|}} e^{-\frac{1}{2\sigma^2}\mathrm{r}^\mathrm{T}\mathrm{S}^{-1}\mathrm{r}}. \quad (8.64)$$

This probability distribution is given in terms of p—the unknown population parameter—and any ML estimates of the variances will be biased (Patterson & Thompson, 1971). Since p is unknown, its estimator $\hat{\mathrm{p}}$ (Eq.8.51) is used instead which is based on the same data as used for the variance estimators which also introduces a bias (Harville, 1974). This dependence reduces the degree of freedoms by the number of parameters P in p ($\hat{\mathrm{p}}$). Patterson & Thompson (1971) and Harville (1974) introduced the reduced maximum likelihood (RML) which provides unbiased estimates of the variances by transforming the data to linearly independent error contrasts. Furthermore, the RML definition of Harville (1974) also expresses the likelihood in terms of the known estimator $\hat{\mathrm{p}}$ instead of the unknown population parameter p. The RML is commonly used in mixed effect regression and should be used used when both fixed model parameters and random effect variances are estimated from the data (e.g Lindstrom & Bates, 1988; Demidenko, 2013; Bates et al., 2015).

The (unweighted) likelihood of Eq. 8.64 according to Harville (1974, 1976) is

$$\mathcal{L}(\mathrm{y}|\mathrm{A}\hat{\mathrm{p}},\sigma^2,\mathrm{S}) = \frac{|\mathrm{A}^\mathrm{T}\mathrm{A}|}{\sqrt{(2\pi)^{N-P}|\sigma^2\mathrm{S}||\sigma^{-2}\mathrm{A}^\mathrm{T}\mathrm{S}^{-1}\mathrm{A}|}} e^{-\frac{1}{2\sigma^2}\hat{\mathrm{r}}^\mathrm{T}\mathrm{S}^{-1}\hat{\mathrm{r}}}, \quad (8.65)$$

where $\hat{\mathrm{r}} = \mathrm{y} - \mathrm{A}\hat{\mathrm{r}}$ are the residuals with respect to the estimator $\hat{\mathrm{p}}$. The determinant $|\sigma^{-2}\mathrm{A}^\mathrm{T}\mathrm{S}^{-1}\mathrm{A}|$ results from the transformation of the likelihood as a function of p to the likelihood as a function of $\hat{\mathrm{p}}$. The likelihood in Eq. 8.65 cannot be split into event-wise terms as shown in Eq. 8.7 because the covariance matrix S has off-diagonal elements (Eq. 8.47). An eigendecomposition of S provides the necessary transformation, such that the likelihood is compliant with Eq. 8.3. To ensure that the weight matrix V remains diagonal as well, both matrices are eigendecomposed with

$$\mathrm{V}\mathrm{S}^{-1}\mathrm{V} = \mathrm{Q}\mathrm{K}^{-1}\mathrm{K}\mathrm{Q}^\mathrm{T}, \quad (8.66)$$

where Q is the eigenvector matrix of $\mathrm{V}\mathrm{S}^{-1}\mathrm{V}$ with the ith column corresponding to the ith eigenvalue in $\mathrm{K}^{-1}\mathrm{K}$. The eigenvector matrix Q of a symmetric matrix is orthonormal, i.e. it holds $\mathrm{Q}^\mathrm{T} = \mathrm{Q}^{-1}$ and with

$$\mathrm{V}\mathrm{S}^{-1}\mathrm{V} = \mathrm{Q}\mathrm{K}\mathrm{Q}^\mathrm{T}\mathrm{Q}^{-1}\mathrm{Q}^\mathrm{T}\mathrm{Q}\mathrm{K}\mathrm{Q}^\mathrm{T}, \quad (8.67)$$

the eigendecomposition is factorized. Furthermore, the eigenvector matrix simultaneously diagonalizes S^{-1} and V, i.e.

$$\mathrm{V} = \mathrm{Q}\mathrm{K}\mathrm{Q}^\mathrm{T}, \quad (8.68)$$

$$\mathrm{S}^{-1} = \mathrm{Q}^{-1}\mathrm{Q}^\mathrm{T}. \quad (8.69)$$

Replacing S with its eigendecomposition gives

$$\mathcal{L}(\mathrm{Q}^\mathrm{T}\mathrm{y}|\mathrm{Q}^\mathrm{T}\mathrm{A}\hat{\mathrm{p}},\sigma^2,) = \frac{|\mathrm{A}^\mathrm{T}\mathrm{Q}\mathrm{Q}^\mathrm{T}\mathrm{A}|}{\sqrt{(2\pi)^{N-P}|\sigma^2||\sigma^{-2}\mathrm{A}^\mathrm{T}\mathrm{Q}^{-1}\mathrm{Q}^\mathrm{T}\mathrm{A}|}} e^{-\frac{1}{2\sigma^2}\hat{\mathrm{r}}^\mathrm{T}\mathrm{Q}^{-1}\mathrm{Q}^\mathrm{T}\hat{\mathrm{r}}}, \quad (8.70)$$

This can be expressed by the product

$$\mathcal{L}(\mathrm{Q}^\mathrm{T}\mathrm{y}|\mathrm{Q}^\mathrm{T}\mathrm{A}\hat{\mathrm{p}},\sigma^2,) = \frac{|\mathrm{A}^\mathrm{T}\mathrm{Q}\mathrm{Q}^\mathrm{T}\mathrm{A}|}{\sqrt{(2\pi)^{N-P}|\sigma^{-2}\mathrm{A}^\mathrm{T}\mathrm{Q}^{-1}\mathrm{Q}^\mathrm{T}\mathrm{A}|}} \times \prod_{i=1}^{N} \frac{1}{\sqrt{|\sigma^2{}_\mathrm{i}|}} e^{-\frac{1}{2\sigma^2}\hat{\mathrm{r}}_\mathrm{i}^\mathrm{T}\mathrm{Q}_\mathrm{i}{}^{-1}\mathrm{Q}_\mathrm{i}^\mathrm{T}\hat{\mathrm{r}}_\mathrm{i}}. \quad (8.71)$$

From the above expression the record-wise weight for the weighted likelihood can be inferred by comparing Eq. 8.71 with Eq. 8.2, and Eq. 8.7 and is given by the diagonal elements of K, i.e. K_i. Thus, the weighted likelihood in terms of its logarithm is expressed as (summarizing constant terms)

$$\ln\mathcal{L}_w(\mathrm{Q}^\mathrm{T}\mathrm{y}|\mathrm{Q}^\mathrm{T}\mathrm{A}\hat{\mathrm{p}},\sigma^2,) = \text{const.} - \frac{1}{2}\sum_{i=1}^{N}\mathrm{K}_\mathrm{i}{}^2\left(\frac{1}{N}\ln|\sigma^{-2}\mathrm{A}^\mathrm{T}\mathrm{Q}\mathrm{K}^{-1}\mathrm{K}\mathrm{Q}^\mathrm{T}\mathrm{A}| + \ln|\sigma^2{}_\mathrm{i}|\right) - \frac{1}{2\sigma^2}\hat{\mathrm{r}}^\mathrm{T}\mathrm{Q}\mathrm{K}^{-1}\mathrm{K}\mathrm{Q}\hat{\mathrm{r}} \quad (8.72)$$

The RML estimator of σ^2 is found from the derivative of Eq. 8.72:

$$\frac{\partial\ln\mathcal{L}_w}{\partial\sigma^2} = \frac{1}{2\sigma^4}\mathrm{s}^\mathrm{T}\mathrm{K}^{-1}\mathrm{K}\mathrm{s} - \frac{1-\frac{P}{N}}{2\sigma^2}\sum_{i=1}^{N}\mathrm{K}_\mathrm{i}{}^2. \quad (8.73)$$

Setting the derivative to zero, solving for σ^2 and substitute the expression using Eq. 8.66

$$\hat{\sigma}^2 = \frac{\hat{\mathrm{r}}^\mathrm{T}\mathrm{Q}\mathrm{K}^{-1}\mathrm{K}\mathrm{Q}^\mathrm{T}\hat{\mathrm{r}}}{\left(1-\frac{P}{N}\right)\mathrm{tr}(\mathrm{K}\mathrm{K})} \quad (8.74)$$

$$= \frac{\hat{\mathrm{r}}^\mathrm{T}\mathrm{V}\mathrm{S}^{-1}\mathrm{V}\hat{\mathrm{r}}}{\left(1-\frac{P}{N}\right)\mathrm{tr}(\mathrm{V}\mathrm{V})}, \quad (8.75)$$

the trace is used in Eq. 8.75 and results from the identity

$$\mathrm{tr}(\mathrm{K}\mathrm{K}) = \sum_{i=1}^{N}\mathrm{K}_\mathrm{i}{}^2 = \mathrm{tr}(\mathrm{V}\mathrm{V}) = \sum_{i=1}^{N}\mathrm{V}_\mathrm{i}{}^2 = N. \quad (8.76)$$

The last identity holds if Eq. 8.55 is invoked and the variance is

$$\hat{\sigma}^2 = \frac{\hat{\mathrm{r}}^\mathrm{T}\mathrm{V}\mathrm{S}^{-1}\mathrm{V}\hat{\mathrm{r}}}{N-P} \quad (8.77)$$

This is the unbiased estimator of the variance and appears frequently with the denominator $N-1$, i.e. for $P=1$. The estimator corrects the bias for the loss of degree of freedoms which is equal to the number of parameters P in the GMM parameter estimator $\hat{\mathrm{p}}$. For generality the variance formulation in Eq. 8.75 is used in the following equations.

The RML estimators of the variance factors τ_k are linked to the variance $\hat{\sigma}^2$ and to the eigenvalue matrix, since it is a function of the variance contrasts, i.e. (τ_E, τ_S, τ_T). The derivative of Eq. 8.72 with respect to

τ_k is

$$\frac{\partial \ln \mathcal{L}_w}{\partial \tau_k} = -\frac{1}{2}\sum_{i=1}^{N} \mathrm{K_i}^2 \left(\frac{1}{N} \frac{\partial}{\partial \tau_k} \ln |\mathrm{A^T Q K^{-1} K Q^T A}| + \frac{\partial}{\partial \tau_k} \ln |_\mathrm{i}| \right) - \frac{1}{2\sigma^2} \hat{\mathrm{r}}^\mathrm{T} \mathrm{Q K} \frac{\partial^{-1}}{\partial \tau_\mathrm{k}} \mathrm{K Q^T} \hat{\mathrm{r}} \quad (8.78)$$

The derivative of a determinant are given by Jacobi's formula which expresses the derivative of the determinant. With the chain rule the derivatives of the log-determinants are

$$\frac{\partial \ln |_\mathrm{i}|}{\partial \tau_k} = \mathrm{tr}\left({}_\mathrm{i}^{-1} \frac{\partial {}_\mathrm{i}}{\partial \tau_k} \right) \quad \text{and} \quad (8.79)$$

$$\frac{\partial \ln |\mathrm{A^T Q K^{-1} K Q^T A}|}{\partial \tau_k} = \mathrm{tr}\left(\left(\mathrm{A^T Q K^{-1} K Q^T A} \right)^{-1} \mathrm{A^T Q K} \frac{\partial^{-1}}{\partial \tau_k} \mathrm{K Q^T A} \right) \quad (8.80)$$

From Eq. 8.5, 8.6, Eq. 8.47, and Eq. 8.69, the derivative of ${}_\mathrm{i}$ is

$$\frac{\partial {}_\mathrm{i}}{\partial \tau_k} = \mathrm{Q_i^T B_k B_k^T Q_i} \quad (8.81)$$

and the derivative of the inverse is

$$\frac{\partial^{-1}}{\partial \tau_k} = -{}^{-1} \frac{\partial}{\partial \tau_\mathrm{k}} {}^{-1} = -{}_\mathrm{i}^{-1} \mathrm{Q^T B_k B_k^T Q^{-1}}. \quad (8.82)$$

Since ${}_\mathrm{i}$ and $\mathrm{K_i}$ are of size 1×1 the sum of weights in Eq. 8.78 and the trace of the derivative of the determinant in Eq. 8.81 can be combined

$$\sum_{i=1}^{N} \mathrm{K_i}^2 \frac{\partial}{\partial \tau_k} \ln |_\mathrm{i}| \quad (8.83)$$

$$= \sum_{i=1}^{N} \mathrm{K_i} {}_\mathrm{i}^{-1} \mathrm{Q_i^T B_k B_k^T Q_i K_i} \quad (8.84)$$

$$= \mathrm{tr}\left(\mathrm{K^{-1} Q^T B_k B_k^T Q K} \right). \quad (8.85)$$

With the diagonalized matrices replaced according to Eq. 8.66 and the fact that the trace is invariant under circular permutation, the eigenvector matrix Q disappears

$$\mathrm{tr}\left(\mathrm{K^{-1} Q^T B_k B_k^T Q K} \right) \quad (8.86)$$

$$= \mathrm{tr}\left(\mathrm{Q^T V S^{-1} B_k B_k^T V Q} \right) \quad (8.87)$$

$$= \mathrm{tr}\left(\mathrm{Q Q^T V S^{-1} B_k B_k^T V} \right) \quad (8.88)$$

$$= \mathrm{tr}\left(\mathrm{V S^{-1} B_k B_k^T V} \right). \quad (8.89)$$

Thus, the derivative can be expressed without the eigendecompositions by replacing the remaining diagonalized matrices in Eq. 8.78 according to Eq. 8.66:

$$\frac{\partial \ln \mathcal{L}_w}{\partial \tau_k} = \frac{1}{2}\Bigg[\mathrm{tr}\left(\mathrm{V S^{-1} B_k B_k^T V} \right) + \mathrm{tr}\left(\left(\mathrm{A^T V S^{-1} V A} \right)^{-1} \mathrm{A^T V S^{-1} B_k B_k^T S^{-1} V A} \right) \frac{\mathrm{tr(VV)}}{N} + \frac{1}{\hat{\sigma}^2} \hat{\mathrm{r}}^\mathrm{T} \mathrm{V S^{-1} B_k B_k^T S^{-1} V} \hat{\mathrm{r}} \Bigg] \quad (8.90)$$

The second term is closely related to the fixed model estimator $\hat{\mathrm{p}}$ (Eq. 8.51). By setting

$$\mathrm{X} = \left(\mathrm{A^T V S^{-1} V A} \right)^{-1} \mathrm{A^T V S^{-1} V}, \quad (8.91)$$

if follows

$$\hat{\mathrm{p}} = \mathrm{X y} \quad (8.92)$$

and

$$\frac{\partial \ln \mathcal{L}_w}{\partial \tau_k} = \frac{1}{2}\Bigg[\mathrm{tr}\left(\mathrm{V S^{-1} B_k B_k^T V} \right) + \mathrm{tr}\left(\mathrm{X B_k B_k^T S^{-1} A} \right) \frac{\mathrm{tr(VV)}}{N} + \frac{1}{\hat{\sigma}^2} \hat{\mathrm{r}}^\mathrm{T} \mathrm{V S^{-1} B_k B_k^T S^{-1} V} \hat{\mathrm{r}} \Bigg]. \quad (8.93)$$

Using X highlights the link between the bias correction in RML and the least squares estimate $\hat{\mathrm{p}}$.

The derivative with respect to the variance factors has no analytic solution for maximization and must be maximized numerically, e.g. by gradient ascent:

$$\boldsymbol{\tau}^{(i+1)} = \boldsymbol{\tau}^{(i)} + \gamma \nabla \mathcal{L}_w, \quad (8.94)$$

where $\boldsymbol{\tau}$ is the vector of variance factors, i.e. with Eq. 8.5 $\boldsymbol{\tau} = (\tau_1, \tau_2, \ldots, \tau_K)^T$. The factor γ is chosen such to guarantee convergence and is updated at each iteration (Barzilai & Borwein, 1988)

$$\gamma = \frac{\left(\boldsymbol{\tau}^{(i)} - \boldsymbol{\tau}^{(i-1)} \right)^T \left(\nabla \mathcal{L}_w \left(\boldsymbol{\tau}^{(i)} \right) - \nabla \mathcal{L}_w \left(\boldsymbol{\tau}^{(i-1)} \right) \right)}{\left\| \nabla \mathcal{L}_w \left(\boldsymbol{\tau}^{(i)} \right) - \nabla \mathcal{L}_w \left(\boldsymbol{\tau}^{(i-1)} \right) \right\|^2} \quad (8.95)$$

The algorithm starts from some initial values and is repeated until sufficient convergence of the parameters is reached. At each iteration, $\hat{\sigma}^2$ and $\hat{\mathrm{p}}$ are updated before the factors $\boldsymbol{\tau}$ are updated. Finally, the maximum likelihood estimates of the variances are:

$$\hat{\boldsymbol{\upsilon}} = \hat{\sigma}^2 \hat{\boldsymbol{\tau}} \quad (8.96)$$

8.8.3 Fisher Information Matrix

Here the entries of the Fisher information matrix in Eq. 8.19 are given. The matrix has six independent derivatives (the matrix is symmetric and the off-diagonal elements are related by their transpose). The residual vector is given by

$$\mathrm{r} = \mathrm{y} - \mathrm{A p} \quad (8.97)$$

All derivatives of the log-likelihood are related to the weighted precision matrix P and/or its derivatives

$$\mathrm{P} = \mathrm{V S^{-1} V} \quad (8.98)$$

$$\frac{\partial \mathrm{P}}{\partial \hat{\tau}_k} = -\mathrm{V S^{-1} B_k B_k^T S^{-1} V} \quad (8.99)$$

$$\frac{\partial^2 \mathrm{P}}{\partial \hat{\tau}_k \hat{\tau}_l} = 2\mathrm{V S^{-1} B_l B_l^T S^{-1} B_k B_k^T S^{-1} V} \quad (8.100)$$

For the variance factors $\hat{\boldsymbol{\tau}}$ follows from Eq. 8.96:

$$\hat{\boldsymbol{\tau}} = \frac{1}{\hat{\sigma}^2} \hat{\boldsymbol{\upsilon}} \quad (8.101)$$

With the chain rule, the derivatives can be represented in terms of the random effects variance vector $\hat{\boldsymbol{v}}$.

$$\frac{\partial \mathrm{P}}{\partial \hat{v}_k} = \frac{\partial \mathrm{P}}{\partial \hat{\tau}_k}\frac{\partial \hat{\tau}_k}{\partial \hat{v}_k} \tag{8.102}$$

$$= \frac{1}{\hat{\sigma}^2}\frac{\partial \mathrm{P}}{\partial \hat{\tau}_k} \tag{8.103}$$

$$\frac{\partial^2 \mathrm{P}}{\partial \hat{v}_k \partial \hat{v}_l} = \frac{\partial}{\partial \hat{\tau}_l}\left(\frac{\partial \mathrm{P}}{\partial \hat{\tau}_k}\frac{\partial \hat{\tau}_k}{\partial \hat{v}_k}\right)\frac{\partial \hat{\tau}_l}{\partial \hat{v}_l} \tag{8.104}$$

$$= \left(\frac{\partial^2 \mathrm{P}}{\partial \hat{\tau}_k \partial \hat{\tau}_l}\frac{\partial \hat{\tau}_k}{\partial \hat{v}_k} + \frac{\partial \mathrm{P}}{\partial \hat{\tau}_k}\underbrace{\frac{\partial^2 \hat{\tau}_k}{\partial \hat{v}_k \partial \hat{v}_l}}_{=0}\right)\frac{\partial \hat{\tau}_l}{\partial \hat{v}_l} \tag{8.105}$$

$$= \frac{1}{\hat{\sigma}^4}\frac{\partial^2 \mathrm{P}}{\partial \hat{\tau}_k \partial \hat{\tau}_l} \tag{8.106}$$

and the second derivatives of the log-likelihood are

$$\frac{\partial^2 \ln \mathcal{L}_w}{\partial \hat{\mathrm{p}} \partial \hat{\mathrm{p}}} = -\frac{1}{\hat{\sigma}^2}\mathrm{A}^\mathrm{T}\mathrm{P}\mathrm{A} \tag{8.107}$$

$$\frac{\partial^2 \ln \mathcal{L}_w}{\partial \hat{\mathrm{p}} \partial \hat{\sigma}^2} = -\frac{1}{\hat{\sigma}^4}\mathrm{A}^\mathrm{T}\mathrm{P}\mathrm{r} \tag{8.108}$$

$$\frac{\partial^2 \ln \mathcal{L}_w}{\partial \hat{\mathrm{p}} \partial \hat{v}_k} = \frac{1}{\hat{\sigma}^2}\mathrm{A}^\mathrm{T}\frac{\partial \mathrm{P}}{\partial \hat{v}_k}\mathrm{r} \tag{8.109}$$

$$\frac{\partial^2 \ln \mathcal{L}_w}{\partial \hat{\sigma}^2 \partial \hat{\sigma}^2} = \frac{\mathrm{tr}(\mathrm{V}\mathrm{V})\left(1-\frac{P}{N}\right)}{2\hat{\sigma}^4} - \frac{1}{\hat{\sigma}^6}\mathrm{r}^\mathrm{T}\mathrm{P}\mathrm{r} \tag{8.110}$$

$$\frac{\partial^2 \ln \mathcal{L}_w}{\partial \hat{\sigma}^2 \partial \hat{v}_k} = \frac{1}{2\hat{\sigma}^4}\mathrm{r}^\mathrm{T}\frac{\partial \mathrm{P}}{\partial \hat{v}_k}\mathrm{r} \tag{8.111}$$

$$\frac{\partial^2 \ln \mathcal{L}_w}{\partial \hat{v}_k \partial \hat{v}_l} = \frac{1}{4}\mathrm{tr}\left(\frac{\partial^2 \mathrm{P}}{\partial \hat{v}_k \partial \hat{v}_l}\mathrm{S}\right) - \frac{1}{2\hat{\sigma}^2}\mathrm{r}^\mathrm{T}\frac{\partial^2 \mathrm{P}}{\partial \hat{v}_k \hat{v}_l}\mathrm{r} - \frac{\mathrm{tr}(\mathrm{V}\mathrm{V})}{2N}\mathrm{tr}\left(\mathrm{H}\frac{\partial \mathrm{P}}{\partial \hat{v}_l}\mathrm{H}\frac{\partial \mathrm{P}}{\partial \hat{v}_k} + \mathrm{H}\frac{\partial^2 \mathrm{P}}{\partial \hat{v}_k \hat{v}_l}\right) \tag{8.112}$$

$$\text{with} \quad \mathrm{H} = \mathrm{A}\left(\mathrm{A}^\mathrm{T}\mathrm{P}\mathrm{A}\right)^{-1}\mathrm{A}^\mathrm{T}. \tag{8.113}$$

For the expected value it holds:

$$\mathbb{E}[\mathrm{A}\mathrm{p}] = \mathrm{y} \tag{8.114}$$

$$\mathbb{E}\left[\mathrm{r}^\mathrm{T}\mathrm{r}\right] = \hat{\sigma}^2\mathrm{tr}\left(\mathrm{S}\right), \tag{8.115}$$

for some nonstochastic matrix . From and Eq. 8.97 and 8.114 follows immediately for Eq. 8.108 and 8.109 that their expected values vanish:

$$\mathbb{E}\left[\frac{\partial^2 \ln \mathcal{L}_w}{\partial \hat{\mathrm{p}} \partial \hat{\sigma}^2}\right] = 0 \tag{8.116}$$

$$\mathbb{E}\left[\frac{\partial^2 \ln \mathcal{L}_w}{\partial \hat{\mathrm{p}} \partial \hat{v}_k}\right] = 0, \tag{8.117}$$

i.e. the model parameters are independent from the variances. With Eq. 8.115 the expected value of the "normal term" reduces to

$$\mathbb{E}\left[\mathrm{r}^\mathrm{T}\mathrm{P}\mathrm{r}\right] = \hat{\sigma}^2\mathrm{tr}\left(\mathrm{P}\mathrm{S}\right)$$

$$= \hat{\sigma}^2\mathrm{tr}(\mathrm{V}\mathrm{V}) \tag{8.118}$$

Let T be the $1 \times K$ vector associated with the expected value of the derivatives of Eq. 8.111:

$$-\mathbb{E}\left[\frac{\partial^2 \ln \mathcal{L}_w}{\partial \hat{\sigma}^2 \partial \hat{v}_k}\right] = -\frac{1}{2\hat{\sigma}^2}\mathrm{tr}\left(\frac{\partial \mathrm{P}}{\partial \hat{v}_k}\mathrm{S}\right) \tag{8.119}$$

$$= -\frac{\mathrm{tr}(\mathrm{V}\mathrm{V})}{2\hat{\sigma}^4}T_k \tag{8.120}$$

$$T_k = \frac{\hat{\sigma}^2}{\mathrm{tr}(\mathrm{V}\mathrm{V})}\mathrm{tr}\left(\frac{\partial \mathrm{P}}{\partial \hat{v}_k}\right) \tag{8.121}$$

and U is the $K \times K$ matrix associated with the expected value of the derivatives of Eq. 8.112:

$$U_{kl} = -\mathbb{E}\left[\frac{\partial^2 \ln \mathcal{L}_w}{\partial \hat{v}_k \partial \hat{v}_l}\right] \tag{8.122}$$

$$= \frac{1}{4}\mathrm{tr}\left(\frac{\partial^2 \mathrm{P}}{\partial \hat{v}_k \partial \hat{v}_l}\mathrm{S}\right) \tag{8.123}$$

The Fisher information matrix is

$$\mathrm{I}(\hat{\mathrm{p}}, \hat{\sigma}^2, \hat{\boldsymbol{v}}) = \begin{pmatrix} \frac{1}{\hat{\sigma}^2}\mathrm{A}^\mathrm{T}\mathrm{P}\mathrm{A} & 0 & 0 \\ 0 & \frac{\mathrm{tr}(\mathrm{V}\mathrm{V})}{2\hat{\sigma}^4} & -\frac{\mathrm{tr}(\mathrm{V}\mathrm{V})}{2\hat{\sigma}^4}\mathrm{T} \\ 0 & -\frac{\mathrm{tr}(\mathrm{V}\mathrm{V})}{2\hat{\sigma}^4}\mathrm{T}^\mathrm{T} & \mathrm{U} \end{pmatrix} \tag{8.124}$$

This matrix can be seen as a block diagonal matrix of two blocks (highlighted by color), where the red block is a 2×2 block matrix. The inverse of a block diagonal matrix is again a block diagonal matrix where each block is inverted separately, allowing a simplified computation of the entire matrix inverse. An arbitrary 2×2 block matrix has the inverse (e.g. Harville, 1997)

$$\begin{pmatrix} \mathrm{A} & \mathrm{B} \\ \mathrm{C} & \mathrm{D} \end{pmatrix}^{-1} = \begin{pmatrix} \mathrm{A}^{-1} + \mathrm{A}^{-1}\mathrm{B}\mathrm{G}^{-1}\mathrm{C}\mathrm{A}^{-1} & -\mathrm{A}^{-1}\mathrm{B}\mathrm{G}^{-1} \\ -\mathrm{G}^{-1}\mathrm{C}\mathrm{A}^{-1} & \mathrm{G}^{-1} \end{pmatrix}^{-1} \tag{8.125}$$

where $\mathrm{G} = \mathrm{D} - \mathrm{C}\mathrm{A}^{-1}\mathrm{B}$ is a non-singular matrix, and A and D are square matrices. The inverse of the block-submatrix of the variances (red block in Eq. 8.124) is

$$\begin{pmatrix} \frac{\mathrm{tr}(\mathrm{V}\mathrm{V})}{2\hat{\sigma}^4} & -\frac{1}{2\hat{\sigma}^2}\mathrm{T} \\ -\frac{1}{2\hat{\sigma}^2}\mathrm{T}^\mathrm{T} & \mathrm{U} \end{pmatrix}^{-1} = \begin{pmatrix} \frac{2\hat{\sigma}^4}{\mathrm{tr}(\mathrm{V}\mathrm{V})} + \mathrm{T}\mathrm{M}\mathrm{T}^\mathrm{T} & \mathrm{T}\mathrm{M} \\ \mathrm{M}\mathrm{T}^\mathrm{T} & \mathrm{M} \end{pmatrix} \tag{8.126}$$

$$\text{with} \quad \mathrm{M} = \left(\mathrm{U} - \frac{\mathrm{tr}(\mathrm{V}\mathrm{V})}{\hat{\sigma}^4}\mathrm{T}^\mathrm{T}\mathrm{T}\right)^{-1} \tag{8.127}$$

The inverse of the Fisher information—which is asymptotically equivalent to the covariance matrix as $N \to \infty$ —is stated as

$$\mathrm{I}(\hat{\mathrm{p}}, \hat{\sigma}^2, \hat{\boldsymbol{v}})^{-1} \sim \mathrm{cov}(\hat{\mathrm{p}}, \hat{\sigma}^2, \hat{\boldsymbol{v}})$$

$$= \begin{pmatrix} \hat{\sigma}^2(\mathrm{A}^\mathrm{T}\mathrm{P}\mathrm{A})^{-1} & 0 & 0 \\ 0 & \frac{2\hat{\sigma}^4}{\mathrm{tr}(\mathrm{V}\mathrm{V})} + \mathrm{T}\mathrm{M}\mathrm{T}^\mathrm{T} & \mathrm{T}\mathrm{M} \\ 0 & \mathrm{M}\mathrm{T}^\mathrm{T} & \mathrm{M} \end{pmatrix} \tag{8.128}$$

The upper left block matrix is equivalent to the model parameter covariance matrix; only the covariance matrix of the random effect variances is asymptotically equivalent to above expression.

不可言說諸佛剎，
皆悉碎末爲微塵，
一塵中剎不可說，
如一一切皆如是。
此不可說諸佛剎，
一念碎塵不可說，
念念所碎悉亦然，
盡不可說劫恒爾。
此塵有剎不可說，
此剎爲塵說更難，
以不可說算數法，
不可說劫如是數。

If untold buddha-lands are reduced to atoms,
In one atom are untold lands,
And as in one,
So in each.
The atoms to which these buddha-lands are reduced in an instant are unspeakable,
And so are the atoms of continuous reduction moment to moment
Going on for untold eons;
These atoms contain lands unspeakably many,
And the atoms in these lands are even harder to tell of.

大方廣佛華嚴經卷第四十五 阿僧祇品第三十

from book 30 'The Incalculable' in the Avatamsaka Sutra (Engl. translation: The Flower Ornament Scripture Cleary, 1993, p. 889ff.)

Chapter 9

Synthesis

There are infinite possibilities to construct model-worlds reflecting the same observed reality. This thesis aims to reflect this indispensable thought, and that the models developed herein are neither perfect nor the only solutions to describe the observations. However, they serve purpose, the purpose to understand the seismic reality better. All models I designed and introduced in the previous chapters are different realizations of the likelihood—one of many means for parameter estimation. Each model realization may result in different results, which ultimately leads to the question of the applicability of those models.

Model development does not exist for its own sake, it is directed and guided by the research question, the mathematics—in general and by personal skill—and the available computational power. With a model at hand, not only the intermediate questions can be answered, but other questions at the periphery may be answered as well. For instance, the development of ACE (Angular Clusterization with Expectation-Maximization, ch. 2) was originally motivated for a faster and more objective way of earthquake type classification for a earthquake catalog used in ground-motion modeling. That the data classifications based on ACE can be applied to other topics and linked to GPS (Global Positioning System) and GMM (Ground-Motion Model) residuals to detect temporal variations (ch. 3 & 4), or the improvement of stress tensor inversions (ch. 5) was not anticipated during the early stages in the development of ACE. In the same way, it was unexpectedly more complicated to incorporate the probabilistic earthquake classification of ACE into ground motion modeling with mixed-effect regression than with a deterministic classification. The final chapter (ch. 8 of the thesis manifests this interdependence of probabilistic data weighting with mixed-effect regression—a concept completely new to GMM development.

While the primary purpose of ACE is to abstract cluster properties of earthquakes, the principal capacity of ICBM (Integrated Combined Baseline Modification, ch. 6) is a robust way to concretely improve waveform data quality by removing data offsets. Consequently, waveforms with ICBM baseline corrections provide less biased estimates of coseismic displacement (ch. 6) and radiated seismic energy (ch. 7). In that way, ICBM affects the waveforms used not only for characterization of strong ground-motion but also for estimates of radiated seismic energy for the GMM of the 2016 Kumamoto earthquake—the first GMM with a station-dependent energy term instead of a single source-related magnitude term. Although ICBM has not been applied to the data for the ACE weighted GMM in ch. 8, because the database of (Bastías & Montalva, 2016) has been used, ICBM can be included in routine data preprocessing for GMMs, as a more general baseline correction beyond basic linear detrending (which is a special case of ICBM).

The continuous improvement and connection of different models in strong-motion seismology improves our image, our understanding, of the nature of hazardous earthquakes and related processes. The landslides triggered by the 2016 Kumamoto earthquake revealed a link between landslide movement direction and the seismic radiation pattern, including the rupture directivity effect. While this link has only been established for the 2016 Kumamoto earthquake in ch. 7, the principles behind this link apply theoretically to all earthquakes triggering landslides. One of the follow-up investigations focuses on the 2018 M_W 6.6 Iburi earthquake (Hokkaido, Japan). The local conditions are similar to the 2016 Kumamoto case, with similar topography and geology and more landslides to the north of the rupture. Some earthquake parameters differ, however, such as a deeper hypocenter and a thrust-faulting regime with no surface rupture (instead of a surface reaching strike-slip rupture). Although station density is comparatively dense, the earthquake struck close to the coast, limiting data availability. With its smaller magnitude, the directivity effect maybe less pronounced or more localized as in the Kumamoto event, nonetheless, the radiation pattern signature is identifiable. The 2016 M_L 6.6 Meinong earthquake in Taiwan showed localized strong ground shaking in direction of the rupture propagation (Lee et al., 2016), highlighting that a moderately sized earthquake can exhibit a strong directivity effect. Whether this is the case for the localized landsliding in the Iburi case remains to be seen.

Site effects and spatial variations in ground motion constitute an increasing part in new ground-motion models. Effects such as the directivity effect are rupture dependent and GMMs with directivity related terms remain case (scenario) specific. Many GMMs with site-related terms are inferred with mixed-effect regression, though limited to its most basic form: A combination of a fixed effect model with one or more random effects, invariant under distance (or location), magnitude, site conditions etc. Most recent developments address these issues by incorporating location dependence through spatially varying coefficients (Landwehr et al., 2016, Fig. 9.1, top), with its foundation in

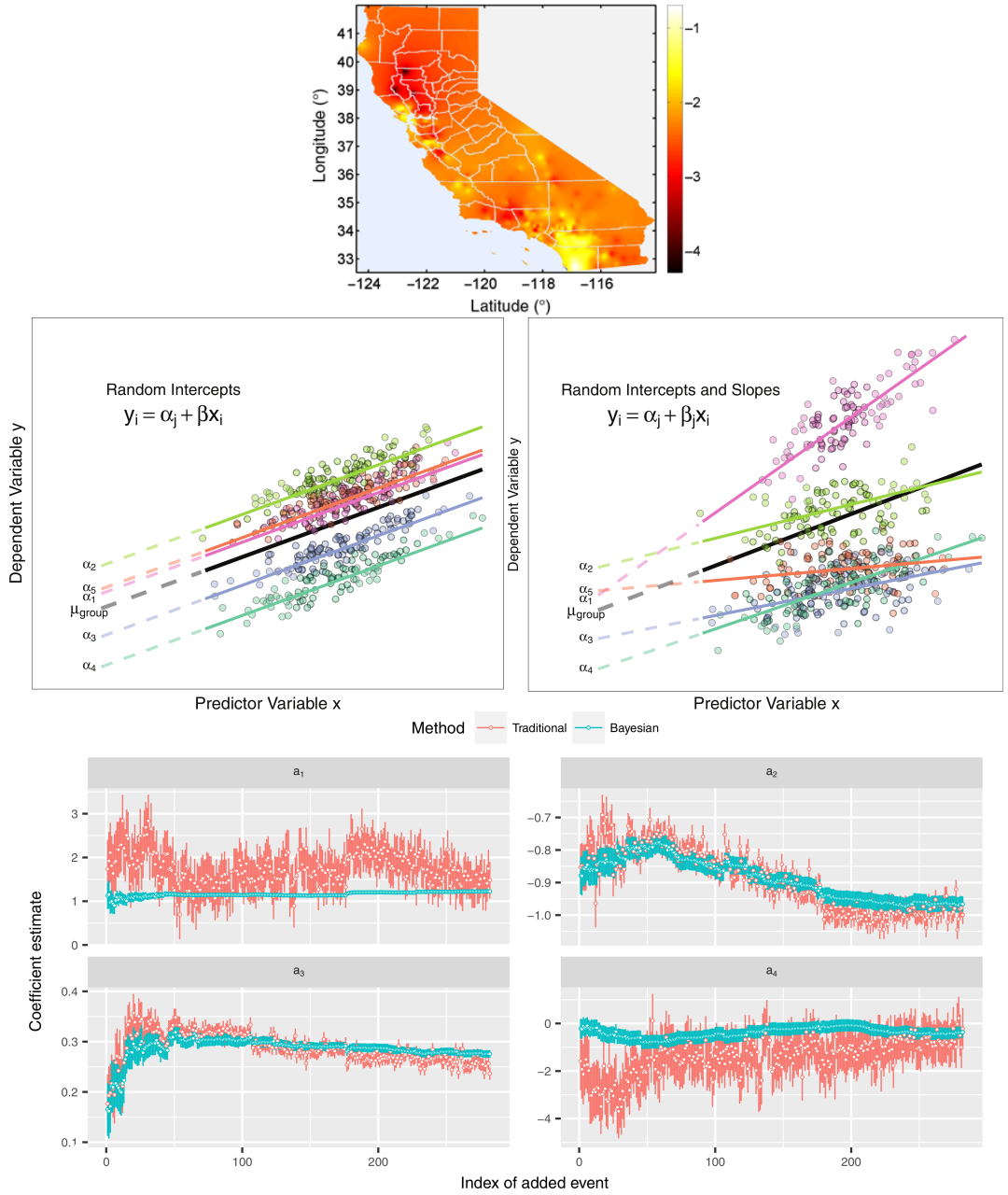

Figure 9.1: Possible areas of imroving GMMs.
Top: Example of a spatially varying, non-ergodic GMM. Map of ln PGA predictions, coded by ground-motion value. Predictor variables are set to M 6, R_{JB} = 10 km, SoF = 0, and V_{S30} = 760 ms^{-1}, in which SoF indicates style-of-faulting. Figure taken from Landwehr et al. (2016).
Middle: Differences between Random Intercept vs Random Slope Models. Left: A random-intercepts model where the outcome variable y is a function of predictor x, with a random intercept for group ID (colored lines). This type of model is the standard mixed-effect model used for GMMs. Because all groups have been constrained to have a common slope, their regression lines (the fixed model) are parallel. Point color corresponds to group ID of the data point. The black line represents the global mean value of the distribution of random effects. Right: A random intercepts and random slopes model, where both intercepts and slopes are permitted to vary by group. Random slope models give the model far more flexibility to fit the data, but require a lot more data to obtain accurate estimates of separate slopes for each group. This kind of model is but one possible extension of the application of mixed effects. In case of GMMs, random slopes could be applied to magnitudes, distances or frequencies. Figures taken from Harrison et al. (2018).
Bottom: Comparison of traditional GMM regression with a Bayesian approach using a prior distribution when updating the model. The estimates shown are for the first four parameters of the fixed effects in Stafford (2019). Vertical lines represent the standard errors in the coefficient estimates. While the traditional updating of the GMM (i.e. adding more data) does not reduce the parameter uncertainties, the Bayesian updating approach reduces uncertainties by using already existing models as basis for the prior distributions. Figure taken from Stafford (2019).

Bayesian inference (in conjunction to its frequentist basis), Stafford (2019) proposed the use of *a priori* information and to formulate prior distributions for the mixed-effect regression based on already existing models (Fig. 9.1, bottom). Random effects with more advanced functional forms than a constant offset are established in mathematics for some time (e.g Demidenko, 2013, 1st ed. from 1987) and are used in other field sich as ecology (e.g Harrison et al., 2018, Fig. 9.1, middle), but remain unused in the seismological context. The extension to the weighted likelihood in ch. 8 establishes the means of data weighting beyond measurement errors and the provided formalism is kept general to consolidate the above mentioned developments.

The temporal variations preceding the 2014 Iquique earthquake (Chile) presented in ch. 3 and 4 illustrate that ground shaking is not stationary with time. While precursory phases are less frequently observed, changes after major earthquakes are more common. For instance, temporal changes in ground shaking after a major earthquake have been accounted for in adjustment coefficients for ground-motion models (Wooddell & Abrahamson, 2014). These coefficients are also frequency dependent with higher attenuation at higher frequencies. A change of source properties and fault healing can explain this variation (Bindi et al., 2018), and accompanied by a change in wave amplitude attenuation these changes result in attenuated aftershock signals. Wang & Ma (2015) found a temporal increase in S-wave attenuation in the two years after the 1999 M_W 7.3 Chichi earthquake (Taiwan) in the hanging wall of the rupture. Following the lead on wave attenuation, I used a similar approach to Drouet et al. (2008) and Wang et al. (2010) and found changes of P-wave attenuation before and after the 2016 Kumamoto earthquake (Fig. 9.2). The region to the northeast of the hypocenter is a geothermal area and low resistivity measurements one month after the earthquake in that area indicate the presence of fluids (Aizawa et al., 2017). The increased attenuation can be at least partially attributed to fluid migration, affecting pore pressure and in consequence the effective stress (Ziegler et al., 2017). The impact on the principal stresses is different due to pore–pressure stress–coupling, resulting in a rotation of the stress tensor (Altmann et al., 2014). Such small stress transients are more likely to be detected with the improved stress tensor inversion introduced in ch. 5 by focusing the inversion only on those events directly associated with the governing stress state. While the classical data binning strategies employed in stress tensor inversion do not ensure that all data in a bin are associated with the same stress tensor, data weights based on ACE are more compliant with the single–stress–tensor assumption.

Understanding variations in strong ground motion—either temporal or spatial—is the scientific challenge in the years to come to improve our knowledge about seismicity and its implications on hazard assessment.

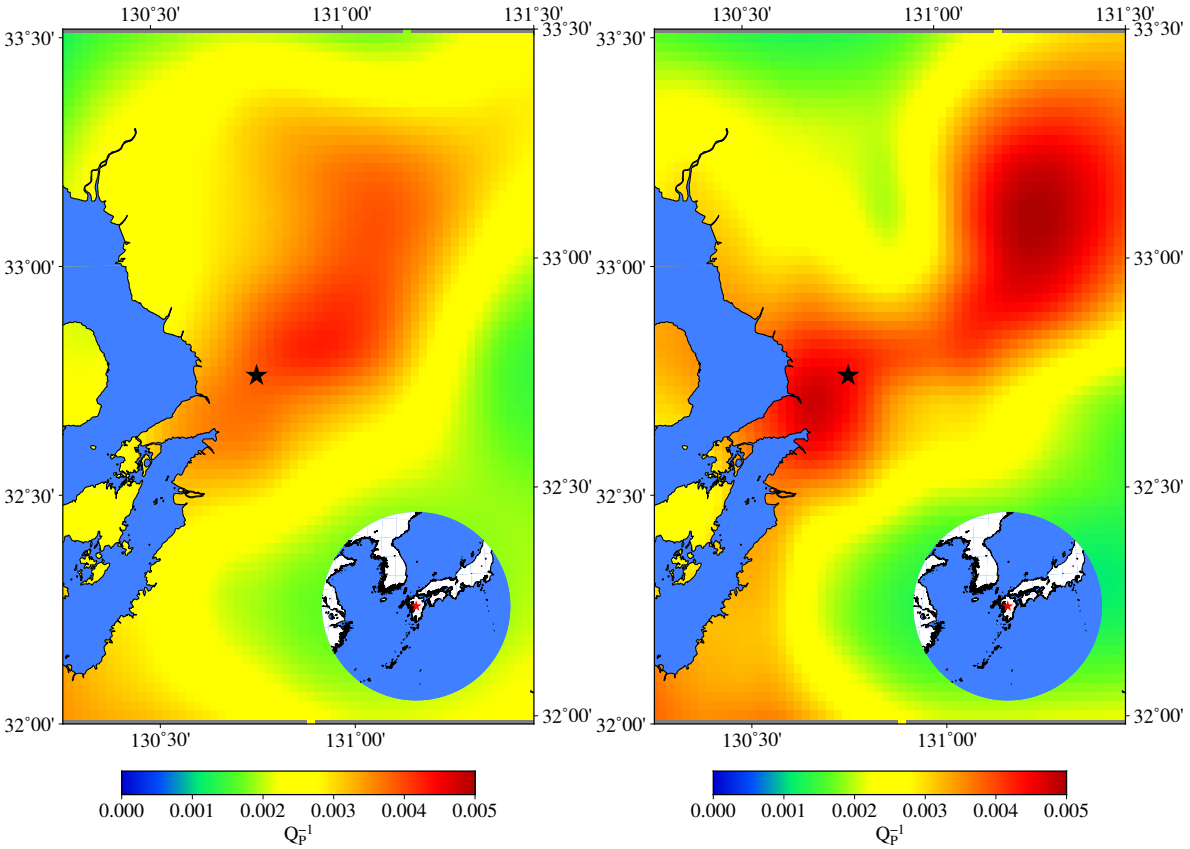

Figure 9.2: Q_P tomography for central Kyushu before (left) and after (right) the 2016 M_W 7.1 Kumamoto earthquake. The hypocenter is shown by the star. While the area to the northeast of the hypocenter (the rupture direction) has already increased attenuation (inverse Q_P) before the 2016 event, attenuation increases even further after the earthquake. The highest increase is in the Yufu municipality to the northeast, where also a geothermal area is located. Therefore, fluid migration could be a possible explanation for changes in Q_P

Bibliography

Abrahamson, N. & Silva, W., 2008. Summary of the Abrahamson & Silva NGA Ground-Motion Relations, *Earthquake Spectra*, 24(1), 67–97.

Abrahamson, N., Gregor, N., & Addo, K., 2016. BC Hydro Ground Motion Prediction Equations for Subduction Earthquakes, *Earthquake Spectra*, 32(1), 23–44.

Abrahamson, N. A. & Youngs, R. R., 1992. A stable algorithm for regression analyses using the random effects model, *Bulletin of the Seismological Society of America*, 82(1), 505.

Aitken, A. C., 1936. IV.—On Least Squares and Linear Combination of Observations., *Proceedings of the Royal Society of Edinburgh*, 55, 42–48.

Aizawa, K., Asaue, H., Koike, K., Takakura, S., Utsugi, M., Inoue, H., Yoshimura, R., Yamazaki, K., Komatsu, S., Uyeshima, M., Koyama, T., Kanda, W., Shiotani, T., Matsushima, N., Hata, M., Yoshinaga, T., Uchida, K., & Tsukashima, Y., 2017. Seismicity controlled by resistivity structure : the 2016 Kumamoto earthquakes , Kyushu Island , Japan, *Earth, Planets and Space*, pp. 2–11.

Akaike, H., 1974. A new look at the statistical model identification, *IEEE Transactions on Automatic Control*, 19(6), 716–723.

Aki, K. & Richards, P. G., 2002. *Quantitative Seismology*, University Science Books, 2nd edn.

Akkar, S., Sandıkkaya, M. A., Şenyurt, M., Azari Sisi, A., Ay, B. Ö., Traversa, P., Douglas, J., Cotton, F., Luzi, L., Hernandez, B., & Godey, S., 2014. Reference database for seismic ground-motion in Europe (RESORCE), *Bulletin of Earthquake Engineering*, 12(1), 311–339.

Al Atik, L., Abrahamson, N., Bommer, J. J., Scherbaum, F., Cotton, F., & Kuehn, N., 2010. The Variability of Ground-Motion Prediction Models and Its Components, *Seismological Research Letters*, 81(5), 794–801.

Allstadt, K., 2013. Extracting source characteristics and dynamics of the August 2010 Mount Meager landslide from broadband seismograms, *Journal of Geophysical Research: Earth Surface*, 118(3), 1472–1490.

Allstadt, K. E., Jibson, R. W., Thompson, E. M., Massey, C. I., Wald, D. J., Godt, J. W., & Rengers, F. K., 2018. Improving Near-Real-Time Coseismic Landslide Models: Lessons Learned from the 2016 Kaikoura, New Zealand, Earthquake, *Bulletin of the Seismological Society of America*, 108(3B), 1649–1664.

Altamimi, Z., Collilieux, X., & Métivier, L., 2011. ITRF2008: an improved solution of the international terrestrial reference frame, *Journal of Geodesy*, 85(8), 457–473.

Altmann, J., Müller, B., Müller, T., Heidbach, O., Tingay, M., & Weißhardt, A., 2014. Pore pressure stress coupling in 3D and consequences for reservoir stress states and fault reactivation, *Geothermics*, 52, 195–205.

Amante, C. & Eakins, B. W., 2009. ETOPO1 1 arc-minute global relief model: procedures, data sources and analysis, Tech. Rep. NESDIS NGDC-24, National Geophysical Data Center, Boulder, Colorado.

Ancheta, T. D., Darragh, R. B., Stewart, J. P., Silva, W., Chiou, B., Wooddell, K., Graves, R., Kottke, A., Boore, D., Kishida, T., & Donahue, J., 2013. PEER NGA-West2 Database, *PEER Report*, (May 2013), p.172.

Anderson, J. G. & Brune, J. N., 1999. Probabilistic Seismic Hazard Analysis without the Ergodic Assumption, *Seismological Research Letters*, 70(1), 19–28.

Anderson, J. G. & Richards, P. G., 1975. Comparison of Strong Ground Motion from Several Dislocation Models*, *Geophysical Journal of the Royal Astronomical Society*, 42(2), 347–373.

Angelier, J., 1979. Determination of the mean principal directions of stresses for a given fault population, *Tectonophysics*, 56(3-4), T17–T26.

Angelier, J., 2002. Inversion of earthquake focal mechanisms to obtain the seismotectonic stress IV-a new method free of choice among nodal planes, *Geophysical Journal International*, 150(3), 588–609.

Arango, M. C., Strasser, F. O., Bommer, J. J., Boroschek, R., Comte, D., & Tavera, H., 2011. A strong-motion database from the Peru – Chile subduction zone, *Journal of Seismology*, 15(1), 19–41.

Argus, D. F., Gordon, R. G., & DeMets, C., 2011. Geologically current motion of 56 plates relative to the no-net-rotation reference frame, *Geochemistry, Geophysics, Geosystems*, 12(11), n/a–n/a.

Arias, A., 1970. MEASURE OF EARTHQUAKE INTENSITY., Tech. rep., Massachusetts Inst. of Tech., Cambridge. Univ. of Chile, Santiago de Chile.

Armijo, R., Carey, E., & Cisternas, A., 1982. The inverse problem in microtectonics and the separation of tectonic phases, *Tectonophysics*, 82(1-2), 145–160.

Asano, K. & Iwata, T., 2016. Source rupture processes of the foreshock and mainshock in the 2016 Kumamoto earthquake sequence estimated from the kinematic waveform inversion of strong motion data, *Earth, Planets and Space*, 68(1), 147.

Astiz, L., Lay, T., & Kanamori, H., 1988. Large intermediate-depth earthquakes and the subduction process, *Physics of the Earth and Planetary Interiors*, 53(1-2), 80–166.

Atkinson, G. M., 2000. Stochastic Modeling of California Ground Motions, *Bulletin of the Seismological Society of America*, 90(2), 255–274.

Baker, J. W., 2007. Quantitative Classification of Near-Fault Ground Motions Using Wavelet Analysis, *Bulletin of the Seismological Society of America*, 97(5), 1486–1501.

Barzilai, J. & Borwein, J. M., 1988. Two-Point Step Size Gradient Methods, *IMA Journal of Numerical Analysis*, 8(1), 141–148.

Bastías, N. & Montalva, G. A., 2016. Chile Strong Ground Motion Flatfile, *Earthquake Spectra*, 32(4), 2549–2566.

Bates, D., Mächler, M., Bolker, B., & Walker, S., 2015. Fitting Linear Mixed-Effects Models Using lme4, *Journal of Statistical Software*, 67(1), 251–264.

Bates, D. M. & DebRoy, S., 2004. Linear mixed models and penalized least squares, *Journal of Multivariate Analysis*, 91(1), 1–17.

Bedford, J., Moreno, M., Schurr, B., Bartsch, M., & Oncken, O., 2015. Investigating the final seismic swarm before the Iquique-Pisagua 2014 M w 8.1 by comparison of continuous GPS and seismic foreshock data, *Geophysical Research Letters*, 42(10), 3820–3828.

Béjar-Pizarro, M., Carrizo, D., Socquet, A., Armijo, R., Barrientos, S., Bondoux, F., Bonvalot, S., Campos, J., Comte, D., de Chabalier, J. B., Charade, O., Delorme, A., Gabalda, G., Galetzka, J., Genrich, J., Nercessian, A., Olcay, M., Ortega, F., Ortega, I., Remy, D., Ruegg, J. C., Simons, M., Valderas, C., & Vigny, C., 2010. Asperities and barriers on the seismogenic zone in North Chile: state-of-the-art after the 2007 Mw 7.7 Tocopilla earthquake inferred by GPS and InSAR data, *Geophysical Journal International*, 183(1), 390–406.

Béjar-Pizarro, M., Socquet, A., Armijo, R., Carrizo, D., Genrich, J., & Simons, M., 2013. Andean structural control on interseismic coupling in the North Chile subduction zone, *Nature Geoscience*, 6(6), 462–467.

Bernard, P. & Madariaga, R., 1984. a New Asymptotic Method for the Modeling of Near-Field Accelerograms, *Bulletin of the Seismological Society of America*, 74(2), 539–557.

Bindi, D., Parolai, S., Grosser, H., Milkereit, C., & Durukal, E., 2007. Empirical ground-motion prediction equations for northwestern Turkey using the aftershocks of the 1999 Kocaeli earthquake, *Geophysical Research Letters*, 34(8), 1–5.

Bindi, D., Cotton, F., Spallarossa, D., Picozzi, M., & Rivalta, E., 2018. Temporal Variability of Ground Shaking and Stress Drop in Central Italy: A Hint for Fault Healing?, *Bulletin of the Seismological Society of America*, 108(4), 1853–1863.

Bird, P., 2003. An updated digital model of plate boundaries, *Geochemistry, Geophysics, Geosystems*, 4(3), 1991.

Boehm, J., Werl, B., & Schuh, H., 2006. Troposphere mapping functions for GPS and very long baseline interferometry from European Centre for Medium-Range Weather Forecasts operational analysis data, *Journal of Geophysical Research: Solid Earth*, 111(B2), n/a–n/a.

Böhner, J. & Selige, T., 2006. Spatial prediction of soil attributes using terrain analysis and climate regionalisation, *SAGA - Analysis and Modelling Applications*, 115, 13–27.

Bommer, J. J. & Abrahamson, N. A., 2006. Why Do Modern Probabilistic Seismic-Hazard Analyses Often Lead to Increased Hazard Estimates?, *Bulletin of the Seismological Society of America*, 96(6), 1967–1977.

Bommer, J. J., Stafford, P. J., & Alarcon, J. E., 2009. Empirical Equations for the Prediction of the Significant, Bracketed, and Uniform Duration of Earthquake Ground Motion, *Bulletin of the Seismological Society of America*, 99(6), 3217–3233.

Boore, D. M., 2003. Simulation of Ground Motion Using the Stochastic Method, *Pure and Applied Geophysics*, 160(3), 635–676.

Boore, D. M. & Bommer, J. J., 2005. Processing of strong-motion accelerograms: Needs, options and consequences, *Soil Dynamics and Earthquake Engineering*, 25(2), 93–115.

Boore, D. M., Azari Sisi, A., & Akkar, S., 2012. Using Pad-Stripped Acausally Filtered Strong-Motion Data, *Bulletin of the Seismological Society of America*, 102(2), 751–760.

Bora, S. S., Scherbaum, F., Kuehn, N., Stafford, P., & Edwards, B., 2015. Development of a Response Spectral Ground-Motion Prediction Equation (GMPE) for Seismic-Hazard Analysis from Empirical Fourier Spectral and Duration Models, *Bulletin of the Seismological Society of America*, 105(4), 2192–2218.

Bott, M. H. P., 1959. The Mechanics of Oblique Slip Faulting, *Geological Magazine*, 96(02), 109.

Bouchon, M., Karabulut, H., Aktar, M., Ozalaybey, S., Schmittbuhl, J., & Bouin, M.-P., 2011. Extended Nucleation of the 1999 Mw 7.6 Izmit Earthquake, *Science*, 331(6019), 877–880.

Bouchon, M., Durand, V., Marsan, D., Karabulut, H., & Schmittbuhl, J., 2013. The long precursory phase of most large interplate earthquakes, *Nature Geoscience*, 6(4), 299–302.

Bowman, D. D. & King, G. C. P., 2001. Accelerating seismicity and stress accumulation before large earthquakes, *Geophysical Research Letters*, 28(21), 4039–4042.

Bray, J. D. & Rodriguez-Marek, A., 2004. Characterization of forward-directivity ground motions in the near-fault region, *Soil Dynamics and Earthquake Engineering*, 24(11), 815–828.

Bray, J. D. & Travasarou, T., 2007. Simplified Procedure for Estimating Earthquake-Induced Deviatoric Slope Displacements, *Journal of Geotechnical and Geoenvironmental Engineering*, 133(4), 381–392.

Brune, J. N., 1970. Tectonic stress and the spectra of seismic shear waves from earthquakes, *Journal of Geophysical Research*, 75(26), 4997–5009.

Burnham, K. P. & Anderson, D. R., 2002. *Model Selection and Multimodel Inference*, Springer, 2nd edn.

Byerlee, J., 1978. Friction of rocks, *Pure and Applied Geophysics PAGEOPH*, 116(4-5), 615–626.

Campillo, M. & Plantet, J., 1991. Frequency dependence and spatial distribution of seismic attenuation in France: experimental results and possible interpretations, *Physics of the Earth and Planetary Interiors*, 67(1-2), 48–64.

Cardinali, C., Pezzulli, S., & Andersson, E., 2004. Influence-matrix diagnostic of a data assimilation system, *Quarterly Journal of the Royal Meteorological Society*, 130(603), 2767–2786.

Carey-Gailhardis, E. & Brunier, B., 1974. Analyse théorique numerique d'un modèle mécanique élementaire appliqué à l'étude d'une population des failles, *Comptes Rendus de l'Academie des Sciences*, 279, 891–894.

Célérier, B., Etchecopar, A., Bergerat, F., Vergely, P., Arthaud, F., & Laurent, P., 2012. Inferring stress from faulting: From early concepts to inverse methods, *Tectonophysics*, 581, 206–219.

Cesca, S., Şen, A. T., & Dahm, T., 2014. Seismicity monitoring by cluster analysis of moment tensors, *Geophysical Journal International*, 196(3), 1813–1826.

Cesca, S., Grigoli, F., Heimann, S., Dahm, T., Kriegerowski, M., Sobiesiak, M., Tassara, C., & Olcay, M., 2016. The M w 8.1 2014 Iquique, Chile, seismic sequence: a tale of foreshocks and aftershocks, *Geophysical Journal International*, 204(3), 1766–1780.

Chen, C.-W., Chen, H., Wei, L.-W., Lin, G.-W., Iida, T., & Yamada, R., 2017. Evaluating the susceptibility of landslide landforms in Japan using slope stability analysis: a case study of the 2016 Kumamoto earthquake, *Landslides*, 14(5), 1793–1801.

Chen, S. X., 1999. Beta kernel estimators for density functions, *Computational Statistics & Data Analysis*, 31(2), 131–145.

Chen, Y.-S., Weatherill, G., Pagani, M., & Cotton, F., 2018. A transparent and data-driven global tectonic regionalization model for seismic hazard assessment, *Geophysical Journal International*, 213(2), 1263–1280.

Chigira, M. & Yagi, H., 2006. Geological and geomorphological characteristics of landslides triggered by the 2004 Mid Niigta prefecture earthquake in Japan, *Engineering Geology*, 82(4), 202–221.

Chiou, B.-J. & Youngs, R. R., 2008. An NGA Model for the Average Horizontal Component of Peak Ground Motion and Response Spectra, *Earthquake Spectra*, 24(1), 173–215.

Choy, G. L. & Cormier, V. F., 1986. Direct measurement of the mantle attenuation operator from broadband P and S Waveforms, *Journal of Geophysical Research: Solid Earth*, 91(B7), 7326–7342.

Cleary, T., 1993. *The Flower Ornament Scripture: A Translation Of The Avatamsaka Sutra*, Shambala Publications, Inc., Boston and London.

Clift, P. & Vannuchi, P., 2004. Controls on tectonic accretion versus erosion in subduction zones: Implications for the origin and recycling of the continental crust, *Reviews of Geophysics*, 42(2), RG2001.

Contreras-Reyes, E., Flueh, E. R., & Grevemeyer, I., 2010. Tectonic control on sediment accretion and subduction off south central Chile: Implications for coseismic rupture processes of the 1960 and 2010 megathrust earthquakes, *Tectonics*, 29(6), n/a–n/a.

Contreras-Reyes, E., Jara, J., Grevemeyer, I., Ruiz, S., & Carrizo, D., 2012. Abrupt change in the dip of the subducting plate beneath north Chile, *Nature Geoscience*, 5(5), 342–345.

Cook, R. D., 1977. Detection of Influential Observation in Linear Regression, *Technometrics*, 19(1), 15.

Cotton, F., Archuleta, R., & Causse, M., 2013. What is Sigma of the Stress Drop?, *Seismological Research Letters*, 84(1), 42–48.

Dadson, S. J., Hovius, N., Chen, H., Dade, W. B., Lin, J.-C. C., Hsu, M.-L. L., Lin, C.-W. W., Horng, M.-J. J., Chen, T.-C. C., Milliman, J., & Stark, C. P., 2004. Earthquake-triggered increase in sediment delivery from an active mountain belt, *Geology*, 32(8), 733–736.

Dang, K., Sassa, K., Fukuoka, H., Sakai, N., Sato, Y., Takara, K., Quang, L. H., Loi, D. H., Van Tien, P., & Ha, N. D., 2016. Mechanism of two rapid and long-runout landslides in the 16 April 2016 Kumamoto earthquake using a ring-shear apparatus and computer simulation (LS-RAPID), *Landslides*, 13(6), 1525–1534.

Dawood, H. M. & Rodriguez-Marek, A., 2013. A Method for Including Path Effects in Ground-Motion Prediction Equations: An Example Using the Mw 9.0 Tohoku Earthquake Aftershocks, *Bulletin of the Seismological Society of America*, 103(2B), 1360–1372.

Dawood, H. M., Rodriguez-Marek, A., Bayless, J., Goulet, C., & Thompson, E., 2016. A Flatfile for the KiK-net Database Processed Using an Automated Protocol, *Earthquake Spectra*, 32(2), 1281–1302.

Delorey, A. A., Vidale, J., Steim, J., & Bodin, P., 2008. Broadband Sensor Nonlinearity during Moderate Shaking, *Bulletin of the Seismological Society of America*, 98(3), 1595–1601.

Delouis, B., Pardo, M., Legrand, D., & Monfret, T., 2009. The Mw 7.7 Tocopilla Earthquake of 14 November 2007 at the Southern Edge of the Northern Chile Seismic Gap: Rupture in the Deep Part of the Coupled Plate Interface, *Bulletin of the Seismological Society of America*, 99(1), 87–94.

Demidenko, E., 2013. *Mixed Models*, Wiley Series in Probability and Statistics, John Wiley & Sons, Inc., Hoboken, NJ, USA, 2nd edn.

Deming, W. E., 1943. *Statistical adjustment of data*, J. Wiley & Sons.

Dempster, A. A., Laird, N. N., & Rubin, D. D. B., 1977. Maximum likelihood from incomplete data via the EM algorithm, *Journal of the Royal Statistical Society Series B Methodological*, 39(1), 1–38.

Derras, B., Bard, P.-Y., & Cotton, F., 2016. Site-Condition Proxies, Ground Motion Variability, and Data-Driven GMPEs: Insights from the NGA-West2 and RESORCE Data Sets, *Earthquake Spectra*, 32(4), 2027–2056.

Dodge, D. A., Beroza, G. C., & Ellsworth, W. L., 1996. Detailed observations of California foreshock sequences: Implications for the earthquake initiation process, *Journal of Geophysical Research: Solid Earth*, 101(B10), 22371–22392.

Domej, G., Bourdeau, C., Lenti, L., Martino, S., & Pluta, K., 2017. Mean landslide geometries inferred from globla database, *94 Italian Journal of Engineering Geology and Environment*, 2, 87–107.

Douglas, J., 2003. What is a Poor Quality Strong-Motion Record?, *Bulletin of Earthquake Engineering*, 1(1), 141–156.

Douglas, J., 2010. Consistency of ground-motion predictions from the past four decades, *Bulletin of Earthquake Engineering*, 8(6), 1515–1526.

Drouet, S., Chevrot, S., Cotton, F., & Souriau, A., 2008. Simultaneous Inversion of Source Spectra, Attenuation Parameters, and Site Responses: Application to the Data of the French Accelerometric Network, *Bulletin of the Seismological Society of America*, 98(1), 198–219.

Dupin, J.-M. M., Sassi, W., & Angelier, J., 1993. Homogeneous stress hypothesis and actual fault slip: a distinct element analysis, *Journal of Structural Geology*, 15(8), 1033–1043.

Dziewonski, A. M., Chou, T.-A., & Woodhouse, J. H., 1981. Determination of earthquake source parameters from waveform data for studies of global and regional seismicity, *Journal of Geophysical Research: Solid Earth*, 86(B4), 2825–2852.

Efron, B., 1979. Bootstrap Methods: Another Look at the Jackknife, *The Annals of Statistics*, 7(1), 1–26.

Ekström, G., Nettles, M., & Dziewoński, A. M., 2012. The global CMT project 2004 – 2010: Centroid-moment tensors for 13,017 earthquakes, *Physics of the Earth and Planetary Interiors*, 200-201, 1–9.

Ester, M., Kriegel, H.-p., S, J., & Xu, X., 1996. A density-based algorithm for discovering clusters in large spatial databases with noise, in *Proceedings of 2nd International Conference on Knowledge Discovery and Data Mining*, pp. 226–231.

Fan, X., Scaringi, G., Xu, Q., Zhan, W., Dai, L., Li, Y., Pei, X., Yang, Q., & Huang, R., 2018. Coseismic landslides triggered by the 8th August 2017 Ms 7.0 Jiuzhaigou earthquake (Sichuan, China): factors controlling their spatial distribution and implications for the seismogenic blind fault identification, *Landslides*, 15(5), 967–983.

Feller, W., 1971. *An introduction to probability and its applications, Vol. II.*, Wiley, New York.

Festa, G., Zollo, A., & Lancieri, M., 2008. Earthquake magnitude estimation from early radiated energy, *Geophysical Research Letters*, 35(22), L22307.

Field, C. & Smith, B., 1994. Robust Estimation: A Weighted Maximum Likelihood Approach, *International Statistical Review / Revue Internationale de Statistique*, 62(3), 405.

Fisher, N. I. & Lee, A. J., 1983. A correlation coefficient for circular data, *Biometrika*, 70(2), 327–332.

Fisher, R. A., 1922. On the mathematical foundations of theoretical statistics, *Philosophical Transactions of the Royal Society of London. Series A, Containing Papers of a Mathematical or Physical Character*, 222(594-604), 309–368.

Fleming, R. W. & Johnson, A. M., 1989. Structures associated with strike-slip faults that bound landslide elements, *Engineering Geology*, 27(1-4), 39–114.

Frankel, A., 2004. Rupture Process of the M 7.9 Denali Fault, Alaska, Earthquake: Subevents, Directivity, and Scaling of High-Frequency Ground Motions, *Bulletin of the Seismological Society of America*, 94(6B), S234–S255.

Frohlich, C., 1992. Triangle diagrams: ternary graphs to display similarity and diversity of earthquake focal mechanisms, *Physics of the Earth and Planetary Interiors*, 75(1-3), 193–198.

Frohlich, C. & Apperson, K. D., 1992. Earthquake focal mechanisms, moment tensors, and the consistency of seismic activity near plate boundaries, *Tectonics*, 11(2), 279–296.

Fuenzalida, A., Schurr, B., Lancieri, M., Sobiesiak, M., & Madariaga, R., 2013. High-resolution relocation and mechanism of aftershocks of the 2007 Tocopilla (Chile) earthquake, *Geophysical Journal International*, 194(2), 1216–1228.

Fujiwara, S., Yarai, H., Kobayashi, T., Morishita, Y., Nakano, T., Miyahara, B., Nakai, H., Miura, Y., Ueshiba, H., Kakiage, Y., & Une, H., 2016. Small-displacement linear surface ruptures of the 2016 Kumamoto earthquake sequence detected by ALOS-2 SAR interferometry, *Earth, Planets and Space*, 68(1), 160.

García, D., Wald, D. J., & Hearne, M. G., 2012. A global earthquake discrimination scheme to optimize ground-motion prediction equation selection, *Bulletin of the Seismological Society of America*, 102(1), 185–203.

Gauss, C. F., 1809. *Theoria motus corporum coelestium in sectionibus conicis solem ambientium*, vol. 7, Perthes et Besser.

Gephart, J. W. & Forsyth, D. W., 1984. An improved method for determining the regional stress tensor using earthquake focal mechanism data: Application to the San Fernando Earthquake Sequence, *Journal of Geophysical Research*, 89(B11), 9305.

Gorum, T., Fan, X., van Westen, C. J., Huang, R. Q., Xu, Q., Tang, C., & Wang, G., 2011. Distribution pattern of earthquake-induced landslides triggered by the 12 May 2008 Wenchuan earthquake, *Geomorphology*, 133(3-4), 152–167.

Gorum, T., Korup, O., van Westen, C. J., van der Meijde, M., Xu, C., & van der Meer, F. D., 2014. Why so few? Landslides triggered by the 2002 Denali earthquake, Alaska, *Quaternary Science Reviews*, 95, 80–94.

Graizer, V., 2006. Tilts in Strong Ground Motion, *Bulletin of the Seismological Society of America*, 96(6), 2090–2102.

Gusman, A. R., Murotani, S., Satake, K., Heidarzadeh, M., Gunawan, E., Watada, S., & Schurr, B., 2015. Fault slip distribution of the 2014 Iquique, Chile, earthquake estimated from ocean-wide tsunami waveforms and GPS data, *Geophysical Research Letters*, 42(4), 1053–1060.

Haendel, A., Specht, S., Kuehn, N. M., & Scherbaum, F., 2015. Mixtures of ground-motion prediction equations as backbone models for a logic tree: an application to the subduction zone in Northern Chile, *Bulletin of Earthquake Engineering*, 13(2), 483–501.

Hanka, W. & Kind, R., 1994. The GEOFON Program.

Hanks, T. C. & Kanamori, H., 1979. A moment magnitude scale, *Journal of Geophysical Research*, 84(B5), 2348.

Hardebeck, J. L. & Hauksson, E., 1999. Role of Fluids in Faulting Inferred from Stress Field Signatures, *Science*, 285(5425), 236–239.

Hardebeck, J. L. & Hauksson, E., 2001a. Stress orientations obtained from earthquake focal mechanisms: What are appropriate uncertainty estimates?, *Bulletin of the Seismological Society of America*, 91(2), 250–262.

Hardebeck, J. L. & Hauksson, E., 2001b. Crustal stress field in southern California and its implications for fault mechanics, *Journal of Geophysical Research: Solid Earth*, 106(B10), 21859–21882.

Hardebeck, J. L. & Michael, A. J., 2004. Stress orientations at intermediate angles to the San Andreas Fault, California.

Hardebeck, J. L. & Michael, A. J., 2006. Damped regional-scale stress inversions: Methodology and examples for southern California and the Coalinga aftershock sequence, *Journal of Geophysical Research: Solid Earth*, 111(B11), n/a–n/a.

Harp, E. L. & Wilson, R. C., 1995. Shaking Intensity Thresholds for Rock Falls and Slides : Evidence from 1987 Whittier Narrows and Superstition Hills Earthquake Strong-Motion Records, *Bulletin of the Seismological Society of America*, 85(6), 1739–1757.

Harrison, X. A., Donaldson, L., Correa-Cano, M. E., Evans, J., Fisher, D. N., Goodwin, C. E., Robinson, B. S., Hodgson, D. J., & Inger, R., 2018. A brief introduction to mixed effects modelling and multi-model inference in ecology, *PeerJ*, 6, 32.

Hartley, H. O. & Rao, J. N. K., 1967. Maximum-Likelihood Estimation for the Mixed Analysis of Variance Model, *Biometrika*, 54(1/2), 93.

Harville, D., 1976. Extension of the Gauss-Markov Theorem to Include the Estimation of Random Effects, *The Annals of Statistics*, 4(2), 384–395.

Harville, D. A., 1974. Bayesian inference for variance components using only error contrasts, *Biometrika*, 61(2), 383–385.

Harville, D. A., 1977. Maximum Likelihood Approaches to Variance Component Estimation and to Related Problems, *Journal of the American Statistical Association*, 72(358), 320–338.

Harville, D. A., 1997. *Matrix Algebra From a Statistician's Perspective*, Springer New York, New York, NY.

Hasegawa, A. & Yoshida, K., 2015. Preceding seismic activity and slow slip events in the source area of the 2011 Mw 9.0 Tohoku-Oki earthquake: a review, *Geoscience Letters*, 2(1), 6.

Haskell, N., 1969. Determination of earthquake energy release and ML using TERRAscope, *Bulletin of the Seismological Society of America*, 59(2), 865–908.

Haskell, N. A., 1964. Total energy and energy spectral density of elastic wave radiation from propagating faults, *Bulletin of the Seismological Society of America*, 54(6), 1811–1841.

Hauser, A., Steffen, H., Del, P., & Falla, C., 1991. Hans Steffen, precursor del concepto Falla Liquiñe-Ofqui, *Andean Geology*, 18(2), 177–179.

Havenith, H. B., Torgoev, A., Schlögel, R., Braun, A., Torgoev, I., & Ischuk, A., 2015. Tien Shan Geohazards Database: Landslide susceptibility analysis, *Geomorphology*, 249, 32–43.

Havenith, H.-B., Torgoev, A., Braun, A., Schlögel, R., & Micu, M., 2016. A new classification of earthquake-induced landslide event sizes based on seismotectonic, topographic, climatic and geologic factors, *Geoenvironmental Disasters*, 3(6).

Hayes, G. P., Herman, M. W., Barnhart, W. D., Furlong, K. P., Riquelme, S., Benz, H. M., Bergman, E., Barrientos, S., Earle, P. S., & Samsonov, S., 2014. Continuing megathrust earthquake potential in Chile after the 2014 Iquique earthquake, *Nature*, 512(7514), 295–298.

Heidbach, O., Tingay, M., Barth, A., Reinecker, J., Kurfeß, D., & Müller, B., 2010. Global crustal stress pattern based on the World Stress Map database release 2008, *Tectonophysics*, 482(1-4), 3–15.

Henderson, C. R., 1975. Best Linear Unbiased Estimation and Prediction under a Selection Model, *Biometrics*, 31(2), 423–447.

Henderson, C. R., Kempthorne, O., Searle, S. R., & von Krosigk, C. M., 1959. The Estimation of Environmental and Genetic Trends from Records Subject to Culling, *Biometrics*, 15(2), 192–218.

Henderson, H. V. & Searle, S. R., 1981. On Deriving the Inverse of a Sum of Matrices, *SIAM Review*, 23(1), 53–60.

Herrmann, R. B., 1985. An extension of random vibration theory estimates of strong ground motion to large distances, *Bulletin of the Seismological Society of America*, 75(5), 1447–1453.

Hetland, E. A. & Simons, M., 2010. Post-seismic and interseismic fault creep II: transient creep and interseismic stress shadows on megathrusts, *Geophysical Journal International*, 181(1), 99–112.

Heuret, A., Lallemand, S., Funiciello, F., Piromallo, C., & Faccenna, C., 2011. Physical characteristics of subduction interface type seismogenic zones revisited, *Geochemistry, Geophysics, Geosystems*, 12(1), 26.

Hill, R. W. & Holland, P. W., 1977. Two Robust Alternatives to Least-Squares Regression, *Journal of the American Statistical Association*, 72(360), 828–833.

Hoaglin, D. C. & Welsch, R. E., 1978. The Hat Matrix in Regression and ANOVA, *The American Statistician*, 32(1), 17.

Hoffmann-Rothe, A., Kukowski, N., Dresen, G., Echtler, H., Oncken, O., Klotz, J., Scheuber, E., & Kellner, A., 2006. *Oblique Convergence along the Chilean Margin: Partitioning, Margin-Parallel Faulting and Force Interaction at the Plate Interface*, pp. 125–146, Springer Berlin Heidelberg, Berlin, Heidelberg.

Holland, P. W. & Welsch, R. E., 1977. Robust regression using iteratively reweighted least-squares, *Communications in Statistics - Theory and Methods*, 6(9), 813–827.

Hovius, N. & Meunier, P., 2012. Earthquake ground motion and patterns of seismically induced landsliding, in *Landslides*, pp. 24–36, eds Clague, J. J. & Stead, D., Cambridge University Press, Cambridge.

Huang, H.-H., Lin, F.-C., Tsai, V. C., & Koper, K. D., 2015. High-resolution probing of inner core structure with seismic interferometry, *Geophysical Research Letters*, 42(24), 10,622–10,630.

Ishibe, T., Tsuruoka, H., Satake, K., & Nakatani, M., 2014. A focal mechanism solution catalog of earthquakes (M $\geq$ 2.0) in and around the Japanese Islands for 1985-1998, *Bulletin of the Seismological Society of America*, 104(2), 1031–1036.

Jaeger, C., 1979. *Rock mechanics and engineering*, Cambridge University Press.

Ji, C., Helmberger, D. V., Wald, D. J., & Ma, K.-F., 2003. Slip history and dynamic implications of the 1999 Chi-Chi, Taiwan, earthquake, *Journal of Geophysical Research: Solid Earth*, 108(B9), 1–16.

Jiang, H., Feng, G., Wang, T., & Bürgmann, R., 2017. Toward full exploitation of coherent and incoherent information in Sentinel-1 TOPS data for retrieving surface displacement: Application to the 2016 Kumamoto (Japan) earthquake, *Geophysical Research Letters*, 44(4), 1758–1767.

Jibson, R. W., 1993. Predicting Earthquake-Induced Landslide Displacements Using Newmark's Sliding Block Analysis, *Transportation Research Record*, 1411(8), 9–17.

Jibson, R. W., 2007. Regression models for estimating coseismic landslide displacement, *Engineering Geology*, 91(2-4), 209–218.

Jibson, R. W., Harp, E. L., & Michael, J. A., 2000. A method for producing digital probabilistic seismic landslide hazard maps, *Engineering Geology*, 58, 271–289.

Johnson, N. L., Kotz, S., & Balakrishnan, N., 1995. *Continuous Univariate Distributions, Vol. 2*, Wiley, 2nd edn.

Jónsson, S., Zebker, H., Segall, P., & Amelung, F., 2002. Fault Slip Distribution of the 1999 Mw 7.1 Hector Mine, California, Earthquake, Estimated from Satellite Radar and GPS Measurements, *Bulletin of the Seismological Society of America*, 92(4), 1377–1389.

Kagan, Y. Y., 1990. Random stress and earthquake statistics: spatial dependence, *Geophysical Journal International*, 102(3), 573–583.

Kagan, Y. Y., 1991. 3-D rotation of double-couple earthquake sources, *Geophysical Journal International*, 106(3), 709–716.

Kagan, Y. Y., 1992. Correlations of earthquake focal mechanisms, *Geophysical Journal International*, 110(2), 305–320.

Kagan, Y. Y., 2000. Temporal correlations of earthquake focal mechanisms, *Geophysical Journal International*, 143(3), 881–897.

Kagan, Y. Y., 2007. Simplified algorithms for calculating double-couple rotation, *Geophysical Journal International*, 171(1), 411–418.

Kagan, Y. Y., 2013. Double-couple earthquake source: symmetry and rotation, *Geophysical Journal International*, 194(2), 1167–1179.

Kagan, Y. Y. & Jackson, D. D., 2015. Likelihood analysis of earthquake focal mechanism distributions, *Geophysical Journal International*, 201(3), 1409–1415.

Kagan, Y. Y. & Knopoff, L., 1985. The two-point correlation function of the seismic moment tensor, *Geophysical Journal International*, 83(3), 637–656.

Kanamori, H., 1986. Rupture Process of Subduction-Zone Earthquakes, *Annual Review of Earth and Planetary Sciences*, 14(1), 293–322.

Kanamori, H. & Cipar, J. J., 1974. Focal process of the great Chilean earthquake May 22, 1960, *Physics of the Earth and Planetary Interiors*, 9(2), 128–136.

Kanamori, H., Mori, J. I. M., Hauksson, E., Heaton, T. H., Hutton, K., & Jones, L. M., 1993. Determination of Earthquake Energy Release and, *Bulletin of the Seismological Society of America*, 83(2), 330–346.

Kato, A. & Nakagawa, S., 2014. Multiple slow-slip events during a foreshock sequence of the 2014 Iquique, Chile M w 8.1 earthquake, *Geophysical Research Letters*, 41(15), 5420–5427.

Kato, A., Obara, K., Igarashi, T., Tsuruoka, H., Nakagawa, S., & Hirata, N., 2012. Propagation of Slow Slip Leading Up to the 2011 Mw 9.0 Tohoku-Oki Earthquake, *Science*, 335(6069), 705–708.

Kato, A., Fukuda, J., Kumazawa, T., & Nakagawa, S., 2016. Accelerated nucleation of the 2014 Iquique, Chile Mw 8.2 Earthquake, *Scientific Reports*, 6(1), 24792.

Keefer, D. K., 1984. Landslides caused by earthquakes, *Geological Society of America Bulletin*, 95(4), 406–421.

Kent, J. T., 1982. The Fisher-Bingham Distribution on the Sphere, *Journal of the Royal Statistical Society. Series B (Methodological)*, 44(1), 71–80.

Kobayashi, T., 2017. Earthquake rupture properties of the 2016 Kumamoto earthquake foreshocks (M j 6.5 and M j 6.4) revealed by conventional and multiple-aperture InSAR, *Earth, Planets and Space*, 69(1), 7.

Koketsu, K., Miyake, H., & Suzuki, H., 2012. Japan Integrated Velocity Structure Model Version 1, in *Proceedings of the 15th World Conference on Earthquake Engineering*, pp. 1–4, Lisbon, Portugal.

Konno, K. & Ohmachi, T., 1998. Ground-Motion Characteristics Estimated from Spectral Ratio between Horizontal and Vertical Components of Microtremor, *Bulletin of the Seismological Society of America*, 88(1), 228–241.

Kotha, S. R., Cotton, F., & Bindi, D., 2018. A new approach to site classification: Mixed-effects Ground Motion Prediction Equation with spectral clustering of site amplification functions, *Soil Dynamics and Earthquake Engineering*, 110(January), 318–329.

Kramer, S. L., 1996. Geotechnical earthquake engineering, *Prentice-Hall, New Jersey*, p. 653.

Kruskal, J. B., 1956. On the shortest spanning subtree of a graph and the traveling salesman problem, *Proceedings of the American Mathematical Society*, 7(1), 48–48.

Kubo, H., Suzuki, W., Aoi, S., & Sekiguchi, H., 2016. Source rupture processes of the 2016 Kumamoto, Japan, earthquakes estimated from strong-motion waveforms, *Earth, Planets and Space*, 2016, 1–13.

Kushnir, A. F., Lapshin, V. M., Pinsky, V. I., & Fyen, J., 1990. Statistically optimal event detection using small array data, *Bulletin of the Seismological Society of America*, 80(6), 1934–1950.

Landwehr, N., Kuehn, N. M., Scheffer, T., & Abrahamson, N., 2016. A Nonergodic Ground Motion Model for California with Spatially Varying Coefficients, *Bulletin of the Seismological Society of America*, 106(6), 2574–2583.

Laplace, P. S., 1986. Memoir on the Probability of the Causes of Events, *Statistical Science*, 1(3), 364–378.

Lay, T., 2015. The surge of great earthquakes from 2004 to 2014, *Earth and Planetary Science Letters*, 409, 133–146.

Lay, T., Kanamori, H., Ammon, C. J., Koper, K. D., Hutko, A. R., Ye, L., Yue, H., & Rushing, T. M., 2012. Depth-varying rupture properties of subduction zone megathrust faults, *Journal of Geophysical Research: Solid Earth*, 117(B4), n/a–n/a.

Lay, T., Yue, H., Brodsky, E. E., & An, C., 2014. The 1 April 2014 Iquique, Chile, M w 8.1 earthquake rupture sequence, *Geophysical Research Letters*, 41(11), 3818–3825.

Lee, C.-T., 2013. Re-Evaluation of Factors Controlling Landslides Triggered by the 1999 Chi – Chi Earthquake, in *Earthquake-Induced Landslides*, no. June in Springer Natural Hazards, pp. 213–224, Springer Berlin Heidelberg, Berlin, Heidelberg.

Lee, S., Yeh, T., & Lin, Y., 2016. Anomalously Large Ground Motion in the 2016 M L 6.6 Meinong, Taiwan, Earthquake: A Synergy Effect of Source Rupture and Site Amplification, *Seismological Research Letters*, 87(6), 1319–1326.

Lehmann, I., 1936. P', *Publications du Bureau Central Seismologique International, Série A, Travaux Scientifique*, 14, 87–115.

Leonard, M., 2010. Earthquake Fault Scaling: Self-Consistent Relating of Rupture Length, Width, Average Displacement, and Moment Release, *Bulletin of the Seismological Society of America*, 100(5A), 1971–1988.

Leyton, F., Pastén, C., Montalva, G., Hurtado, G., Leopold, A., Ruiz, S., & Saéz, E., 2017. Towards a Geophysical Characterizarion of the Chilean Strong-Motion Stations, in *16th World Conference on Earthquake Engineering*, no. 4943, p. 12, Santiago de Chile.

Li, S., Moreno, M., Bedford, J., Rosenau, M., & Oncken, O., 2015. Revisiting viscoelastic effects on interseismic deformation and locking degree: A case study of the Peru-North Chile subduction zone, *Journal of Geophysical Research: Solid Earth*, 120(6), 4522–4538.

Lin, J., 1991. Divergence measures based on the Shannon entropy, *IEEE Transactions on Information Theory*, 37(1), 145–151.

Lin, P.-S., Chiou, B., Abrahamson, N., Walling, M., Lee, C.-T., & Cheng, C.-T., 2011. Repeatable Source, Site, and Path Effects on the Standard Deviation for Empirical Ground-Motion Prediction Models, *Bulletin of the Seismological Society of America*, 101(5), 2281–2295.

Lindstrom, M. J. & Bates, D. M., 1988. Newton-Raphson and EM Algorithms for Linear Models for Repeated-Measures Data, *Journal of the American Statistical Association*, 83(404), 1014–1022.

Lisle, R. J., 2013. A critical look at the Wallace-Bott hypothesis in fault-slip analysis, *Bulletin de la Societe Geologique de France*, 184(4-5), 299–306.

Lomnitz, C., 2004. Major Earthquakes of Chile: A Historical Survey, 1535-1960, *Seismological Research Letters*, 75(3), 368–378.

Loveless, J. P. & Meade, B. J., 2011. Spatial correlation of interseismic coupling and coseismic rupture extent of the 2011 M W = 9.0 Tohoku-oki earthquake, *Geophysical Research Letters*, 38(17), n/a–n/a.

Lund, B. & Slunga, R., 1999. Stress tensor inversion using detailed microearthquake information and stability constraints: Application to Ölfus in southwest Iceland, *Journal of Geophysical Research: Solid Earth*, 104(B7), 14947–14964.

Marc, O., Hovius, N., Meunier, P., Gorum, T., & Uchida, T., 2016. A seismologically consistent expression for the total area and volume of earthquake-triggered landsliding, *Journal of Geophysical Research: Earth Surface*, 121(4), 640–663.

Marc, O., Meunier, P., & Hovius, N., 2017. Prediction of the area affected by earthquake-induced landsliding based on seismological parameters, *Natural Hazards and Earth System Sciences*, 17(7), 1159–1175.

Marc, O., Behling, R., Andermann, C., Turowski, J. M., Illien, L., Roessner, S., & Hovius, N., 2019. Long-term erosion of the Nepal Himalayas by bedrock landsliding: the role of monsoons, earthquakes and giant landslides, *Earth Surface Dynamics*, 7(1), 107–128.

Mardia, K. V. & Jupp, P. E., 1999. *Directional Statistics*, John Wiley & Sons, Inc.

Markatou, M., Basu, A., & Lindsay, B. G., 1998. Weighted Likelihood Equations with Bootstrap Root Search, *Journal of the American Statistical Association*, 93(442), 740–750.

Martel, S., 2004. Mechanics of landslide initiation as a shear fracture phenomenon, *Marine Geology*, 203(3-4), 319–339.

Martínez-Garzón, P., Ben-Zion, Y., Abolfathian, N., Kwiatek, G., & Bohnhoff, M., 2016. A refined methodology for stress inversions of earthquake focal mechanisms, *Journal of Geophysical Research: Solid Earth*, 121(12), 8666–8687.

Massa, M., Barani, S., & Lovati, S., 2014. Overview of topographic effects based on experimental observations: meaning, causes and possible interpretations, *Geophysical Journal International*, 197(3), 1537–1550.

Massey, C., Townsend, D., Rathje, E., Allstadt, K. E., Lukovic, B., Kaneko, Y., Bradley, B., Wartman, J., Jibson, R. W., Petley, D. N., Horspool, N., Hamling, I., Carey, J., Cox, S., Davidson, J., Dellow, S., Godt, J. W., Holden, C., Jones, K., Kaiser, A., Little, M., Lyndsell, B., McColl, S., Morgenstern, R., Rengers, F. K., Rhoades, D., Rosser, B., Strong, D., Singeisen, C., & Villeneuve, M., 2018. Landslides Triggered by the 14 November 2016 Mw 7.8 Kaikoura Earthquake, New Zealand, *Bulletin of the Seismological Society of America*, 108(3B), 1630–1648.

Matsumoto, J., 1989. Heavy rainfalls over East Asia, *International Journal of Climatology*, 9(4), 407–423.

Maufroy, E., Cruz-Atienza, V. M., & Gaffet, S., 2012. A Robust Method for Assessing 3-D Topographic Site Effects: A Case Study at the LSBB Underground Laboratory, France, *Earthquake Spectra*, 28(3), 1097–1115.

Maufroy, E., Cruz-Atienza, V. M., Cotton, F., & Gaffet, S., 2015. Frequency-scaled curvature as a proxy for topographic site-effect amplification and ground-motion variability, *Bulletin of the Seismological Society of America*, 105(1), 354–367.

Maury, J., Cornet, F. H., & Dorbath, L., 2013. A review of methods for determining stress fields from earthquakes focal mechanisms; Application to the Sierentz 1980 seismic crisis (Upper Rhine graben), *Bulletin de la Societe Geologique de France*, 184(4-5), 319–334.

Mavrommatis, A. P., Segall, P., Uchida, N., & Johnson, K. M., 2015. Long-term acceleration of aseismic slip preceding the M w 9 Tohoku-oki earthquake: Constraints from repeating earthquakes, *Geophysical Research Letters*, 42(22), 9717–9725.

McClung, D. M., 1981. Fracture mechanical models of dry slab avalanche release, *Journal of Geophysical Research: Solid Earth*, 86(B11), 10783–10790.

McKenzie, D. P., 1969. The relation between fault plane solutions for earthquakes and the directions of the principal stresses, *Bulletin of the Seismological Society of America*, 59(2), 591–601.

Meier, M.-A., Werner, M. J., Woessner, J., & Wiemer, S., 2014. A search for evidence of secondary static stress triggering during the 1992 M w 7.3 Landers, California, earthquake sequence, *Journal of Geophysical Research: Solid Earth*, 119(4), 3354–3370.

Meng, L., Huang, H., Bürgmann, R., Ampuero, J. P., & Strader, A., 2015. Dual megathrust slip behaviors of the 2014 Iquique earthquake sequence, *Earth and Planetary Science Letters*, 411, 177–187.

Menke, W., 2012. *Geophysical data analysis: discrete inverse theory: MATLAB edition*, vol. 45, Academic press.

Métois, M., Socquet, A., & Vigny, C., 2012. Interseismic coupling, segmentation and mechanical behavior of the central Chile subduction zone, *Journal of Geophysical Research: Solid Earth*, 117(B3), 1–16.

Métois, M., Socquet, A., Vigny, C., Carrizo, D., Peyrat, S., Delorme, A., Maureira, E., Valderas-Bermejo, M.-C., & Ortega, I., 2013. Revisiting the North Chile seismic gap segmentation using GPS-derived interseismic coupling, *Geophysical Journal International*, 194(3), 1283–1294.

Métois, M., Vigny, C., & Socquet, A., 2016. Interseismic Coupling, Megathrust Earthquakes and Seismic Swarms Along the Chilean Subduction Zone (38° – 18°S), *Pure and Applied Geophysics*, 173(5), 1431–1449.

Meunier, P., Hovius, N., & Haines, A. J., 2007. Regional patterns of earthquake-triggered landslides and their relation to ground motion, *Geophysical Research Letters*, 34(20), 1–5.

Meunier, P., Hovius, N., & Haines, J. A., 2008. Topographic site effects and the location of earthquake induced landslides, *Earth and Planetary Science Letters*, 275(3-4), 221–232.

Meunier, P., Uchida, T., & Hovius, N., 2013. Landslide patterns reveal the sources of large earthquakes, *Earth and Planetary Science Letters*, 363, 27–33.

Michael, A. J., 1984. Determination of stress from slip data: Faults and folds, *Journal of Geophysical Research: Solid Earth*, 89(B13), 11517–11526.

Michael, A. J., 1987. Use of focal mechanisms to determine stress: A control study, *Journal of Geophysical Research*, 92(B1), 357.

Michael, A. J., 1991. Spatial variations in stress within the 1987 Whittier Narrows, California, aftershock sequence: New techniques and results, *Journal of Geophysical Research*, 96(B4), 6303.

Miles, S. B. & Keefer, D. K., 2009. Evaluation of CAMEL - comprehensive areal model of earthquake-induced landslides, *Engineering Geology*, 104(1-2), 1–15.

Montalva, G. A., Bastías, N., & Rodriguez Marek, A., 2017. Ground Motion Prediction Equation for the Chilean Subduction Zone, *Bulletin of the Seismological Society of America*, 107(2), 901–911.

Moore, J. D. P., Yu, H., Tang, C.-H., Wang, T., Barbot, S., Peng, D., Masuti, S., Dauwels, J., Hsu, Y.-J., Lambert, V., Nanjundiah, P., Wei, S., Lindsey, E., Feng, L., & Shibazaki, B., 2017. Imaging the distribution of transient viscosity after the 2016 M w 7.1 Kumamoto earthquake, *Science*, 356(6334), 163–167.

Motagh, M., Schurr, B., Anderssohn, J., Cailleau, B., Walter, T. R., Wang, R., & Villotte, J.-P., 2010. Subduction earthquake deformation associated with 14 November 2007, Mw 7.8 Tocopilla earthquake in Chile: Results from InSAR and aftershocks, *Tectonophysics*, 490(1-2), 60–68.

National Research Institute for Earth Science and Disaster Prevention, 2014. Disaster Research Institute for Science and Technology Research Materials "1: 50,000 landslide topography map".

National Research Institute for Earth Science and Disaster Prevention, 2016. Sediment movement distribution map by the Kumamoto earthquake (updated in 2016.6.27).

Newman, A. V. & Okal, E. A., 1998. Teleseismic estimates of radiated seismic energy: The E/M 0 discriminant for tsunami earthquakes, *Journal of Geophysical Research: Solid Earth*, 103(B11), 26885–26898.

Newmark, N. M., 1965. Effects of Earthquakes on Dams and Embankments, *Géotechnique*, 15(2), 139–160.

Nigam, N. C. & Jennings, P. C., 1969. Calculation of Response Spectra From Strong-Motion Earthquake Records, *Bulletin of the Seismological Society of America*, 59(2), 909–922.

Obara, K. & Kato, A., 2016. Connecting slow earthquakes to huge earthquakes, *Science*, 353(6296), 253–257.

Österreicher, F. & Vajda, I., 2003. A new class of metric divergences on probability spaces and its applicability in statistics, *Annals of the Institute of Statistical Mathematics*, 55(3), 639–653.

Ozawa, S., Nishimura, T., Munekane, H., Suito, H., Kobayashi, T., Tobita, M., & Imakiire, T., 2012. Preceding, coseismic, and postseismic slips of the 2011 Tohoku earthquake, Japan, *Journal of Geophysical Research: Solid Earth*, 117(B7), n/a–n/a.

Pardo, M., Comte, D., & Monfret, T., 2002. Seismotectonic and stress distribution in the central Chile subduction zone, *Journal of South American Earth Sciences*, 15(1), 11–22.

Park, B. U. & Marron, J. S., 1990. Comparison of Data-Driven Bandwidth Selectors, *Journal of the American Statistical Association*, 85(409), 66–72.

Parzen, E., 1962. On Estimation of a Probability Density Function and Mode, *The Annals of Mathematical Statistics*, 33(3), 1065–1076.

Pascal, C., 2002. Interaction of faults and perturbation of slip: Influence of anisotropic stress states in the presence of fault friction and comparison between Wallace-Bott and 3D distinct element models, *Tectonophysics*, 356(4), 307–322.

Patterson, H. D. & Thompson, R., 1971. Recovery of inter-block information when block sizes are unequal, *Biometrika*, 58(3), 545–554.

Patzwahl, R., Mechie, J., Schulze, A., & Giese, P., 1999. Two-dimensional velocity models of the Nazca Plate subduction zone between 19.5°S and 25°S from wide-angle seismic measurements during the CINCA95 project, *Journal of Geophysical Research: Solid Earth*, 104(B4), 7293–7317.

Paudel, P. P., Omura, H., Kubota, T., & Devkota, B., 2008. Characterization of terrain surface and mechanisms of shallow landsliding in upper Kurokawa watershed, Mt Aso, western Japan, *Bulletin of Engineering Geology and the Environment*, 67(1), 87–95.

Pawluszek, K. & Borkowski, A., 2017. Impact of DEM-derived factors and analytical hierarchy process on landslide susceptibility mapping in the region of Rożnów Lake, Poland, *Natural Hazards*, 86(2), 919–952.

Peterson, J. R., 1993. Observations and Modeling of Seismic Background Noise, Tech. rep., Geological Survey (US).

Peyrat, S., Madariaga, R., Buforn, E., Campos, J., Asch, G., & Vilotte, J. P., 2010. Kinematic rupture process of the 2007 Tocopilla earthquake and its main aftershocks from teleseismic and strong-motion data, *Geophysical Journal International*, 182(3), 1411–1430.

Piña Valdés, J., Socquet, A., Cotton, F., & Specht, S., 2018. Spatiotemporal Variations of Ground Motion in Northern Chile before and after the 2014 Mw 8.1 Iquique Megathrust Event, *Bulletin of the Seismological Society of America*, 108(2), 801–814.

Pisarenko, V. F., Kushnir, A. F., & Savin, I. V., 1987. Statistical adaptive algorithms for estimation of onset moments of seismic phases, *Physics of the Earth and Planetary Interiors*, 47(C), 4–10.

Planchon, O. & Darboux, F., 2001. A fast, simple and versatile algorithm to fill the depressions of digital elevation models, *CATENA*, 46(2-3), 159–176.

Pondrelli, S., Salimbeni, S., Morelli, A., Ekström, G., Postpischl, L., Vannucci, G., & Boschi, E., 2011. European – Mediterranean Regional Centroid Moment Tensor catalog: Solutions for 2005 – 2008, *Physics of the Earth and Planetary Interiors*, 185(3-4), 74–81.

Radiguet, M., Cotton, F., Manighetti, I., Campillo, M., & Douglas, J., 2009. Dependency of Near-Field Ground Motions on the Structural Maturity of the Ruptured Faults, *Bulletin of the Seismological Society of America*, 99(4), 2572–2581.

Rivera, L. & Cisternas, A., 1990. Stress Tensor and Fault Plane Solutions for a Population of Earthquakes, *Bulletin of the Seismological Society of America*, 80(3), 600–614.

Roback, K., Clark, M. K., West, A. J., Zekkos, D., Li, G., Gallen, S. F., Chamlagain, D., & Godt, J. W., 2018. The size, distribution, and mobility of landslides caused by the 2015 M w 7.8 Gorkha earthquake, Nepal, *Geomorphology*, 301, 121–138.

Romeo, R., 2000. Seismically induced landslide displacements: A predictive model, *Engineering Geology*, 58(3-4), 337–351.

Rosenblatt, M., 1956. Remarks on Some Nonparametric Estimates of a Density Function.

Rudnicki, J. W. & Freund, L. B., 1981. On energy radiation from seismic sources, *Bulletin of the Seismological Society of America*, 71(3), 583–595.

Ruiz, S., Metois, M., Fuenzalida, A., Ruiz, J., Leyton, F., Grandin, R., Vigny, C., Madariaga, R., & Campos, J., 2014. Intense foreshocks and a slow slip event preceded the 2014 Iquique Mw 8.1 earthquake, *Science*, 345(6201), 1165–1169.

Sahai, H. & Ageel, M. I., 2000. *The Analysis of Variance*, Birkhäuser Boston, Boston, MA, 1st edn.

Sahakian, V., Baltay, A., Hanks, T., Buehler, J., Vernon, F., Kilb, D., & Abrahamson, N., 2018. Decomposing Leftovers: Event, Path, and Site Residuals for a Small Magnitude Anza Region GMPE, *Bulletin of the Seismological Society of America*, XX(Xx).

Sanderson, C. & Curtin, R., 2016. Armadillo: a template-based C++ library for linear algebra, *The Journal of Open Source Software*, 1(Sanderson 2010), 26.

Sato, T., Hiratsuka, S., & Mori, J., 2013. Precursory Seismic Activity Surrounding the High-Slip Patches of the 2011 Mw 9.0 Tohoku-Oki Earthquake, *Bulletin of the Seismological Society of America*, 103(6), 3104–3114.

Sato, T., Chigira, M., & Matsushi, Y., 2017. Topographic and Geological Features of Landslides Induced by the 2016 Kumamoto Earthquake in the Western Part of the Aso Caldera, *DPRI Annuals*, 60B, 431–452.

Savage, J. C., 1966. Radiation from a realistic model of faulting, *Bulletin of the Seismological Society of America*, 56(2), 577–592.

Schnabel, P. B. & Bolton Seed, H., 1973. Accelerations in rock for earthquakes in the western United States, *Bulletin of the Seismological Society of America*, 63(2), 501–516.

Scholz, C. H., 1998. Earthquakes and friction laws, *Nature*, 391(6662), 37–42.

Schurr, B., Asch, G., Rosenau, M., Wang, R., Oncken, O., Barrientos, S., Salazar, P., & Vilotte, J.-P., 2012. The 2007 M7.7 Tocopilla northern Chile earthquake sequence: Implications for along-strike and downdip rupture segmentation and megathrust frictional behavior, *Journal of Geophysical Research: Solid Earth*, 117(B5), n/a–n/a.

Schurr, B., Asch, G., Hainzl, S., Bedford, J., Hoechner, A., Palo, M., Wang, R., Moreno, M., Bartsch, M., Zhang, Y., Oncken, O., Tilmann, F., Dahm, T., Victor, P., Barrientos, S., & Vilotte, J.-P., 2014. Gradual unlocking of plate boundary controlled initiation of the 2014 Iquique earthquake, *Nature*, 512(7514), 299–302.

Schwarz, G., 1978. Estimating the Dimension of a Model, *The Annals of Statistics*, 6(2), 461–464.

Scott, C. P., Arrowsmith, J. R., Nissen, E., Lajoie, L., Maruyama, T., & Chiba, T., 2018. The M 7 2016 Kumamoto, Japan, Earthquake: 3-D Deformation Along the Fault and Within the Damage Zone Constrained From Differential Lidar Topography, *Journal of Geophysical Research: Solid Earth*, 123(7), 6138–6155.

Searle, S., 1971. *Linear Models*, John Wiley & Sons, New York, Chichester, Weinheim, Brisbane, Singapore, Toronto.

Shannon, C. E., 1948. A Mathematical Theory of Communication, *Bell System Technical Journal*, 27(3), 379–423.

Shirahama, Y., Yoshimi, M., Awata, Y., Maruyama, T., Azuma, T., Miyashita, Y., Mori, H., Imanishi, K., Takeda, N., Ochi, T., Otsubo, M., Asahina, D., & Miyakawa, A., 2016. Characteristics of the surface ruptures associated with the 2016 Kumamoto earthquake sequence, central Kyushu, Japan, *Earth, Planets and Space*, 68(1), 191.

Shoja-Taheri, B. Y. J. & Anderson, J. G., 1988. THE 1978 TABAS, IRAN, EARTHQUAKE: AN INTERPRETATION OF THE STRONG MOTION RECORDS, *Bulletin of the Seismological Society of America*, 78(1), 142–171.

Sidle, R. C. & Chigira, M., 2004. Landslides and debris flows strike Kyushu, Japan, *Eos, Transactions American Geophysical Union*, 85(15), 145–156.

Silver, P. G. & Jordan, T. H., 1982. Optimal estimation of scalar seismic moment, *Geophysical Journal of the Royal Astronomical Society*, 70(3), 755–787.

Smith, O. & Adelfang, S., 1981. Gust Model Based on the Bivariate Gamma Probability Distribution, *Journal of Spacecraft and Rockets*, 18(6), 545–549.

Socquet, A., Valdes, J. P., Jara, J., Cotton, F., Walpersdorf, A., Cotte, N., Specht, S., Ortega-Culaciati, F., Carrizo, D., & Norabuena, E., 2017. An 8 month slow slip event triggers progressive nucleation of the 2014 Chile megathrust, *Geophysical Research Letters*, 44(9), 4046–4053.

Somerville, P., Irikura, K., Graves, R., Sawada, S., Wald, D., Abrahamson, N., Iwasaki, Y., Kagawa, T., Smith, N., & Kowada, A., 1999. Characterizing Crustal Earthquake Slip Models for the Prediction of Strong Ground Motion, *Seismological Research Letters*, 70(1), 59–80.

Somerville, P. G., Smith, N. F., Graves, R. W., & Abrahamson, N. a., 1997. Modification of Empirical Strong Ground Motion Attenuation Relations to Include the Amplitude and Duration Effects of Rupture Directivity, *Seismological Research Letters*, 68(1), 199–222.

Song, K., Wang, F., Dai, Z., Iio, A., Osaka, O., & Sakata, S., 2017. Geological characteristics of landslides triggered by the 2016 Kumamoto earthquake in Mt. Aso volcano, Japan, *Bulletin of Engineering Geology and the Environment*, 78(1), 167–176.

Specht, S., Heidbach, O., Cotton, F., & Zang, A., 2017. Data-driven earthquake focal mechanism cluster analysis, Tech. rep., GFZ German Research Centre for Geosciences, Potsdam.

Spudich, B. P., Chiou, B. S. J., Graves, R., Collins, N., & Somerville, P., 2004. A Formulation of Directivity for Earthquake Sources Using Isochrone Theory, *U.S. Geol. Surv. Open-File Rept. 2004-1268*, p. 54.

Spudich, P. & Chiou, B. S. J., 2008. Directivity in NGA earthquake ground motions: Analysis using isochrone theory, *Earthquake Spectra*, 24(1), 279–298.

Spudich, P., Bayless, J., Baker, J., Chiou, B. S. J., Rowshandel, B., Shahi, S., & Somerville, P., 2013. Final Report of the NGA-West2 Directivity Working Group, Tech. Rep. Final, Pacific Earthquake Engineering Research Center.

Stafford, P. J., 2014. Crossed and Nested Mixed-Effects Approaches for Enhanced Model Development and Removal of the Ergodic Assumption in Empirical Ground-Motion Models, *Bulletin of the Seismological Society of America*, 104(2), 702–719.

Stafford, P. J., 2019. Continuous integration of data into ground-motion models using Bayesian updating, *Journal of Seismology*, 23(1), 39–57.

Stein, S. & Wysession, M. E., 2003. *An Introduction to Seismology, Earthquakes, and Earth Structure*, Blackwell Publishing.

Stewart, J. P., Douglas, J., Javanbarg, M., Bozorgnia, Y., Abrahamson, N. A., Boore, D. M., Campbell, K. W., Delavaud, E., Erdik, M., & Stafford, P. J., 2015. Selection of Ground Motion Prediction Equations for the Global Earthquake Model, *Earthquake Spectra*, 31(1), 19–45.

Strasser, F. O., Abrahamson, N. A., & Bommer, J. J., 2009. Sigma: Issues, Insights, and Challenges, *Seismological Research Letters*, 80(1), 40–56.

Strasser, F. O., Arango, M. C., & Bommer, J. J., 2010. Scaling of the Source Dimensions of Interface and Intraslab Subduction-zone Earthquakes with Moment Magnitude, *Seismological Research Letters*, 81(6), 941–950.

Street, J. O., Carroll, R. J., & Ruppert, D., 1988. A Note on Computing Robust Regression Estimates Via Iteratively Reweighted Least Squares, *The American Statistician*, 42(2), 152.

Tang, R., Fan, X., Scaringi, G., Xu, Q., van Westen, C. J., Ren, J., & Havenith, H.-B., 2018. Distinctive controls on the distribution of river-damming and non-damming landslides induced by the 2008 Wenchuan earthquake, *Bulletin of Engineering Geology and the Environment*, pp. 1–19.

Tarantola, A., 2005. *Inverse problem theory and methods for model parameter estimation*, SIAM: Society for Industrial and Applied Mathematics, 1st edn.

Tassara, A. & Echaurren, A., 2012. Anatomy of the Andean subduction zone: three-dimensional density model upgraded and compared against global-scale models, *Geophysical Journal International*, 189(1), 161–168.

Taylor, S. R., Bonner, B. P., & Zandt, G., 1986. Attenuation and scattering of broadband P and S waves across North America, *Journal of Geophysical Research: Solid Earth*, 91(B7), 7309–7325.

Tichelaar, B. W. & Ruff, L. J., 1993. Depth of seismic coupling along subduction zones, *Journal of Geophysical Research: Solid Earth*, 98(B2), 2017–2037.

Tinti, E., Fukuyama, E., Piatanesi, A., & Cocco, M., 2005. A Kinematic Source-Time Function Compatible with Earthquake Dynamics, *Bulletin of the Seismological Society of America*, 95(4), 1211–1223.

Tompkins, M. J. & Christensen, N. I., 2001. Ultrasonic P - and S -wave attenuation in oceanic basalt, *Geophysical Journal International*, 145(1), 172–186.

Torgoev, A. & Havenith, H. B., 2016. 2D dynamic studies combined with the surface curvature analysis to predict Arias Intensity amplification, *Journal of Seismology*, 20(3), 711–731.

Townend, J. & Zoback, M. D., 2001. Implications of earthquake focal mechanisms for the frictional strength of the San Andreas fault system, *Geological Society, London, Special Publications*, 186(1), 13–21.

Travasarou, T., Bray, J. D., & Abrahamson, N. A., 2003. Empirical attenuation relationship for Arias Intensity, *Earthquake Engineering & Structural Dynamics*, 32(7), 1133–1155.

Tucker, L. R., 1951. *A method for synthesis of factor analysis studies*, Washington, DC: Department of the Army.

Uchide, T., Horikawa, H., Nakai, M., Matsushita, R., Shigematsu, N., Ando, R., & Imanishi, K., 2016. The 2016 Kumamoto – Oita earthquake sequence: aftershock seismicity gap and dynamic triggering in volcanic areas, *Earth, Planets and Space*, 68(1), 180.

Vackar, J., Burjanek, J., & Zahradnik, J., 2015. Automated Detection of Long-Period Disturbances in Seismic Records; MouseTrap Code, *Seismological Research Letters*, 86(2A), 442–450.

Vavryčuk, V., 2011. Principal earthquakes: Theory and observations from the 2008 West Bohemia swarm, *Earth and Planetary Science Letters*, 305(3-4), 290–296.

Vine, F. J. & Matthews, D. H., 1963. Magnetic Anomalies Over Oceanic Ridges, *Nature*, 199(4897), 947–949.

von Neumann, J., 1951. *Various techniques used in connection with random digits*, vol. 12, U. S. Nat. Bureau of Standards.

von Rebeur-Paschwitz, E., 1889. The Earthquake of Tokio, April 18, 1889, *Nature*, 40(1030), 294–295.

von Specht, S., Heidbach, O., Cotton, F., & Zang, A., 2018. Uncertainty reduction of stress tensor inversion with data-driven catalogue selection, *Geophysical Journal International*, 214(3), 2250–2263.

Wallace, R. E., 1951. Geometry of Shearing Stress and Relation to Faulting, *The Journal of Geology*, 59(2), 118–130.

Wang, R., 2003. Computation of deformation induced by earthquakes in a multi-layered elastic crust—FORTRAN programs EDGRN/EDCMP, *Computers & Geosciences*, 29(2), 195–207.

Wang, R., Schurr, B., Milkereit, C., Shao, Z., & Jin, M., 2011. An Improved Automatic Scheme for Empirical Baseline Correction of Digital Strong-Motion Records, *Bulletin of the Seismological Society of America*, 101(5), 2029–2044.

Wang, Y.-J. & Ma, K.-F., 2015. Investigation of the Temporal Change in Attenuation Within the Ruptured Fault Zone of the 1999 Mw7.3 Chi-Chi, Taiwan Earthquake, *Pure and Applied Geophysics*, 172(5), 1291–1304.

Wang, Y.-J., Ma, K.-F., Mouthereau, F., & Eberhart-Phillips, D., 2010. Three-dimensional Qp - and Qs -tomography beneath Taiwan orogenic belt: implications for tectonic and thermal structure, *Geophysical Journal International*, 180(2), 891–910.

Warren, L. M., 2014. Dominant fault plane orientations of intermediate-depth earthquakes beneath South America, *Journal of Geophysical Research: Solid Earth*, 119(7), 5762–5785.

Weber, B., 2002. Tragwerksdynamik: Vorlesung, Sommersemester 2002, p. 170.

Wegener, A., 1915. Die Entstehung der Kontinente und Ozeane: Braunschweig, *Sammlung Vieweg*, 23, 94.

Wegener, A., 1924. The origin of oceans and continents, *Trans. JGA Skerl. Originally published as Die Entstehung der Kontinente und Ozeane, 3rd ed.(Braunschweig: Friedrich Vieweg und Sohn, 1922). New York: Dutton.*

Wessel, P., Smith, W. H. F., Scharroo, R., Luis, J., & Wobbe, F., 2013. Generic Mapping Tools: Improved version released, *EOS Trans. AGU*, 94(45), 409–410.

Weston, J., Ferreira, A. M., & Funning, G. J., 2012. Systematic comparisons of earthquake source models determined using InSAR and seismic data, *Tectonophysics*, 532-535, 61–81.

Wielandt, E. & Streckeisen, G., 1982. The leaf-spring seismometer: Design and performance, *Bulletin of the Seismological Society of America*, 72(6A), 2349–2367.

Wilson, D., Ringler, A. T., & Hutt, C. R., 2017. Detection and Characterization of Pulses in Broadband Seismometers, *Bulletin of the Seismological Society of America*, 107(4), 1773–1780.

Wolfinger, R. & O'connell, M., 1993. Generalized linear mixed models a pseudo-likelihood approach, *Journal of Statistical Computation and Simulation*, 48(3-4), 233–243.

Wooddell, K. E. & Abrahamson, N. A., 2014. Classification of Main Shocks and Aftershocks in the NGA-West2 Database, *Earthquake Spectra*, 30(3), 1257–1267.

Xu, P., 2004. Determination of regional stress tensors from fault-slip data, *Geophysical Journal International*, 157(3), 1316–1330.

Yagi, Y., Okuwaki, R., Enescu, B., Kasahara, A., Miyakawa, A., & Otsubo, M., 2016. Rupture process of the 2016 Kumamoto earthquake in relation to the thermal structure around Aso volcano, *Earth, Planets and Space*, 68(1).

Yamada, M., Heaton, T., & Beck, J., 2007. Real-Time Estimation of Fault Rupture Extent Using Near-Source versus Far-Source Classification, *Bulletin of the Seismological Society of America*, 97(6), 1890–1910.

Yamada, M., Kumagai, H., Matsushi, Y., & Matsuzawa, T., 2013. Dynamic landslide processes revealed by broadband seismic records, *Geophysical Research Letters*, 40(12), 2998–3002.

Yamada, M., Mangeney, A., Matsushi, Y., & Matsuzawa, T., 2018. Estimation of dynamic friction and movement history of large landslides, *Landslides*, d(April), 1–12.

Yoffe, E. H., 1951. LXXV. The moving griffith crack, *The London, Edinburgh, and Dublin Philosophical Magazine and Journal of Science*, 42(330), 739–750.

Yokota, Y. & Koketsu, K., 2015. A very long-term transient event preceding the 2011 Tohoku earthquake, *Nature Communications*, 6(1), 5934.

Yoshida, K., Miyakoshi, K., Somei, K., & Irikura, K., 2017. Source process of the 2016 Kumamoto earthquake (Mj7.3) inferred from kinematic inversion of strong-motion records, *Earth, Planets and Space*, 69(1), 64.

Youngs, R., Abrahamson, N., Sadigh, K., & Makdisi, F., 1995. Magnitude-dependent variance of peak ground acceleration, *Bulletin of the Seismological Society of America*, 85(4), 1161–1176.

Youngs, R. R., Chiou, S.-J., Silva, W. J., & Humphrey, J. R., 1997. Strong Ground Motion Attenuation Relationships for Subduction Zone Earthquakes, *Seismological Research Letters*, 68(1), 58–73.

Yuan, R.-M., Deng, Q.-H., Cunningham, D., Xu, C., Xu, X.-W., & Chang, C.-P., 2013. Density Distribution of Landslides Triggered by the 2008 Wenchuan Earthquake and their Relationships to Peak Ground Acceleration, *Bulletin of the Seismological Society of America*, 103(4), 2344–2355.

Zaliapin, I. & Ben-Zion, Y., 2011. Asymmetric distribution of aftershocks on large faults in California, *Geophysical Journal International*, 185(3), 1288–1304.

Zaliapin, I., Gabrielov, A., Keilis-Borok, V., & Wong, H., 2008. Clustering analysis of seismicity and aftershock identification, *Physical Review Letters*, 101(1), 4–7.

Zang, A. & Stephansson, O., 2010. *Stress field of the Earth's crust*, Springer Science & Business Media.

Zevenbergen, L. W. & Thorne, C. R., 1987. Quantitative analysis of land surface topography, *Earth Surface Processes and Landforms*, 12(1), 47–56.

Zhao, J. X., 2006. Attenuation Relations of Strong Ground Motion in Japan Using Site Classification Based on Predominant Period, *Bulletin of the Seismological Society of America*, 96(3), 898–913.

Ziegler, M. O., Heidbach, O., Zang, A., Martínez-Garzón, P., & Bohnhoff, M., 2017. Estimation of the differential stress from the stress rotation angle in low permeable rock, *Geophysical Research Letters*, 44(13), 6761–6770.

Zoback, M. L., 1992. First- and second-order patterns of stress in the lithosphere: The World Stress Map Project, *Journal of Geophysical Research*, 97(B8), 11703.